THE ROLE OF GROUNDWATER FLOW IN THE GENESIS OF STRATABOUND ORE DEPOSITS : A QUANTITATIVE ANALYSIS

by

Grant Garven

B.Sc. The University of Regina, 1976

M.S. The University of Arizona, 1980

A THESIS SUBMITTED IN PARTIAL FULFILMENT OF

THE REQUIREMENT FOR THE DEGREE OF

DOCTOR OF PHILOSOPHY

in

THE FACULTY OF GRADUATE STUDIES

(Department of Geological Sciences)

We accept this thesis as conforming

to the required standard

THE UNIVERSITY OF BRITISH COLUMBIA

October 1982

In presenting this thesis in partial fulfilment of the requirements for an advanced degree at the University of British Columbia, I agree that the Library shall make it freely available for reference and study. I further agree that permission for extensive copying of this thesis for scholarly purposes may be granted by the head of my department or by his or her representatives. It is understood that copying or publication of this thesis for financial gain shall not be allowed without my written permission.

Department of Geological Sciences

The University of British Columbia
1956 Main Mall
Vancouver, Canada
V6T 1Y3

Date October 6, 1982

TO

AUDREY

ABSTRACT

Many conceptual models have been proposed to explain the fluid-flow mechanism responsible for the origin of carbonate-hosted lead-zinc deposits such as those in the Mississippi Valley and at Pine Point. This study is devoted to the quantitative investigation of one ore-genesis mechanism : gravity-driven groundwater-flow systems.

Numerical modeling techniques are used to develop a self-contained computer code for two-dimensional simulation of regional transport processes along cross sections through sedimentary basins. The finite-element method is applied to solve the steady-state, fluid-flow and heat-transport equations, and a moving-particle random-walk model is developed to predict the dispersion and advection of aqueous components. The program EQ3/EQ6 is used to compute possible reaction-path scenarios at the ore-forming site. Full integration of geochemical calculations into the transport model is currently impractical because of computer-time limitations.

Results of a sensitivity analysis indicate that gravity-driven groundwater-flow systems are capable of sustaining favorable fluid-flow rates, temperatures, and metal concentrations for ore formation near the thin edge of a basin. Dispersive processes render long-distance transport of metal and sulfide in the same fluid an unlikely process in the genesis of large ore deposits, unless metal and sulfide are being added to the fluid along the flow path. The transport of metal in sulfate-type brines is a more defensible model, in which case the presence of reducing agents control the location of ore deposition. Hydrodynamic conditions that could result in ore formation through mixing of two fluids are rare.

The theoretical approach is a powerful tool for gaining insight into the role of fluid flow in ore genesis and in the study of specific ore districts. A preliminary model of the Pine Point deposit suggests paleoflow rates on the order of 1.0 to 5.0 m^3/m^2 yr, paleoconcentrations of zinc on the order of 1.0 to 5.0 mg/kg $\cdot$ H_2O, and paleotemperatures in the range 60°C to 100°C. Under these conditions, the time required for the formation of Pine Point would be on the order of 0.5 to 5.0 million years.

TABLE OF CONTENTS

TABLE OF CONTENTS -- Continued

LIST OF TABLES

LIST OF TABLES -- Continued

LIST OF ILLUSTRATIONS

LIST OF ILLUSTRATIONS -- Continued

LIST OF ILLUSTRATIONS -- Continued

LIST OF ILLUSTRATIONS -- Continued

LIST OF ILLUSTRATIONS -- Continued

LIST OF ILLUSTRATIONS -- Continued

ACKNOWLEDGEMENTS

It is a great pleasure to express my appreciation to Allan Freeze for his invaluable advice, continuous encouragement, and generous support. I am particularly indebted to him for suggesting the research topic, and for the day-to-day interactions that we have shared. Many hours of discussion were shared with Gordon Jamieson, Keith Loague, Tom Nicols, and Jennifer Rulon, which are also sincerely appreciated. It is also a pleasure to acknowledge my discussion with Craig Bethke, Jon Collins, Colin Godwin, Roger Macqueen, and Denis Norton. Brian Hitchon of the Alberta Research Council provided salinity cross sections of Alberta and Keith Williams of the Geological Survey of Canada supplied useful geologic information on the District of Mackenzie. I especially wish to acknowledge the help of Thomas Wolery of the Lawrence Livermore Laboratory for providing access to his geochemical models EQ3/EQ6. The manuscript benefited from the valuable suggestions of Tom Brown, John Sharp Jr., and Leslie Smith.

This research was supported by a grant to Allan Freeze from the Natural Sciences and Engineering Research Council of Canada. The University of British Columbia Computing Centre contributed substantial computer time that helped complete the project. I am also grateful for the scholarship support provided over the period 1979-1982 by the Natural Science and Engineering Research Council of Canada.

CHAPTER 1

INTRODUCTION

Numerical modeling is used in this thesis to gain insight into the role of groundwater flow in the genesis of ore deposits in sedimentary basins. Although this approach to the problem is new, the idea that warm, meteoric-derived fluids are responsible for the origin of many types of ore deposits has been around for over a century. Daubrée (1887) concluded that hot water was the most important agent in the formation of ore deposits. He believed these waters were not always of magmatic origin, but could be meteoric waters that become heated at depth. His theories presuppose the existence of large-scale groundwater-flow systems.

Since the early theories regarding ore genesis, the origins of hydrothermal fluids have been long debated. Three possible sources exist for the warm, saline brines that are known to have formed ore deposits: magmatic, connate, and meteoric. Connate waters refer to those fluids that are trapped in sediments at the time of sedimentation. Compaction of sedimentary column may eventually cause the expulsion of these fluids in subsiding, sedimentary basins. Meteoric waters usually refer to those fluids that are an active part of the earth's hydrologic cycle, and have originated at the land surface. Both connate and meteoric waters can take on a wide variety of chemical compositions, which depend on the original fluid composition, rate of flow, and mineralogy of the porous media, among other factors. The term groundwater is used here to describe any subsurface water, without reference to origin or salinity.

White (1968) concluded that, whatever the fluid origin, an ore-forming, hydrothermal system requires four major characteristics:

(1) A dispersed source of ore constituents, whether it be a sedimentary rock sequence, volcanic flows, or igneous intrusives.

(2) A fluid capable of acquiring ore-forming elements from source beds.

(3) Transport of the ore-forming fluid may require large distances.

(4) A suitable environment of deposition to selectively precipitate ore.

Much research has been devoted to the geology and geochemistry implications of these four characteristics, and a large suite of case studies and data have been accumulated. Groundwater is the fundamental fluid genetically relating all stages of ore deposition and yet modern theories of hydrogeology have not seen widespread application in the field of economic geology. Few studies consider the hydrogeologic influence on the transport of ore-forming fluids, and fewer yet assess the flow rates needed to produce an ore deposit.

This study relates to a specific type of ore occurrence known as an epigenetic, stratabound deposit. The origin of such deposits is widely known to involve the flow of warm, saline fluids through porous media. The term epigenetic means that the fluids deposited the ore minerals after the rocks were consolidated, and the term stratabound is used because the deposits are generally confined to specific beds in a stratigraphic succession. The ores do not occur as concentrated layers, but are found as pore-space fillings, cave and solution-cavity linings, and infilled fracture or breccia zones (Stanton, 1972). Small-scale textures and structures genetically distinguish these ores from other types of mineral deposits that occur in sedimentary beds.

The stratabound ore deposits of epigenetic origin can be grouped into five major associations:

(1) Carbonate-hosted lead-zinc

(2) Sandstone-hosted uranium-vanadium-copper

(3) Shale-and sandstone-hosted copper

(4) Sandstone-hosted lead-zinc

(5) Conglomerate-hosted gold-uranium

In many cases, the ore-bearing strata indicate clear signs that mineralization is largely controlled by permeability and porosity. Mineralogy is usually simple and nondiagnostic. Sphalerite and galena are the dominant sulfides in many ore deposits, but chalcopyrite, pyrite, marcasite and chalcocite are also important. In other deposits, oxides of uranium, vanadium, and copper dominate; and yet in others native copper, gold, and silver form major mining districts. Gangue minerals associated with the ore vary from one group to another. The absence of extensive host-rock alteration, simple structure and mineralogy, and pore-space filling textures provide ample evidence that deposition occurred from aqueous solutions in an environment of relatively low temperature and pressure. The association of deposits with major paleoaquifers also suggests that large volumes of ore-forming fluids played an important role in the formation of the deposits.

The carbonate-hosted lead-zinc association and sandstone-uranium association are by far the most abundant stratabound ore deposits. Important North American lead-zinc ores occur in the upper and middle areas of the Mississippi Valley, the tri-state area of Missouri-Kansas-Oklahoma, the southern Appalachians, the Pine Point area of the Great Slave Lake region, and the Cornwallis Island region of the Canadian Arctic. Sandstone-uranium-type districts are best represented by the deposits of the Colorado Plateau, the Powder River basin in Wyoming, and the Grants district of New Mexico. Both of these ore associations have

received large amounts of geological and geochemical research, which in turn makes them ideal subjects for hydrologic studies. For the purposes of this study, however, only the carbonate-hosted lead-zinc deposits will be discussed in further detail. The interested reader is referred to Stanton (1972) and Wolf (1976) for general references on stratabound deposits, and the papers by Fischer (1968, 1970) and Adler (1976) for further details on the sandstone-uranium associations.

In spite of the large amount of field data on carbonate-hosted lead-zinc deposits, the role of fluid flow in ore genesis has not been clearly established. If paleoaquifer systems acted as conduits for long-distance transport of ore-forming constituents from wide areas, many questions arise as to the mechanism of brine formation and movement, location and area of source beds, porosity and permeability effects on concentration patterns, timing of mineralization, and the flow rates required for the deposition of major ore bodies. There are also fluid-related questions with respect to geochemical supply and geothermal gradients in sedimentary basins.

Theoretical foundations and numerical modeling techniques are well established in both groundwater hydrology and low-temperature, aqueous geochemistry. It should be possible, therefore, to perform quantitative studies of various ore-genesis theories, perhaps even simulate or predict ore occurrence. To the writer's knowledge, no one has yet fully quantified the role of groundwater flow in stratabound ore formation.

Norton and Cathles (1979) have studied the cooling histories of intruded plutons using finite-difference modeling of fluid flow and heat transport. Their work is directed to high-temperature environments accompanying porphyry copper deposits. The first concerted effort to apply groundwater-type calculations in stratabound ore genesis modeling was by

White (1971). His analysis consisted of making one-dimensional estimates of the fluid flow needed to form the White Pine copper deposit, Michigan. White found that a gravity-based flow system provided more than enough flow to deposit the ore body. Sharp (1978) introduced the power of numerical techniques by solving the coupled equations for one-dimensional momentum and energy transport in compacting basins. He showed that compaction of the Ouachita basin, with subsequent faulting, could have generated sufficient flow rates to account for lead-zinc mineralization in southeastern Missouri. The relation between groundwater flow and uranium mineralization in the Colorado Plateau has just begun to be assessed through numerical modeling, as demonstrated by Ortiz et al. (1980) and Sanford (1982).

The purpose of this thesis is to quantitatively evaluate the role of groundwater flow in the genesis of stratabound ore deposits. Special attention is paid to lead-zinc deposits in carbonate rocks for the purpose of illustration, but it is felt that the results of the study have wide application to other types of stratabound ores. The main goal is to establish fundamentals on the physics of ore genesis and the possible constraints imposed on the system by hydrodynamics. Numerical modeling is used to solve the equations governing the flow of variable-density groundwater, heat transport, mass transport of metal or sulfur, and multi-component aqueous equilibria. Because of the limitation of one-dimensional analyses, two-dimensional modeling is utilized. Simulations are first performed in simple, hypothetical cross sections so as to identify the effects of various model parameters. The complexity of the basin is then gradually increased, until it eventually begins to mirror real sedimentary basins. The role of groundwater flow is clarified by documenting how variations in certain parameters constrain the flow rates, subsurface

temperatures, and concentrations of metal in brines moving through a representative basin. An additional goal is to estimate the necessary and sufficient conditions for the formation of a large ore deposit. It is hoped that this approach will also provide quantitative insight into the validity of a model of gravity-driven groundwater flow for stratabound ore deposits. Finally, the thesis presents a preliminary hydrogeologic analysis of the Pine Point ore deposit, Northwest Territories.

CHAPTER 2

CONCEPTUAL MODELS FOR THE ORIGIN OF CARBONATE-HOSTED LEAD-ZINC DEPOSITS OF THE MISSISSIPPI VALLEY TYPE

Lead-zinc deposits in carbonate rocks constitute some of the oldest known ore occurrences in North America and have received a tremendous amount of geologic research. Exploration remains very active, especially in southeastern Missouri, Pine Point, N.W.T., and in the Canadian Arctic. According to Stanton (1972), the carbonate-hosted ore deposits are the principal source of lead and zinc in the United States and Europe, and contribute a significant supply in Canada and northern Africa.

The number of papers devoted to the so-called Mississippi Valley-type deposits are numerous. Recent reviews on the geology and origin can be found in Ohle (1980), and Anderson and Macqueen (in press). Individual deposits differ in many details, but several features are common to all. Table 1 summarizes the important characteristics of carbonate-hosted lead-zinc deposits.

The majority of the ore bodies are found in limestone and dolomite rocks, or nearby sandstone and shale beds. The carbonate host usually occurs as part of a reef structure or barrier complex where dolomitization has played a major role in controlling ore deposition by enhancing the permeability and porosity of the strata. The ore bodies commonly occur in undeformed strata, although fold structures and breccia zones can act to localize mineralization. Igneous intrusives, which could be potential sources of ore solutions, are absent. Most deposits are found at shallow depths (less than 1000 m) and near the margins of large, sedimentary basins.

Table 1. Characteristics of carbonate-hosted lead-zinc deposits (after Snyder, 1968 and Macqueen, 1976)

(1) Ore occurrence in host rock.

In limestone and dolomite.
Near margins of sedimentary basins.
Over basement highs.

(2) Structural patterns of districts.

Ore is not related to major faults.
Minor fractures, dissolution and subsidence control mineralization patterns.

(3) Types of ore-bearing structures.

Stratigraphic traps.
Reefs, bioherms, and associated structures.
Breccias, often associated with solution collapse.
Fractures, solution channels, and caves.
Size of ore body related to size of entraping structures in carbonate strata.

(4) Mineralogical features.

Open-space fillings, replacements less important or absent.
Galena, sphalerite, barite, calcite, dolomite, and quartz are most abundant.
Fluorite, celestite, pyrite, chalcopyrite, native sulfur, and bitumen occur in minor quantities.
Mineral zonation is distinctive in some deposits.
Sulfur-isotope studies indicate shallow crustal sources, probably biogenic origin.
Paragenetic studies difficult to interpret because of changing fluids with time.
Fluid inclusions are mainly Na-Ca-Cl brines.
Temperatures of precipitation range from 50° to $150^{\circ}C$.
Solution of limestone prior and during ore precipitation is common and probably a necessary feature for deposition.

In some regions, the location of ore bodies are clearly related to basement structures such as Precambrian arches. Mineralogy is simple, with galena, sphalerite, barite, calcite, dolomite, and quartz dominating. Secondary in abundance are fluorite, celestite, pyrite, marcasite, chalcopyrite, native sulfur, and bitumen. Fluid-inclusion studies of the sulfide minerals indicate that the ore-forming fluids were basinal brines with salinities of 10% to 30% equivalent weight as NaCl and at temperatures of 50° to $150^{\circ}C$. The geochemical character of the fluids is, in many respects, very similar to present-day oil-field brines (Hitchon, 1977).

Geologic Setting

To demonstrate the detailed nature of a carbonate-hosted lead-zinc deposit requires an examination of individual ore districts. Perhaps more important from the point of view of understanding the role of basinal-brine flow is the regional setting of the ore deposit with respect to the sedimentary basin. For these purposes, we will now take a brief look at two of the larger deposits in North America: Southeast Missouri and Pine Point, Northwest Territories.

Southeast Missouri District

The Southeast Missouri lead deposits occur near the sides of a Precambrian high that crops out as the St. Francois Mountains, about 100 km south of St. Louis. Figure 1 shows the regional geology and location of the mining district, as well as the associated tectonic features of the mid-continent region of the United States. The deposits are found in Cambrian and Ordovician strata that overlie a domal structure known as the Ozark uplift. North of the district, these Paleozoic strata are covered by younger beds that become part of the Illinois basin in the northeast,

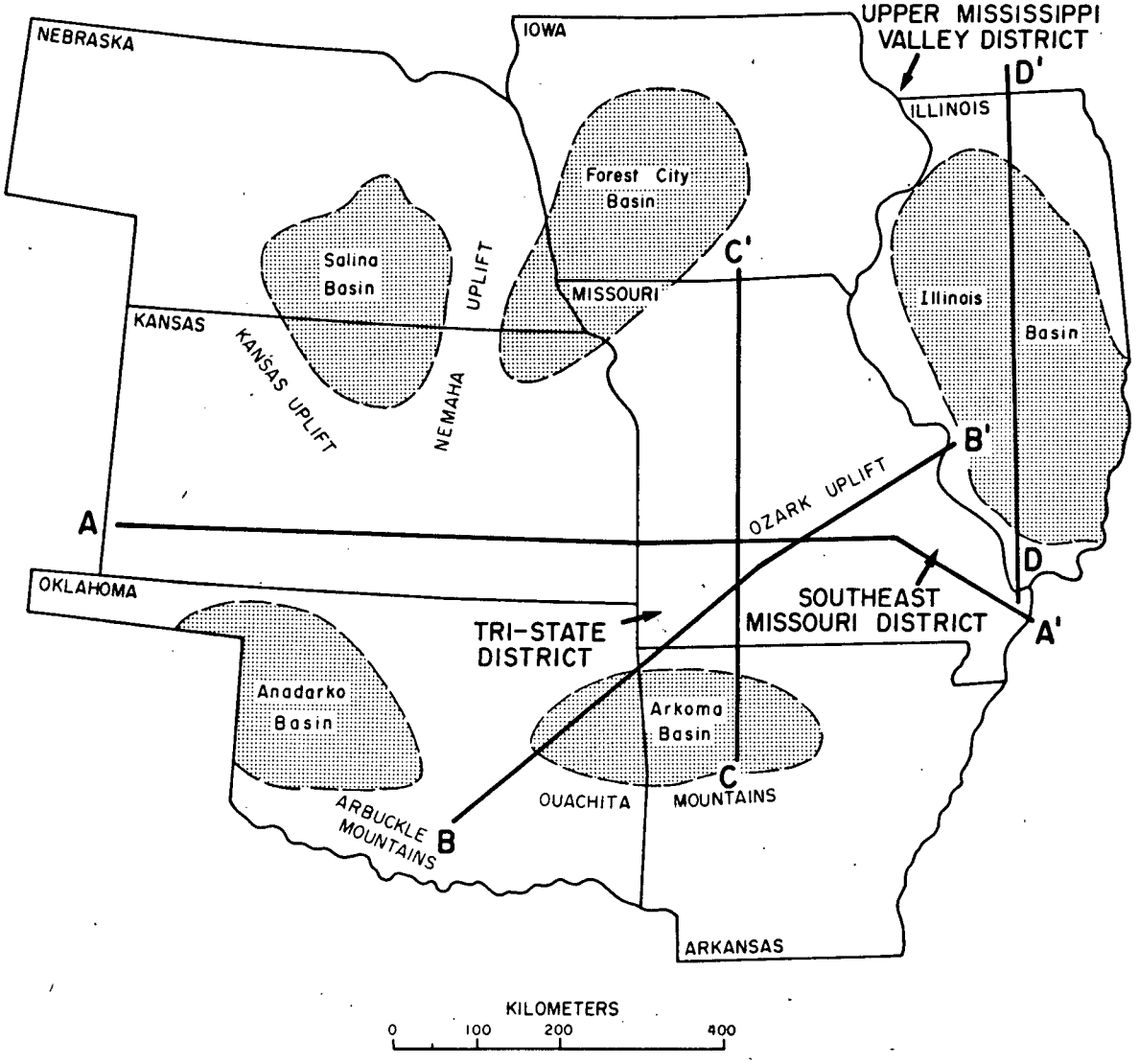

Figure 1. Geologic structure of mid-continent region and location of cross sections (after Oetking, Feray, and Renfro, 1966).

and part of the Forest City basin in the northwest. In the south, the strata extend into the structural complex sections of the Ouachita Mountains, which were uplifted in late Pennslyvanian-Permian (Sharp, 1978). The general stratigraphy of the mid-continent region is depicted on the cross sections given in Figure 2. Notice should be made of the shape and thickness of the sedimentary cover.

Good descriptions of the geology and origin of the deposits in the Southeast Missouri district can be found in Snyder and Gerdemann (1968), Gerdemann and Myers (1972), and Davis (1977). The ore-host strata consist of mainly the Bonneterre Formation and underlying Lamotte Formation. The Lamotte Fm. is a quartz-rich sandstone unit that unconformably rests on the Precambrian surface. It is fine-grained, arkosic, permeable, and attains a thickness of about 100 m. The Bonneterre overlies the Lamotte sandstone beds and it consists predominantly of dolomite. Reef facies and associated structures are the main hosts for the lead deposits. Ore bodies range in size up to tens of millions of tons, which are distributed over two major subdistricts, the Viburnum Trend and Old Lead Belt. Both subdistricts are spatially related to pinchouts, buried ridges, bar reefs, and other features associated with the barrier reef, which formed an island complex in Late Cambrian time. The Bonneterre Formation varies in thickness from 100 m to 400 m in southeast Missouri. About 250 m of dolomite and shale presently overlie the Bonneterre.

Galena is the dominant sulfide mineral in the ore district, but sphalerite and chalcopyrite can become locally abundant. Galena chiefly occurs as sheets along bedding planes, pore-space fillings, and as fracture fillings. Davis (1977) estimates that over 35 million tons of lead was deposited in southeast Missouri. Grades of 10-15% metal are common and

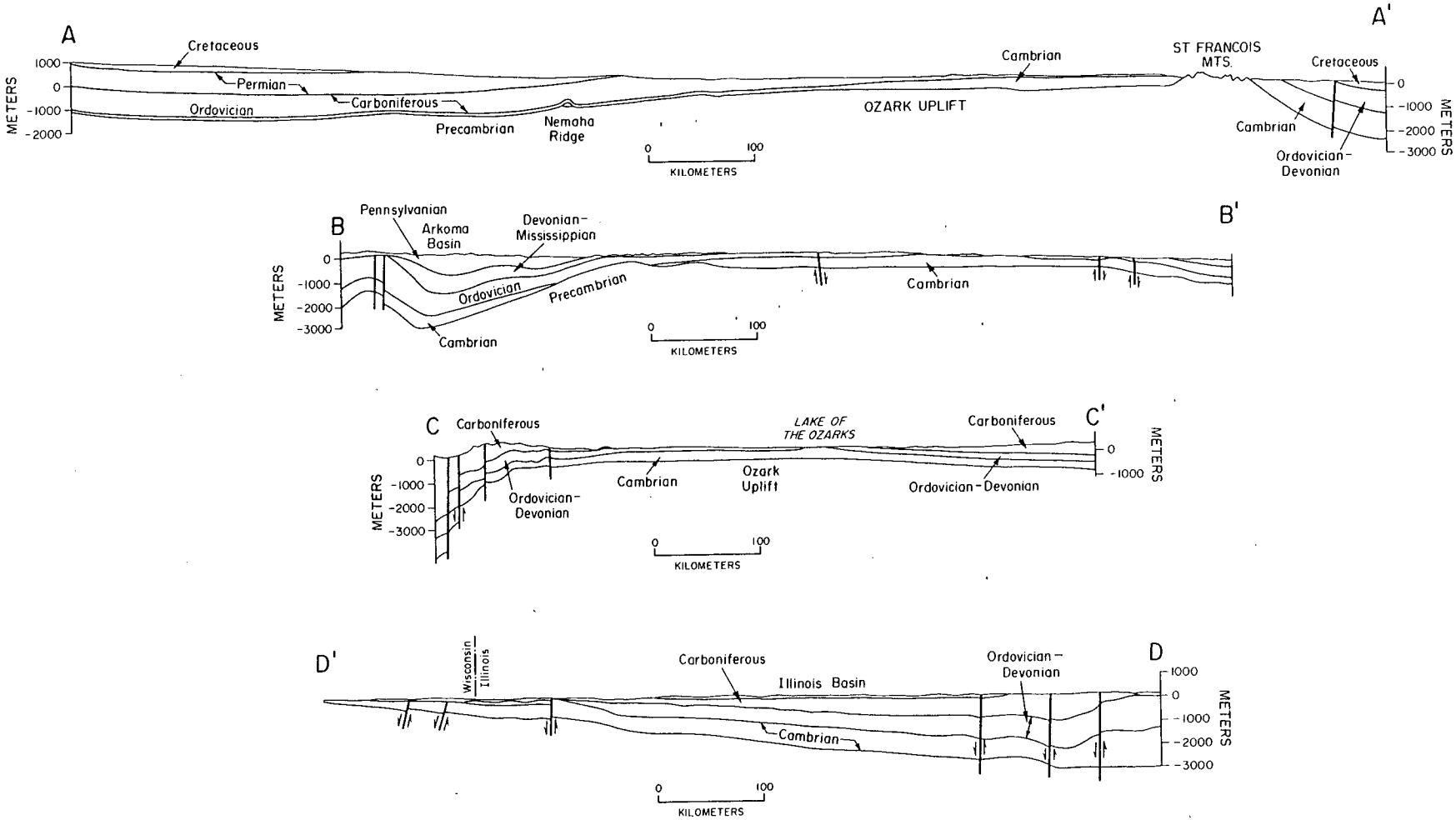

Figure 2. Regional cross sections through mid-continent area (after Oetking, Feray, and Renfro 1960; and Bennison, 1978).

brecciated zones may exceed 30%. Dolomite is the most abundant gangue mineral while calcite and quartz are present in smaller amounts. Textural data suggest that the ore minerals were precipitated and dissolved repetitively during ore formation (Sverjensky, 1981).

According to Snyder and Gerdemann (1968), metal-bearing brines were probably driven out of the adjacent sedimentary basins sometime after compaction of the sediments. Flow was through the very permeable Lamotte Sandstone towards the pinchout edge, where flow was eventually forced up into permeable sections of the Bonneterre Formation. Metals precipitated as sulfides on encountering hydrogen sulfide gas in the porous, carbonate-reef complex. Evidence from fluid inclusion studies suggest temperatures of formation of 80° to $120^{\circ}C$ (Roedder, 1967; Sverjensky, 1981), and brine salinities equivalent to 20-30% NaCl. Recently, Sverjensky (1981) has shown that various lines of geologic evidence suggest that base metals were transported together with reduced sulfur in the same solution to the sites of deposition. Precipitation could have been caused by an increase in pH on reaction of brines with the carbonates or possibly because of a temperature drop.

Pine Point District

Figure 3 shows the geologic setting of the Pine Point ore deposits in relation to the Western Canada sedimentary basin. Pine Point is located on the south shore of Great Slave Lake, about 800 km north of Edmonton, Alberta. As in the case of the Missouri ores, numerous articles have been written on the geology and origin of the Pine Point deposits. Some of the classic references on this deposit include Beales and Jackson (1966), Campbell (1967), Jackson and Beales (1967), and Skall (1975). Recent work by Kyle (1977, 1980, 1981) are the most current contributions

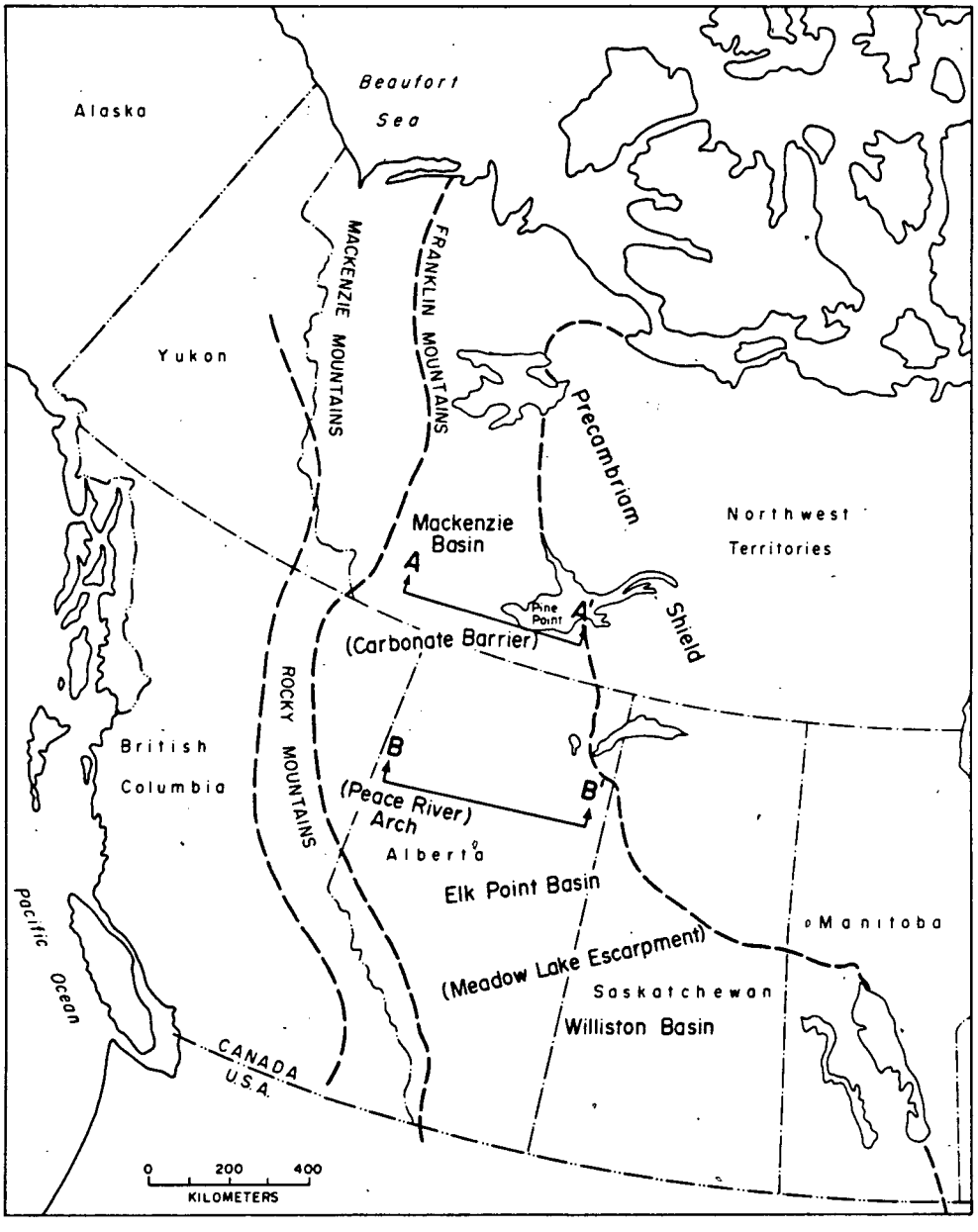

Figure 3. Geologic structure of the Western Canada sedimentary basin (after Bassett and Stout, 1967).

in the literature.

The Pine Point district occurs near the present-day, eastern edge of the Western Canada sedimentary basin where over 500 m of Paleozoic strata rest on crystalline rocks of the Precambrian basement. Norris (1965) reported that up to 100 m of lower Paleozoic (Ordovician?) red beds and evaporitic dolomite overlie the granitic basement in the Great Slave Lake region. Above the red beds is a complex succession of Middle Devonian evaporites and carbonates, which include the ore-bearing dolomite facies of a barrier complex (Figure 3). Collectively, these beds can reach a thickness in excess of 400 m. All of the Paleozoic formations dip gently to the west into much thicker sections of the basin, as shown by the two regional sections in Figure 4. The lines of the cross section are given in Figure 3. To the west, the Middle Devonian strata become overlain by thick shale beds of Upper Devonian age, which in turn are buried by Late Paleozoic and Cretaceous strata. Descriptions regarding the geology of western Canada can be found in McCrossan and Glaister (1964).

The Keg River Barrier separated a deep-water environment of the Mackenzie basin from the back-reef evaporite-forming conditions of the Elk Point basin during the Devonian period. Skall (1975) provides a detailed interpretation of the barrier at Pine Point, and Williams (1981) has prepared several geologic maps of the complex facies patterns associated over the entire length of the barrier. At Pine Point, the barrier-complex strata overlie about 100 m of anhydrite and gypsum of the Chinchaga Formation. The platform of the barrier is built on a 50 m thick, uniform dolomite known as the Keg River Formation. The carbonate-barrier complex is represented by several distinct facies that are collectively known as the Pine Point Group (Skall, 1975). This is the main ore-bearing zone and it reaches a thickness of 150 m. The upper portion of the Pine Point Group contains a

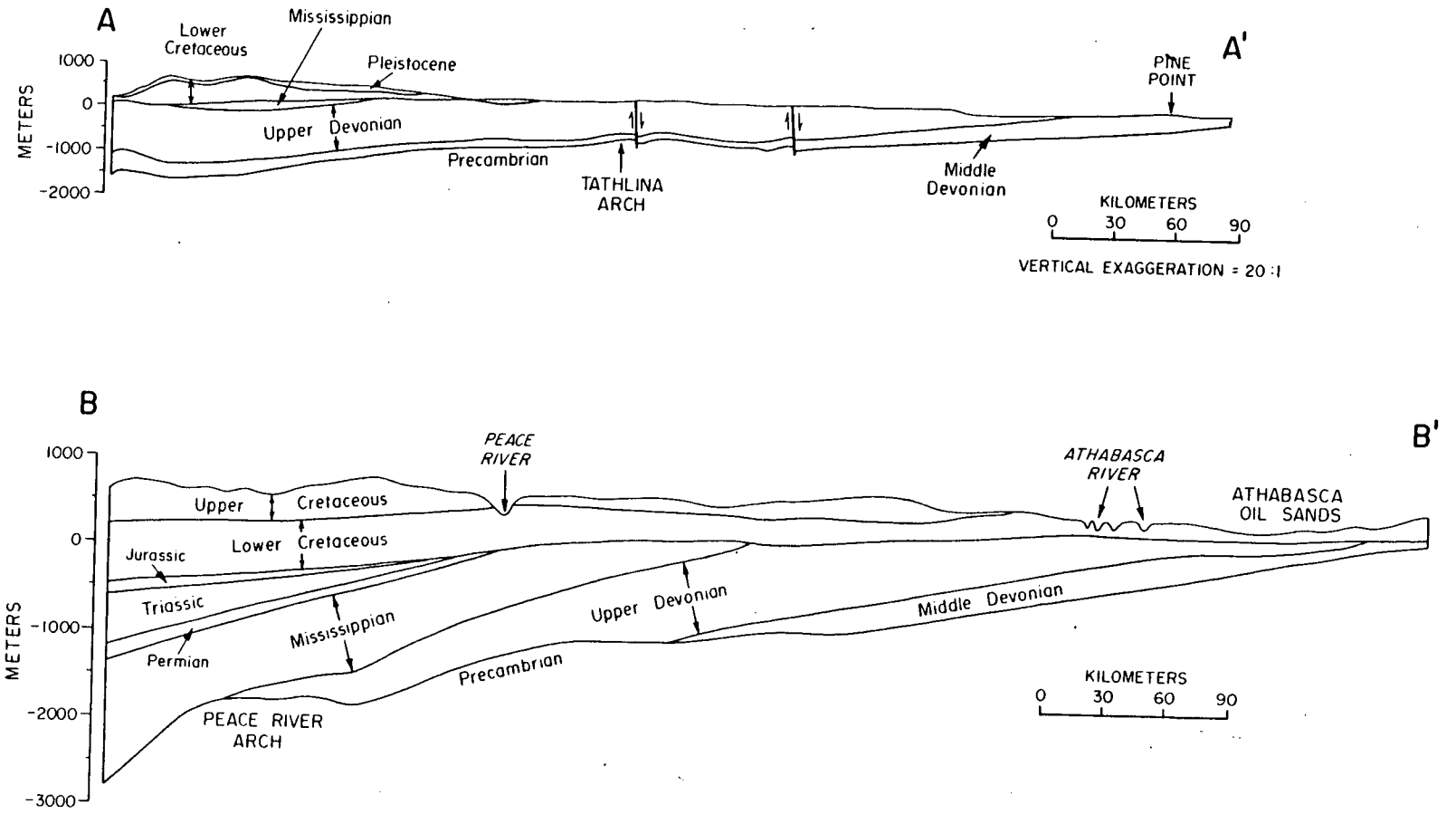

Figure 4. Regional cross sections through the Western Canada sedimentary basin (after Gussow, 1962; and Douglas, et al., 1973).

highly cavernous facies, better known as the Presqu'ile Facies. Over 50 massive and tabular ore bodies have been found in the barrier complex, over an area of 1000 km^2 (Kyle, 1980). Ore-control is largely influenced by paleo-solution features in the karstic facies. Above the Pine Point Group are about 75 m of shale and dolomite of the Watt Mountain and Slave Point Formations.

Sphalerite is the predominant sulfide mineral at Pine Point, followed by galena, pyrite and marcasite. Dolomite is ubiquitous and other gangue minerals include calcite, celestite, anhydrite, and gypsum. Native sulfur is present, and pockets of heavy oil and bitumen are commonly encountered. Sphalerite occurs as encrustations in cavities, as colloform features, and disseminations (Jackson and Beales, 1967). Galena generally tends to form coarser, cavity fillings than sphalerite. Kyle (1977) believes the sphalerite and galena precipitated together, but with the sphalerite probably starting slightly earlier. Approximately 100 million tons of lead-zinc ore is present at Pine Point, and metal grades range around an average of 9% (Kyle, 1980).

Jackson and Beales (1967) proposed that the barrier complex acted as the main conduit for transporting metal-rich brines from shales compacting in the Mackenzie basin, and sulfur from the evaporites of the Elk Point basin. Reduction of sulfur to H_2S(gas) caused precipitation of the ore in the reef complex near Pine Point, because of the abundant supply of organic matter in the area. This scenario of ore genesis fits quite well with the observed field data of mineralization at Pine Point. The work recently presented by Kyle (1980, 1981) also supports the basinal brine hypothesis advanced by Jackson and Beales. Kyle suggests that ore occurrence is strongly controlled on a local scale by the location of breccia zones that

allowed mixing between paleokarst aquifers. Roedder (1968) has estimated, from fluid-inclusion studies, that the ore-forming brines were at temperatures of 51° to 91°C and had salinities 10%-23% NaCl.

Conceptual Models of Ore Genesis

The topic of ore genesis in sedimentary basins has been the subject of much controversy ever since studies of stratabound deposits began. Many conceptual models have been proposed to explain the origin of the ores, especially the carbonate-hosted lead-zinc deposits. Ridge (1976) and Davis (1977) outline the chronological development of the various theories. The general model of warm, metal-rich brines flowing through paleoaquifers and depositing ore at sites where reduced sulfur was available is widely accepted. Fluid inclusion and stable-isotope data, along with many geologic observations, support this basinal-brine model. In spite of the general concensus of this model, Ohle (1980) points out that disagreement still exists as to: the origin of the brine, the driving mechanism for flow, the role of hydrodynamics, the means by which metals and sulfur are transported in solution, the source of reduced sulfur, the nature of the source beds of metal, the causes for precipitation, the timing of mineralization, and the reasons why deposits occur where they are now. Ohle's comments emphasize that there is plenty of room for further research along several avenues. However, there has been progress in placing constraints on certain aspects of the basinal brine model, and this progress is now summarized.

Fluid Flow Mechanism

Consider the schematic cross section of a sedimentary basin shown in Figure 5. It represents two stages in the evolution of a laterally composite basin. The upper section A-B depicts the structure of the basin

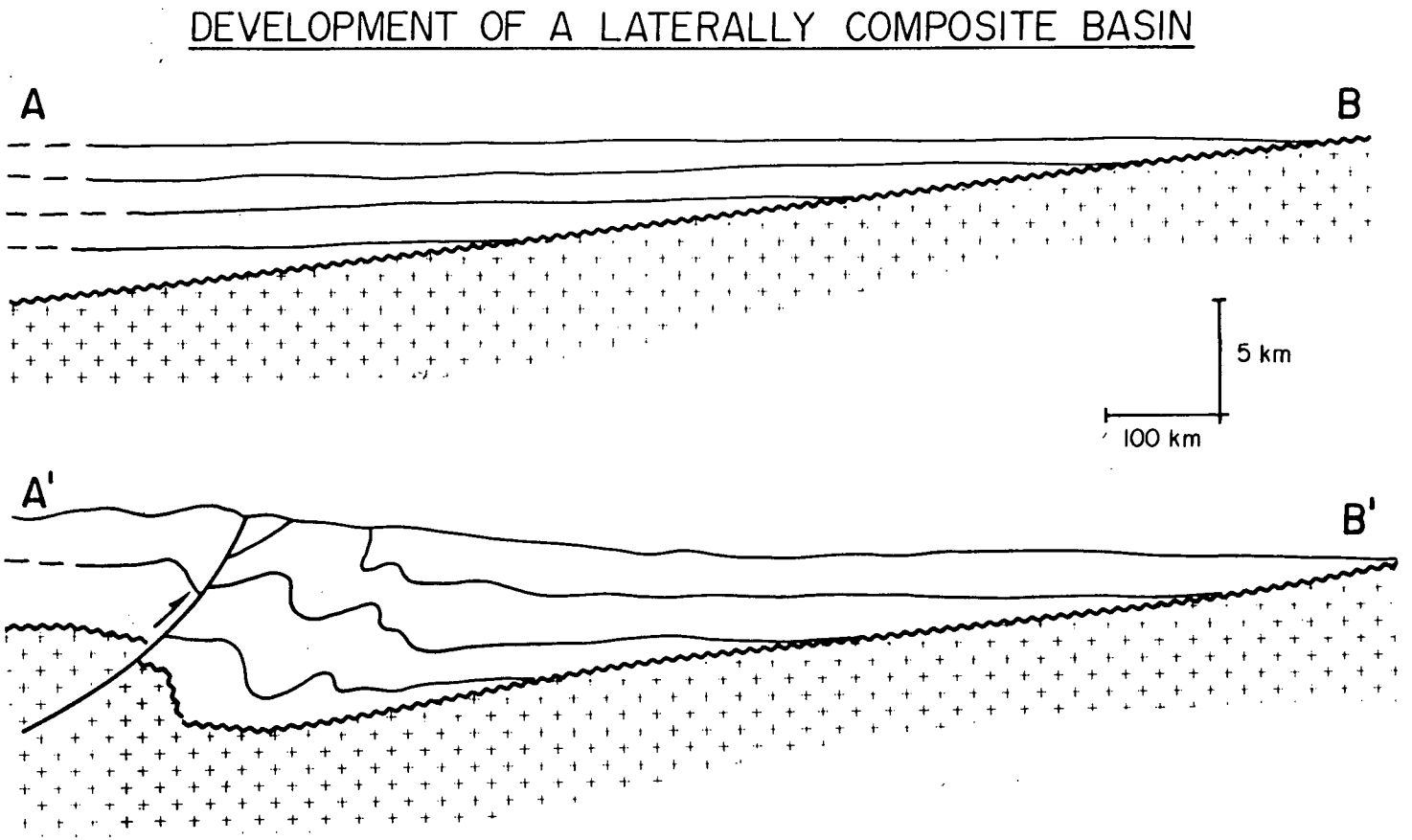

Figure 5. Schematic representation of the youthful and mature stages in the evolution of a sedimentary basin (after Levorsen, 1967).

at a youthful stage when sediment loading causes general subsidence. Shallow, epeiric seas encompass the entire region in the youthful stage. At some later time, gradual and widespread uplift causes the basin to emerge as seas regress from the region. Orogenic movements eventually uplift the "western" end of the basin, which results in deformation of the sedimentary pile and creation of a mountain belt through overthrusting. As orogenesis continues, substantial downwarping may occur, along with deposition of thick continental-type sediments. Section A'-B' in Figure 5 depicts a period in geologic time when tectonic activity in the area is quiescent and the basin has evolved to a mature stage in its history. A topographic gradient is established across the basin and surface-drainage systems are well developed.

This model of basin evolution applies to a large number of sedimentary basins that Levorsen (1967) classifies as laterally composite in origin. He discusses several field examples from all over the world, and their importance as petroleum producers. Many of the sedimentary basins associated with stratabound ore formation are of this type. The sections presented in Figures 2 and 4 serve as good examples for demonstrating the general stratigraphic character and wedge-shaped nature of these basins.

The flow of fluids through sedimentary basins can be caused by the gradients in a variety of energy potentials (van Everdingen, 1968). The potential gradients most important to fluid flow, however, are those components of elevation and pressure that contribute to the fluid potential. Hubbert (1940) showed that the fluid potential represents the mechanical energy per unit mass of fluid, and that flow is always from regions of high energy towards regions in which it is lower. Hubbert also showed that the fluid potential at any point in a basin is simply the hydraulic head multiplied by the acceleration due to gravity. Hydraulic head consists of two

components: the elevation of the point of interest, and the pressure head at that point. Measurement of the field distribution of hydraulic head will determine, therefore, the fluid-flow direction in porous media.

Hitchon (1976) has reviewed the history of the development of fluid-flow models of sedimentary basins, and their implications to stratabound ore genesis. In the youthful-basin stage (Figure 5), compaction of sediments is the primary mechanism for fluid movement. Most of the fluid-potential losses by compaction are incurred soon after deposition, with fluid flow directed upwards to the sea bottom (or downwards with reference to the depositional surface). Continued sedimentation, basin subsidence, and compaction results in further fluid expulsion with burial. Excess pore-fluid pressures may develop in permeable sandstone or carbonate strata if fluid flow becomes restricted by the rapid deposition of low-permeability clays, or other causes. The possibility then arises that faulting could bleed-off this excess pressure by allowing fluid flow up into shallower stratigraphic levels. The development of excess fluid pressures is a temporary phenomena that will eventually dissipate with time, provided faulting does not interrupt the compaction process.

A compaction-driven flow model for driving deeply-buried metal-rich brines into shallow aquifers and out to the basin margin is commonly called upon to explain the origin of carbonate-hosted lead-zinc deposits. Noble (1963) introduced the concept to originally explain a wide variety of stratabound ores, and Dozy (1970) later expanded on the hypothesis for the carbonate-hosted lead-zinc deposits. Jackson and Beales (1967) popularized its possible role in the formation of the Pine Point deposit. Quantitative modeling of compaction in the Ouachita basin by Sharp (1978) has shown that compaction-driven flow would have been sufficient to account for the ore

deposition in southeast Missouri, provided several pulses of compaction-expelled brines reached the edge of the basin.

In the mature stage of a sedimentary basin's evolution, the effects of compaction are likely to be negligible as the basin is now uplifted and all of the strata are well indurated (Figure 5). Any transient processes initiated through burial are also likely to have long dissipated. Fluid flow is now primarily driven through the potential gradient created by the water-table configuration, which is commonly a subdued replica of the basin topography. Groundwater flow is from areas of higher elevation to regions of lower elevation. The exact character of the flow paths depends upon the size of the basin and its shape, the relief on the water table, and the nature of permeability changes in the subsurface. Figure 6 demonstrates the conceptual picture of the gravity-driven fluid-flow system in a large basin. Fluid flow is directed across the thick shale sequence and focused into an extensive basal carbonate aquifer, which discharges at the basin margin. Unlike the compaction-driven model, regional gravity-driven flow is most appropriately treated as a steady-state system. So long as the topography of the basin is not changing appreciably, compared to the total thickness of the basin, then the case of dynamic equilibrium (steady state) is a valid approximation to the fluid flow regime (Freeze and Cherry, 1979, p. 194). This condition is probably satisfied in mature basins, at least for time intervals shorter than a few million years.

Quantitative studies of steady-state groundwater flow systems was begun by Tóth (1962, 1963), and later expanded upon by Freeze and Witherspoon (1966, 1967, 1968) who used numerical models to investigate a wide variety of hypothetical cross sections and field problems. Both studies sought to examine the effects of topography and geology on groundwater flow. Figures 7

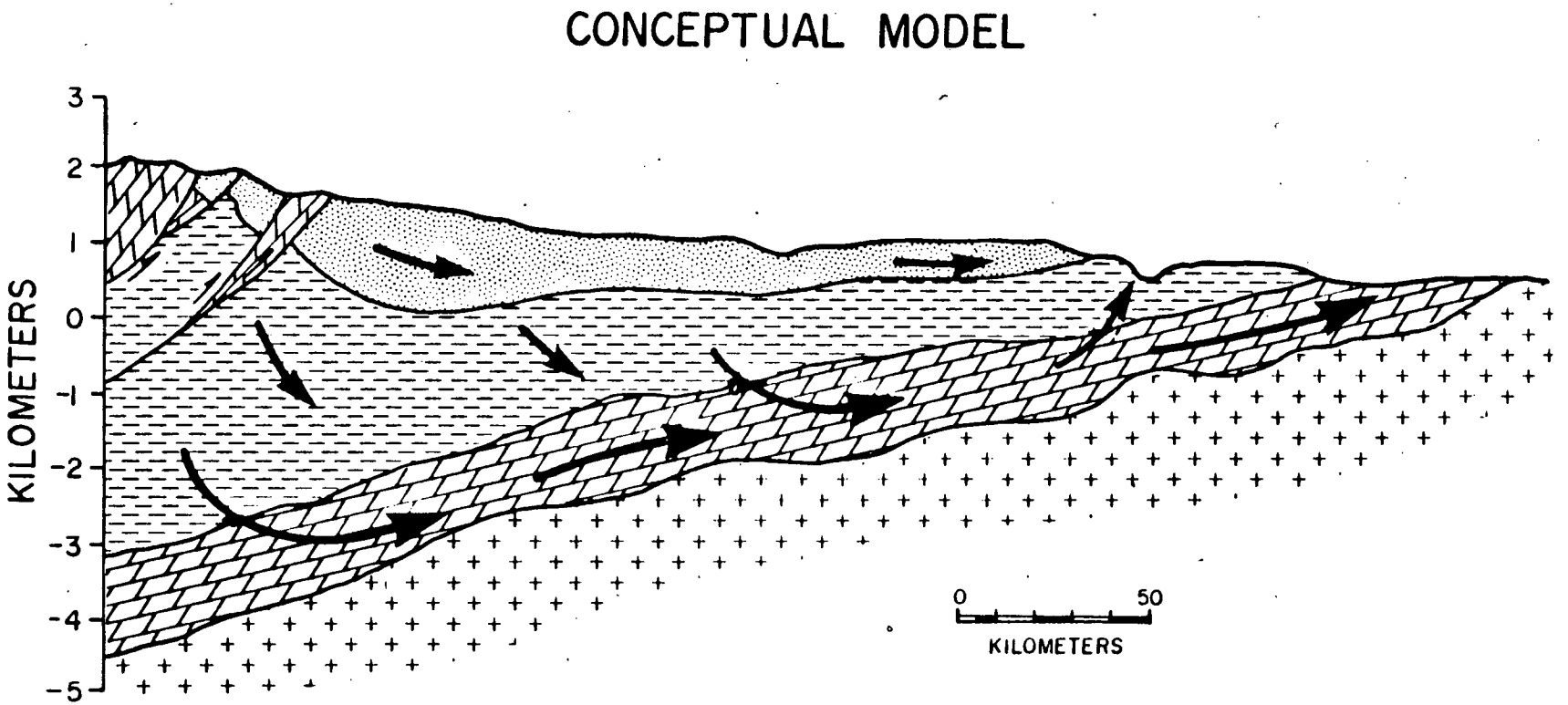

Figure 6. Conceptual model of gravity-driven fluid flow in sedimentary basins.

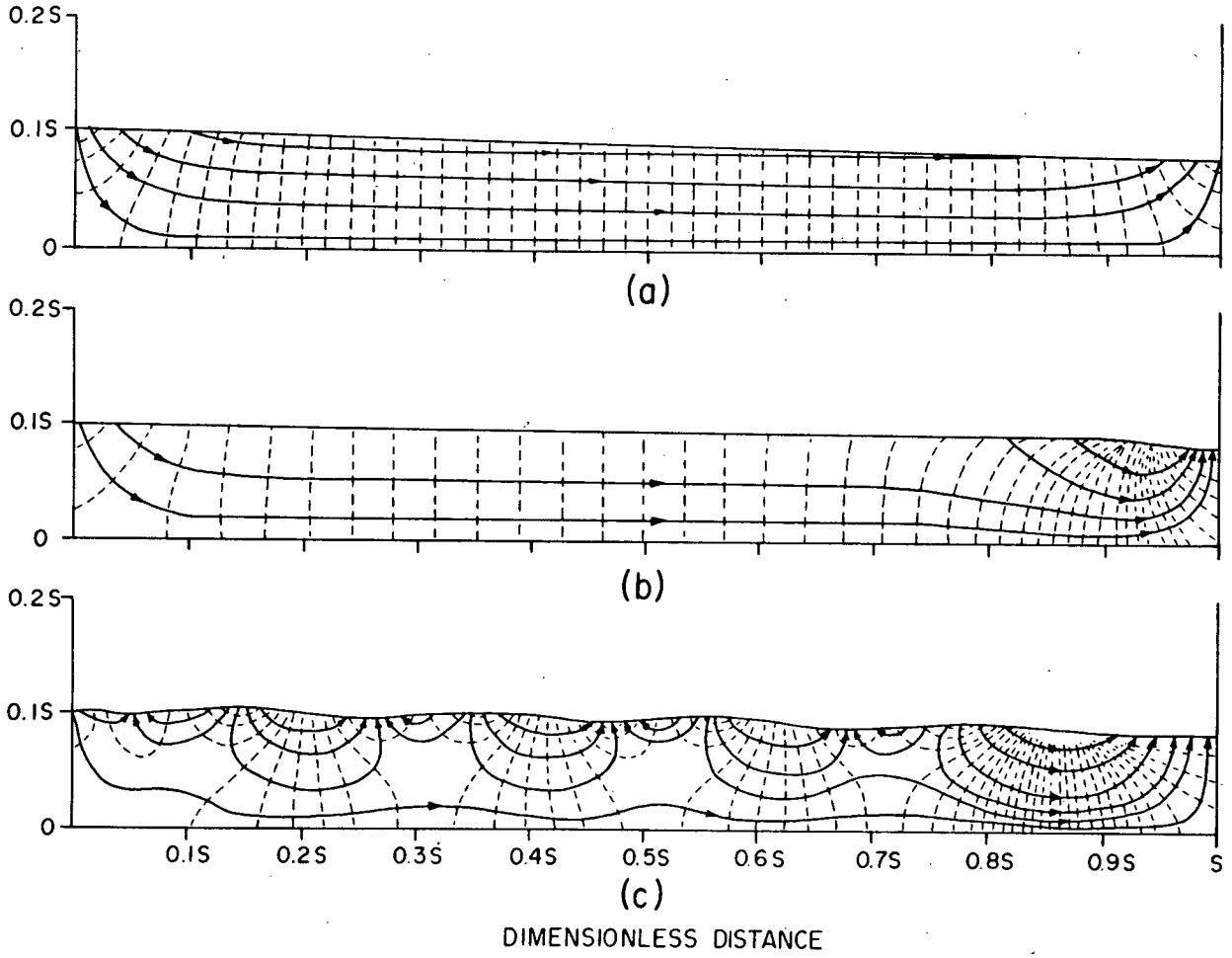

Figure 7. Effect of topography on regional groundwater flow (after Freeze and Witherspoon, 1967).

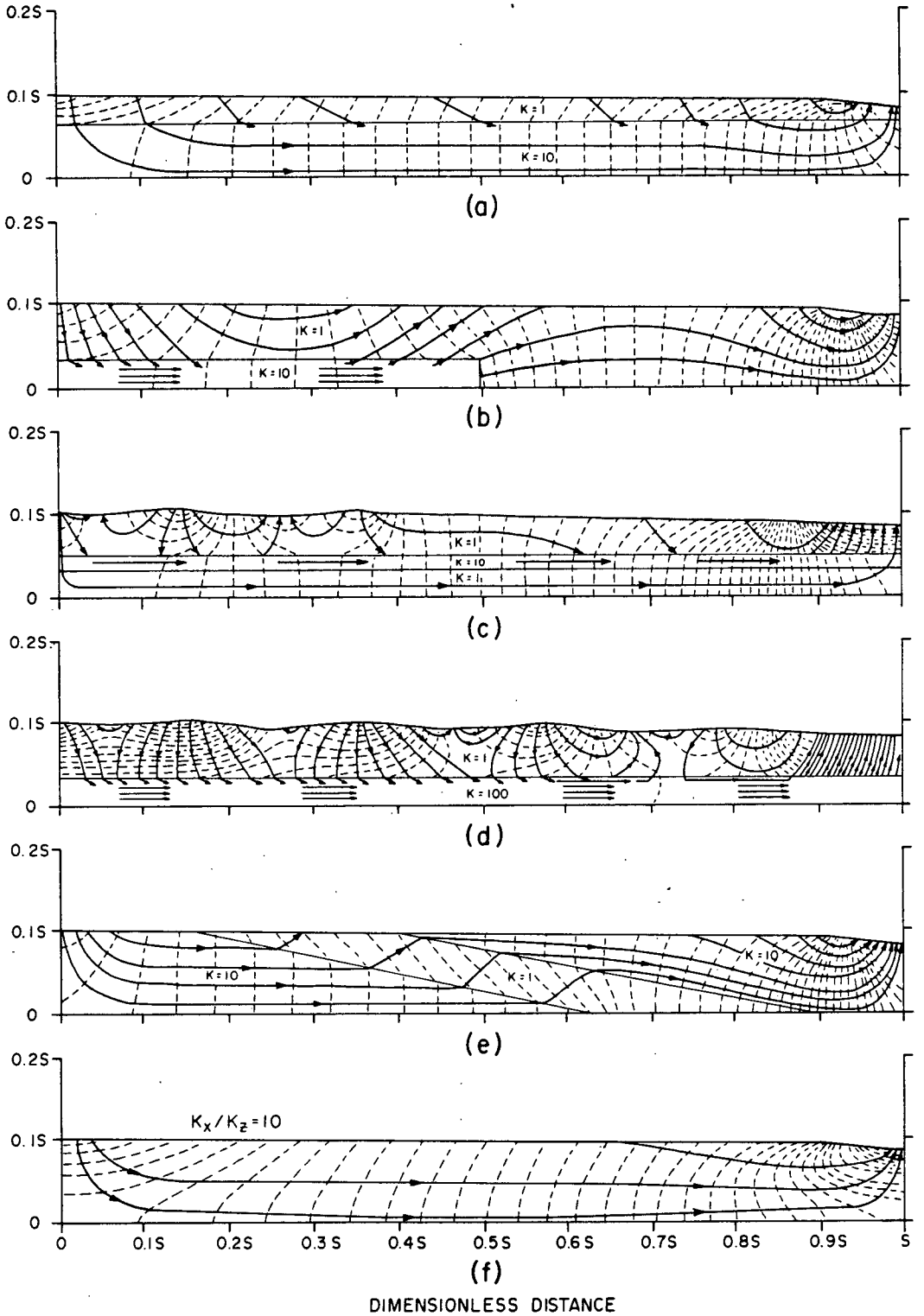

Figure 8. Effect of geology on regional groundwater flow (after Freeze and Witherspoon, 1967).

and 8 show some of the modeling results given by Freeze and Witherspoon (1967). The flow nets shown here are of a true-to-scale basin section, which is of dimensionless length S and thickness of 0.1S. The dimensionless form of the models allow the results to be applied to any size of sedimentary basin with similar length-to-depth ratio. The dashed lines (Figures 7, 8) represent hydraulic-head contours, and the direction of fluid flow is indicated by flowlines. The upper surface of the region of flow represents the water table, while the bottom represents an impermeable basement. The two vertical boundaries are also impermeable and coincide with regional groundwater divides. These occur because of the symmetry imposed on flow systems by valleys and highlands. Fluid flow is from areas of high fluid potential (hydraulic head) to regions of lower fluid potential.

In Figure 7, the effect of topography is demonstrated with three models, one with a constant slope on the water table, one with a break in slope near the right side of the basin, and another with an irregular water-table configuration. All of the sections assume a homogeneous and isotropic porous medium. The uniform slope of Figure 7a creates a single flow system across the entire basin. The change in slope in Figure 7b produces two flow systems; a regional system and a local flow system, both of which discharge into the valley depression. Numerous recharge and discharge subsystems are superimposed on the regional system when an irregular topography exists in a basin (Figure 7c). Depending on its original location in the basin, a water particle containing metal may be discharged after a short distance of transport or carried into the large flow system.

Figure 8 shows the effect of geology on regional flow patterns. The relative hydraulic conductivity (permeability) is indicated by the dimensionless number in each layer. The main effect of a buried aquifer is

to focus flow down across lower permeability strata in recharge areas, and discharge flow up across the low permeability beds in discharge areas. Increasing the permeability contrast between layers increases the hydraulic-head gradients in the overlying aquitard. Notice in Figure 8b that the presence of a pinchout causes a discharge of flow near the center of the basin, which would not have been interpreted from considering topography alone (Figure 7b). The combined effect of irregular topography and geology is shown in Figures 8c and 8d. Topographic effects will not always dominate flow control in a basin, especially if a highly permeable aquifer is present (Figure 8d). More complicated flow patterns can also arise in the case of dipping beds (Figure 8e), and if the rocks are anisotropic with respect to hydraulic conductivity (Figure 8f).

The concept of gravity-driven fluid-flow regimes in stratabound ore genesis has not received the same attention as that given to the compaction-driven flow mechanism over recent years, at least in North America. This model proposes that small amounts of ore-forming constituents are leached from the sedimentary section and transported by gravity-driven flow systems to sites of deposition, perhaps at the discharge end of the basin. It is clear from Figure 6, that the large volumes of low-permeability shales would constitute potential source beds and at the same time serve to focus fluid flow down into carbonate or sandstone aquifers. The action of water-rock reactions, membrane filtration, and presence of evaporites would easily transform the shallow meteoric waters into brines as they flow through deeper parts of the basin. The main requirement is that some form of paleotopographic gradient exist in order to drive the gravity-based flow systems. Cox (1911) and Siebenthal (1915) advocated this mechanism for the origin of lead-zinc ores of the Mississippi Valley district, and it is

commonly cited to explain the genesis of sandstone-hosted uranium deposits (Butler, 1969; Adler, 1976). Regional hydrodynamic studies by Hitchon (1969a, 1969b) and Tóth (1978) of Alberta confirm the importance of gravity-driven cross-formational flow in sedimentary basins. Tóth (1980) has also demonstrated that gravity-induced flow is the principal agent in the transport and accumulation of hydrocarbons in geologically mature basins.

We can conclude, therefore, that both compaction-and gravity-driven flow systems are important mechanisms of flow. The particular model that dominates depends on the stage of basin evolution. Hitchon (1976, 1977) is the one researcher who has emphasized the importance of both mechanisms in the origin of oil fields and ore deposits. He believes that compaction may be a more efficient generator of hydrocarbons, and that gravity flow may be more efficient for metals. Models of the type given in Figures 7 and 8 should help to quantify the importance of groundwater flow systems in ore genesis. This subject is treated in greater detail in the chapters to follow.

Fluid Composition and Temperature

A large amount of fluid-inclusion data has proven beyond little doubt that the carbonate-hosted lead-zinc deposits were formed by metal-bearing brines of sodium-calcium-chloride composition with salinities of 10-30% NaCl (Roedder, 1976). Some inclusions contain high concentrations of metal and methane, and droplets of oil are not uncommon. Concentration of reduced sulfur is generally low.

The saline character of fluid inclusions has led a number of authors to make comparisons of present-day oil-field brines to ancient ore-forming solutions. The work by Billings et al. (1969), Carpenter et al. (1974), and Hitchon (1977) support the hypothesis that basinal brines are in fact the ore-forming fluids. The origin of present-day brines in

sedimentary basins can be attributed to a number of subsurface processes. Suffice to say that the presence of evaporites, water-rock interactions, and membrane filtration are mainly responsible for the occurrence of brines. Bredehoeft et al. (1963) discuss a mathematical model for membrane filtration, which is capable of producing brine salinities similar to those observed in the deep subsurface. Other types of processes may be equally important.

The temperature of mineralization can also be estimated from inclusion data. The majority of carbonate-hosted lead-zinc deposits fall in the range of 50°C to 150°C, with temperatures around 100°C accepted as the average or representative value of this ore-forming environment (Roedder, 1967). At least a few kilometers of sediments are needed to attain these temperatures under the average geothermal gradients existing today. The dilemma facing us here is that most of the ores occur at shallow depth, and based on geologic evidence were probably formed at depths less than 2 km. Locally high geothermal gradients at the depositional site could be caused by a heat source, but heat redistribution due to fluid flow from deep in the basin is likely a better explanation (White, 1974; Hanor, 1979).

Source, Transport, and Precipitation of Metals

Fundamental to the basinal-brine model is the concept of an original source bed from which metal species can be expelled into aqueous solutions, either by compaction flow or gravity-based flow. Eventually the metals are transported through aquifers and precipitated at the depositional site. Jackson and Beales (1967) argue that shales make good source rocks because they usually contain more Zn and Pb than other lithologies. They favored a mechanism where the metal ions would be released from the clays upon compaction of the basin. Macqueen (1976) and Kyle (1980) make the point that early compaction of sediments result in large volumes of low salinity

waters, which are poorer carriers of metals than highly saline brines. Granite, carbonates, evaporites, feldspathic sandstone, and red-bed cements have also been considered as suitable source beds by various authors. Each lithology has its pros and cons, depending on the geology of the basin in question. For carbonate-hosted lead-zinc deposits, shales and organic-rich carbonates remain the most attractive source beds for metals. Carpenter et al. (1974) concluded that cross-formational flow of potassium-rich brines across marine shales is an important mechanism for the origin of metal-rich brines.

The exact mechanism by which metals are released from source rocks is unclear. According to Anderson and Macqueen (in press), the release of metals may take place through desorption phenomena, recrystallization processes, and thermal alteration of metal-organic complexes. Whatever the mechanism, field observations and experimental studies confirm that chloride-rich brines can leach trace amounts of metals from various rock types (Ellis, 1968; Bischoff et al., 1981; and others).

The geochemistry of metal transport and precipitation has received a large amount of theoretical and experimental research. Because of this, the geochemistry of hydrothermal solutions has become the most quantitative branch of ore-genesis studies. Excellent review papers on the geochemistry of the carbonate-hosted lead-zinc deposits are provided by Anderson (1978), Barnes (1979), Skinner (1979), and Anderson and Macqueen (in press).

Skinner (1979) summarizes the recent findings on the general chemistry of hydrothermal fluids. The formation of complex ions in solution is now known to be the primary mechanism for transporting metal species in ore-depositing flow systems. Complexing substantially increases the solubilities of metals, while also inhibiting sulfide precipitation. This

provides a means for the long-distance transport of metals in fluid flow systems. Complexes also show greater increases in metal solubility with increasing temperatures.

Both chloride complexes and sulfide complexes have been called upon to explain the transport of metals in ore genesis. Chloride complexes form in the presence of high concentrations of chloride ion and can carry large amounts of lead and zinc in solution, so long as sulfide ($H_2S(aq)$, HS^-) concentrations are low. The brine must be acidic in character (pH<4) if appreciable amounts of metal and sulfide are transported in the same solution, otherwise immediate precipitation results. The important role of chloride complexing in ore genesis was pioneered by Helgeson (1964).

Barnes and Czamanske (1967) proposed that complexes of reduced sulfur provide an alternative model to metal-chloride brines, which would overcome the problem of transporting acidic-type solutions through carbonate aquifers. Sulfide complexes require large amounts of reduced sulfur in solution to be stable with relatively low, metal concentrations. Alkaline pH conditions, however, can exist if metals are transported as bisulfide complexes.

The relative importance of these two types of complexes is still debated by geochemists. In both cases, one of the ore-forming components must be at a low concentration in order to transport large quantities of the other component over large distances. Fluid-inclusion data and modern brines almost always indicate low sulfide content, but high chloride compositions. These observations, along with equilibria calculations have led a number of researches, including Anderson (1973), Giordano and Barnes (1979), and Sverjensky (1981), to conclude that metal-bisulfide complexing is not a geologically significant transport mechanism for the genesis of carbonate-hosted lead-zinc deposits. Anderson (1973, 1975) believes that metal

transport is attributed to chloride complexing in sulfide-free brines. Sverjensky (1981) argues, however, that metals and sulfide can be transported together in a solution at equilibrium with carbonates, although metal concentrations will be low. Recent data presented by Giordano and Barnes (1981) indicates that organic-based complexes may also play an important role in metal transport.

The precipitation of sulfide minerals can be attributed to several mechanisms, which Skinner (1979) groups into four main categories:

(1) Temperature changes.

(2) Pressure changes.

(3) Water-rock interaction.

(4) Mixing of different solutions.

The cooling of an ore-forming brine causes precipitation by reducing solubilities of metal sulfides and lowering the stability of the complex ions transporting the metals. A temperature drop of 20°C or more is needed to remove a lot of mass out of solution (Skinner, 1979). Temperature drops would have to occur over very short distances in order to concentrate an ore body. Pressure changes also cause mineral solubilities to vary, but pressure effects are probably not important in the formation of stratabound ore deposits at shallow depths.

Chemical reactions between the brine and porous media constitute an important means of precipitating ore deposits. For example, the dissolution of carbonates and hydrolysis of feldspars will cause the pH in acidic brines to rise, which reduces the stability of complexes and results in precipitation of sulfide minerals. The presence of H_2S or other forms of reduced sulfur will also react with metal-rich brines to deposit galena

and sphalerite. The effects of carbonaceous compounds are equally important in precipitating metals, mainly through a change in oxidation state of the fluid. They may also take part in the reduction of sulfate by anaerobic bacteria to produce H_2S. Other forms of reducing agents such as methane or pre-existing pyrite can cause ore deposition. The type of water-rock mechanism called upon to form an ore deposit will depend on the type of geochemical model that is favored. If metal and reduced sulfur are transported together, then pH rise or temperature drop are likely candidates. If metals are transported alone or with sulfate in a brine, then addition of reduced sulfur or sulfate reduction is required at the ore-forming site (Anderson, 1978).

Mixing of two separate fluids is a mechanism that avoids the equilibrium constraints imposed on a single-solution model where metal and sulfide travel together. This mechanism could produce large quantities of ore in a short period of time. Precipitation could be caused by an increase in sulfide, temperature drop, salinity changes, or pH rise when the fluids mix. It will be shown later that special geologic situations are needed to develop hydrodynamic patterns conducive to mixing of one fluid carrying metal and another carrying sulfide.

Source of Sulfur

It is generally agreed upon that hydrogen sulfide gas is the likely source of sulfide for many cases of ore precipitation. What remains in controversy is how the H_2S arrived on the scene and where it came from. A number of researchers have drawn attention to the close genetic relationships between oil fields and ore deposits (e.g. Hitchon, 1977). The evolution of hydrocarbons and their migration may be important to the

deposition of ore at sites where metal-rich brines mixed with H_2S derived from petroleum reservoirs. Anderson (1975) showed that a continuous supply of H_2S is required, because realistic in situ volumes could not account for the deposition of a major ore body. Brine-derived sulfate could be reduced to H_2S at sites containing anaerobic bacteria and organic matter, which would overcome the supply problem of petroleum reservoirs. One strike against this model in some ore environments is that sulfate-reducing bacteria become inactive above temperatures of 80°C (Skinner, 1979). Sulfate can be reduced inorganically in the presence of methane, as suggested by Barton (1967), but Anderson (1975) points out that this would be gradual and it would not explain the dominant association of lead-zinc ores to carbonate rocks. Another interesting process for reducing sulfate at temperatures above 75°C is presented by Orr (1974) to explain the generation of large volumes of H_2S in deep petroleum reservoirs. It involves the reaction of sulfate with small amounts of H_2S to produce elemental sulfur, which in turn reacts with organic matter to produce more hydrogen sulfide. Macqueen and Powell (in press) found that this method of sulfate reduction helps explain some of the features observed in the Pine Point ore deposits. They believe the reduced sulfur was produced in situ by small amounts of pre-existing H_2S in the reef complex. The sulfate-reduction process continued as warm (75°-100°C), metal-bearing brines passed through the organic-rich reef environment.

We seem to be given three possible sources for reduced sulfur:

(1) Migration of petroleum-derived H_2S over long distances and through aquifers isolated from metal-brine transport paths.

(2) Transport of small amounts of dissolved H_2S and metal in the same brine.

(3) Sulfate reduction of metal-sulfate brines at sites containing abundant organic matter and anaerobic bacteria.

The first model requires two fluids converging at a common discharge area. It has the advantage that high metal or sulfide concentrations could exist in each aquifer, thereby allowing large amounts of ore to deposit in a short period of time. As mentioned earlier, a two-fluid mixing model demands a special hydrogeologic condition. The second model requires large volumes of slightly acidic brine, and probably long periods of fluid flow. It could be appropriate for the Southeast Missouri district where the extensive Lamotte sandstone aquifer acted as a major conduit for delivering brines to overlying carbonate reefs or other permeable zones in the Bonneterre Formation. The third model can tolerate a wider range of geochemical conditions for the metal-bearing brine (Anderson, 1973), but ore occurrence is controlled by the location of suitable supply of organic material and bacteria. At environments such as Pine Point, sulfate reduction provides a very plausible mechanism. The occurrence of uniform mineralogical features (Ohle, 1980), and general absence of extensive well-rock alteration suggests that in situ sulfate reduction may be the major cause of ore deposition in many basins.

Timing and Paths of Fluid Migration

The geology of carbonate-hosted lead-zinc deposits give few clues when it comes to interpreting critical genetic relationships such as the age of the deposit, duration of mineralization, or paths of fluid movement. Field estimates of local fluid flow directions have been made through mineralogical studies, but they seldom give insight on the regional hydrodynamic system. In districts such as Pine Point and Southeast Missouri, the

identification of likely paleoaquifers is made easy by the presence of extensive porous dolomite and sandstone formations. A two-fluid mixing model demands that the brines be hydraulically isolated, until the point of mixing near the basin margin. Long distance transport of brines in a sedimentary basin is certainly possible, but to avoid mixing through cross-formational flow or dispersive processes may require restrictive hydraulic constraints.

The age and duration of mineralization of lead-zinc ore deposits is currently unknown except that they are post-lithification of the host rock. Estimates of the time needed to form an ore deposit can be made by assuming representative values of metal concentrations and flow rates. Roedder (1976) believes the possible geologic time span is wide, ranging from 1000 years to 10 million years. Based on a hydrologic model, White (1971) estimated that a period of 1 million years to 100 million years is geologically reasonable for the White Pine copper deposit in northern Michigan. Sverjensky (1981) concluded that the entire Southeast Missouri lead district could have formed in a period of 67,000 to 1 million years, assuming lead concentrations of 1 to 18 ppm and flow rates of about 30 $m^3/m^2/yr$ across an area of 100 m by 10 km. These estimates indicate that the duration of ore deposition may be relatively short in comparison to other geologic processes.

Summary

It is clear that many problems regarding the origin of carbonate-hosted lead-zinc deposits remain to be completely solved. Only some of these problems were identified here. Ohle (1980), and Anderson and Macqueen (in press) present much more thorough reviews of the problems at hand and suggestions for future research.

The primary concern of this study is to develop a quantitative

understanding of the role of the gravity-driven groundwater flow model in ore formation. The flow nets of Figures 7 and 8 show that a wide variety of subsurface flow patterns can exist, and suggest that further consideration of the factors controlling fluid flow will be useful in constraining conceptual models of ore genesis. The types of questions that this analysis will try to answer include the following:

(1) What is the exact nature of gravity-driven fluid-flow systems in sedimentary basins?

(2) What factors influence flow patterns in the subsurface, and the rates of fluid movement through large basins?

(3) How is the subsurface temperature pattern of a basin affected by fluid flow?

(4) Are ordinary geothermal conditions adequate to sustain temperatures of ore formation near the edge of a basin?

(5) Can fluid-flow systems effect the concentrations of metal-bearing brines as they flow through a basin?

(6) Can fluid-flow models and reaction-path models constrain the geochemical models of transport and deposition?

(7) Can gravity-driven flow systems produce major ore deposits in reasonable periods of geologic time?

Numerical models are developed in the next two chapters for the purpose of seeking quantitative answers to these questions.

CHAPTER 3

FUNDAMENTALS OF TRANSPORT PROCESSES IN ORE GENESIS

In order to evaluate the conceptual models of ore genesis in a quantitative way, four main types of information are needed:

(1) Flow patterns and fluid velocities.

(2) Temperatures.

(3) Concentration patterns of metal or sulfide.

(4) Masses of minerals dissolved and precipitated.

Fluid-flow patterns and velocities can be determined by analyzing the forces causing flow in porous media. For the purpose of this study, the porous medium is assumed to be rigid, and the variation in a gravity-based fluid potential is the only mechanism causing fluid transport. Subsurface temperatures depend on thermal conduction and the convection effects of fluid flow. The concentrations of transported chemical species will be controlled by fluid velocities, flow patterns, mechanical dispersion, and molecular diffusion. If the rocks are chemically reactive, mass transfer between the aqueous phase and mineral phases will occur via water-rock reactions. The mass of minerals produced or destroyed will depend on equilibria constraints. This study will treat the theory of fluid flow, heat transport, and mass transport in a relatively complete way; the theory of mass-transfer processes and chemical equilibrium is reviewed in a shorter fashion.

The principles of transport processes are based on the laws of fluid dynamics, thermodynamics, and heat and mass transport. Common to all types of processes is the transport of some quantity or property, a driving

force, and a general move toward equilibrium. The property being transported may be mass, momentum, thermal energy, electrical charge, or any other physical quantity. All of these transport processes can be described by mathematical expressions, many of which are developed in this chapter. The theory given here is not new; many references on the physics of transport theory are available, including the well-known texts of Bird, Stewart, and Lightfoot (1960), Bear (1972), and Slattery (1972). An excellent review of the literature concerning transport theory and geologic processes is given by Domenico (1977).

Governing Equations

The treatment of transport phenomena in porous media requires a continuum approach where average values of media parameters are introduced, in order to pass from the microscopic, pore-size scale to a macroscopic, continuum level. This transformation is straightforward in unconsolidated sediments or sedimentary rocks, but there are inherent difficulties in formations with abundant fractures or cavernous openings. In the continuum approach, the scale of the transport problem is taken at a level such that average media properties are representative. This avoids the more complicated analysis of flow through individual fractures. For the regional study of fluid flow in sedimentary basins, a continuum porous-media model is certainly justified.

The equations governing fluid flow, heat transport, mass transport, and geochemical equilibrium are now presented and discussed individually. Simplifications are made to each transport equation, so as to satisfy the needs of a preliminary assessment of the role of fluid flow in ore genesis. Many of the equations, except those governing geochemical equilibrium, are written in vectorial notation. For the purpose of this study, only two

spatial dimensions (x, z) are used in modeling the transport processes. It is a relatively easy task to extend the equations to their three-dimensional form.

Fluid Flow

The equation of conservation of mass for a single-phase fluid is written by Bear (1972) as

$$\frac{\partial(\phi\rho)}{\partial t} + \nabla\cdot(\rho\bar{q}) = 0 \tag{3-1}$$

where

ϕ = porosity (dimensionless fraction)

ρ = fluid density $[M/L^3]$

$\bar{q} = (q_x, q_z)$, specific discharge vector or Darcy velocity $[L^3/L^2\cdot t]$

t = time $[t]$

$\nabla = (\frac{\partial}{\partial x}\bar{i} + \frac{\partial}{\partial z}\bar{k})$

The first term represents the net rate of mass accumulation within a unit control volume, while the second term accounts for the net mass flux out of the control volume. This continuity equation assumes that the porous media is rigid, and that the mass flux carried by the average fluid velocity is much greater than any flow due to velocity fluctuations along the flow path. The media is also assumed to be fully saturated with a liquid phase only and no fluid sources or sinks are present.

The specific discharge vector $\bar{q}$ is given by the following general form of Darcy's law

$$\bar{q} = \frac{\bar{\bar{k}}}{\mu}(\nabla p + \rho g \nabla Z) \tag{3-2}$$

where

$\bar{\bar{k}}$ = intrinsic permeability (tensor) [L^2]

μ = dynamic viscosity [M/Lt]

p = fluid pressure [M/Lt^2]

g = gravitational acceleration constant [L/t^2]

Z = elevation of reference point above datum [L]

Equation (3-2) applies to homogeneous or inhomogeneous fluids (variable density) and it assumes that fluid flow is laminar in nature. It is possible to derive this form of Darcy's law from a formal analysis of conservation of fluid momentum, as expressed by the Navier-Stokes equations, (e.g. Bear, 1972; Dagan, 1972; Sorey, 1978), although the simplified form of this relationship was originally presented empirically by Darcy on the basis of laboratory experiments.

For homogeneous fluids, the concept of hydraulic head can be introduced, which represents the energy per unit weight of fluid

$$h = \frac{p}{\rho_0 g} + Z \tag{3-3}$$

where

h = hydraulic head [L]

ρ_0 = reference density (constant) [M/L^3]

Equation (3-2) then reduces to the familiar form of Darcy's law with

$$\bar{q} = \bar{\bar{K}}\nabla h \tag{3-4}$$

and

$$\bar{\bar{K}} = \frac{\bar{\bar{k}}\ \rho_0 g}{\mu_0} \tag{3-5}$$

where

$\bar{\bar{K}}$ = hydraulic conductivity (tensor) [L/t]

μ_0 = reference dynamic viscosity [M/Lt]

Hubbert (1940) shows that the hydraulic head is strictly valid only under isothermal and adiabatic conditions where the fluid is of homogeneous composition. For these reasons, pressure-based equations rather than head-based equations are traditionally used in petroleum and geothermal reservoir analysis.

The formation of stratabound ore deposits is dependent on the flow of variable-density brines in nonisothermal aquifers. It is necessary, therefore, to employ Equation (3-2) rather than (3-4) in our fluid-flow calculations. One problem with Equation (3-2), however, is that static pressure is included with the component responsible for fluid movement, the dynamic pressure increment. Bear (1972) and Frind (1980) recommend replacing the pressure variable with an equivalent fresh-water hydraulic head, as defined by Equation (3-3). Frind (1980) suggests this formulation reduces inaccuracy in the numerical solution of the fluid-flow equation. Upon substituting the hydraulic-head relation of (3-3) into (3-2), they arrive at the following expression (Bear, 1972, p. 654)

$$\bar{q} = -\frac{\bar{\bar{k}}\ \rho_0 g}{\mu}\ \nabla h - \frac{\bar{\bar{k}}\ (\rho-\rho_0)g}{\mu}\ \nabla Z \qquad (3\text{-}6)$$

The static pressure component is eliminated and the Darcy equation is now reduced to the two driving forces: the hydraulic gradient and a buoyancy term. It must be recognized that the hydraulic head in (3-6) is no longer a potential function as it is in the case of homogeneous fluid flow. In fact, mathematically there doesn't exist a unique hydraulic potential in inhomogeneous fluids because of rotations caused by density gradients. The subject of inhomogeneous fluid flow is treated in greater detail by de Josselin de Jong (1960, 1969), Yih (1961), Lusczynski (1961), Bear (1972), and Dagan (1972).

Further transformations can be made on Equation (3-6) in order to eliminate intrinsic permeability in favor of hydraulic conductivity. After multiplying both sides of (3-6) by μ_0/μ_0 and ρ_0/ρ_0, and collecting terms

$$\bar{q} = \frac{-\bar{\bar{k}}\,\rho_0 g}{\mu_0}\,\frac{\mu_0}{\mu}\,\nabla h \;\frac{-\bar{\bar{k}}\,\rho_0 g}{\mu_0}\,\frac{(\rho-\rho_0)}{\rho_0}\,\frac{\mu_0}{\mu}\,\nabla Z \tag{3-7}$$

or

$$\bar{q} = -\bar{\bar{K}}\,\frac{\mu_0}{\mu}\,[\nabla h + \frac{(\rho-\rho_0)}{\rho_0}\,\nabla Z] \tag{3-8}$$

This equation can be simplified further by introducing relative viscosity and density terms, such that

$$\bar{q} = \bar{\bar{K}}\,\mu_r\,(\nabla h + \rho_r \nabla Z) \tag{3-9}$$

where

$\mu_r = \frac{\mu_0}{\mu}$, relative viscosity (dimensionless)

$\rho_r = \frac{(\rho-\rho_0)}{\rho_0}$, relative density (dimensionless)

The fluid continuity equation [Equation (3-1)] now becomes

$$\frac{\partial(\phi\rho)}{\partial t} + \nabla\cdot\,[-\bar{\bar{K}}\,\rho\mu_r\,(\nabla h + \rho_r \nabla Z)] = 0 \tag{3-10}$$

The transient term on the far left can be expanded using the chain rule of differentiation in the usual manner (Freeze and Cherry, 1979) to obtain

$$\nabla\cdot\,[\bar{\bar{K}}\,\rho\mu_r(\nabla h + \rho_r \nabla Z)] = \rho S_s\,\frac{\partial h}{\partial t} \tag{3-11}$$

where

S_s = specific storativity [1/L]

Two types of fluid-flow problems can be solved with Equation (3-11): steady-state flow and transient (nonsteady) flow. Steady-state conditions

occur when at any given point in the flow field the magnitude and direction of specific discharge (Darcy velocity) are constant with time. In transient flow, the magnitude and direction of the Darcy velocity vary with time. Problems concerning regional groundwater flow are commonly treated in steady-state format (Freeze and Cherry, 1979). This implies that the hydraulic-head distribution does not change significantly with time, and that the spatial distribution of fluid density is relatively constant. For steady-state flow, the transient side of Equation (3-11) is set to zero and the continuity expression now becomes (Bear, 1972; Dagan, 1972)

$$\nabla \cdot [\bar{\bar{K}}\rho\mu_r(\nabla h + \rho_r \nabla Z)] = 0 \tag{3-12}$$

The use of steady-state theory in the modeling of regional fluid flow in large sedimentary basins is approximately satisfied by the time span involved in ore formation. The basic assumption being made is that the configuration of the water table (or topography) remains nearly constant over time, or that fluctuations in the water-table configuration are small relative to the thickness of the sedimentary basin (Freeze and Witherspoon, 1966).

Solving Equation (3-12) for the hydraulic head requires that suitable boundary conditions are provided, along with material and fluid properties of the flow system. The porous medium can be heterogeneous and anisotropic with respect to hydraulic conductivity, and porosity can vary in space. The fluid can be inhomogeneous and nonisothermal, such that density and viscosity are functions of pressure, temperature and solute concentration.

The terms in the hydraulic conductivity tensor are computed for a x-z coordinate system as

$$K_{xx} = K_1\cos^2\theta + K_2\sin^2\theta \tag{3-13a}$$

$$K_{zz} = K_1\sin^2\theta + K_2\cos^2\theta \tag{3-13b}$$

$$K_{xz} = K_{zx} = (K_1-K_2)\sin\theta\cos\theta \tag{3-13c}$$

where

K_1, K_2 = principal hydraulic conductivities [L/t]

θ = angle between K_1 and x-coordinate (radians)

In most of the modeling results presented here, the principal directions of hydraulic conductivity will be oriented parallel to the x-z axis, in which case $\theta=0$ and $K_{xx} = K_1$, $K_{zz} = K_2$, $K_{xz} = K_{zx} = 0$.

With the boundary-value problem fully specified, the hydraulic-head solution can then be used to calculate the specific discharge (Darcy velocity) from Equation (3-9). The average linear velocity (Freeze and Cherry, 1979) is given by

$$\bar{v} = \frac{\bar{q}}{\phi} \tag{3-14}$$

where ϕ is the porosity. It represents the volumetric fluid flux across the actual unit cross-sectional area of porous medium. Dividing by the porosity corrects for the fact that flow is in reality through the pore spaces only, and not the full cross-sectional area of continuum. The specific-discharge vector $\bar{q}$ is used to compute the effects of convection in heat transport, while the average linear-velocity vector $\bar{v}$ is used to predict the movement of solutes in mass transport.

Heat Transport

An expression for the conservation of thermal energy in a saturated porous medium can be written as

$$[\phi\rho c_{vf} + (1-\phi)\rho_s c_{vs}] \frac{\partial T}{\partial t} + \rho c_{vf} \bar{q}\cdot\nabla T = \nabla\cdot[\bar{\bar{k}}\nabla T] + \nabla\cdot[\phi\bar{\bar{D}}_H \nabla T] \tag{3-15}$$

where

c_{vf} = specific heat of fluid $[L^2/t^2T]$

c_{vs} = specific heat of solids $[L^2/t^2T]$

ρ_s = density of solids $[M/L^3]$

T = temperature $[T]$

$\bar{\bar{\kappa}}$ = effective thermal conductivity(tensor) $[ML/t^3T]$

$\bar{\bar{D}}_H$ = coefficient of thermal dispersion (tensor) $[ML/t^3T]$

It is possible to write the heat equation in various other forms. References in the groundwater literature include Stallman (1963), Bear (1972), Dagan (1972), Domenico and Palciauskas (1973), Witherspoon et al. (1975), Sorey (1978), and Faust and Mercer (1979). The mathematical and physical content of these various forms is nearly identical.

The first term on the left side of Equation (3-15) represents the net rate of thermal energy gain per unit volume of porous medium. It assumes thermal equilibrium between the pore fluid and rock, or in other words the temperature of the fluid is the same as the solid framework. The second term on the left-hand side describes the amount of heat flux due to convection. On the right side of (3-15), the first term is the net rate of heat loss per unit volume by conduction, and the last term gives the net heat transfer by the spreading effects of mechanical dispersion. Terms accounting for viscous dissipation of heat, energy increases by compression, and heat sinks or sources are neglected. The production and loss of heat caused by organic or inorganic reactions are also neglected.

The bulk thermal conductivity of the solid-liquid matrix is much easier to measure than the individual thermal conductivities of the fluid κ_f and solids κ_s (Dagan, 1972). Therefore an effective thermal conductivity κ is commonly utilized, which can be defined as a geometric mean

$$\kappa = \kappa_f^{\phi} \cdot \kappa_s^{(1-\phi)} \tag{3-16}$$

Other forms of this expression can be implemented (see Woodside and Messmer, 1961 or Bear, 1972), but Equation (3-16) is sufficient for this study. Notice that the thermal conductivity tensor of Equation (3-15) is now reduced to a scalar by assuming the media is isotropic with respect to thermal conductivity.

Bear (1972) states that the coefficient of thermal dispersion D_H is similar to the coefficient of mechanical dispersion used in mass-transport theory. The functional form of the thermal dispersion tensor in the x-z plane of a thermally isotropic media becomes (Rubin, 1974; Tyvand, 1977; Sorey, 1978; Pickens and Grisak, 1979)

$$\phi(D_H)_{xx} = \rho c_{vf} \frac{(\varepsilon_L q_x^2 + \varepsilon_T q_z^2)}{q} \tag{3-17a}$$

$$\phi(D_H)_{zz} = \rho c_{vf} \frac{(\varepsilon_T q_x^2 + \varepsilon_L q_z^2)}{q} \tag{3-17b}$$

$$\phi(D_H)_{xz} = \phi(D_H)_{zx} = \rho c_{vf} (\varepsilon_L - \varepsilon_T) \frac{\cdot q_x \; q_z}{q} \tag{3-17c}$$

where

ϕ = porosity

ε_L = longitudinal thermal dispersivity [L]

ε_T = transverse thermal dispersivity [L]

$q = (q_x^2 + q_z^2)^{\frac{1}{2}}$, vector resultant of the specific discharge [L/t]

For small-scale heat transport problems, thermal dispersion is small compared to conduction. On the regional scale, however, thermal dispersion can become significant (Mercer and Faust, 1981). Mathematical analysis have shown that thermal dispersion increases the stability of a fluid-flow field and inhibits the start of convection currents in free-convection heat-flow

problems (Weber, 1975; Tyvand, 1981).

With these definitions, the heat-transport equation can now be rewritten as

$$\nabla\cdot(\bar{\bar{E}}\nabla T) - \rho c_{vf}\,\bar{q}\,\nabla T = [\phi\rho c_{vf} + (1-\phi)\rho_s c_{vs}]\,\frac{\partial T}{\partial t} \tag{3-18}$$

where the combined thermal conduction-dispersion tensor $\bar{\bar{E}}$ is given by

$$\bar{\bar{E}} = \kappa + \phi\bar{\bar{D}}_H \tag{3-19}$$

Given appropriate initial and boundary conditions, the solution of the heat equation produces the spatial temperature distribution as a function of time. For the case of regional heat flow, a steady-state solution is usually adequate, provided the fluid-flow pattern is steady and boundary conditions are not changing appreciably with time (Domenico and Palciauskas, 1973). Under steady-state conditions, Equation (3-18) reduces to

$$\nabla\cdot(\bar{\bar{E}}\nabla T) - \rho c_{vf}\,\bar{q}\,\nabla T = 0 \tag{3-20}$$

As in the case of regional groundwater flow, the use of (3-20) in ore-genesis modeling is also partly justified because of the time scale involved. Any thermal perturbations caused by sudden uplift or climatic changes would probably dissipate after several thousand years. A relatively stable fluid-flow and heat-flow regime are envisaged in the mature stage of basis evolution.

Mass Transport

The equation for conservation of mass of the s-th constituent (component) in a multicomponent system is written as (Bear, 1972; Schwartz and Domenico, 1973; Carnahan, 1975)

$$\frac{\partial(\phi\rho c_s)}{\partial t} + \sum_{r=1}^{\hat{\hat{r}}} \nu_{sr} R_r = \nabla\cdot(\phi\rho\bar{\bar{D}}\nabla c_s) - \nabla\cdot(\phi\rho\bar{v}c_s) \tag{3-21}$$

where

s = subscript index, $s = 1, 2, \ldots \hat{s}$

$\hat{s}$ = total number of components in solution

c_s = mass concentration of component s per unit mass of fluid (dimensionless)

ν_{sr} = stoichiometric coefficient of s in reaction r (dimensionless)

R_r = rate of reaction r $[M/L^3t]$

r = reaction index, $r = 1, 2, \ldots \hat{r}$

$\hat{r}$ = total number of reactions

$\bar{\bar{D}}$ = dispersion coefficient (tensor) $[L^2/t]$

ϕ = porosity (fraction)

ρ = fluid density $[M/L^3]$

$\bar{v}$ = average linear velocity $[L/t]$

This expression is commonly known as the advection-dispersion equation in groundwater theory. In petroleum engineering, the process involving dispersion and advective transport is called miscible displacement (Garder, 1964). Derivations of Equation (3-21) are found in Reddell and Sunada (1970), Rumer (1972), Bear (1972), Konikow and Grove (1977), and others.

The transient (first) term in (3-21) describes the net rate of mass accumulation within a specified control volume. Geochemical reactions are represented under the summation symbol, the terms of which are negative for the addition of a chemical component and positive for removal. Any type of reaction can be involved, including precipitation, dissolution, complexing, radioactive decay, and ion exchange. Discussion of equilibrium geochemistry is postponed until a later section.

The first term on the right-hand side of Equation (3-21) represents the net mass flux from an elemental volume by the processes of mechanical dispersion and chemical diffusion. The last term in the equation reflects

the mass transport due to advection. In a multicomponent aqueous system, there is one mass balance equation for each transported component.

The dispersion tensor $\bar{\bar{D}}$ has been studied in great detail by various investigators, both from a theoretical point of view and with an experimental approach. The coefficient of dispersion depends on the flow velocity, on the molecular diffusivity of the aqueous species, and the medium characteristics. The functional form is usually written as (Bear, 1972)

$$\bar{\bar{D}} = \bar{\bar{\alpha}} \frac{v_x v_z}{v} + \bar{\bar{T}} D_d \tag{3-22}$$

where

$\bar{\bar{\alpha}}$ = dispersivity coefficient (fourth-rank tensor) [L]

$\bar{\bar{T}}$ = tortuosity coefficient (second-rank tensor) (dimensionless)

D_d = apparent diffusion coefficient in porous media [L^2/t]

The dispersivity tensor is a characteristic of the porous medium alone, which contains 81 components in three-dimensional space (Bear, 1972). If the porous medium is isotropic with respect to dispersion, then it can be shown that $\bar{\bar{D}}$ has its principal components along the direction of flow and transverse to it. In the isotropic case, the dispersivity tensor reduces to two constants: the longitudinal dispersivity α_L and the transverse dispersivity α_T. For practical purposes, the tortuosity tensor $\bar{\bar{T}}$ is usually assumed to be a constant and set equal to unity. Under these conditions, the hydrodynamic dispersion tensor is written as

$$D_{xx} = \alpha_L \frac{v_x^2}{v} + \alpha_T \frac{v_z^2}{v} + D_d \tag{3-23a}$$

$$D_{zz} = \alpha_T \frac{v_x^2}{v} + \alpha_L \frac{v_z^2}{v} + D_d \tag{3-23b}$$

$$D_{xz} = D_{zx} = (\alpha_L - \alpha_T) \frac{v_x v_z}{v} \tag{3-23c}$$

This simplified formulation of the dispersion tensor appears to be widely accepted (Bear, 1972; Bredehoeft and Pinder, 1972; Pickens and Lennox, 1976; and others).

For media that are anisotropic with respect to mass-transport parameters, researchers have been unable to derive any practical form of the dispersion tensor. Poreh (1965) derived an equation for axisymmetric media, which is limited to specific fluid-flow conditions. De Josselin de Jong (1969) concluded that the mass-transport equation developed for the isotropic case can theoretically only be extended to the anisotropic case if the dispersion coefficient is expressed by an infinite series. Some studies have made use of Equation (3-23) along with an anisotropic fluid-flow model in order to match field observations (Segol and Pinder, 1976; Schwartz and Crowe, 1980). An alternative approach is to use a stochastic analysis as done by Smith and Schwartz (1980). To date, however, it is fair to say that the problem of dealing with anisotropy in mass transport parameters has yet to be resolved.

Bear (1972) and Ahlstrom et al. (1977) show that the mass-transport equation can be simplified in the case of incompressible fluid flow where the total mass density of the fluid remains nearly constant and areal change in porosity is also small. In this case, the advection-dispersion equation becomes

$$\frac{\partial C_s}{\partial t} + \sum_{r=1}^{\hat{r}} \nu_{rs} R_r = \nabla \cdot (\bar{\bar{D}} \nabla C_s) - \bar{v} \nabla C_s \qquad (3\text{-}24)$$

where

s = aqueous components, $s = 1, 2, \ldots \hat{s}$

C_s = mass concentration per unit volume $[M/L^3]$

This form of the equation is the most common style used in hydrology and so it will be adopted here. Konikow and Grove (1977) warn that it is only

approximate because the presence of sinks or sources and density variations introduce terms into the advection part of the expression, which are not accounted for in (3-24).

The solution of Equation (3-24) in theory will provide the spatial and time-varying concentrations of each aqueous component in the fluid-flow system. It is shown later that in practice the solution of mass-transport equations in reactive aqueous systems is currently impractical. Simplifications, such as uncoupling geochemical reactions and limiting the number of modeled components to less than a few, help alleviate the problem.

Equations of State

Fluid density and viscosity can vary significantly with temperature, solute concentration, and to a lesser degree with pressure, over the range of conditions encountered in sedimentary basins. In order to model the flow of basinal brines, we need functional relationships of the form

$$\rho = \rho(p, T, C) \tag{3-25a}$$

and

$$\mu = \mu(p, T, C) \tag{3-25b}$$

Equations of this format can be obtained from engineering handbooks (e.g. Perry and Chilton, 1973), and from geothermal studies (e.g. Mercer and Pinder, 1974; Huyakorn and Pinder, 1977; Sorey, 1978). Unfortunately, none of these references present equations of state that are complete enough to model the full range of likely temperatures and salinities encountered in the formation of stratabound ore deposits.

Fortunately, experimental data on the density and viscosity of aqueous NaCl solutions has been recently collected and correlated by Kestin et al. (1978), and Kestin, Khalifa and Correia (1981). Earlier compilations on the density of sodium-chloride solutions can be found in Rowe and Chou

(1970), and Haas (1976). The Kestin equations will be used here because of their completeness. These equations cover a temperature range from 20° to 150°C, a NaCl concentration range from 0.0 to 6.0 molal (about 25% weight equivalent), and a pressure range from 0.1 to 35.0 MPa. The experimental results have an estimated uncertainty of $\pm$ 0.5% (Kestin, et al., 1981).

The fluid density equation is of the following form

$$\frac{1}{\rho} = A - Bp - Cp^2 + wD + w^2E - wFp - w^2Gp - \frac{Hp^2}{2}w \qquad (3\text{-}26)$$

where

$\rho = \rho\ (p,\ T,\ w_{NaCl})$, fluid density (kg/m^3)

p = pressure

T = temperature (^{o}C)

w = mass fraction of sodium-chloride solution (dimensionless)

The functions A, B, C, D, E, F, G, and H are written as fitted polynomial expressions which are temperature dependent.

The correlation equation for dynamic viscosity is given by (Kestin, et al., 1981)

$$\mu = \mu^0\ (1 + \beta p) \qquad (3\text{-}27)$$

where

$\mu = \mu(p,\ T,\ C_{NaCl})$ dynamic viscosity (Pa•s)

μ^0 = hypothetical zero-pressure viscosity (Pa•s)

β = pressure coefficient of viscosity (10^9Pa)

p = fluid pressure (10^9Pa)

The polynomial expressions used in evaluating μ^0 and β are listed in Kestin et al. (1981).

Figures 9 and 10 show plots of the variation in density and viscosity with temperature, and for selected values of NaCl molality (m_{NaCl}), as

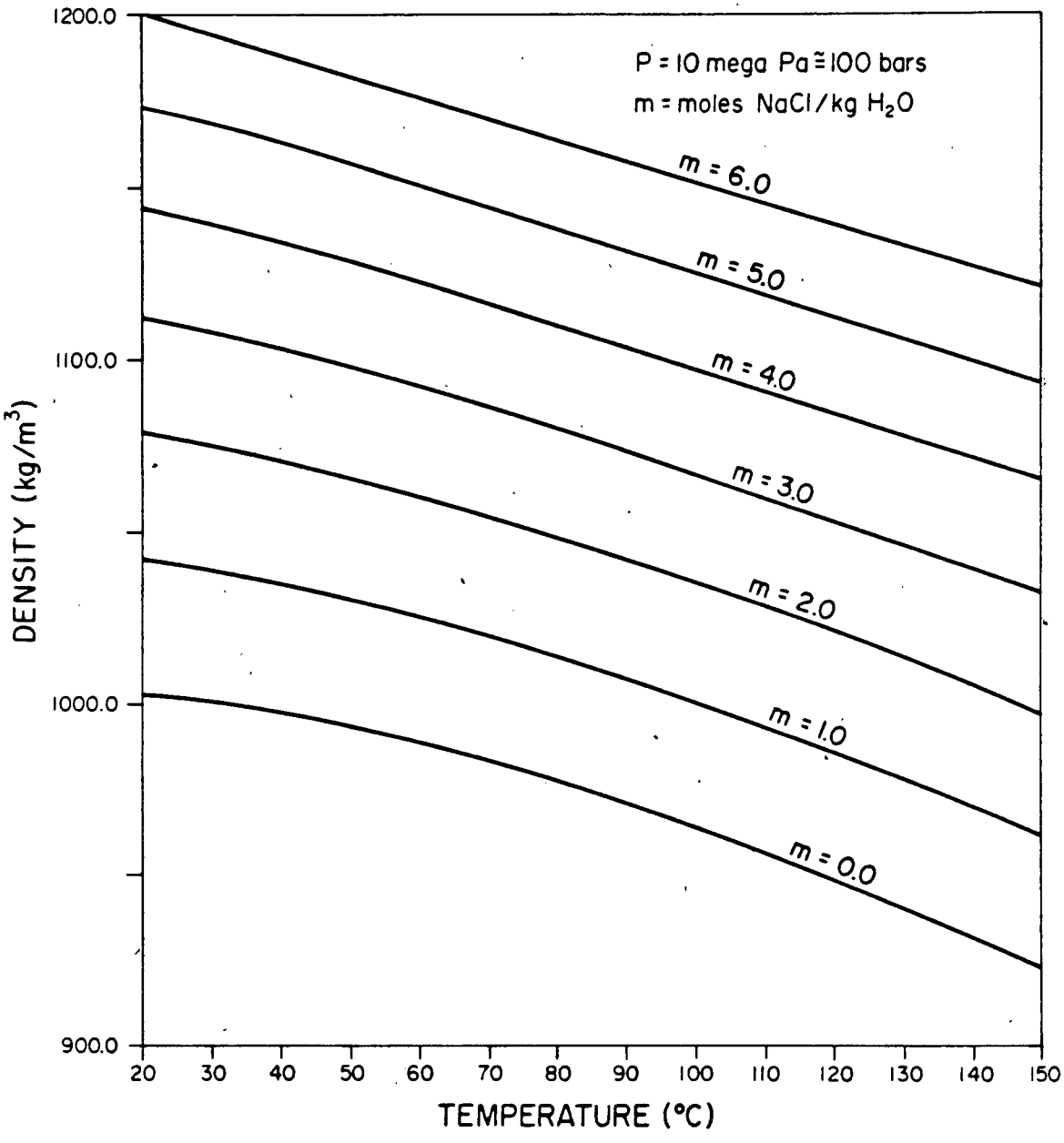

Figure 9. Variation in water density with temperature and NaCl concentration at a depth of 1 km.

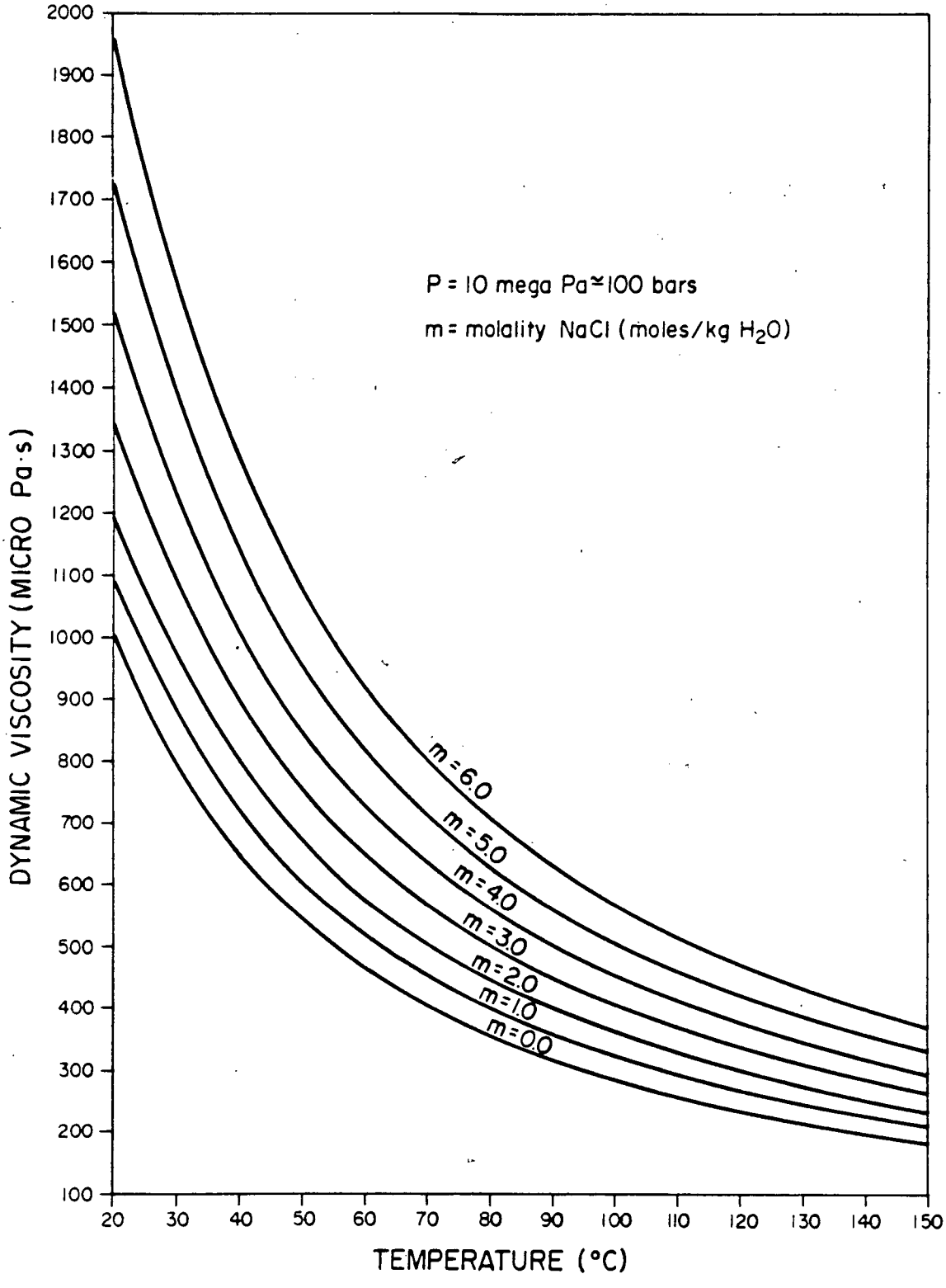

Figure 10. Variation in water viscosity with temperature and NaCl concentration at a depth of 1 km.

calculated from Kestin's equations of state. Both density and viscosity exhibit a strong dependency on temperature and salinity. The range of conditions depicted on these graphs are similar to the subsurface environments expected in the genesis of stratabound ore deposits.

At a depth of 1 km (i.e. hydrostatic pressure of 10 MPa ≃ 100 bars), fluid density changes from 1003 kg/m^3 at 20°C to 979 kg/m^3 at 75°C, assuming m_{NaCl} = 0.0. The effect of higher salinity is to increase density. For example, a 3.0 m NaCl brine has a density of 1083 kg/m^3 at 75°C (Figure 9).

Viscosity shows more dramatic variations than density, especially with temperature (Figure 10). Dynamic viscosity drops from 998 micro Pa•s at 20°C to 381 micro Pa•s at 75°C, for fresh water at 10 MPa pressure (1 centipoise = 1000 micro Pa•s at a temperature of 75°C and 1 km depth).

The effect of pressure on density and viscosity is small, over the temperatures and depths suggested for stratabound ore formation. In the pressure range of 0.1 to 35.0 MPa (about 4 km depth), fresh-water density changes from 998 to 1003 kg/m^3, at a temperature of 50°C. Viscosity increases slightly from 547 to 553 micro Pa•s under the same pressure range and temperature (Kestin, et al., 1981).

Both the fluid density and viscosity equations of state are needed to solve the coupled equations of fluid flow and heat transport. If the modeling also calls upon for the transport of Na and Cl, then the advection-dispersion equations for these components would be coupled to the fluid-flow and heat-transport equations through the fluid density and viscosity effects.

Geochemical Equilibrium and Reaction Paths

The calculation of chemical equilibrium between aqueous solutions and minerals is essential in quantitatively evaluating ore formation in a porous medium. In theory, it also provides the reaction terms in the mass-transport

equation. The reaction of an aqueous phase with a mineral assemblage causes mass to be transferred among the phases, perhaps creating new minerals, dissolving existing minerals, or changing the fluid composition as the chemical system is driven to overall equilibrium. In porous media, the extent to which a reaction takes place will depend on the composition of the fluid, rock mineralogy, and flow rate (Helgeson, 1979). Thermodynamic constraints such as pressure, temperature, and fixed chemical potentials of the system components provide the most useful criteria in modeling geochemical reactions. Some reactions will also depend on kinetic constraints, but unfortunately kinetic data are unknown or unobtainable for many reactions of interest in ore genesis.

The geochemical modeling approach taken in this study is based purely on equilibrium thermodynamics, and the techniques pioneered by Helgeson (1968) and Helgeson et al. (1970). It utilizes the thermodynamic constraints that are required to achieve equilibrium in order to compute mass transfer and distribution of chemical components during water-rock reactions. Helgeson (1979) briefly reviews some of the other theoretical approaches that have been applied to modeling geochemical mass transfer.

An expression relating the change in the energy of a closed thermodynamic system, as a result in a change in its chemical composition, is given by Gibb's equation (Helgeson, 1968; Van Zeggeren and Storey, 1970)

$$dG = \sum_i \mu_i^* dn_i$$

where

dG = Gibb's free energy increment

μ_i^* = chemical potential of the i-th component

dn_i = infinitesimal change in the number of moles of the i-th component.

This equation assumes that pressure and temperature are held constant. The condition of chemical equilibrium occurs at the minimum free-energy level of the system, where $dG=0$. The problem of computing the distribution of compo-

nents or species in the aqueous phase at equilibrium reduces therefore to solving (3-29) for the set of n_i values that minimize G, subject to the additional constraint of mass conservation.

Several approaches can be used to solve this minimization problem, but two main types have prevailed in computing geochemical equilibrium. One technique involves the direct application of optimization theory, while the second method formulates the problem as a set of nonlinear equations based on equilibrium constants (Van Zeggeren and Storey, 1970). The latter approach involves the substitution of expressions for the chemical potentials in terms of activities. The result is a set of mass-action and mass-balance equations, which constrain the equilibrium distribution of components among all phases (Helgeson, 1968).

As an example, consider the problem of calculating an equilibrium model for a single fluid phase in which there are J components and I associated equilibria constraints in reactions. Wolery and Walters (1975) studied this problem from a numerical point of view. Their system can be described by J mass-balance equations and I mass-action equations, including the condition of electro-neutrality (charge balance),

$$m_{T,j} = m_j + \sum_{i=1}^{r} \nu_{ji}\, m_i \qquad j = 1, 2, \ldots. J \qquad (3\text{-}29)$$

$$m_i = K_i' \prod_{j=1}^{J} m_j^{\nu ji} \qquad i = 1, 2, \ldots. I \qquad (3\text{-}30)$$

$$\sum_{j=1}^{J} z_j\, m_j + \sum_{i=1}^{I} z_i\, m_i = 0 \qquad (3\text{-}31)$$

where

$m_{T,j}$ = total concentration of component j (moles/kg H_2O)

m_j = concentration of j-th free ion (moles/kg H_2O)

m_i = concentration of associated complex (moles/kg H_2O)

ν_{ji} = number of moles of j-th component per mole of i-th complex (dimensionless)

K_i' = apparent thermodynamic association constant for i-th complex (dimensionless)

z_j, z_i = net electric charge on species

Thermodynamic data are tabulated in the literature and values of K' are known for many reactions (Robie and Waldbaum, 1968; Helgeson, 1969; Helgeson and Kirkham, 1974a). Activities may be used instead of molal concentrations, in which case

$$a = \gamma m \tag{3-32}$$

but the activity coefficient γ demands an estimate of the ionic strength I of the solution, which is calculated from (Wolery and Walters, 1975)

$$I = \tfrac{1}{2} \left[\sum_{j=1}^{J} m_j z_j^2 + \sum_{i=1}^{I} m_i z_i^2 \right] \tag{3-33}$$

The activity coefficient is then computed from the Debye-Hückel equation or other means (Garrels and Christ, 1965; Helgeson and Kirkham, 1974b).

Simultaneous solution of Equations (3-29) through (3-33) provides a complete description of the distribution of aqueous species in equilibrium.

The set of governing equations for a system containing an aqueous phase and minerals is more involved. Table 2 shows the full set of governing equations, as written by Wolery (1978, 1979a). It assumes a closed system $\tilde{E}$ (the equilibrium subsystem) where the total elemental compositions n_ε^t are specified at a fixed temperature and pressure. Only pure minerals are treated in Table 2. Solid-solution reactions for minerals of variable composition are deleted from Wolery's original set of equations, so as to simplify the presentation given here.

The equations for equilibrium are expressed

Table 2. Equations governing chemical equilibrium in a system containg $\hat{\varepsilon}$ elements, $\hat{s}$ species and $\hat{\lambda}$ minerals (after Wolery, 1979a)

Mass balance for each element ($\varepsilon = 1, \hat{\varepsilon}$)

$$n_\varepsilon^t = \sum_{s=1}^{\hat{s}} \tau_{\varepsilon s}\, n_s + \sum_{\lambda=1}^{\hat{\lambda}} \tau_{\varepsilon\lambda}\, n_\lambda$$

Charge balance in the aqueous phase ($s = 2, \hat{s}$)

$$0 = \sum_{s=2}^{\hat{s}} Z_s n_s$$

Mass action for intra-aqueous reactions ($r = 1, \hat{r}$)

$$K_r' = a_{s^*}^{\nu_{rs^*}}\, f_{O_2}^{\nu_{r\tilde{s}}} \prod_{s=1}^{\dot{s}} a_s^{\nu_{rs}}$$

where $s^* > \tilde{s}$ refers to species destroyed in the r-th reaction

Mass action for minerals of fixed composition ($\lambda = 1, \hat{\lambda}$)

$$K_\lambda' = f_{O_2}^{\nu_{\lambda\tilde{s}}} \prod_{s=1}^{\dot{s}} a_s^{\nu_{rs}}$$

Activity-concentration relation for aqueous species ($s = 2, \hat{s}$)

$$a_s = \gamma_s m_s$$

Definition of equivalent stoichiometric ionic strength

$$\tilde{I} = \sum_{s=2}^{\tilde{s}} \tau_{\varepsilon^\pm}\, m_s \qquad \text{where } \varepsilon^\pm = \text{Na or Cl}$$

Definition of true ionic strength

$$I = \tfrac{1}{2} \sum_{s=2}^{\hat{s}} m_s\, z_s^2$$

Activity of liquid water

$$\log a_w = \frac{-2}{2.303}\, \tilde{I}\, \hat{\phi}_e \qquad \text{where}$$

$\hat{\phi}_e$ = osmotic coefficient (Helgeson et al., 1970)

Table 2. (Continued)

Activity coefficients of aqueous species

$$\log \gamma_s = f_s(I)$$ where

$f_s(I)$ = function depending on ionic strength and type of species (Wolery, 1979a)

Molal concentration of species

$$m_s = \omega \frac{n_s}{n_w}$$

Glossary of symbols

ε = chemical element subscript

$\hat{\varepsilon}$ = total number of elements

s = aqueous species subscript

w = water subscript ($s = 1$)

$\tilde{s}$ = aqueous species in basis set

$\hat{s}$ = total number of species

$\dot{s}$ = number of basis species = $\hat{\varepsilon} = \tilde{s} - 1$

s^* = subscript of species being destroyed in r-th reaction

r = reaction subscript

$\hat{r}$ = number of independent reactions = $\hat{s} - \tilde{s}$

λ = pure mineral subscript

$\hat{\lambda}$ = number of minerals

$\hat{\phi}_e$ = osmotic coefficient

n = mass of species, in moles

n_ε^t = total mass of ε - th element

z_s = electrical charge on species s

m_s = molal concentration (moles/kg H_2O)

λ_s = activity coefficient of species s

a = thermodynamic activity

I = true ionic strength

$\tilde{I}$ = equivalent ionic strength

f_{O_2} = fugacity of oxygen in aqueous phase

ω = water constant = 55.51

τ = composition coefficient (moles element per formula weight)

ν_{rs} = reaction or stoichiometric coefficient (moles of s in r-th reaction)

K' = equilibrium constant for reaction

in a format that assumes a specific ordering. Wolery has chosen to write the first $\dot{s}$ species ($s = 1$ denotes H_2O) as corresponding to a one-to-one basis with the elements and associated mass-balance equations. Oxygen fugacity is used as the redox parameter in writing the equations, such as (Wolery, 1978)

$$0 \rightleftarrows - Fe^{3+} - \tfrac{1}{2} H_2O + Fe^{2+} + H^+ + \tfrac{1}{4} O_2(g, aq) \qquad (3\text{-}34)$$

The species $O_2(g, aq)$ marks the redox parameter and is denoted as the $\tilde{s}$-th species ($\tilde{s} = \dot{s} = 1$). It can also be assigned with the charge-balance equation (Wolery, 1978). The remaining aqueous species, from $s = \tilde{s} + 1$ to $\hat{s}$, are represented by the $\hat{r}$ aqueous reactions in which they are involved. Wolery calls the first $\tilde{s}$ species the basis species and shows that all reactions can be written in terms of the basis species and their associated species for the reaction.

Further detailed explanation of Table 2 is given in Wolery (1978, 1979a) and need not be repeated here. Suffice to say that the unknown masses of species are easily found by simultaneous solution of these equations. A discussion of factors such as the effect of pressure and temperature on equilibrium constants, the calculation of the activity of water, the calculation of activity coefficients, and treatment of solid-solution phenomena are also omitted here. The evaluation of these factors is presented elsewhere (e.g. Helgeson, 1968; Helgeson et al., 1970). With the distribution of aqueous species in hand, we can now proceed to consider the prediction of mass transfer as a function of reaction progress.

Helgeson (1979) presents an excellent review of reaction-path theory, and summarizes the application of the theory in studying ore-forming hydrothermal systems through the numerical approach first introduced by Helgeson (1968) and Helgeson et al. (1970). Predicting the exact path of a reaction and the amounts of mass transfer in a system requires introducing a reaction-

progress variable ξ^*, such that

$$\frac{d\xi^*}{dt} = -\frac{dn}{dt} = R \tag{3-35}$$

where

ξ^* = moles of substance reacted

n = mass of substance present

t = time

R = rate expression for the reaction

Rather than define an individual progress variable for each reaction, Helgeson (1968) assigns an overall reaction-progress variable for the geochemical process being modeled. It generally refers to the irreversible reaction of the aqueous phase with one of the minerals in the reacting porous media. The rates at which other minerals react with the fluid can be expressed in relation to the overall progress variable by specifying relative rates of reactions (Helgeson et al., 1970; Brown, 1977).

The numerical solution of Equation (3-35) can be accomplished in more than one way. Wolery's (1978, 1979a) approach is based on the techniques developed by Helgeson (1968) and Helgeson et al. (1970), but his governing equations are formulated differently. A comparison of the methods is given by Wolery (1979a). In Wolery's models, the reaction path is traced by changing the mass-balance constraints (n_ε^t) on the closed system $\tilde{E}$ and by specifying a set of reactant-tracking coefficients ζ, which correspond to a set of reactants $\hat{\eta}$. The tracking coefficients are interpreted as relative-rate constants, and as such Equation (3-35) is recast for the η-th reactant in a power series (Wolery, 1979a)

$$\frac{-dn_\eta}{d\xi^*} = \zeta_{1\eta} + \zeta_{2\eta}(\xi^*) + \zeta_{3\eta}(\xi^*)^2 \tag{3-36}$$

The change in the bulk-elemental composition of the system $\tilde{E}$ as a function of

ξ^* is given by (Wolery, 1979a)

$$\frac{dn_\varepsilon^t}{d\xi^*} = - \sum_{\eta=1}^{\hat{n}} \tau_{\varepsilon\eta} \frac{(dn_\eta)}{d\xi^*} \tag{3-37}$$

Upon integration,

$$n_\varepsilon^t = n_\varepsilon^t\Big|_{\xi^*=0} + \sum_{\eta=1}^{\hat{n}} \tau_{\varepsilon\eta} \left[\zeta_{1\eta}(\xi^*) + \zeta_{2\eta} \frac{(\xi^*)^2}{2} + \zeta_{3\eta} \frac{(\xi^*)^3}{3}\right] \tag{3-38}$$

The result of solving (3-38) is a continuous description of the changes in fluid composition and amounts of minerals produced or destroyed during the reaction process, without reference to space or time. Temperature and pressure changes can also be accounted for in these calculations, as can the effects of a flow-through system (Helgeson et al., 1970; Wolery, 1979a).

Coupling of Transport Phenomena

In this chapter, all of the transport equations are written in terms of individual fluxes caused by independent driving forces that are represented by gradients in pressure, density, temperature, solute concentration, or chemical potential. Although the equations may be physically "coupled" through interdependency on fluid properties and velocity, the possibility of interaction between the driving forces has yet to be addressed.

Freeze and Cherry (1979) show that these driving forces may interact with each other to produce cross-transport phenomena (coupled processes). For example, in addition to hydraulic-head gradients, the flow of fluids through a porous medium may be caused by temperature gradients, electrical gradients, or salinity gradients. Similar relationships may also exist for the flow of heat and mass transport in porous media. Bear (1972, p. 85) and Domenico (1977) discuss the theory behind cross-transport phenomena, which is based on a thermodynamic analysis referred to as Onsager's theory.

In practice, however, there are few data on the suite of phenomenological coefficients needed to quantitatively evaluate the role of cross effects in groundwater flow. The data which are available suggests that cross effects are small. Dagan (1972) estimated that the cross effects caused by the salinity gradient on heat flow (Dufour effect), and the effects of a temperature gradient on mass transport (Soret effect) are about three-orders of magnitude smaller than the direct driving forces. Carnahan (1975) presents a detailed derivation of coupled phenomena in porous media through a thermodynamic analysis. He calculated that the effect of a temperature gradient to cause fluid flow is small under normal conditions, the ratio of the thermal effect to Darcy flow being about 3×10^{-3}. Carnahan (1975) also shows that geochemical reaction rates are not thermodynamically coupled to other transport processes, although there is coupling between the reactions themselves.

Based on the available data, it is safe to conclude that coupled phenomena are relatively unimportant when compared to the primary transport processes involved in stratabound ore genesis. The effects of cross terms, therefore, are neglected in this study.

Summary of Equations and Assumptions

The mathematical treatment of the physics of transport processes is now complete. Equations have been presented that describe inhomogeneous fluid flow, heat transport, and mass transport in reactive porous media. The purpose of this discussion is to provide a theoretical framework for modeling subsurface fluid velocities, temperatures, transport patterns, and geochemical reactions in the formation of carbonate-hosted lead-zinc deposits of the Mississippi Valley type. Table 3 gives the complete set of simplified equations. Before continuing on to the next chapter, which deals

Table 3. Governing Equations

Darcy's law

$$\bar{q} = -\bar{\bar{K}}\mu_r (\nabla h + \rho_r \nabla Z) = \bar{v}\phi$$

Fluid Flow

$$\nabla\cdot (\rho\bar{q}) = 0$$

Heat Transport

$$\nabla\cdot (\bar{\bar{E}}\nabla T) - \rho c_{vf} \cdot \bar{q}\nabla T = 0$$

Mass Transport

$$\frac{\partial C_s}{\partial t} + \sum_{r=1}^{\hat{r}} \nu_{rs} R_r = \nabla\cdot(\bar{\bar{D}}\nabla C_s) - \bar{v}\cdot\nabla C_s \qquad ; s = 1, 2, \ldots. \hat{s}$$

Equations of state

$$\rho = \rho\ (p, T, C_{NaCl})$$

$$\mu = \mu\ (p, T, C_{NaCl})$$

Geochemical equilibrium and reaction mass transfer

mass balance: $$n_\varepsilon^t = \sum_{s=1}^{\hat{s}} \tau_{\varepsilon s}\, n_s + \sum_{\lambda=1}^{\hat{\lambda}} \tau_{\varepsilon\lambda}\, n_\lambda \qquad ; \varepsilon = 1, 2, \ldots. \hat{\varepsilon}$$

charge balance: $$0 = \sum_{s=2}^{\hat{s}} z_s\, n_s$$

mass action for aqueous species:

$$K_r' = (a_{s*})^{\nu_{rs*}} (f_{O_2})^{\nu_{r\tilde{s}}} \prod_{s=1}^{\dot{s}} a_s^{\nu_{rs}} \qquad ; r = 1, 2, \ldots. \hat{r}$$

mass action for minerals:

$$K_\lambda' = (f_{O_2})^{\nu_{\lambda\hat{s}}} \cdot \prod_{s=1}^{\dot{s}} a_s^{\nu_{\lambda s}} \qquad ; \lambda = 1, 2, \ldots. \hat{\lambda}$$

reaction tracking:

$$n_\varepsilon^t = n_\varepsilon^t\Big|_{\xi^*=0} + \sum_{\eta=1}^{\hat{\eta}} \tau_{\varepsilon\eta} \cdot \left[\zeta_{1\eta}(\xi^*) + \xi_{2\eta}\frac{(\xi^*)^2}{2} + \xi_{3\eta}\frac{(\xi^*)^3}{3}\right]$$

with the subject of solution procedure, we should reflect on the main assumptions and limitations behind the governing equations. They can be summarized in point form as follows.

(1) Transport processes are assumed to occur in a fully saturated porous medium, and under conditions of laminar fluid flow. The equation models fractured media as a continuum.

(2) The porous medium can be heterogeneous and anisotropic with respect to hydraulic conductivity.

(3) The porous medium is rigid and well indurated. Stress-strain phenomena such as compaction are not considered.

(4) Changes in porosity due to geochemical reactions are assumed to not effect regional fluid-flow patterns or velocities.

(5) Gravity-driven hydraulic-head gradients are the only driving forces causing fluid flow. The fluid-flow equation, however, does take into account the effects of variable temperature and salinity.

(6) Fluid density and viscosity are nonlinear functions of pressure, temperature, and salinity. Local density gradients are assumed to be small.

(7) The fluid-flow regime is at steady state.

(8) Temperature of the pore fluid and host rock are equal, indicating thermal equilibrium.

(9) The porous medium can be heterogeneous and anisotropic with respect to thermal properties. Thermal conductivity, however, is more easily handled as an isotropic parameter.

(10) Both heat conduction and convection are accounted for in the heat-transport equation. The influence of thermal dispersion is also included.

(11) The heat-flow regime is at steady state.

(12) The mechanical dispersion and diffusion of a solute are modeled as a

Fickian-type process. In the absence of dispersion, mass is advected through porous media at the average linear velocity of the fluid.

(13) It is assumed that the porous medium is isotropic with respect to dispersion processes. Under this condition, the dispersion tensor can be reduced to two terms: a longitudinal and transverse dispersion coefficient.

(14) Mass transport processes are treated as transient problems.

(15) Geochemical mass transfer through reactions appears as a source-sink term in the advection-dispersion equation. These terms are evaluated through the thermodynamic constraints imposed by equilibrium, and reaction-path modeling.

(16) Reaction-path theory is assumed to provide the best approach to modeling reaction progress and multicomponent mass transfer. If more than one reactant are present, relative reaction rates must be specified.

(17) The effect of thermodynamic coupling between the transport processes are considered to be small when compared to the main driving forces.

The problem ahead of us now is to solve the system of equations (Table 3) for the dependent variables of fluid flow, heat transport, and mass transport in a chosen two-dimensional domain, given a set of initial and boundary conditions. Although cross-transport phenomena have been eliminated from the analysis, the equations are still physically coupled because of the interdependency between pressure, temperature, and concentration in the equations, and because of the influence of these fields on the fluid properties. The solution of this complex, boundary-value problem is treated in the following chapter.

CHAPTER 4

DEVELOPMENT OF THE NUMERICAL MODELS

The procedure of mathematical modeling evolves along an organized route of analysis. Freeze (1978) lists a four-step process:

(1) Identification of the physical problem and formulation of a conceptual model.

(2) Determination of the governing equations and formulation of a mathematical model.

(3) Solution of the mathematical model, given initial and boundary conditions.

(4) Interpretation of the model results in light of geologic data and model calibration.

Table 4 summarizes many of the modeling decisions that must be made in order to construct a mathematical model of transport processes in stratabound ore formation. We have already described the problem of stratabound ore genesis, and presented a set of equations that govern transport processes in two-dimensional representations of sedimentary basins along cross sections. Simplifications have been made to some of these equations in order to reduce the complexity of the analysis. The conceptual model presented earlier (Figure 6) also gives the general size and shape of the cross sections in which we want to simulate areal variations in fluid velocity, temperature, concentration of species, and reaction progress.

The next step in the analysis is to develop a method for solving the mathematical model. The purpose of this chapter is to describe the

Table 4. Modeling decisions

Fluid Flow	One, two, or three dimensions Single phase, multiphase Saturated, unsaturated Homogeneous, inhomogeneous fluid Gravity drive, compaction drive Steady, transient
Heat Transport	One, two, or three dimensions Convection, conduction, dispersion Thermal equilibrium, nonequilibrium Steady, transient
Mass Transport	One, two, or three dimensions Single species, multicomponent Advection, mechanical dispersion, diffusion Steady, transient
Geochemistry	Lumped, distributed (time, space) Reactions, retardation Relative reaction rates, kinetics Closed, open, flow-through
Media	Porous media, fractured rock (discrete, continuum) Rigid, unconsolidated Reactive, nonreactive Homogeneous, heterogeneous Isotropic, anisotropic
Region of Flow and Scale of Study	Regional, local Sedimentary basin, aquifer
Idealization of Geology	Stratigraphy (general, detailed) Parameter values
Initial and Boundary Conditions	Prescribed value Constant, time-varying
Numerical Solution	Finite difference Finite element Integrated finite difference Random walk (Monte Carlo) Method of characteristics Optimization methods Newton-Raphson iteration, direct inversion Taylor-series expansions

solution procedure and to construct a practical, quantitative tool for studying ore genesis in sedimentary basins.

Numerical Formulation of the Governing Equations

Mathematical models (problems) can be solved through analytical techniques or by numerical methods. The analytical techniques provide a closed-form solution to the problem, which in theory can be exact, so long as the region of flow is very simple and the equations can be linearized. The main advantage of numerical methods is their ability to solve mathematical problems in which analytical solutions are too difficult to obtain. In modeling multidimensional fluid flow and other transport processes in basins, this is almost always the case.

The coupled and nonlinear nature of our governing transport equations (Table 3) demand a numerical method of solution. The solution technique must allow the media properties, the general geology, and the size of the study region to be easily varied. Analytical techniques could be applied, but this approach would require major simplifications to the problem at hand. It will be shown later, however, that the numerical approach also has limitations in solving this complex set of equations.

The numerical method used in solving partial differential equations involves dividing the flow domain into a grid or mesh consisting of many small blocks or cells called elements. In this discretization of the flow domain, each element is defined by corner points called nodes. Several techniques are then available to replace the partial differential equation by a system of algebraic equations. Properties of the porous medium, such as permeability, porosity, thermal conductivity, dispersivity and others, are specified for each element in the mesh. Suitable modifications of the algebraic equations

are also made to satisfy initial and boundary conditions. These systems of equations can be solved by matrix-inversion methods for the value of the dependent variable at each nodal point in the mesh, thereby producing a spatial solution over the flow domain. In theory, the numerical solution will approach the exact solution as the number of elements increases. A different method of numerical analysis is needed to solve the highly non-linear system of equations representing chemical equilibrium and reaction progress. Instead of discretizing spatial coordinates, it is necessary to discretize the reaction-progress variable.

In this study, the finite-element method is used to solve the equations governing fluid flow and heat transport. The problem of multi-component mass transport is solved through the development of a code that uses moving-particle random-walk theory. Geochemical reactions are simulated through the EQ3/EQ6 code, which was written by Wolery (1979a). It applies Newton-Raphson iteration along with finite-difference theory to predict reaction paths. General discussions on each of the numerical methods used in this study are given below. Further reference on mathematical modeling in hydrogeology can be found in Freeze and Cherry (1979), Mercer and Faust (1981), and Wang and Anderson (1982). A review of numerical modeling in aqueous geochemistry is given in Nordstrom, et al. (1979).

Fluid Flow

The Galerkin-based finite-element method has been applied to numerous problems of flow and transport in porous media. Finite-element theory has received much attention in hydrogeology, and therefore only the highlights of its formulation are presented here. The interested reader is referred to the texts of Bathe and Wilson,(1976), Pinder and Gray (1977),

and Zienkiewicz (1977) for more detail on the method.

The region of study is first subdivided into a set of finite elements, with the corners of the elements represented by nodes. The dependent variable of interest (hydraulic head) is approximated over the elements, usually in a linear fashion so that the numerical value of the dependent variable is easily interpolated at any given point. The size and shape of the elements are arbitrary, but generally the mesh is made fine enough to model complicated boundaries and lithology changes. Triangular-shaped elements are commonly used because of their simplicity and ease of application in two-dimensional problems.

The next step is to rewrite the equation of fluid flow (Table 3) into an operator form as

$$L(h) = \nabla \cdot [\bar{\bar{K}} \rho \mu_r (\nabla h + \rho_r \nabla Z)] = 0 \qquad (4\text{-}1)$$

The problem is to find an approximate solution to this equation. According to the Galerkin method, the approximate solution h^N is given by the following interpolation formula (Neuman, 1973)

$$h \cong h^N = \sum_{m=1}^{N} h_m \, \xi_m^e \qquad (4\text{-}2)$$

where

h = hydraulic head (exact solution)

N = total number of nodes in the mesh

h_m = hydraulic-head coefficient at node m

ξ_m^e = local coordinate function or Chapeau function associated with the m-th node and e-th element

The coefficients h_m are computed to satisfy the boundary conditions and the necessary requirement of orthogonality, namely that the relation

$$\sum_e \iint_{R^e} L(h^N) \cdot \xi_n^e \, dR^e = 0 \qquad ; n = 1, 2, \ldots. N \quad (4\text{-}3)$$

is valid throughout the entire two-dimensional flow domain (R^e) of the elements. The local coordinate functions ξ_n^e are chosen to have a value of unity at node n and are zero at other nodes in the mesh. If ξ^e is assumed to vary linearly across an element, then the Chapeau function can be written as

$$\xi_n^e = \frac{(a_n + b_n x + c_n z)}{2\Delta^e} \quad (4\text{-}4)$$

where Δ^e is the area of the element. The constants a_n, b_n, c_n, and the area Δ^e are easily computed from the nodal coordinates. For a triangle with nodes at each vertex, these constants are given by

$$\begin{aligned} b_1 &= z_1 - z_3 & c_1 &= x_3 - x_2 \\ b_2 &= z_3 - z_1 & c_2 &= x_1 - x_3 \\ b_3 &= z_1 - z_2 & c_3 &= x_2 - x_1 \end{aligned} \quad (4\text{-}5)$$

and

$$2\Delta = b_1 \cdot c_2 - c_1 \cdot b_2$$

where (x_1, x_2, x_3) and (z_1, z_2, z_3) are the local coordinates for the nodes n = 1, 2, 3 in the triangle. The derivatives of the Chapeau function are easily computed from Equation (4-4).

After substituting Equations (4-1) and (4-2) into (4-3), and using Green's first identity (Neuman, 1973), the result is a system of equations.

$$A_{nm} \cdot h_m + B_n = Q_n \qquad ; m, n = 1, 2, \ldots. N \quad (4\text{-}6)$$

where A_{nm} is an N x N matrix, and B_n and Q_n are vectors of size N. The conductance (stiffness) matrix A_{nm} is given by

$$A_{nm} = \sum_e A^e_{nm} = \sum_e \iint_{R^e} \bar{\bar{K}}\, \rho\mu_r\, \nabla\xi^e_n \cdot \nabla\xi^e_m\, dR^e$$

$$= \sum_e \frac{\rho\mu_r}{4\Delta}[K_{xx}b_n b_m + K_{xz}\,(c_n b_m + b_n c_m) + K_{zz}c_n c_m] \tag{4-7}$$

It should be noted that the conductance matrix is symmetric, sparse, and banded. It is also diagonally dominant and positive definite.

The buoyancy vector B_n is written as

$$B_n = \sum_e B^e_n = \sum_e \iint_{R^e} \bar{\bar{K}}\rho\mu_r\, \rho_r\, \nabla Z \cdot \nabla\xi^e_n\, dR^e$$

$$= \sum_e \frac{\rho\mu_r\, \rho_r}{2}\,(K_{xz}b_n + K_{zz}c_n) \tag{4-8}$$

Lateral fluid flux is lumped into the vector Q_n, which is represented by

$$Q_n = \sum_e Q^e_n = -\sum_e \int_{\Gamma^e} q\, \xi^e_n\, d\Gamma^e$$

$$= -\sum_e \frac{q \cdot L^e}{2} \tag{4-9}$$

where Γ^e signifies element boundaries and L^e is the length of the element side experiencing a flux q. The vector Q_n vanishes if no boundaries in the finite-element mesh are of the prescribed-flux type, or if the prescribed flux is zero, as is the case on an impermeable boundary.

The specific discharge (Darcy velocity) is calculated for each element using the formulation given by Pickens and Grisak (1979),

$$q^e_x = -\sum_{m=1}^{3} \left(K_{xx}\, \mu_r\, \frac{\partial\xi^e_m}{\partial x} \cdot h_m + K_{xz}\, \mu_r\, \frac{\partial\xi^e_m}{\partial z} \cdot h_m + K_{xz}\, \frac{\mu_r\, \rho_r}{3}\right)$$

$$= -\sum_{m=1}^{3} \left(K_{xx}\, \mu_r\, \frac{b_m}{2\Delta} \cdot h_m + K_{xz}\, \mu_r\, \frac{c_m}{2\Delta} \cdot h_m + K_{xz}\, \frac{\mu_r\, \rho_r}{3}\right) \tag{4-10}$$

and

$$q_z^e = - \sum_{m=1}^{3} \left(K_{zx}\, \mu_r \frac{\partial \xi_m^e}{\partial x} h_m + K_{zz}\, \mu_r \frac{\partial \xi_m^e}{\partial z} h_m + K_{zz} \frac{\mu_r\, \rho_r}{3}\right)$$

$$= - \sum_{m=1}^{3} \left(K_{zx}\, \mu_r \frac{b_m}{2\Delta} h_m + K_{zz}\, \mu_r \frac{c_m}{2\Delta} h_m + K_{zz} \frac{\mu_r\, \rho_r}{3}\right) \qquad (4\text{-}11)$$

These two vectors are needed to solve the equations governing heat and mass transport.

The system of equations represented by Equation (4-6) can be solved using a direct method such as Gaussian elimination. Computational speed is increased by taking advantage of the symmetric and banded nature of the conductance matrix. Only half of the matrix band needs to be stored in the computer because of symmetry. If the hydraulic head is known (i.e. prescribed) for the p-th node in the grid, then the p-th equation in (4-6) is replaced by a dummy expression

$$A_{pp} \cdot h_p = \text{known head value} \qquad (4\text{-}12)$$

The coefficient $A_{pp} = 1.0$ and the constant head value is substituted into other equations in the system where h_p is present. The known terms are then transferred to the right-hand side of Equation (4-6) in order to preserve symmetry. The treatment of prescribed-flux nodes involves modifying the Q_n vector, as discussed earlier.

Upon solving (4-6) for the hydraulic heads, the Darcy veolcities are computed using Equations (4-10) and (4-11). Flow rates will be constant over individual elements, but discontinuous across element boundaries. A continuous velocity field can be obtained numerically by solving Equations (4-3), (4-10), and (4-11) simultaneously (Pinder and Gray, 1977), but the amount of computation increases dramatically.

The finite-element method is generally preferred over other numerical techniques, such as the finite-difference method, for several

reasons. First, the finite-element technique is capable of accurately modeling complex boundary shapes. Second, anisotropic media properties are easily treated, while other methods have difficulties. Third, boundary conditions of prescribed flux are better accounted for in the finite-element method. Finally, the numerical accuracy is generally greater than the finite-difference method. Other types of interpolation schemes, beside the linear model, can also be implemented to achieve greater accuracy with fewer elements. The improved accuracy of the finite-element method becomes especially important when it comes to solving the heat-transport equation, because of the added difficulty associated with the convection term.

Heat Transport

The finite-element method is also used in this study to solve the steady-state heat equation. Using the same mesh, the operator in this case is written as

$$L(T) = \nabla \cdot [\bar{\bar{E}} \nabla T] - \rho c_{vf} \bar{q} \nabla T = 0 \qquad (4\text{-}13)$$

Once again the approximate solution is written in terms of an interpolation formula

$$T \simeq T^N = \sum_{m=1}^{N} T_m \xi_m^e \qquad (4\text{-}14)$$

where ξ_m^e are the same Chapeau functions defined for fluid flow, and T_m are the temperature coefficients to be determined. As before, we set

$$\sum_e \iint_{R^e} L(T^N) \cdot \xi_n^e \, dR^e = 0 \qquad ; n = 1, 2, \ldots. N \qquad (4\text{-}15)$$

Substituting Equations (4-13) and (4-14) into (-15), and integrating gives

$$S_{nm} T_m = F_n \qquad ; m, n = 1, 2, \ldots. N \qquad (4\text{-}16)$$

where S_{nm} is an N x N matrix and F_n is a vector of size N. The thermal

conductance matrix S_{nm} is expressed as

$$S_{nm} = \sum_e S^e_{nm} = \sum_e \iint_{R^e} (\bar{\bar{E}}\, \nabla\xi^e_n \cdot \nabla\xi^e_m + \rho c_{vf}\, \bar{q}\, \xi^e_n \cdot \nabla\xi^e_m)\, dR^e$$

$$= \sum_e \Big[\frac{1}{4\Delta} (E_{xx}\, b_n\, b_m + E_{xz}\, (b_n\, c_m + c_n\, b_m) + E_{zz}\, c_n\, c_m)$$

$$+ \frac{\rho c_{vf}}{6} (q_x\, b_m + q_z\, c_m)\Big] \qquad (4\text{-}17)$$

This matrix is also banded, diagonally dominant, and positive definite, but asymmetric. The asymmetry is caused by convection terms in (4-17).

The lateral flux vector F_n is represented by

$$F_n = \sum_e F^e_n = - \sum_e \int_{\Gamma^e} J \cdot \xi^e_n\, d\Gamma^e$$

$$= - \sum_e \frac{J\, L^e}{2} \qquad (4\text{-}18)$$

where Γ^e signifies element boundaries and L^e is the length of the element side experiencing a heat flux J. The term F_n vanishes if the prescribed flux is zero, such as on insulated (no heat flow) boundaries.

The systems of equations represented by (4-16) is easily solved using Gaussian elimination. In this case, however, the full band of the matrix must be stored because of its asymmetry.

Mass Transport

In groundwater hydrology, the equation of mass transport is usually solved by the method of characteristics and finite-element techniques (e.g. Reddell and Sunada, 1970; Pinder and Cooper, 1970: Pinder, 1973). Finite-difference models have also been applied, but they commonly encounter numerical dispersion problems, which are caused by truncation errors (Anderson, 1979).

An alternative numerical technique is the moving-particle random-walk method. Instead of approximating numerically the partial differential

equations, the random-walk simulates the physical behavior of the mass-transport system. This is accomplished by tracking a large number of particles as they are advected and dispersed through porous media. The particles are discrete quantities of mass that represent the chemical components dissolved in the fluid. The advection of mass is simulated by physically moving each particle a specified distance in space. This distance is calculated from the local, average linear velocity of the fluid and specified time-step size. Processes such as mechanical dispersion and diffusion are simulated by allowing the particles to take a random step in space. The magnitude of the random step is a function of the time-step size, the dispersive properties of the media, and a random variable. The random-walk simulation, like the other numerical methods, is also performed on a discretized mesh. Probability theory is used to transform the particle distribution over the mesh into concentrations of the transported aqueous species.

Random-walk theory is presented elsewhere in the literature (Feller, 1961; Haji-Sheikh and Sparrow, 1966; Pipes and Harvill, 1970), and need not be given here. In fact, it isn't necessary to understand the detailed mathematics behind this form of Monte Carlo simulation in order to be convinced of its ability to solve the mass-transport equation. Bear (1969) evaluates a simple, one-dimensional random-walk problem to prove this point. Extensions can also be made up to three-dimensional space, but through a more complicated analysis (see Bear, 1972).

The application of random-walk modeling in hydrogeology is not new, although the use of it is relatively recent when compared to the other numerical methods. It was introduced for solving groundwater-pollution problems by Ahlstrom (1975) and Schwartz (1975). The report by Ahlstrom

et al. (1977) was the first detailed explanation of the numerical approach. Since then, other particle-type codes have been published (e.g. Schwartz and Crowe, 1980; Prickett, Naymik, and Lonnquist, 1981). Random-walk modeling has been applied in a variety of studies that range from field investigations (e.g. Naymik and Barcelona, 1981) to theoretical analyses of dispersion phenomena (e.g. Schwartz, 1977; Evenson and Dettinger, 1979; Smith and Schwartz, 1980).

Ahlstrom et al. (1977) provide an excellent discussion of the advantages and disadvantages of particle codes over other numerical methods. They conclude that the main advantage is its ability to minimize numerical dispersion in transport models. Particle codes are also easy to program, regardless of the number of chemical components in the transport system. Their main disadvantage is the large amount of computer time and storage required, especially for highly accurate solutions. Ahlstrom et al. (1977) show that four times as many particles must be used to double the accuracy of a random-walk simulation. In spite of this disadvantage, the moving-particle random-walk method is probably one of the better approaches for modeling multicomponent, mass transport in sedimentary basins.

The numerical implementation of the random-walk method is simple. The aqueous components are represented by a finite number of particles that are assumed to move independently from each other, and are of zero size. Each particle can be tagged with more than one aqueous component, if we assume particle movement is not affected by the type of species transported. Associated with each particle is a set of spatial coordinates (x_k, z_k) for the k-th particle, and a set of discrete quantities of mass n_k^s for the s-th component in the k-th particle.

During a single time step Δt, each particle is separately advected

and dispersed, as shown in Figure 11. The new location of a particle after advection is simply calculated from

$$x_k^* = x_k^t + v_x \cdot \Delta t \tag{4-19a}$$

$$z_k^* = z_k^t + v_z \cdot \Delta t \tag{4-19b}$$

The local velocity vector (v_x, v_z) is supplied from the finite-element solution to the fluid-flow equation [see Equations (4-10) and (4-11)].

Ahlstrom et al. (1977) show that the magnitude of the random-walk step is related to the root-mean-square distance $(2D \cdot \Delta t)^{\frac{1}{2}}$, which is derived from the Gaussian distribution. The random walk is divided into a component coincident with the flow vector $\bar{v}$, and a component traverse to the flow path (Figure 11). The step length is generated in a random fashion by sampling a probability distribution having the proper root-mean-square value and zero arithmetic mean. Ahlstrom et al., utilize a uniform distribution and derive the following expressions for the random-walk components

$$\Delta x' = (24\ D_L\ \Delta t)^{\frac{1}{2}} \cdot [0.5 - (\Phi)_0^1] \tag{4-20a}$$

$$\Delta z' = (24\ D_T\ \Delta t)^{\frac{1}{2}} \cdot [0.5 - (\Phi)_0^1] \tag{4-20b}$$

where

D_L = longitudinal dispersion coefficient $[L^2/t]$

D_T = transverse dispersion coefficient $[L^2/t]$

$(\Phi)_0^1$ = random number between 0 and 1

The dispersion coefficients are computed from

$$D_L = \alpha_L \cdot v + D_d \tag{4-21a}$$

$$D_T = \alpha_T \cdot v + D_d \tag{4-21b}$$

where

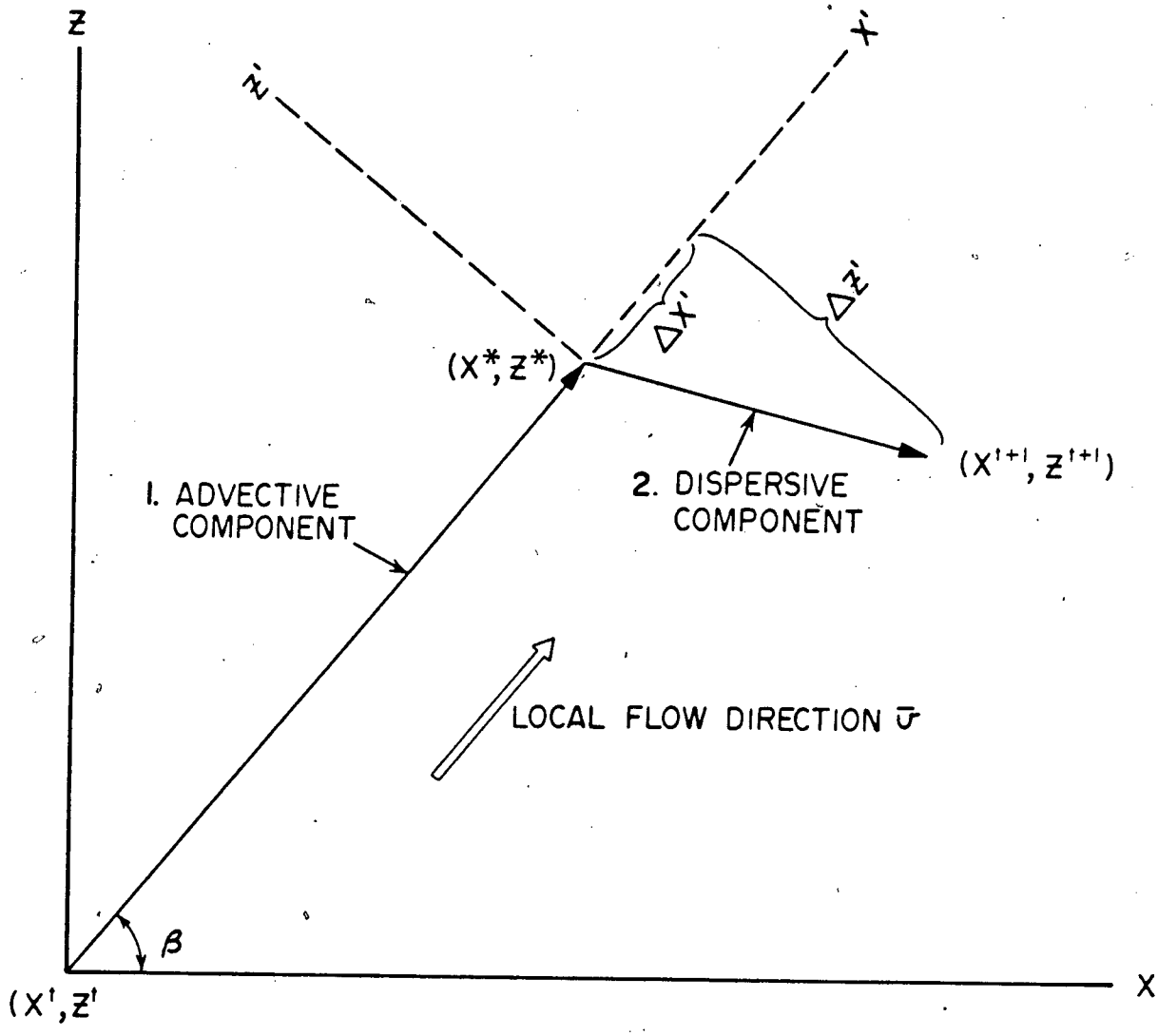

Figure 11. Vector diagram showing particle-transport component during a single time step Δt.

α_L = longitudinal dispersivity [L]

α_T = transverse dispersivity [L]

D_d = effective diffusivity [L^2/t]

v = average linear velocity [L/t]

The new position of a particle at the end of a time step is now known. It can be translated from the (x′, z′) coordinate system (Figure 11) to the base coordinates (x, z) by using the formulas

$$x_k^{t+1} = x_k^* + (\Delta x' \cdot \cos\beta - \Delta z' \cdot \sin\beta) \tag{4-22a}$$

$$z_k^{t+1} = z_k^* + (\Delta x' \cdot \sin\beta + \Delta z' \cdot \cos\beta) \tag{4-22b}$$

where β is the angle between the flow vector and the x axis, and (x_k^*, z_k^*) are the coordinates of the particle after the advective step (Figure 11). The same calculations are performed for each particle and repeated until the end of the simulation.

Spatial concentration patterns are obtained by superimposing a discretized mesh over the particle distribution, and then tabulating the number of particles in each cell of the mesh. The total mass of each chemical component in a cell is found by summing the masses over all particles present. Knowing the volume and porosity of the cell allows the mass to be expressed as a concentration value. These calculations are only needed at the end of those time steps for which a spatial concentration pattern is desired.

A moving-particle simulation can be run in two different modes. In one type of simulation, a single set of particles is released at a point source, and then its movement is tracked through the mesh. This is analogous to watching an instantaneous slug of dye that has been injected into a flow field, and is eventually dispersed as it passes through the system. The

second type of simulation involves a continuous release of new particles at the source location for all time. This type of simulation could represent a source bed from which mass is being continuously released as a heated brine passes through. After a sufficiently-long simulation of continuous release, the concentration pattern will stabilize to a steady form. Both types of simulation will show an equal concentration change as mass is transported through the groundwater-flow system.

The presence of sources or sinks are accounted for by selectively removing or adding particles, or by changing the component masses associated with existing particles in the mesh (Alhstrom et al., 1977). Chemical reactions will require that mass quantities be redistributed within each cell in which reactions occur. To accomplish this mass transfer, the mass of a given component for a given particle is adjusted so that equilibrium and reaction path constraints are satisfied at the end of a time step. Ahlstrom et al., (1977) suggest modifying the mass of each particle in the reaction cell L by the ratio of the new concentration to the old concentration

$$n_k^{s,t+1} = \left[\frac{C_L^{s,t+1}}{C_L^{s,t}} \right] \cdot n_k^{s,t} \qquad (4\text{-}23)$$

where $n_k^{s,t+1}$ represents the s-th component mass in particle k at the new time level t + 1. The numerical procedure for calculating the new equilibrium concentrations is presented in the next section.

Boundary conditions impose certain restrictions on the transport of mass in a fluid-flow system. Impermeable boundaries may demand that mass is not allowed to cross them. Therefore, a particle model must check at each time step that mass is not transported past no-flow boundaries during the advection or dispersion steps. A similar accounting procedure must be made

along free-flow boundaries. Particles can be created at inflow boundaries (e.g. recharge areas), and allowed to disappear from the basin at natural discharge boundaries. Other types of phenomena may occur at boundaries that may require particle paths to be truncated, left undispersed, or adsorbed (Evenson and Dettinger, 1979). In this study, particles are either reflected on impermeable boundaries, or allowed to enter or exit freely on free-flow boundaries such as the water table. The treatment of impermeable boundaries will be discussed in greater detail in a later section.

Geochemical Equilibrium and Reaction Paths

Geochemical modeling of water-rock interaction has been an active area of research ever since Helgeson (1968) and Helgeson et al. (1970) introduced the theory of reaction-path modeling and demonstrated their computer program PATH. Many other numerical models have been developed, over the past decade, to predict speciation and reaction progress in aqueous systems. Nordstrom et al. (1979) and Wolery (1979a) present detailed discussions on the origin of the various computer programs used in geochemistry, and review the special advantages and disadvantages of each code.

Wolery's (1978, 1979a) geochemical program EQ3/EQ6 is currently the most versatile code that has been documented. It offers a number of simulation options, some of which include the calculation of reaction processes under a temperature gradient and in a flow-through environment. EQ3/EQ6 is used in this study, and the discussion that follows is based entirely on Wolery's approach to solving the equations governing chemical equilibrium (Table 2).

The solution of this set of equations is achieved in a series of calculations involving the following steps (Wolery, 1979a):

(1) The bulk composition of the chemical system is specified by the number of moles of each element (n^t_ε, $\varepsilon = 1, \hat{\varepsilon}$).

(2) The governing equations are reformulated so as to reduce the number of operating variables to a set of unknowns, which are expressed in a logarithmic format.

(3) An initial calculation of the distribution of species is made using the method of monotone sequences (Wolery and Walters, 1975).

(4) A very small amount of reactant is introduced into the system. A new distribution of species is then determined by solving the system of equations by Newton-Raphson iteration.

(5) The value of each operating variable at a new point of reaction progress (ξ^*) is estimated from a Taylor's series expansion. The derivatives of this expansion are determined from finite-difference calculations.

(6) The aqueous system is re-equilibriated using Newton-Raphson iteration on the new set of mass constraints, thereby correcting the predicted estimates made in step (5).

(7) Mineral phases that become saturated with respect to the fluid phase are precipitated using a variety of criteria listed by Wolery (1979a).

Steps (5) to (7) are repeated until all the reactant is destroyed or the system becomes saturated with respect to a reactant. The formulation of the governing equations in terms of common logarithms is given in Wolery (1978, 1979a). The set of operating variables includes the masses of an independent basis set of aqueous species, the oxygen fugacity, the ionic strength parameters, and masses of minerals present in the system. These operating variables are written as a vector $\bar{z}$

$$\bar{z} = (\ell_w, \ell_{s=2}, \ldots, \ell_{s=\hat{s}}, \log f_{O_2}, \log \hat{I}, \log I, \ell_{\lambda=1}, \ldots, \ell_{\lambda=\hat{\lambda}}) \quad (4\text{-}24)$$

where the symbols are the same as those defined in Table 2, except ℓ denotes

a logarithmic mass ($\log_{10}$). Initial conditions are determined for $\bar{z}$ by means of the montone-sequence algorithm described by Walters and Wolery (1975). This iterative technique is less sensitive to initial conditions than other methods and handles a wide variety of input data.

Newton-Raphson iteration is used to solve the equilibrium equations during reaction-path calculations because it is usually fast to converge. Once an estimate has been made for $\bar{z}$, the error can be determined from the residual vector $\bar{\alpha}$, which contains the equilibrium equations. The Newton-Raphson method computes a correction vector $\bar{\delta}$ from the equation

$$[J] \cdot \bar{\delta} = -\bar{\alpha} \tag{4-25}$$

where [J] is the Jacobian matrix ($\partial\alpha_i/\partial z_j$), and i, j range over the elements in $\bar{z}$ (Carnahan, Luther, and Wilkes, 1969, p. 319). The correction vector $\bar{\delta}$ is solved directly from Equation (4-25) by using Gaussian elimination. A new estimate of the basis variables is then made for the next iteration (m + 1) from

$$\bar{z}_{m+1} = \bar{z}_m + \bar{\delta}_m \tag{4-26}$$

The iterative process converges as $\bar{\alpha}$ approaches a value of zero. Wolery (1979a) discusses the several methods he uses to aid convergence in EQ3/EQ6.

Starting estimates of the operating variables at new points of reaction progress can now be determined from a Taylor's series expansion for the k-th component, which is expressed in terms of previously computed points as

$$z_k\Big|_{\xi^*} = z_k\Big|_{\xi^*_1} + (\Delta\xi^*) \cdot \frac{dz_k}{d\xi^*}\Big|_1 + \frac{(\Delta\xi^*)^2}{2!} \cdot \frac{d^2z_k}{d\xi^{*2}}\Big|_3 + \ldots \tag{4-27}$$

where the subscript 1 denotes the most recent point of reaction progress. Wolery (1979a) shows that the derivatives can be written in finite-difference form. The accuracy of the reaction-path model will depend on the step size

$\Delta\xi^*$, although truncation errors may accumulate even where terms as high as the sixth-order are used in the Taylor's series (Wolery, 1979a). In EQ3/EQ6, the step size is repeatedly cut until convergence is obtained in Newton-Raphson iteration and the error is reduced to a desired tolerance.

At this stage, the geochemical model consists of a closed system in which the relative rates of dissolution of a set of reactants are assumed to be the only rate-limiting functions. Other types of reaction-path models are also considered by Wolery (1979a, 1980). The one of most practical interest to ore genesis is the flow-through model. It allows product minerals to be periodically removed from the reacting system so as to simulate compositional changes in the fluid as it flows through the reacting media. These transfers do not, however, take into account fluid-flow rates nor are they associated with specific spatial coordinates.

EQ3/EQ6 can also be used to simulate the effect of a temperature gradient on the composition of a fluid packet. (Wolery (1979a, 1979b) treats this problem by modeling the temperature as a function of reaction progress

$$T = T_0 + \Theta_1 \xi^* + \Theta_2 (\xi^*)^2 + \Theta_3 (\xi^*)^3 \qquad (4\text{-}28)$$

where

T_0 = temperature (^oC) at $\xi^* = 0$

Θ_1, Θ_2, Θ_3 = temperature-tracking coefficients

As in the case of reaction tracking, the variation in temperature is an arbitrary function and functional expressions other than a power series could be applied. In practical applications, the reaction-progress variable is usually set equal to the temperature (i.e. $\Theta_1 = 1$ and $\Theta_2 = \Theta_3 = 0$). Wolery's codes contain a thermodynamic base that allows calculations at any temperature value between 0^oC and 350^oC.

The final result of a geochemical simulation is a continuous description of the concentration of aqueous species and masses of minerals precipitated or dissolved during the reaction process.

Solution Procedure

The next step is to design a solution method for combining the algorithms of the numerical techniques. The nature of this procedure can be simple or complex, depending on the degree of coupling between the physical processes.

The Complete Transport Model

Consider a flow region as shown in Figure 12. Suppose this cross section represents a sedimentary basin for which the areal variation in fluid velocity, temperature, concentration and reaction-path geochemistry are to be modeled. Superimposed on the section is a finite-element mesh. The lower boundary (A-B) is the base of the sedimentary rock sequence, which unconformably rests on a crystalline basement. This surface is impermeable to fluid flow and mass transport. A constant geothermal flux occurs along the basal boundary. The two lateral boundaries (A-D and B-C) are also impermeable to fluid flow and mass transport. However, they are imaginary flow boundaries that occur at groundwater divides, as discussed for Figures 7 and 8. The lateral boundaries are also chosen to be insulative to heat flow (see Domenico and Palciauskas, 1973), and coincide with the groundwater divides. A water-table surface (C-D) forms the upper boundary to the region of flow. It is assumed to remain in a constant position over geologic periods of at least a few million years. The temperature along the water table is the mean annual air temperature and it is assumed to remain nearly constant. Chemical species are free to enter or leave the flow domain only along the

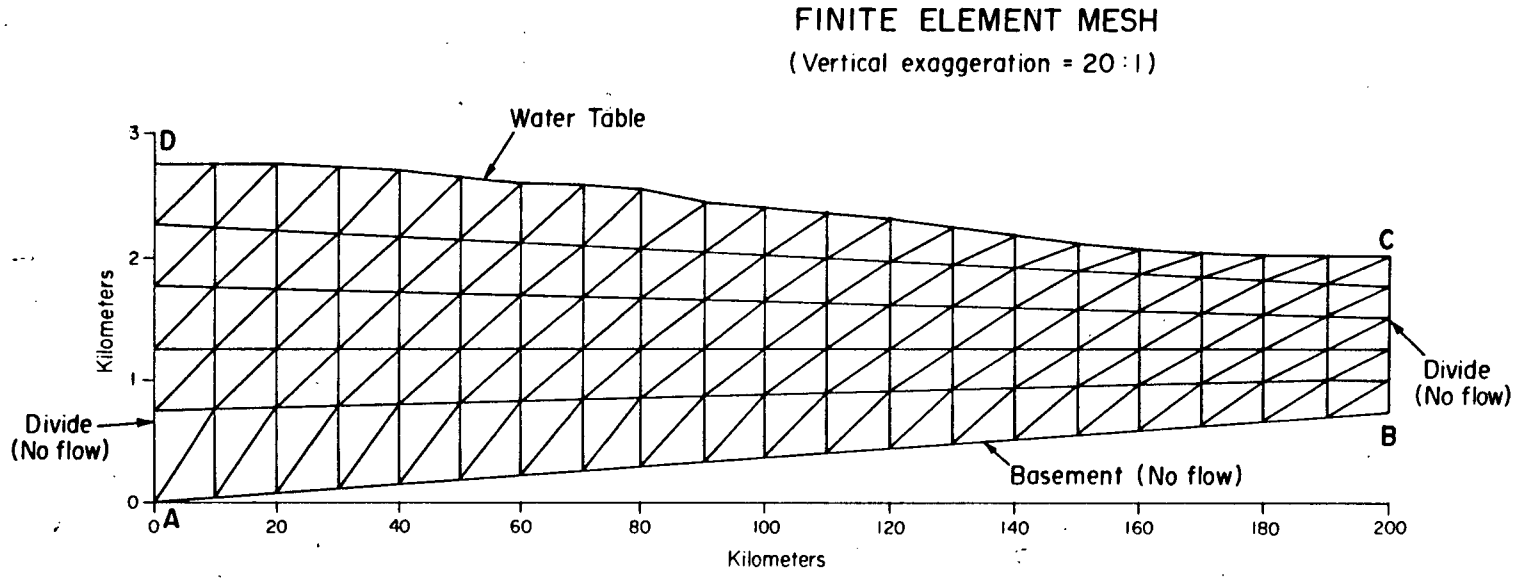

Figure 12. Region of flow and finite-element mesh for two-dimensional analysis of transport processes in sedimentary basins.

water table, but concentrations can be modified through reactions along the flow paths. The components of fluid flow, heat transport, and mass transport normal to the profile are assumed to be negligible, thereby justifying the two-dimensional representation of the basin. In other words, the third dimension normal to the cross section is of infinite extent.

Our goal is to predict multicomponent mass transport in the geologic section. Salinity and temperature gradients exist in the basin, and they must be determined in the numerical solution. The fluid-flow and heat-transport problems are coupled through their common dependence on density and viscosity. Fluid properties will also depend on the concentration of dissolved salts, especially NaCl in brine-flow systems. The fluid-flow equation and heat equation are therefore coupled to the mass-transport equations. The number of chemical components and the possible reactions will depend on the character of the pore fluid and types of mineral assemblages encountered as water flows through the basin. Variation in temperature and salinity will also require that these effects be incorporated in the geochemical calculations.

In summary, the coupling between all of the transport equations demands that they be solved simultaneously, or at least successively in some type of iterative technique. The equations of fluid flow and heat transport ought to be solved together at every time step of the mass-transport simulation. Similarly, geochemical mass transfer ought to be computed for each cell in the mesh at each time step, so as to maintain local equilibrium. The simulation would be finished after the desired number of time steps have been completed, or perhaps when a steady state has been achieved.

This fully integrated transport has not yet been solved. Several authors have developed various sets of governing equations, but no one has

designed a practical technique for simulating simultaneous inhomogeneous fluid flow, heat transport, and multicomponent mass transport with dispersion in reactive porous media. The studies by Schwartz and Domenico (1973), Fletcher and Vidale (1975), and Norton and Taylor (1979) represent the state-of-the-art in the geological sciences for modeling mass transport in reactive porous media. All three use the reaction-path approach in computing chemical mass transfer along one-dimensional flow paths. None of these finite-difference codes take into account effects of dispersion, although the work by Fletcher and Vidale (1975) does include molecular diffusion. The mass-transport code of Ahlstrom et al., (1977) also contains an equilibrium sub-model, however, it does not predict precipitation or dissolution of mineral masses. Chapman (1982) has succeeded in coupling a geochemical model for simulation of mass transport in rivers. He uses an analytical solution to represent one-dimensional mass transport of a nonreactive pulse of mass, and then modifies the pulse concentration for precipitation, adsorption, and sedimentation processes as it travels down stream. Other types of models have been developed to simulate mass transport in reactive media, although they are commonly limited to a few reactions for which kinetic data are available (Hill, 1978; Li, 1980). Mass-balance models of the type introduced by Plummer and Back (1980) may prove to be the most practical approach in modeling reactions in regional flow systems.

A Simplified Model

The moving-particle random-walk model can be used to simulate mass transport through reactive media. To calculate geochemical mass transfer, flow rate, and temperature for each cell in a mesh, and at every time step, is a formidable and currently impractical task. It is clear that an alternative numerical procedure must be employed that will simplify the

problem to a manageable form. This is especially desirable for the purpose of running the large number of simulations required by a sensitivity analysis.

Figure 13 outlines the numerical procedure chosen in this study. One major simplification is to limit the number of transported components to a single solute, such as metal or sulfide. Furthermore, the mass-transport equation is uncoupled from the computation of geochemical equilibrium. Geochemical reactions are assumed, therefore, to not affect the concentration or the path of the solute reaching the ore-forming site. The amounts of minerals and speciation during ore precipitation can be computed for any cell in the mesh, but this is accomplished outside of the transport code by running the EQ3/EQ6 program separately. For the purpose of this study, only the temperature and nonreacted concentration of a proposed depositional cell are used as input to EQ3/EQ6. The geochemical model is only used to provide possible scenarios of ore precipitation at the depositional site, and not reactions along the flow path.

A second major simplification is to assume that salinity gradients are constant in space and time. This allows the mass-transport equation for a salt component to be eliminated from the problem, which uncouples the transient dependence of fluid properties on salt concentrations. A salinity profile can still be inserted to make the fluid-flow model more realistic of basinal brines, but its effects are only felt in the fluid-flow and heat-flow solutions. Solute concentrations along the flow path will be influenced indirectly by salinity because of the change salinity will cause on fluid velocity. The variation in salinity in the basin can be specified by the program user as either a linear gradient with depth or as an arbitrary distribution based on field data.

Referring once again to Figure 13, control parameters are read in

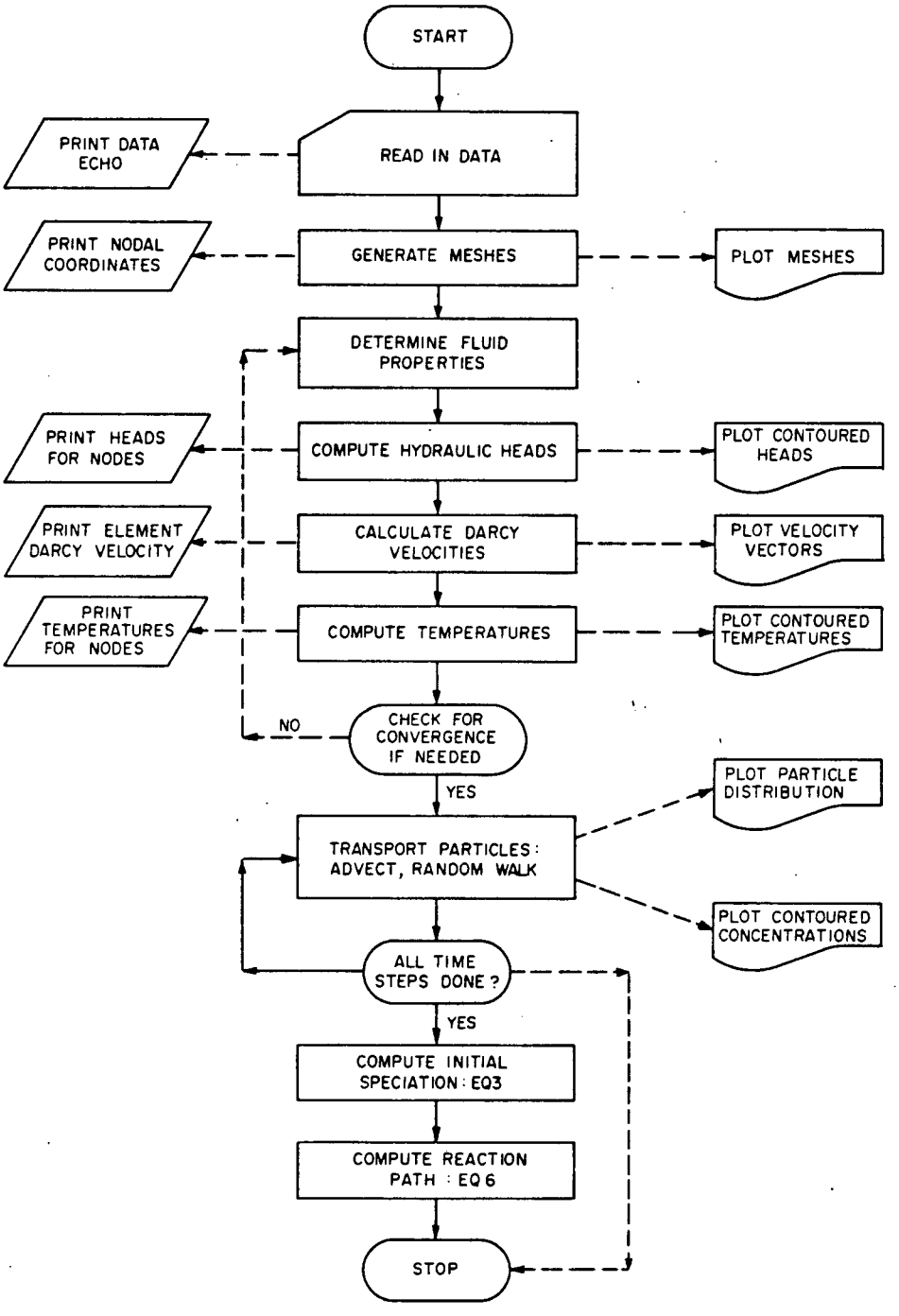

Figure 13. Flow chart for simplified transport code. (Dashed lines indicate route is optional.)

first which set up the simulation options, the size and shape of the mesh, the geologic configuration of the stratigraphic units, the material properties, and reference fluid properties. The computer program then generates two meshes. One of the grids is composed of triangular elements (Figure 12), and is used in solving the coupled fluid-flow and heat-transport equations. The other mesh is constructed by combining triangles to form quadrilateral-shaped cells, which are used in calculating concentrations and tracking particles in the random-walk solution to the mass transport equation. Both grids have the same nodal coordinates. Boundary conditions of prescribed head and temperature, as well as prescribed flux, are accounted for in the code. For the transport model, the number of input particles and their initial locations are also included as input data.

At the start of a simulation, the steady-state hydraulic-head distribution is computed first by assuming there are no salinity or temperature gradients present. Using the nodal values of the computed hydraulic head, average linear velocities are then computed for each triangular element in the mesh. The steady-state heat equation is solved next to find the temperature pattern. With the new values of pressure and temperature, and inputted salinity profile, fluid densities and viscosities are calculated from the equations of state. These four steps are repeated until the iterations converge to a stable temperature solution. Convergence is achieved when the maximum temperature change between iterations is less than a specified tolerance for all nodes in the mesh. Most problems solved in this study required less than 5 iterations, for a tolerance level of $1^{\circ}C$.

After obtaining the steady-state velocity distribution, the next step is to solve the mass-transport problem for a nonreactive solute. The source bed of the injected mass is specified by the user. Particle movement

is composed of an advected and random-walk component. At the end of each displacement, a check is made to ensure that particles are properly conserved if they encounter any boundaries. The coordinates of each particle, and the tags that identify the cell location, are continuously updated through the simulation. The size of the time step is constant, and it must be chosen carefully so as to ensure particles reside in any given cell for at least a few time steps. If the particle motion per time step is too large, the statistical accuracy of the solution will weaken and the particles may become very difficult to track without performing time-consuming grid searches.

Two basic types of information are provided by the mass-transport model: the path of transport, and the concentration decrease caused by the dilution effect of dispersion. The easiest way to obtain these results is to release a certain mass of particles at a chosen source location, and then follow the pulse as it moves through the basin. Given enough time steps, all of the particles will eventually leave the mesh along discharge zones at the water table. Particles crossing no-flow barriers are reflected back into the mesh in order to meet this boundary condition. The number of particles leaving free-flow boundaries (i.e. water table) are tabulated, along with their exit position, for later reference. Particle motion from one hydro-stratigraphic unit to another requires special handling because of the problems involved when fluid velocities change suddenly between cells. The technique used in this study is to modify the particle step size by the ratio of the velocities between cells.

If a steady-state particle distribution is sought, then mass must be continuously released from the source bed until a steady pattern emerges. For the scale of the problem modeled here, the cost of a steady-state solution is prohibitive because of the large number of particles (tens of

thousands) that must be tracked to obtain an accurate solution.

In this study, only the single-pulse method is utilized in predicting the transport path. The pulse of particles is released from a single cell location, in any part of the basin. An initial concentration of Co is assigned to the source cell. As the mass is transported along the flow path, dispersive processes reduce the concentration of the pulse, which is simulated by the spreading of the particle cluster. Relative concentrations C/Co can be computed at any specified time step in the simulation period by simply tabulating the mass of particles in each cell, as discussed earlier. The concentration value of the cell is then assigned to a fictitious point in the center of the cell for contouring purposes. Experience with the random-walk model provides the only criteria for selecting the number of particles needed and the best size of time step. Reasonably accurate solutions are obtained with 1000 to 2000 particles, although as few as 500 particles can be used in some situations.

The particle model gives the areal and transient variation in the concentration of one of the ore-forming components, such as zinc, lead, or reduced sulfur. This concentration pattern is based on the assumption that advection and dispersion are the only processes effecting the concentration of the component between source bed and depositional site. Reaction scenarios at the proposed ore-forming site can be made by making further assumptions regarding the general composition of the brine carrying the component to the site. Usually this is not difficult because the general compositions of ore-forming brines are well known from fluid-inclusion data and present-day basinal brines.

With the ore-forming component concentration in hand, and reasonable assumptions made for brine composition, EQ3/EQ6 is then used to assess a

variety of possible precipitation mechanisms for the depositional site. This program package consists of two separate codes, EQ3 and EQ6, and supporting thermodynamic data files. About 180 aqueous species and 175 minerals exist in the data files, which are supported in equilibrium calculations up to 350°C. Accurate modeling of saline aqueous solutions is limited to ionic strengths of less than about one molal in EQ3/EQ6 (Wolery, 1979a). As shown in Figure 13 and discussed earlier, EQ3 calculates an initial distribution of species, which is then used as an input model for EQ6. The simulation then proceeds by dissolving the specified set of reactants, while tracking the composition of the fluid and predicting the amounts of secondary minerals precipitated. EQ6 finishes a simulation when the total mass of the reactants are consumed, the specified temperature change is achieved, or when the system becomes saturated (equilibriates) with respect to the reactants.

The description of the simulation procedure is now completed. Execution times for the transport model and EQ3/EQ6 vary with the size of the finite-element mesh, stratigraphic complexity, number of particles transported, and geochemical nature of the reaction-path simulation. An average transport simulation commonly takes about one minute of Central Processing Unit (CPU) time to process on the Amdahl 470 V8 computer at the University of British Columbia. A single reaction-path simulation also takes about one minute of CPU time, for the types of simple simulations to be presented later. Longer execution times may be required in complicated problems.

Model Verification

The transport code developed for this study has received considerable testing, as is outlined in the following pages. The fluid-flow part of the

code was verified by running several test-data decks in another finite-element routine, which was written by Pickens and Lennox (1976). Comparisons were only made for the case of an isothermal, fresh-water basin. Similarly for the heat-transport subroutine, results of several simulations were compared to model results presented elsewhere, in this case by Betcher (1977). Only the mass-transport subroutine was tested in further detail, mainly because the use of moving-particle random-walk codes is relatively new in hydrogeologic modeling.

Solute-transport models are commonly verified by comparing the numerical answer to analytical solutions of the advection-dispersion equation. Bear (1972, p. 627) presents several analytical expressions that can be used for testing purposes. One of the simplest problems is to solve for the spread of a concentration front in a semi-infinite column. The fluid velocity is assumed to be uniform and the solute can either be injected as a single slug or continuously released at one end of the column. Schwartz (1975, 1978) and Ahlstrom et al. (1977) compare their particle-code solutions to the analytical solution of this one-dimensional problem. Both studies show that the accuracy of a particle model depends on the number of particles used, the time step, and the cell sizes in the mesh. They found that a few thousand particles are needed to produce highly accurate solutions in many transport problems.

The same type of one-dimensional test was applied to the particle code developed in this study. Several simulations were conducted to establish the working ability of the algorithm. The results and conclusion duplicate those of Schwartz (1975) and Ahlstrom et al., (1977). The model was also compared against a two-dimensional simulation given by Schwartz (1978).

The problem with one-dimensional tests is that they do not verify the numerical treatment of the two-dimensional boundary conditions, which are

encountered in modeling sedimentary basins. Particle models commonly treat impermeable boundaries as being reflective, but the theory isn't clear on why particles have to be reflected. Evenson and Dettinger (1977) suggest that particles could alternatively be adsorbed on boundaries, or their paths truncated. A new boundary-value problem was therefore designed to help investigate this question, and to test the accuracy of the code in two dimensions. The remainder of this section discusses these tests.

Consider the transport of a nonreactive solute in a uniform velocity field v, which is directed along the + axis in the x - z plane. The flow region is bounded in the z - direction by parallel, impermeable boundaries at z = L and z = - L, and is of infinite extent in the x - direction. At time t = 0, a slug of solute with mass M is instantaneously injected into the flow field at the coordinate origin (0, 0). The porous medium is isotropic and homogeneous, with porosity ϕ. The problem at hand is to solve for the transient concentration pattern as the solute is advected and dispersed through the flow region.

Mathematically, the concentration distribution is found by solving the following partial differential equation

$$\frac{\partial C}{\partial t} = D_L \frac{\partial^2 C}{\partial x^2} + D_T \frac{\partial^2 C}{\partial z^2} - v \frac{\partial C}{\partial x} \tag{4-29a}$$

subject to the conditions that

$$C\ (x,\ z,\ o) = \frac{M}{\phi}\ \delta(x) \cdot \delta(z) \quad \text{for } t \leq o \tag{4-29b}$$

$$\frac{\partial C}{\partial z} = o \text{ at } z = +L,\ -L \qquad \text{for } t > o \tag{4-29c}$$

$$C\ (x,\ z,\ t) \text{ is bounded for } |x| \to \infty \tag{4-29d}$$

where

C = concentration of solute $[M/L^3]$

D_L = longitudinal dispersion coefficient $[L^2/t]$

D_T = transverse dispersion coefficient $[L^2/t]$

v = fluid velocity $[L/t]$

ϕ = porosity

δ = dirac-delta function

The analytical solution of this problem is too lengthy to present here, but the derivation can be obtained from the author upon writing. In short, it involves the use of Green's functions and the method of images, both of which are described in advanced mathematics texts (e.g. Carslaw and Jaeger, 1959). The final result is

$$C(x, z, t) = \frac{(M/\phi)}{4\pi t(D_L D_T)^{1/2}} \cdot \exp\left[\frac{-(x-vt)^2}{4D_L t}\right] \cdot \left\{ \exp\left[\frac{-z^2}{4D_T t}\right] + \exp\left[\frac{-(z-2L)^2}{4D_T t}\right] + \exp\left[\frac{-(z-2L)^2}{4D_T t}\right]\right\} \quad (4\text{-}30)$$

The last two exponential terms in this equation account for the boundary effects in the transport problem. Until the solute mass spreads out enough to be affected by the boundaries, the influence of these terms is small.

The numerical solution of Equation (4-29) is completed with the moving-particle model and the mesh shown in Figure 14. Notice that the vertical scale is expanded to twice the horizontal scale so as to illustrate details of the grid. The top and bottom boundaries are represented as no-flow barriers, while the two lateral borders allow particles to enter or leave freely. The flow region is 460 m long by 75 m wide, and the porous medium has the following parameter values: $\phi = 0.10$, $v = 1.0$ m/yr, and $D_L = D_T = 3\ m^2/yr$. The original amount of mass released at point Q (Figure 14) is $M = 1.0 \times 10^4$ mg. At $t = 0$, 5000 particles are instantaneously

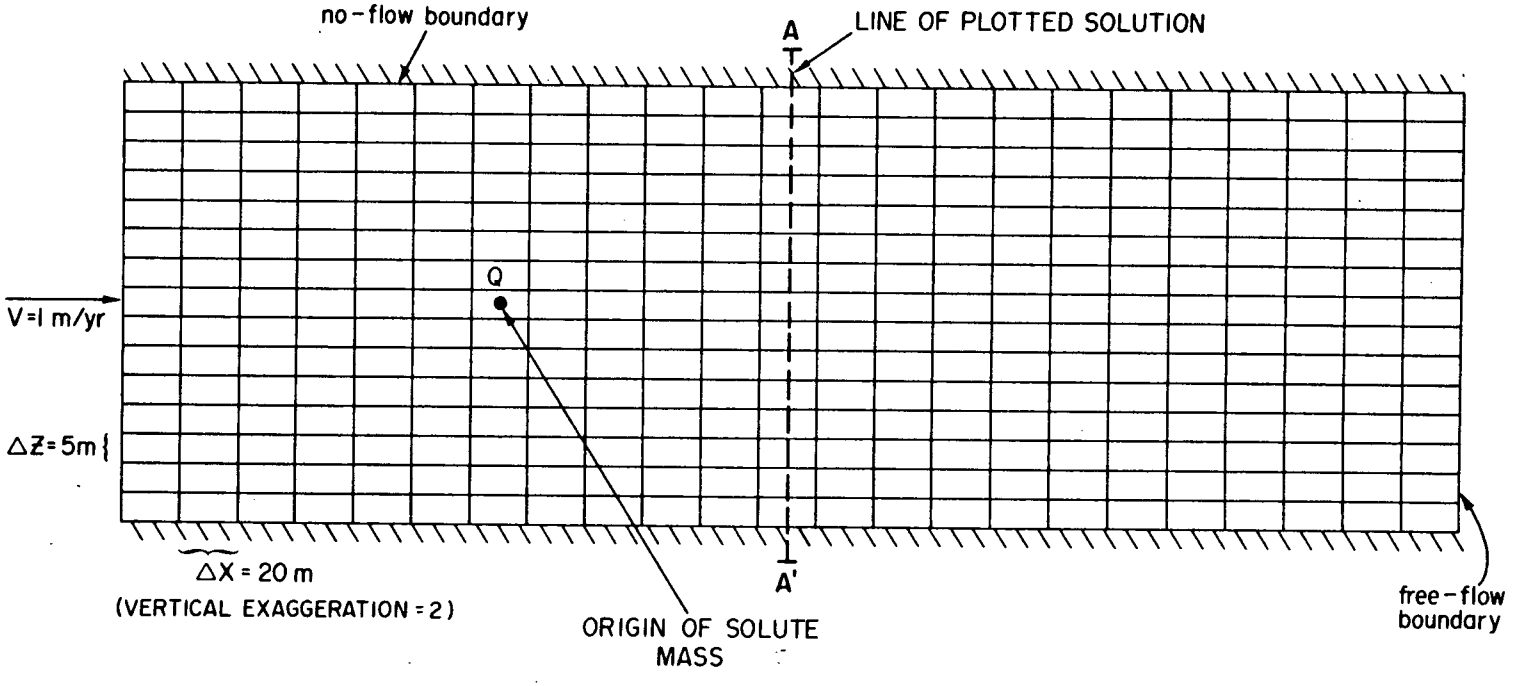

Figure 14. Mesh used in testing moving-particle code against analytical solution at A-A'.

released with an assigned mass of 2 mg each. A time-step of 0.5 yr is used in running the simulation over a time interval of 100 years. As the cloud of particles move across the field, particles are dispersed both along the flow path and transverse to it. The particle cloud eventually encounters the two barrier boundaries at z = +L, -L.

Three separate simulations are made to test three different ways of treating particles that cross no-flow boundaries. The first method reflects particles back into the mesh, the second method truncates their path at the barrier, and the third method arbitrarily takes the ejected particle and relocates it at the center of the cell from which it left. Figure 15 illustrates the results of the three simulations, for the traverse line A-A′ marked in Figure 14. This position of the solute pulse corresponds to t = 100 years. The concentrations in each cell along A-A′ are plotted on the ordinate, and distance from the center line on the abscissa The graphs also contain the computed analytical solution from Equation (4-30), with x = 100 m and t = 100 yr.

These results verify that a reflective type boundary condition is the proper technique to use in simulating no-flow barriers. Truncating the path of the particle or relocating the particle are unjustified from a mathematical point of view. Both the truncation and relocation techniques over estimate the amount of mass near the center of the distribution, and under estimate the concentration near the real barriers (Figure 15).

Simulation Example

In order to demonstrate the full use of the simplified numerical procedure, a sample simulation is present in Figure 16. It is meant to show the modeling approach only and should not be taken as a final result. The simulation does, however, give a typical selection of the types of computer

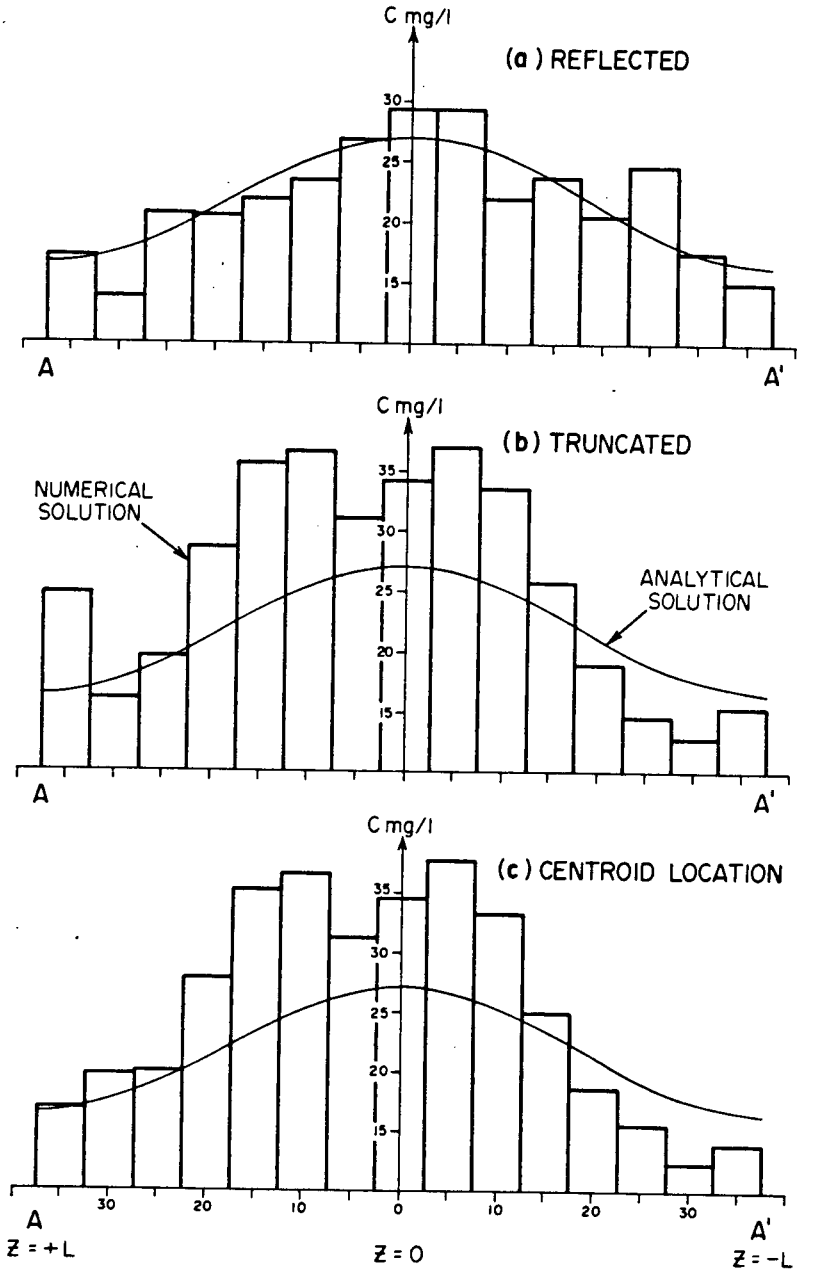

Figure 15. Comparison of moving-particle random-walk solutions of three-different treatments of particles crossing no-flow boundaries with analytical solution.

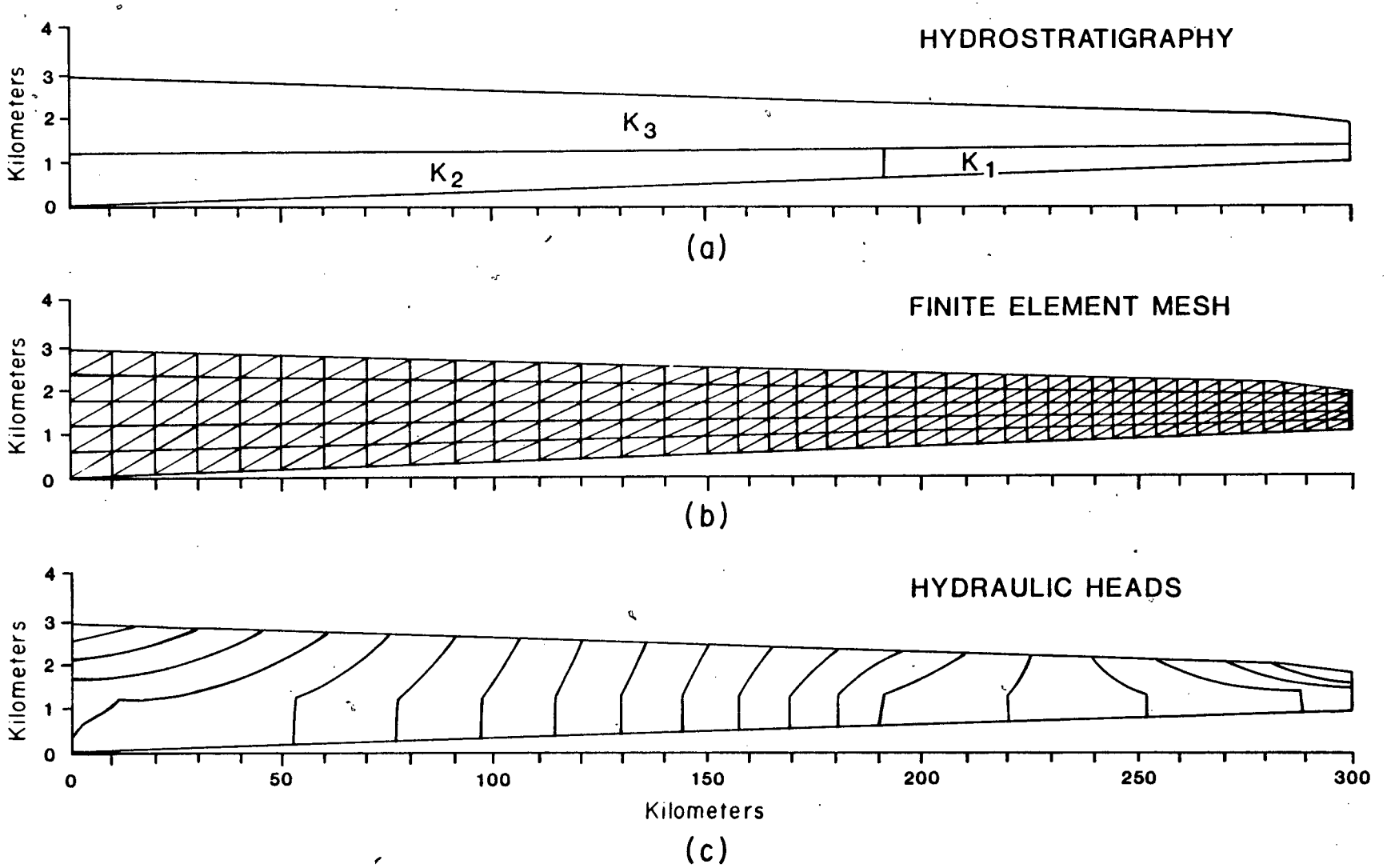

Figure 16. Simulation example.

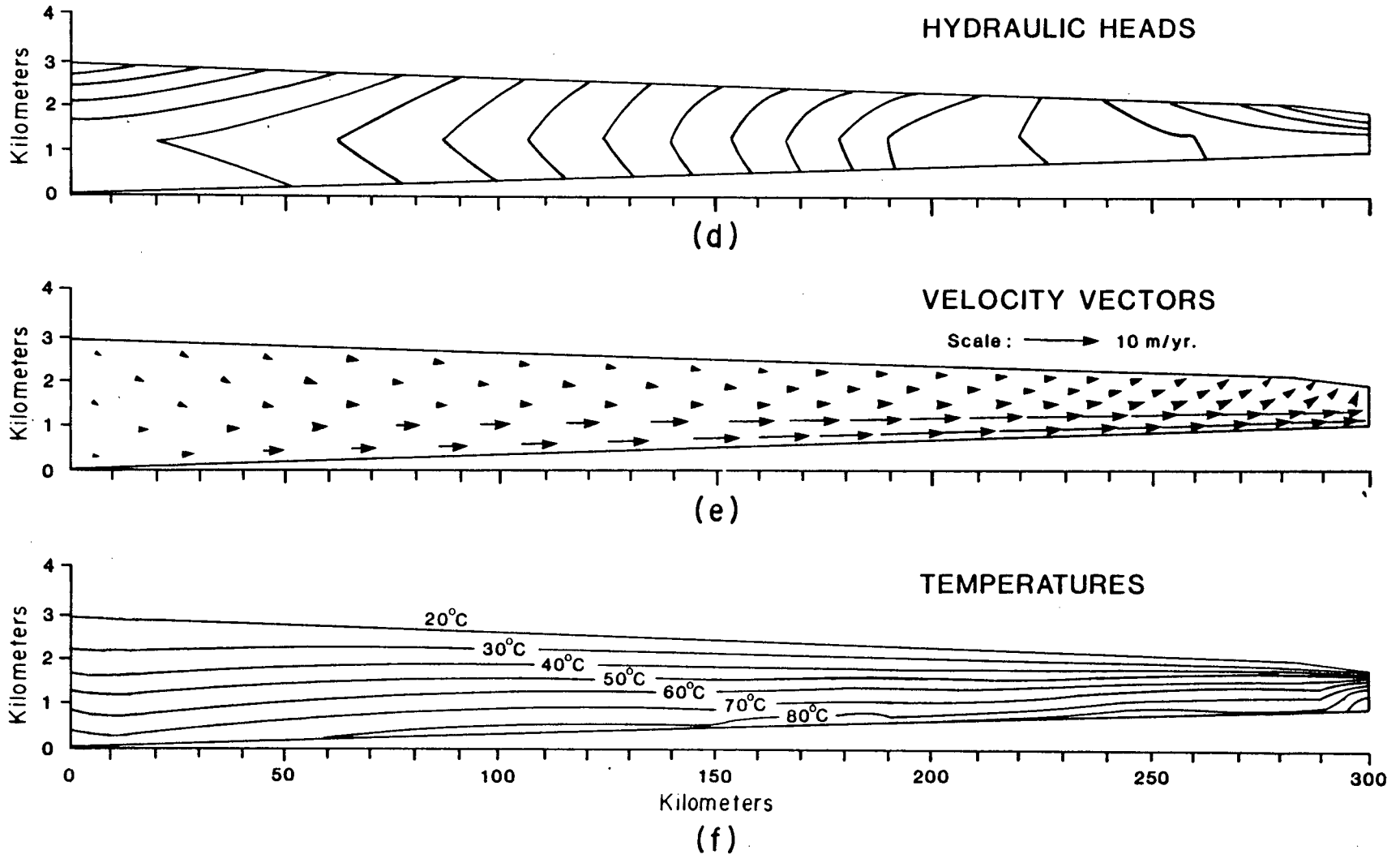

Figure 16. (Continued)

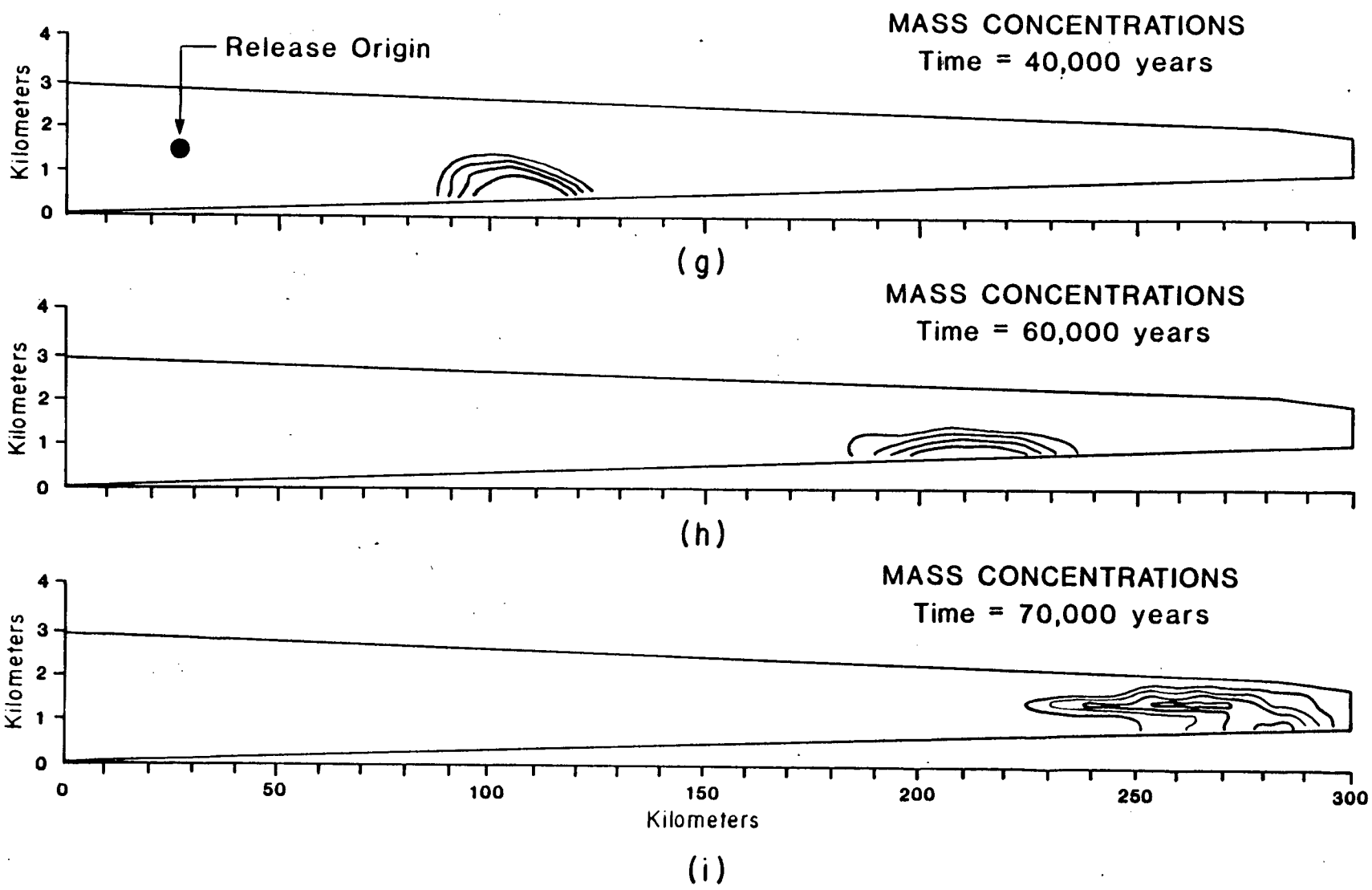

Figure 16. (Continued)

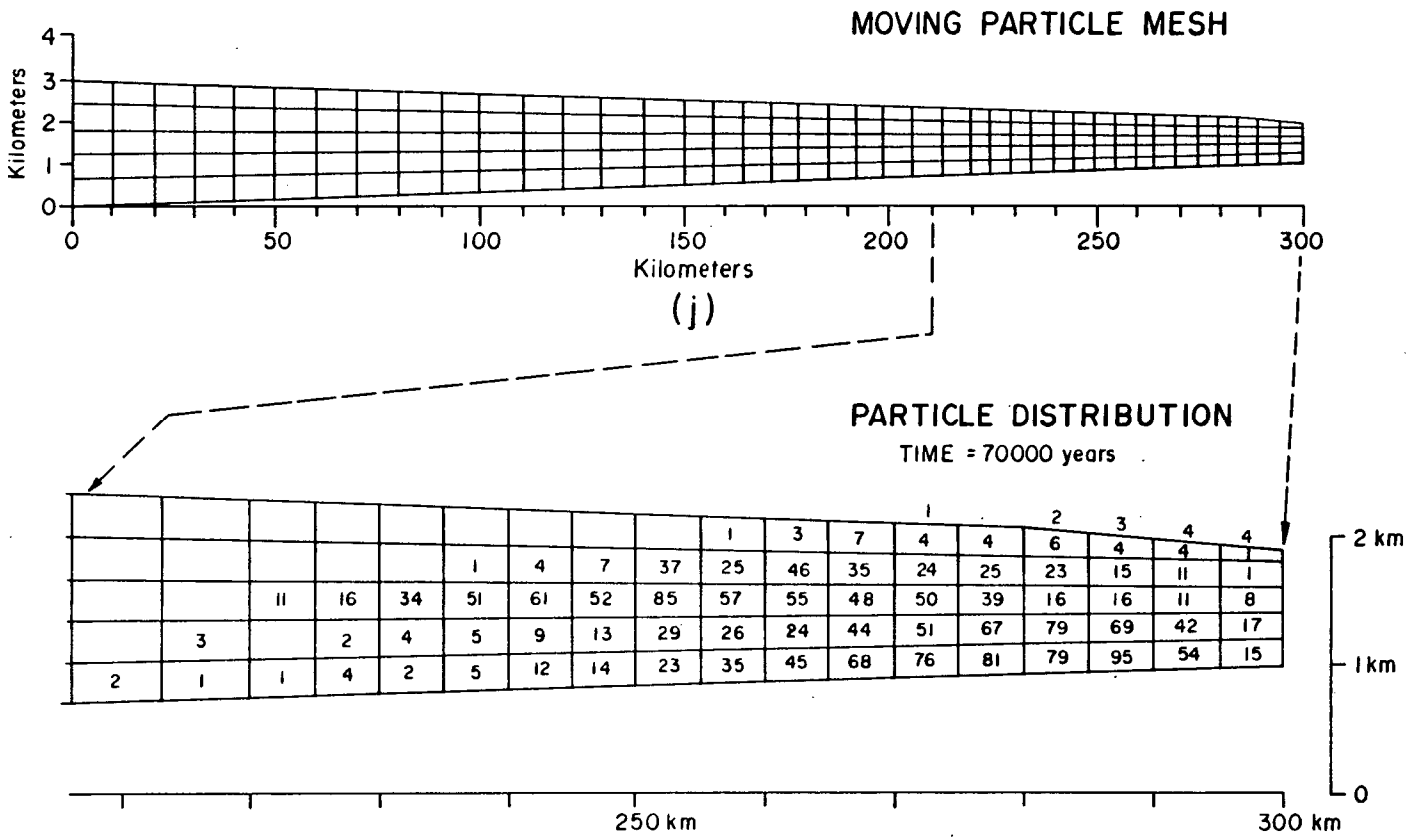

Figure 16. (Continued)

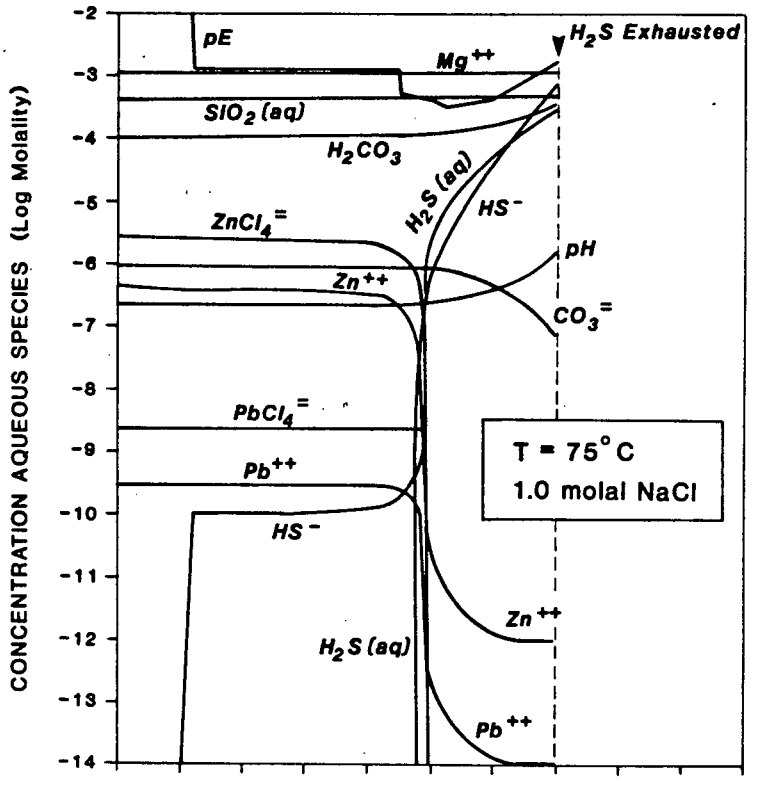

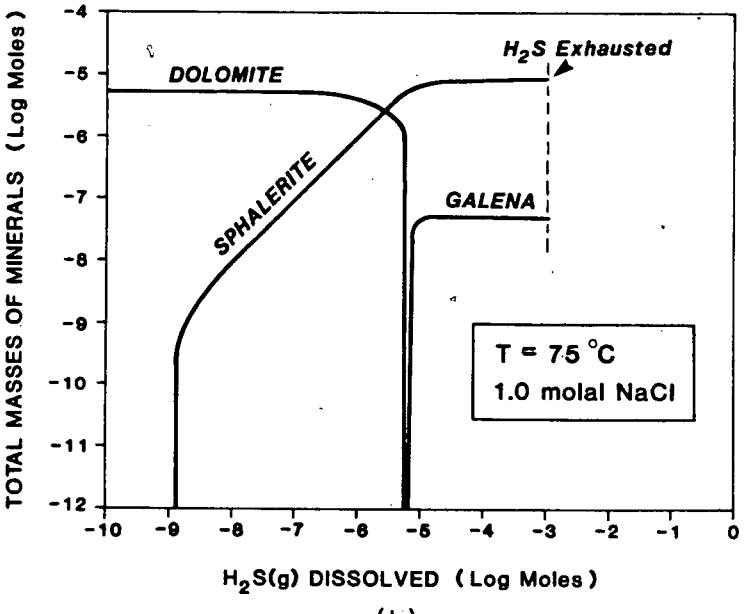

(k)

Figure 16. (Continued)

plots generated by the code. Table 5 lists values of the parameters used in this simulation. The numbers chosen for these parameters are justified in the next chapter. For now it is sufficient to say that they are somewhat arbitrary, but the numbers are representative of media properties and brine compositions that occur in sedimentary basins. Approximately 50 seconds of CPU time was needed to run this transport problem (Figures 16a to 16h), and 65 seconds was used in predicting the reaction-path model (Figure 16i).

Figure 16a is a schematic cross section of a sedimentary basin. The wedge-shape profile is designed to reflect the major features considered in the conceptual model of Figure 6. The length of the basin is 300 km and the stratigraphic sequence varies in thickness from 3000 m at x = 0 km, down to 900 m at x = 300 km. In this section, the vertical scale is expanded to 10 times that of the horizontal scale for illustrative purposes.

The geology of the basin is very simple. It consists of three main stratigraphic units, which have different hydraulic properties (Table 5). The lower boundary forms the contact of the permeable, sedimentary sequence with an impermeable, crystalline basement. The basement surface dips gently to the left side of the diagram at a rate of about 3.3 m/km. The beds marked K_1 and K_2 in Figure 16a produce an extensive basal aquifer, representative of a karstic-type carbonate unit which passes down dip into a less permeable limestone-dolomite facies. Overlying the basal aquifer is a thick sequence of low-permeability mudstones (K_3). The K_1 unit is the most permeable unit in the section (Table 5). It has a hydraulic conductivity that is 100 times greater than the K_3 beds and 5 times greater than the hydraulic conductivity of the K_2 beds. An anisotropy ratio (K_{xx}/K_{zz}) of 100:1 is assumed for all strata in the basin. This value is chosen to represent the inherent anisotropy within individual sedimentary beds, and the layered heterogeneity that

Table 5. Model parameter data for simulation example

Parameter	Symbol	Hydrostratigraphic Unit 1	2	3	Field Units
Fluid Flow					
Porosity	ϕ	0.20	0.15	0.10	fraction
Horizontal hydraulic conductivity	K_{xx}	500.0	100.0	5.0	m/yr
Vertical hydraulic conductivity	K_{zz}	5.0	1.0	0.05	m/yr
Reference fluid density	ρ_0	998.2 (all units)			kg/m^3
Reference fluid viscosity	μ_0	1.0×10^{-3}(all units)			kg/m•s or Pa•s
Salinity gradient	-	0.005 (all units)			% NaCl/m
Heat Transport					
Thermal conductivity of fluid	κ_f	0.63 (all units)			W/m^oC
Thermal conductivity of solids	κ_s	3.0	3.0	2.0	W/m^oC
Specific heat capacity of fluid	c_{vf}	4187.0 (all units)			J/kg^oC
Specific heat capacity of solids	c_{vs}	1005.0 (all units)			J/kg^oC
Longitudinal thermal dispersivity	ε_L	100.0	100.0	1.0	m
Transverse thermal dispersivity	ε_T	1.0	1.0	1.0	m
Geothermal heat flux at base	J	70.0 (constant)			mW/m^2
Temperature at water table	T_0	20.0 (constant)			^oC

(Continued on next page)

Mass Transport

Longitudinal dispersivity	α_L	100.0	100.0	1.0	m
Transverse dispersivity	α_T	1.0	1.0	1.0	m
Apparent diffusion coefficient	D_d	3.0×10^{-3}	3.0×10^{-3}	3.0×10^{-3}	m^2/yr

Geochemical Reactions/Mass Transfer

	Species	Concentration (per kg H_2O)	
Initial equilibrium constraints:	Na	1.0 moles	pH = 6.8
	Cl	1.0 moles	Eh = +0.58 volts
	Zn	0.50 mg	T = 75°C
	Pb	0.01 mg	Calcite, Dolomite and Quartz are initially in equilibrium with the fluid
	CO_2	0.01 moles	
	SO_4	100 mg	

Reactant: 1.0×10^{-3} moles of dissolved $H_2S(g) \simeq 35$ mg/kg H_2O

reactant-tracking coefficients $\zeta_1 = 0$ $\zeta_2 = 1$ $\zeta_3 = 0$

exists at a finer scale than the stratigraphy depicted in a regional representation.

The boundary conditions are the same as those described for Figure 12. The bottom is impermeable to fluid flow and mass flux, and a constant geothermal flux J is prescribed along its length. The two lateral boundaries are barriers to fluid flow, heat flow, and mass transport. The upper surface is the water table, which is composed of two linear-slope segments. It is meant to reflect a basin with a gentle topographic gradient. Mass is allowed to leave the basin where groundwater discharges across the water table. The temperature along the upper boundary is fixed at the mean annual air temperature.

Figure 16b shows the finite-element mesh used in solving the fluid-flow and heat-transport equations. It consists of 252 nodes and 410 triangular elements. The same nodes are utilized in constructing quadrilateral-shaped cells that are used for tracking particle movement and computing concentrations.

Figures 16c, 16d, 16e, and 16f display the numerical solution to the coupled problem of inhomogeneous fluid flow and heat transport. In Figures 16c and 16d, the hydraulic-head solutions are plotted with a 50 m contour-interval. By definition, the hydraulic head is equal to the elevation at the water table. Therefore, the contour values take on the elevation of the point at which it intersects the water-table surface. The hydraulic-head pattern in Figure 16c is derived from the first iteration of calculations, in which there are no salinity or temperature gradients present. Upon completing six iterations of solving the fluid-flow and heat equations, the coupled solutions converge to the patterns shown in Figures 16d and 16f. A linear salinity gradient of 0.005% NaCl/m is assumed to exist with depth, but only below the 2 km elevation level. Above this datum the water is assumed to be

fresh. This salinity gradient produces a maximum salinity of 10% NaCl at the thick end of the wedge-shape basin.

The velocity field of the basin is easily calculated upon knowing the hydraulic-head solution, salinity profile, and temperature distribution. Figure 16e shows the average linear velocity vectors for the simulation example. The orientation of the arrows indicate the direction of flow and the length of the arrows indicate the magnitude of the velocity value. A velocity value is calculated for each triangular element in the mesh (Figure 16b), but only half of the vectors are plotted for clarity. Notice that the presence of the basal carbonate aquifers causes fluid flow to be directed down across the shale beds in the elevated end of the basin (i.e. x = 0 to x = 150 km), and discharged upwards at the basin margin. The influence of permeability changes is best illustrated by the sharp bends in the hydraulic-head contours, but these changes are also marked by the velocity-vector pattern. Velocities vary in the basin from an average of 0.2 m/yr in the K_3 unit to over 10.0 m/yr in the K_1 beds.

Heat transport is affected by both thermal convection and conduction, as shown by the temperature pattern in Figure 16f. Much of the bending and spacing of the isotherms is due to the thermal conductivities of the stratigraphic units and the geothermal flux imposed along the base of the section. However, significant convection effects are also included in the numerical solution. This is especially evident in the recharge end of the basin where downward fluid flow depresses the temperature, and in the discharge end of the basin where upward fluid flow elevates the temperature (Figure 16f). In this simulation, temperatures easily exceed 100°C at the very end of the section, primarily because of the influence of fluid flow. Conduction alone would not produce these warm temperatures at such a shallow

depth, under normal heat flow conditions.

Figure 16g shows the results of the random-walk solution to the advection-dispersion equation. The purpose of this simulation is to predict the movement and dispersion of a metal-bearing fluid packet, which is released from an arbitrary source location in the shale beds, at the recharge end of the basin (see Figure 16g). Only the concentration patterns at four-different times are plotted. The contour values represent 3%, 6%, 9%, and 12% of the original concentration Co released at the source. Notice that as the pulse travels through the basin, dispersion causes the plume to spread out with time as concentrations weaken. The maximum concentration of solute reaching the edge of the basin is approximately 15% of the source Co. Figure 16j shows the detailed particle distribution at t = 70000 yr. These numbers represent the actual number of particles counted in each cell at that specific time step. Also plotted is the cumulative particle discharge at the water table. If a simulation is run long enough, all of the particles will discharge to the surface. The particle-discharge distribution along the water table provides qualitative information as to the nature of mass transport in the basin. The use of this information is shown later.

So far we have not specified what type of metal species was transported or the original source concentration. The main assumption is that the solute is nonreactive along the flow path. Because the concentrations are expressed as a dimensionless fraction (percent) of the source value, the simulation can be used for any concentration level of interest. If the source, for example, is sustaining a zinc concentration of 3 mg/kg H_2O, then about 0.5 mg/kg H_2O will reach the aquifer zone near the edge of the basin ($x \simeq 250$ km). We can then use this value as input to geochemical reaction-

path models.

Suppose the ore-forming site is located at a depth of about 1 km in the K_1 unit and near x = 250 km (Figure 16a). The temperature at this depth is approximately 75°C and the salinity is 7% NaCl (about 1.0 molal). Let's assume that approximately 35 mg/kg H_2O (10^{-3} m) of H_2S (gas) is being continuously made available through sulfate reduction in the organic-rich carbonate aquifer. Figure 16k shows the resulting reaction path and fluid speciation as the metal-bearing brine encounters H_2S at the proposed ore-forming site. The initial composition assumed for the brine is listed in Table 5. Only a selected group of the aqueous species present are plotted in Figure 16k. As H_2S begins to dissolve, the brine first precipitates dolomite, which later dissolves, but addition of further H_2S causes sphalerite and galena to precipitate. The oxidation state becomes highly reduced and the pH becomes more acidic as the reaction progresses. Approximately 0.72 mg of sphalerite and 0.01 mg of galena are produced per kg of water. At the same time 0.97 mg of dolomite and 35.0 mg of H_2S are dissolved.

The time required to deposit an average size ore body can now be made by using the flow rates computed earlier. The average linear velocity near this site is about 9.0 m/yr (Figure 16e), therefore, the specific discharge (flow rate per unit area) is about 1.8 $m^3/m^2 \cdot yr$. The volume flow rate can be calculated by assuming an area through which the flow is taking place. A short calculation shows that for an effective discharge area 200 m thick by 10 km wide, about 2600 kg/yr of sphalerite would be precipitated at the proposed ore site. To deposit 100 million tons of 5% Zn will require, therefore, about 2.5 million years under this flow rate and brine-reaction scenario.

It is clear that the transport models and reaction-path simulations can provide a significant amount of information about the role of fluid flow in ore genesis, and its effects on subsurface temperatures, mass-transport patterns, and deposition rates in the ore-forming process. It should be possible to learn much more about the factors affecting ore genesis in sedimentary basins by continuing this analysis in greater detail, and by comparing simulated models to actual field situations.

CHAPTER 5

EVALUATION OF TRANSPORT PROCESSES IN ORE GENESIS: QUANTITATIVE RESULTS

The purpose of this chapter is to carry out a detailed sensitivity analysis with the numerical models. The goal of these experiments is to determine the influence of various factors on the transport processes involved in the formation of carbonate-hosted lead-zinc deposits. Through the simulations, the model of a gravity-driven flow system will be fully tested, and a comprehensive set of conditions and parameter constraints will emerge to help establish the role of regional groundwater flow in ore genesis.

A sensitivity analysis can take one of two different routes, depending on the purpose of the study. One approach is called site-specific because the modeling is designed for a particular geologic basin or specific ore deposit. It can yield detailed information, provided an adequate amount of data can be collected to calibrate the model. The second approach is known as generic because the simulations are carried out on hypothetical basins. Such models are designed to reflect many of the geologic features observed in real sedimentary basins, but are purposely kept simple in order to be of general use in understanding the phenomena being studied. For the generic approach, a range of realistic input data is chosen to assess general mechanisms and to assess the sensitivity of the model results to a change in the numerical value of any particular parameter. Generic modeling forms the main basis of analysis in this study.

The simulation results given below are divided into several sections, as outlined in Table 6. First, the factors affecting fluid flow, heat

Table 6. Outline of sensitivity analysis

Simulation Parameter	Figure
Fluid Flow	
Isotropic hydraulic conductivity	18
Anisotropic hydraulic conductivity	19
Layering	20
Discontinuous layers (pinchouts)	21,22
Temperature-dependent flow	23,24,25,26
Salinity-dependent flow	27,28,29,30
Combined temperature and salinity effects	31
Salinity gradient	32
Basin size	33,34,35
Basement structure	36,37,38,39
Water-table configuration (topography)	40,41,42,43,44
Heat Transport	
Hydraulic conductivity	45,46
Thermal conductivity (isotropic)	47
Layering	48
Thermal dispersion	49,50,51
Geothermal flux	52,53
Surface temperature (climate)	54
Basin size	55
Basement structure	56,57
Water-table configuration (topography)	58
Mass Transport	
Hydraulic conductivity	59,60
Maximum pulse concentration	61
Layering	62
Isotropic dispersivity	64
Longitudinal dispersivity	65,66
Geologic configuration	67,68
Geochemical Equilibrium and Reaction Paths	
Aqueous sulfur species stability fields	69,70
Galena and sphalerite solubility as a function of:	
a) pH and reduced sulfur content	71
b) salinity	72
c) temperature	73
Metal-sulfate brine model:	
a) reaction with hydrogen sulfide	74
b) reaction with methane	75
c) reaction with pyrite	76
Metal-sulfide brine model:	
a) reaction with dolomite	77
b) effect of cooling	78

transport, and mass transport are independently and systematically examined. All of these simulations are performed in a simple, two-layer basin model. A variety of more complex geologic configurations are also introduced, although the discussion is kept brief. Following the transport modeling, a review is made of the factors influencing metal concentrations in brines. Using some of the conceptual models proposed for ore precipitation, several reaction-path simulations are then conducted and evaluated. To close the chapter, a preliminary simulation is finally presented of the Pine Point lead-zinc deposits, Northwest Territories.

Factors Controlling Fluid-Flow Patterns and Velocities

There has been much work in hydrogeology on the effect of variations in controlling parameters on regional groundwater flow. The work by Tóth (1962, 1963) and Freeze and Witherspoon (1966, 1967, 1968) were already discussed earlier (see Figures 7 and 8). They found that the most important factors affecting flow patterns are:

(1) depth to length ratio of the basin,

(2) topography or water-table configuration

(3) stratigraphy and the resulting variations in the hydraulic conductivity

From the point of view of defining the role of hydrodynamics in ore genesis, some of the most interesting results of these earlier studies are those that demonstrate how basin-wide aquifers serve to direct flow across less permeable beds and focus flow toward major discharge areas.

In this section, some of these controlling factors are examined in greater detail. Although part of the analysis is similar to that given by Freeze and Witherspoon (1967), it is included here for the purpose of completeness and review. Differences also exist because of the scale of the basin

being modeled, and the fact that salinity and temperature effects are accounted for in this study.

As a starting point, consider a sedimentary basin of the shape and size depicted by the finite-element mesh shown in Figure 17. The region of flow is based on the same criteria as those specified for the simulation example (Figure 16). This mesh is used throughout the sensitivity analysis, unless otherwise specified. It consists of 410 triangular elements and 252 nodes. Topographic relief (water-table configuration) varies linearly with a total drop of 1000 m over the 300 km length of the basin. The vertical scale of the plot (Figure 17) is exaggerated by a factor of 10:1 in order to show the simulation results. The true-to-scale diagram of the basin is plotted directly above the mesh to illustrate the nature of the vertical exaggeration.

Hydraulic Conductivity

The quantity of fluid that is able to flow through a basin to form an ore deposit depends on many factors. The basic relationship governing the flow is Darcy's law (Table 3). For fixed fluid properties and a constant hydraulic-head gradient, the magnitude of flow is solely determined by the hydraulic conductivity of the porous medium. The range of values of hydraulic conductivity of geologic materials is very wide. Table 7 shows the range established for a variety of lithologies, as listed by Freeze and Cherry (1979). Porosity is also important in that it is used to calculate the average linear velocity of the fluid. Table 8 lists the porosity range of values for the common rock types, which is based on data given by Davis (1969) and Freeze and Cherry (1979).

The simplest hydrogeologic model of a sedimentary basin is the case of a homogeneous and isotropic section. Figure 18 shows the results of a

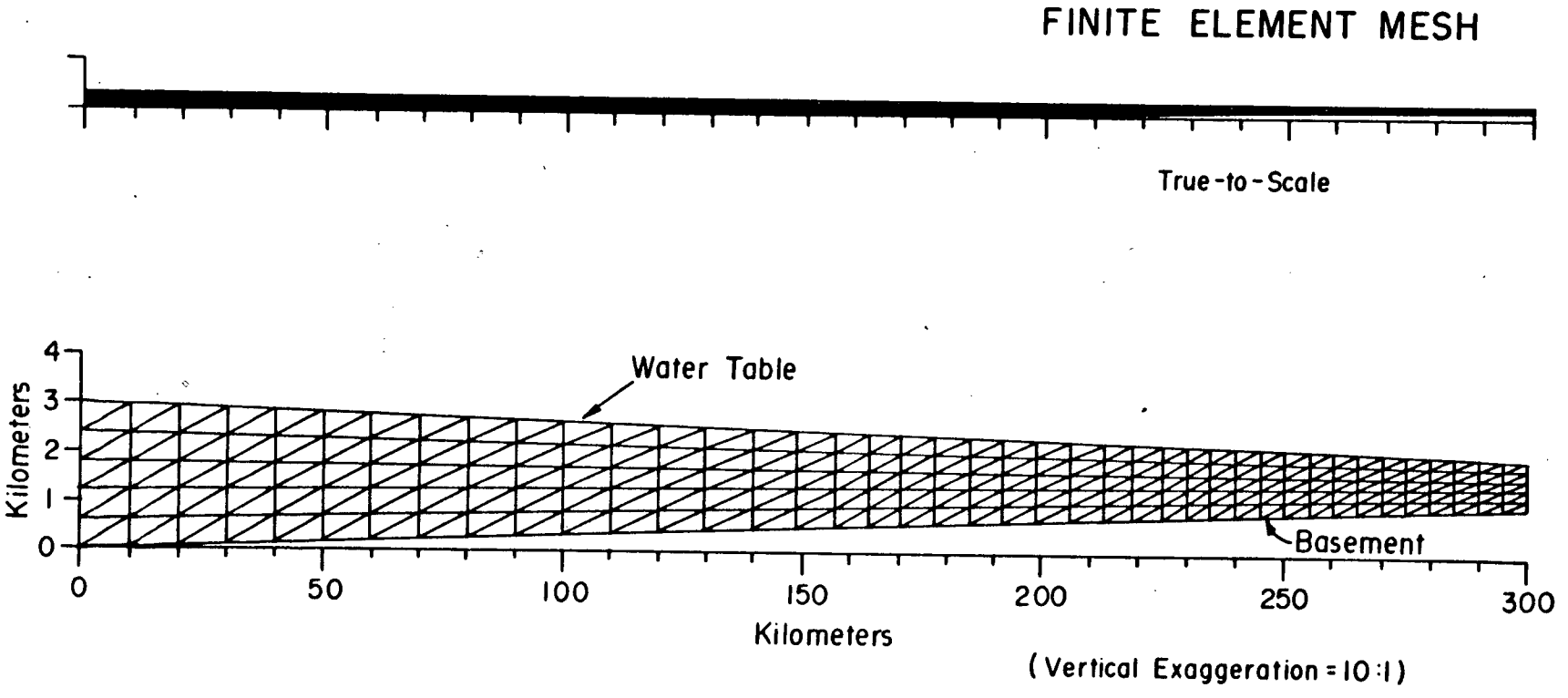

Figure 17. Finite-element mesh and basin dimensions for sensitivity analysis.

Table 7. Hydraulic conductivity and intrinsic permeability range of geologic materials.

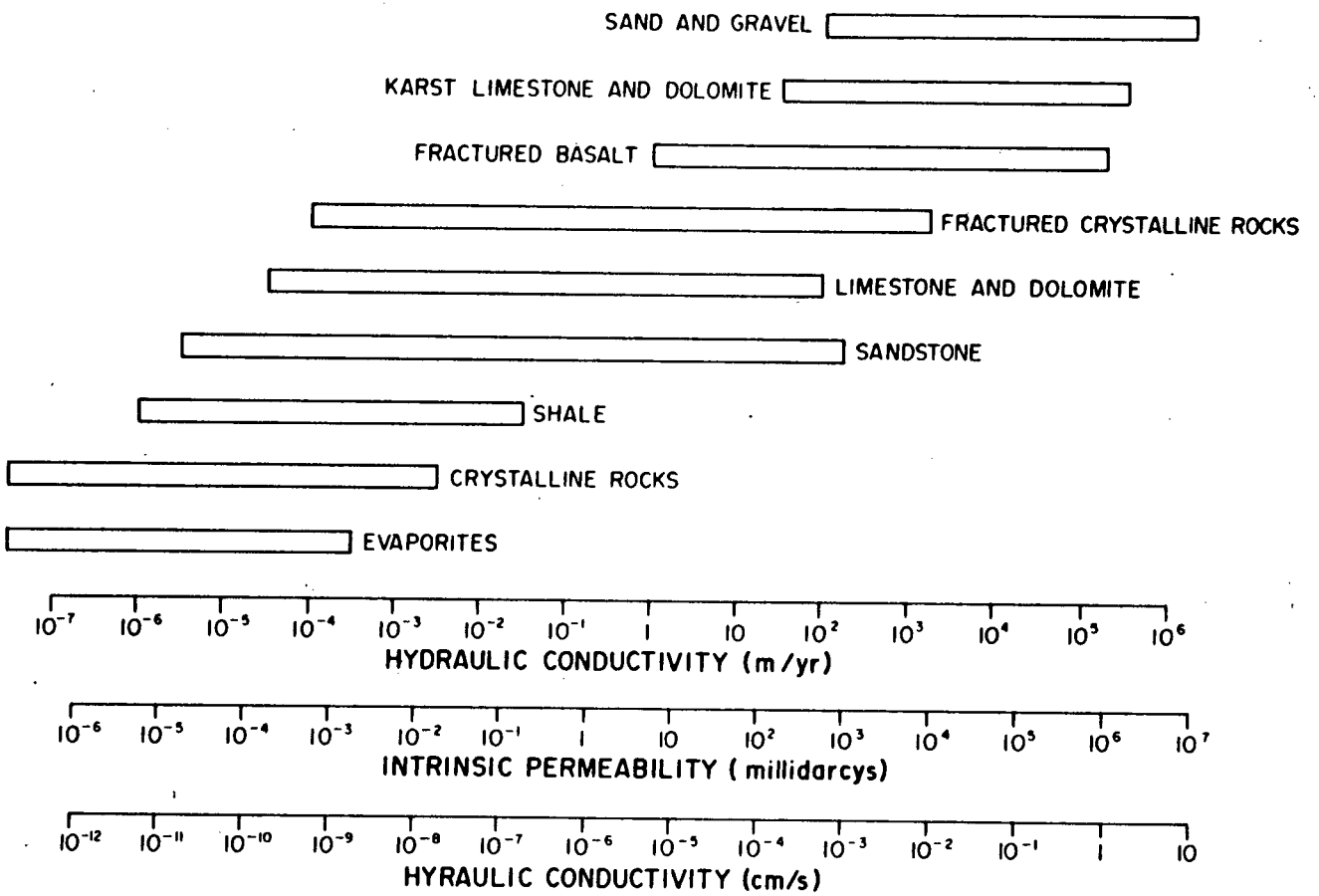

Table 8. Porosity values of geologic materials.

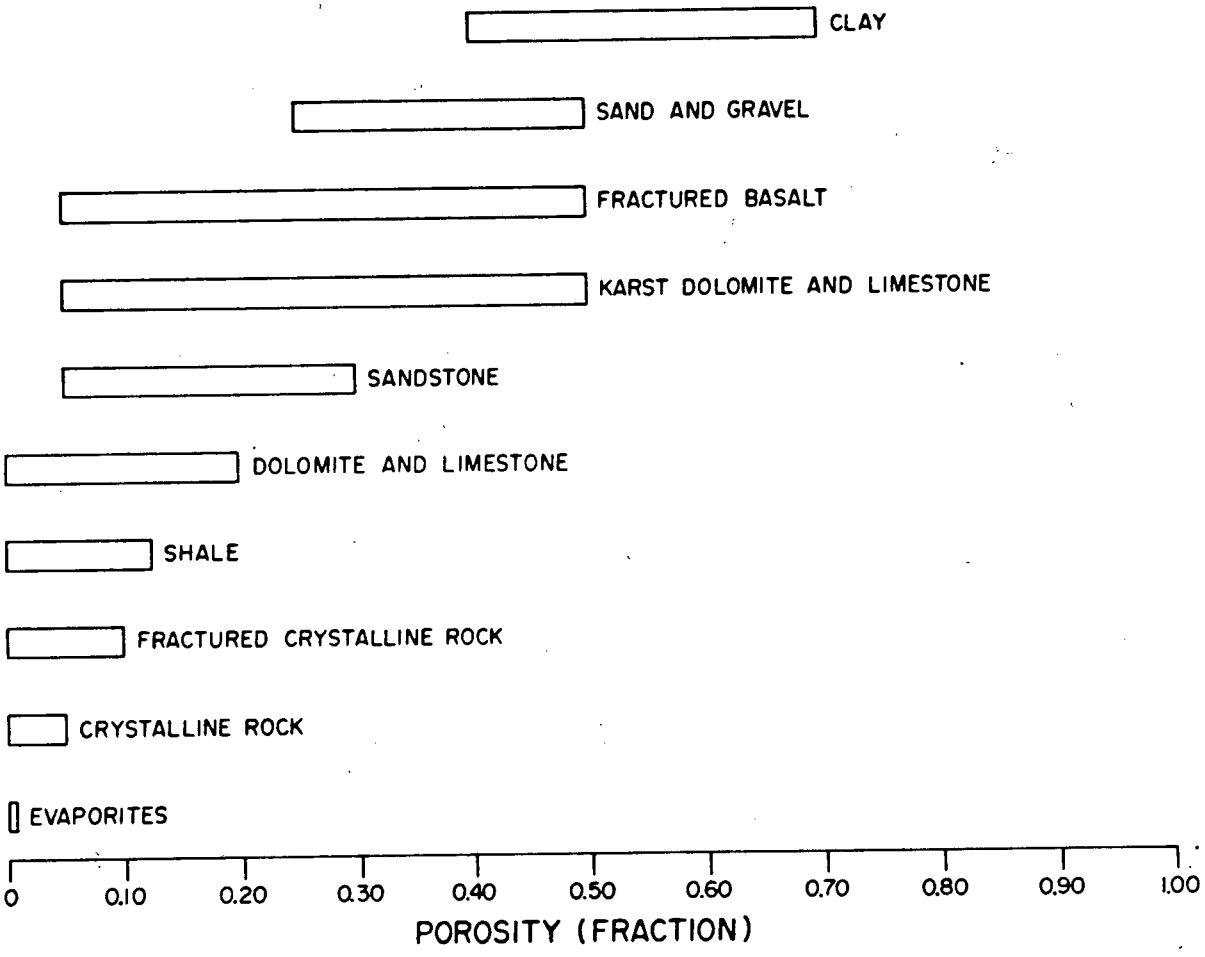

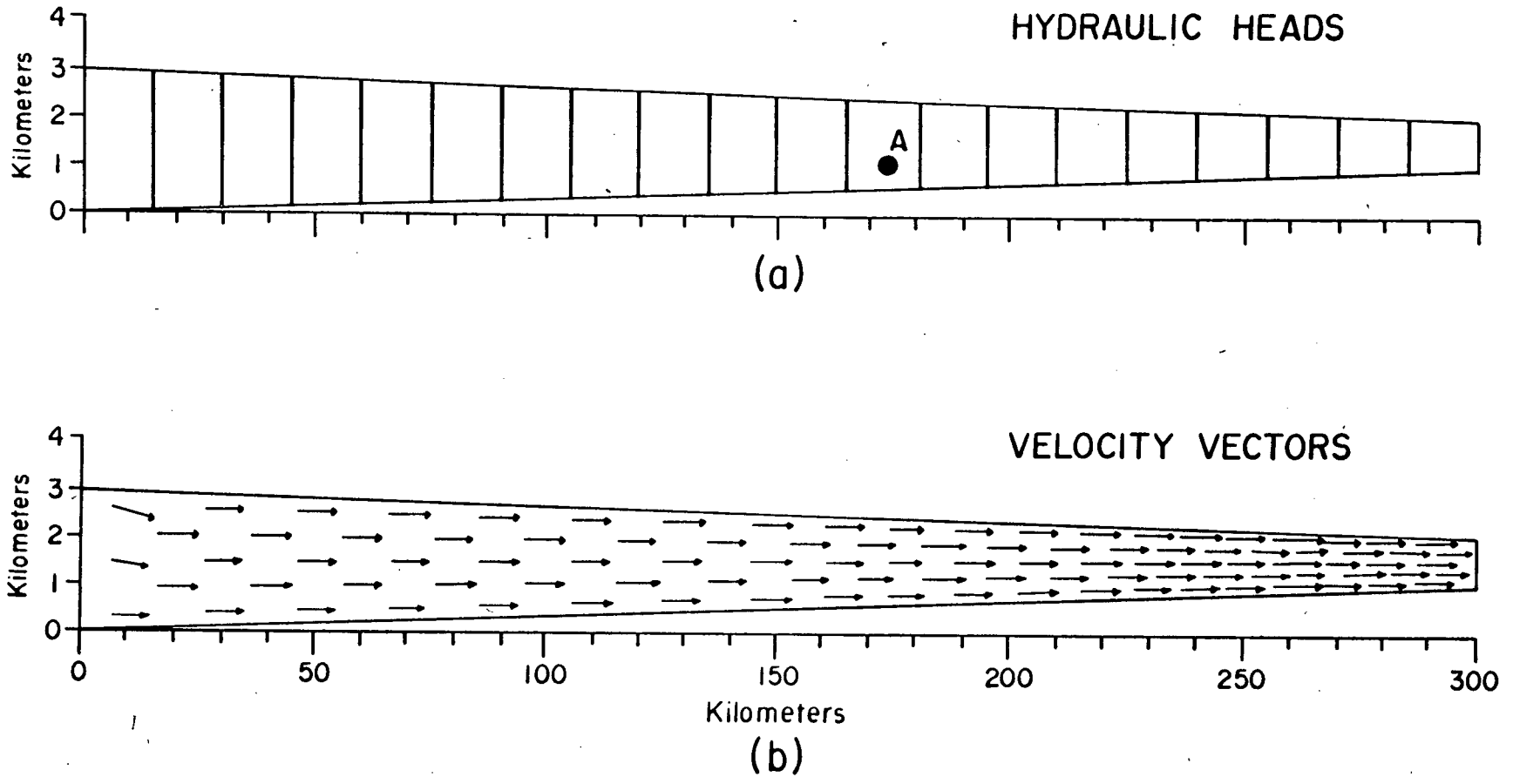

Figure 18. Homogeneous-isotropic basin showing relationship of fluid velocity and hydraulic conductivity.

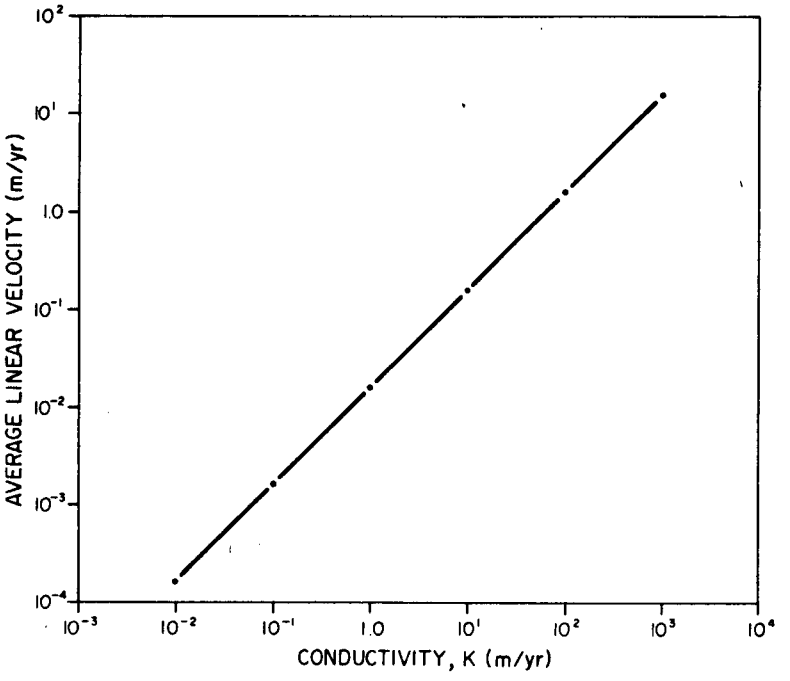

(c)

Figure 18. (Continued)

simulation of this case. The effects of temperature and salinity are excluded from the fluid model for the time being. Flow is uniform and horizontal, except at the extreme ends of the basin. The thin nature of the section (in true to scale), linear slope in the water table, and homogeneity of the basin fill produces vertical hydraulic-head contours. Under these conditions, the fluid velocity will be a linear function of hydraulic conductivity. Figure 18c shows the results of changing the permeability of the basin medium, for the reference point marked A on the cross section (Figure 18a). Porosity is set equal to a constant 0.15 for each model.

Sedimentary rocks are rarely isotropic with respect to hydraulic conductivity. Anisotropy arises from lithological features within beds, and from the layered heterogeneity that exists on a regional scale. The ratio of horizontal to vertical hydraulic conductivity, K_{xx}/K_{zz}, commonly reaches values of 100.0 for regional situations (Freeze and Cherry, 1979). Even higher ratios may occur for the scale of the basin being modeled here.

Figure 19 illustrates the effect of a representative anisotropy ratio of 100:1 on the fluid-flow regime. The main effect is a more pronounced delineation of recharge and discharge areas, as shown by the flexing of the hydraulic-head contours at the ends of the section. Average linear velocities vary along the base of the section, from about 1.0 m/yr near x = 50 km to 2.2 m/yr near x = 250 km. The ratio in the horizontal and vertical components of the velocity vector will depend on the anisotropy ratio, among other factors. In Figure 19, the horizontal hydraulic conductivity is K_{xx} = 100 m/yr and the vertical hydraulic conductivity is K_{zz} = 1 m/yr. These particular values give a horizontal velocity v_x = 2.3 m/yr and an upward vertical velocity $v_z = 5.4 \times 10^{-3}$ m/yr at reference mark A, using a porosity value of 0.15.

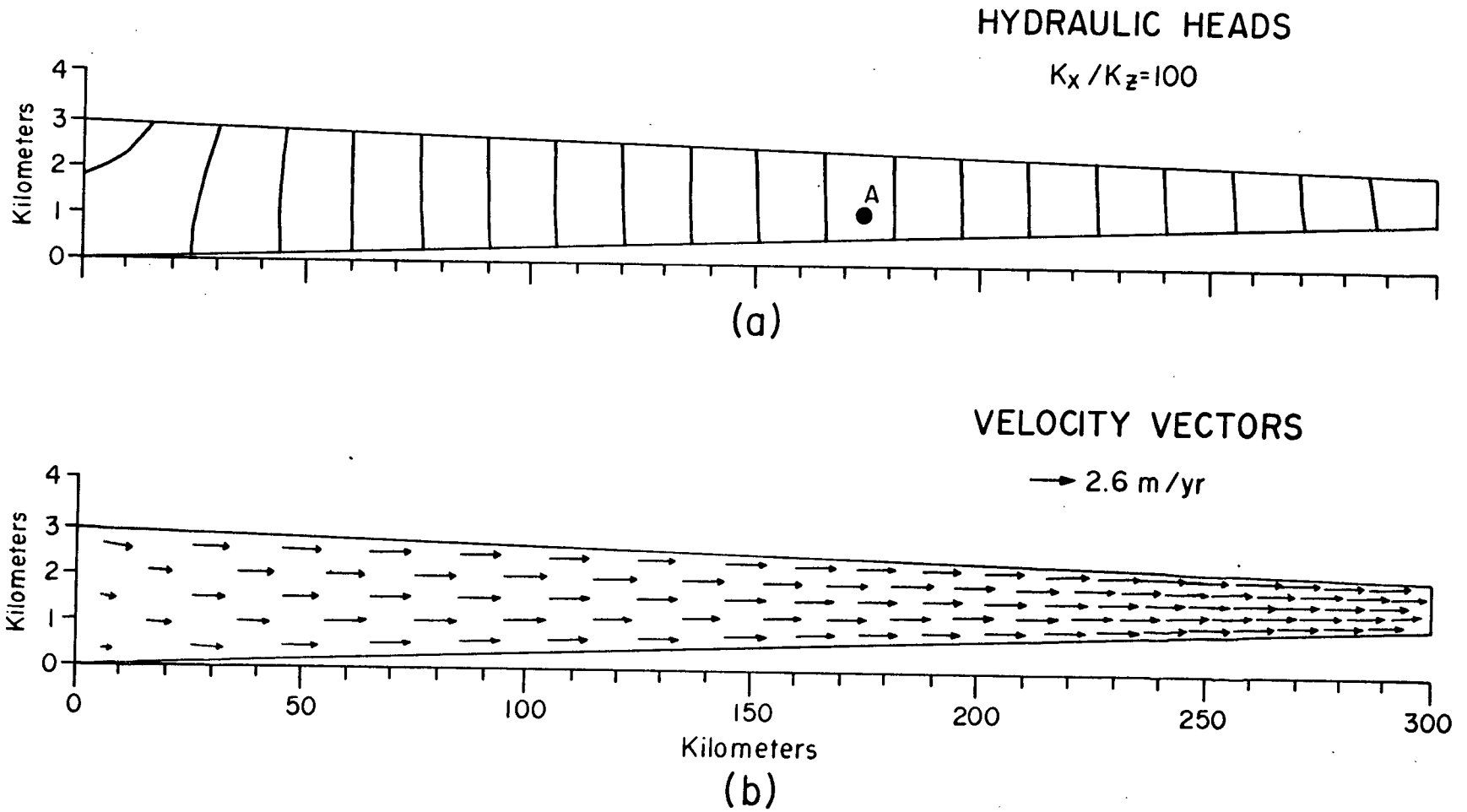

Figure 19. Effect of anisotropy on fluid flow.

Several numerical experiments were run to test the sensitivity of the modeling results to dipping strata. The effect of inclining the principal directions of hydraulic conductivity appears to be negligible for bedding dips of 0.3° (3 m/km). Flow patterns are effected, however, if the beds dip at gradients exceeding 5°. It would be advisable to account for this factor in any studies that consider the formation of ore bodies in structurally complex stratigraphic sequences. For the purpose of this study, only horizontal or gently-dipping strata are considered further.

In a steady-state flow system, the porosity is required only in computing the average linear velocity terms from the values of specific discharge (Table 3). Porosity does not affect the flow pattern or the volume flow rate. For example, the specific discharge at the reference point A in Figure 19 is $q = 0.33\ m^3/m^2 \cdot yr$. The average linear velocity will be 33.0 m/yr, 3.3 m/yr, and 1.65 m/yr for assumed porosities of 0.01, 0.10, and 0.20 respectively.

Homogeneous sections are not very realistic representations of the geologic character of most sedimentary basins. Although some foreland basins might approach the homogeneous case, it is safe to conclude that heterogeneous systems are more common (see Figures 2 and 4). Hydraulically, a layered sedimentary basin is very conducive to the focusing of flow as we have already seen in the earlier flow models (Figures 7, 8, and 16). Focusing is not present in the homogeneous basin model of Figure 18.

Consider the simple, two-layer model shown in Figure 20a. The bottom layer is a carbonate 'aquifer' with a hydraulic conductivity $K_{xx} = 100$ m/yr and a porosity $\phi = 0.15$. The upper layer represents a less permeable shale unit, in which $K_{xx} = 10$ m/yr and $\phi = 0.10$. Anisotropy in both layers is assigned a representative of 100:1. Fluid flow is now directed through the

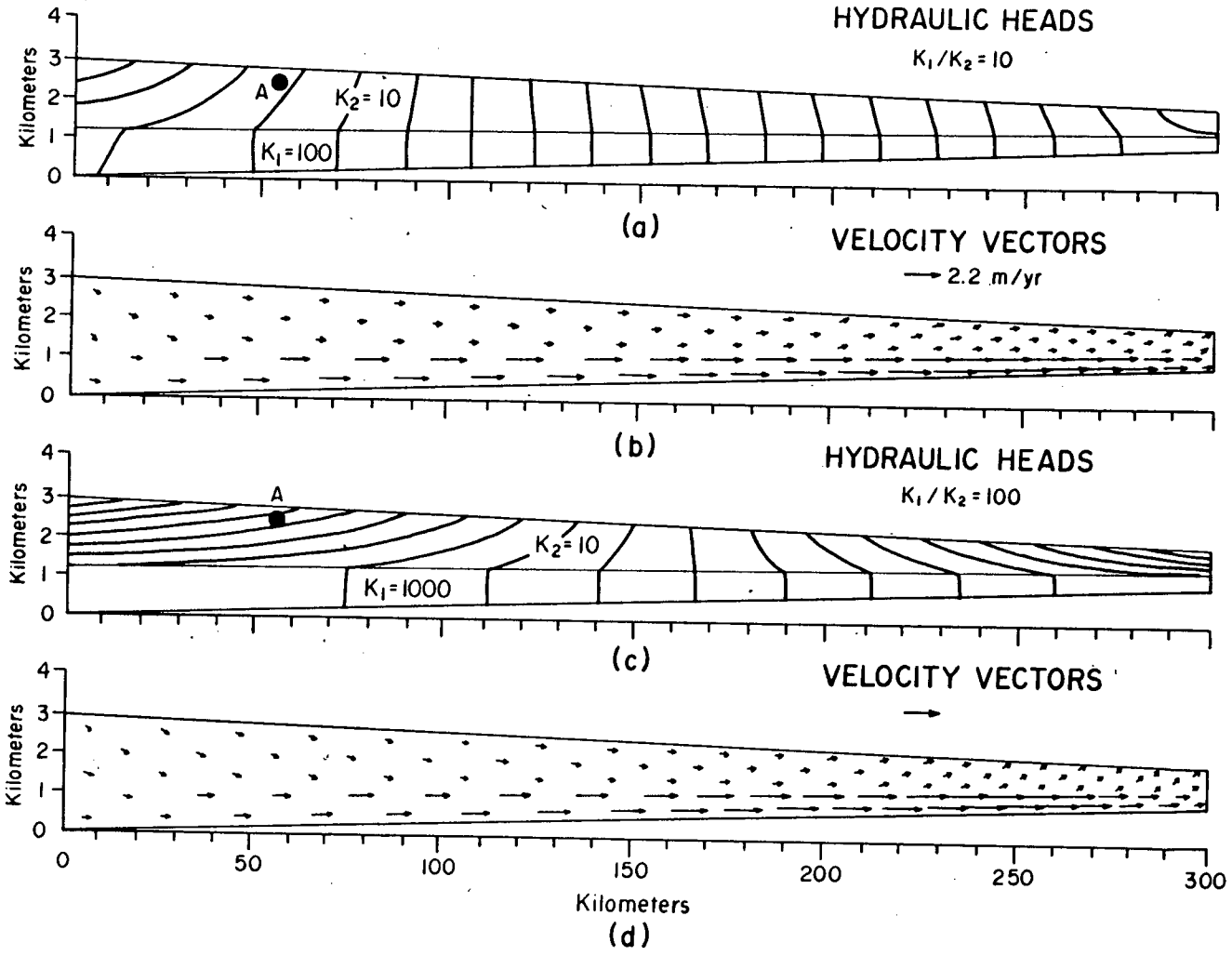

Figure 20. Effect of layering on fluid flow.

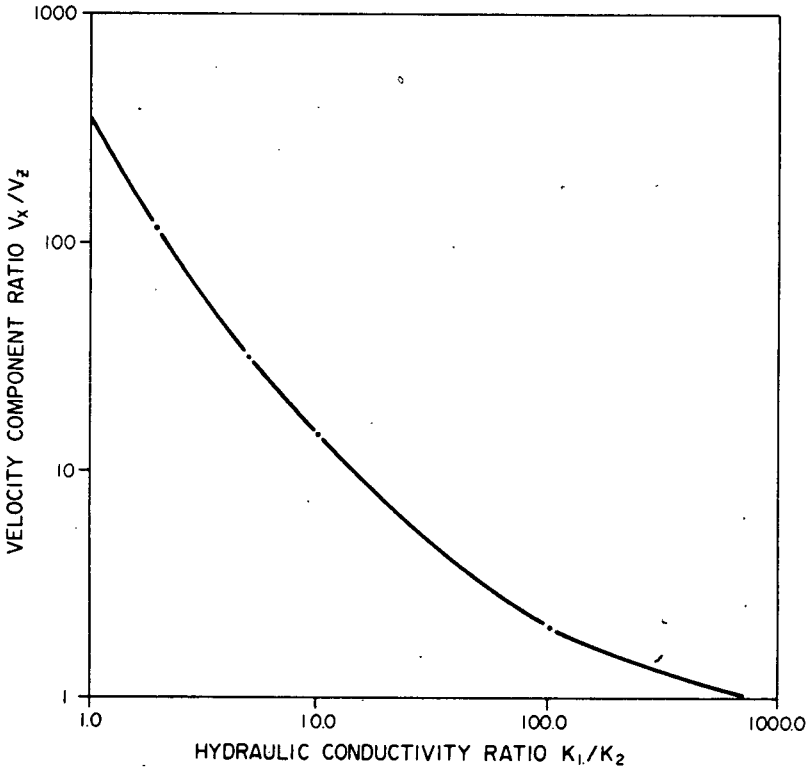

(e)

Figure 20. (Continued)

shale beds down into the aquifer in the recharge uplands, flows laterally across the basin, and is eventually forced up along the discharge end of the basin. The ratio of hydraulic-conductivity values of the two layers controls the degree of vertical fluid flux recharging the basal aquifer. A greater permeability contrast between aquitard and aquifer produces a sharper bending of the hydraulic-head contours, as shown by the contrast ratio K_1/K_2 = 100 in Figure 20c. Groundwater flow in the shale formation (K_2) is mostly downward in the left-half of the basin and upwards in the right-half of the section. Notice that the areas of highest flow are located in the basal aquifer and near the basin margin.

Figure 20e shows a graph of the horizontal to vertical velocity ratio as a function of the hydraulic contrast of the two-layer model. It summarizes the results at the reference site A (Figure 20a) for several simulations. The hydraulic conductivity of the shale aquitard K_2 is kept at a constant 10 m/yr. The vertical fluid flux is nearly equivalent to the horizontal flux for ratios of K_1/K_2 exceeding 100. We will see in later simulations the importance of the permeability contrast in influencing mass transport patterns.

The effects of pinchouts on flow systems are shown in Figures 21 and 22. Both models assume horizontal hydraulic conductivities of 1000 m/yr and 10 m/yr for the aquifer and aquitard respectively. The horizontal permeability is taken to be 100 times the vertical permeability. In Figure 21, the average velocity in the aquifer is 4 m/yr, while in Figure 22 the velocity is about 7 m/yr. An expanded picture of the shallow-aquifer lens (Figure 22) illustrates a situation where shallow-derived H_2S-bearing waters would continuously recharge the partial basal aquifer from above while metal-bearing brines are also recharging the aquifer at the upstream end of the lens. A similar type of flow regime also exists in Figure 16 (Chapter 4).

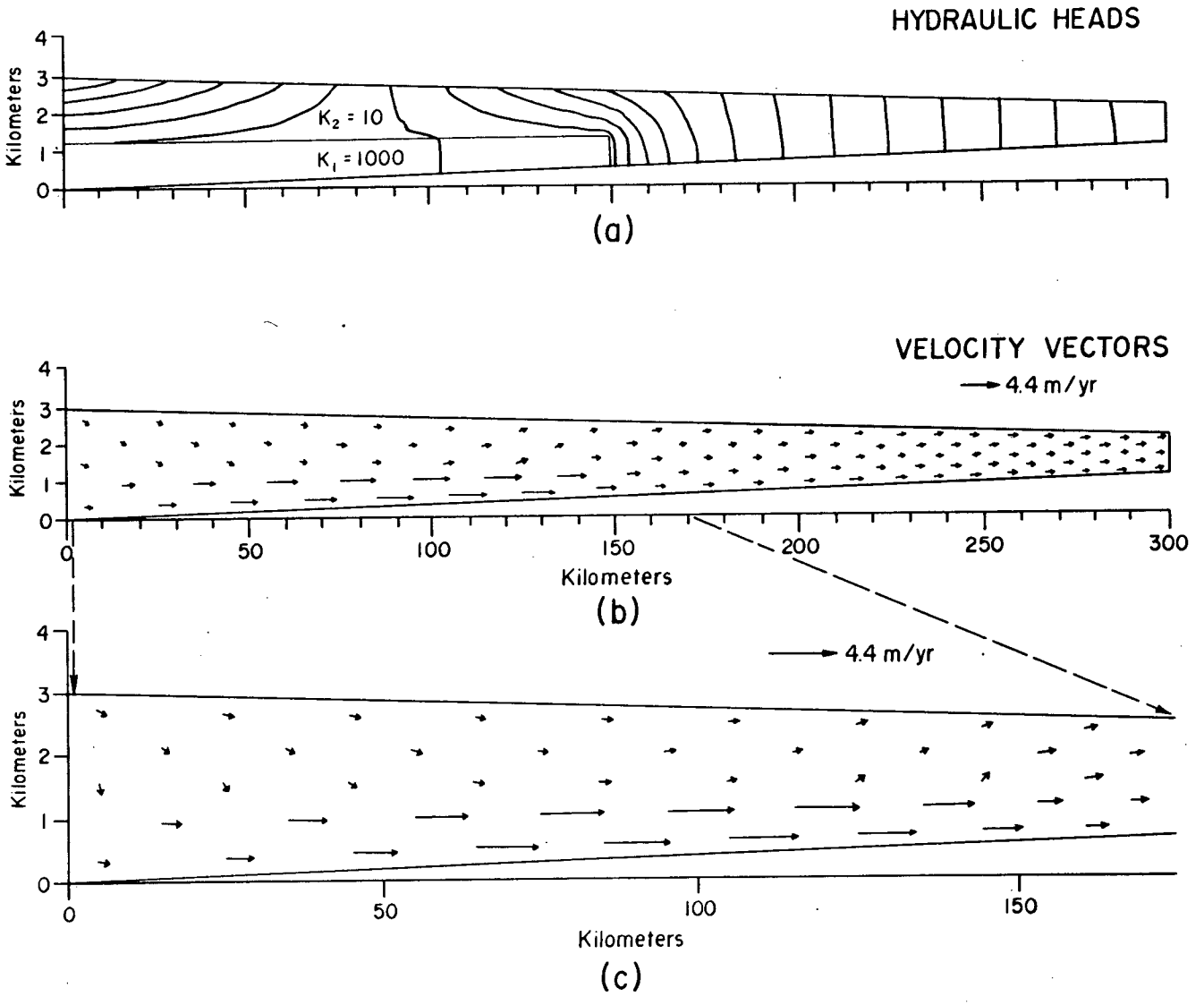

Figure 21. Effect of aquifer lens in upstream end of basin.

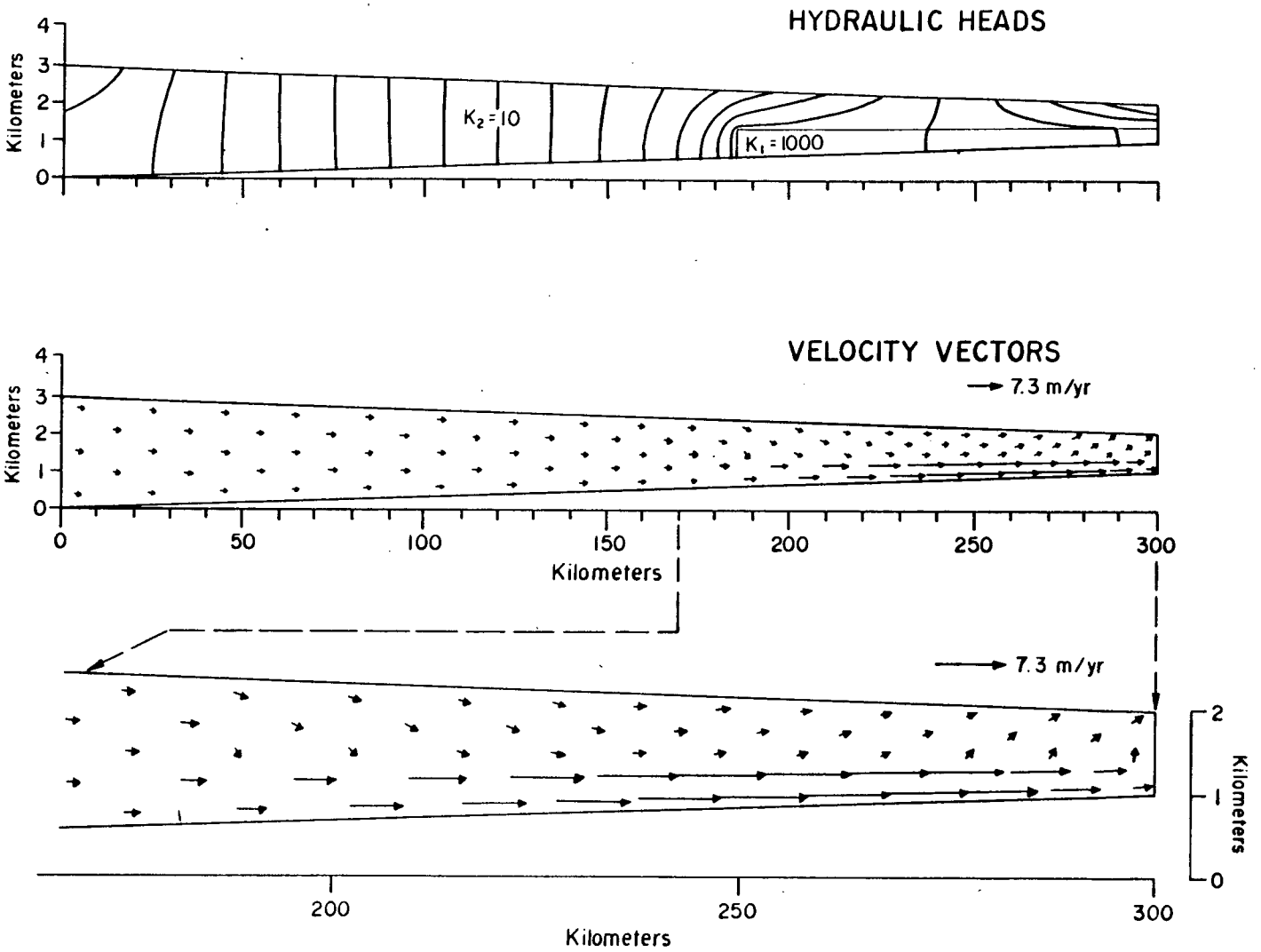

Figure 22. Effect of aquifer lens in downstream end of basin.

Other types of layered stratigraphy can be studied through similar modeling. A number of earlier studies, such as Freeze and Witherspoon (1967) and Freeze (1969), give many examples of the effects of layering on fluid-flow patterns. Although many of these are of interest, space does not permit an examination of every case. The basin-wide aquifer model treated above is simple and well-suited for a preliminary analysis of ore genesis. We will only proceed, therefore, to examine the two-layer model in greater detail

Temperature and Salinity Gradients

The flow models presented so far have assumed that no temperature or salinity gradients exist in the basin. This assumption is commonly made in the modeling of shallow groundwater systems, but it is not realistic in the analysis of flow in large sedimentary basins.

The purpose of this section is to look at the effect of variable density and viscosity in the development of regional flow systems in sedimentary basins. Figures 9 and 10 (Chapter 3) show the relationships of water density and viscosity as a function of temperature and salinity. As noted earlier, these equations of state are numerically incorporated into Equation (3-9), which is the more complete form of Darcy's law. Because no previous studies have assessed the role of temperature and salinity gradients in regional flow, a somewhat detailed evaluation will be made.

The first set of simulations to be presented assume that there is only a temperature gradient across the two-layer basin. Figure 23 shows the temperature field and resulting flow diagrams for the case in which fluid density is allowed to vary with temperature alone. The temperature pattern is computed from the numerical solution of the heat-transport equation. The discussion of factors controlling heat flow is reserved for later, and for now we will just present the solution without explanation. The hydraulic

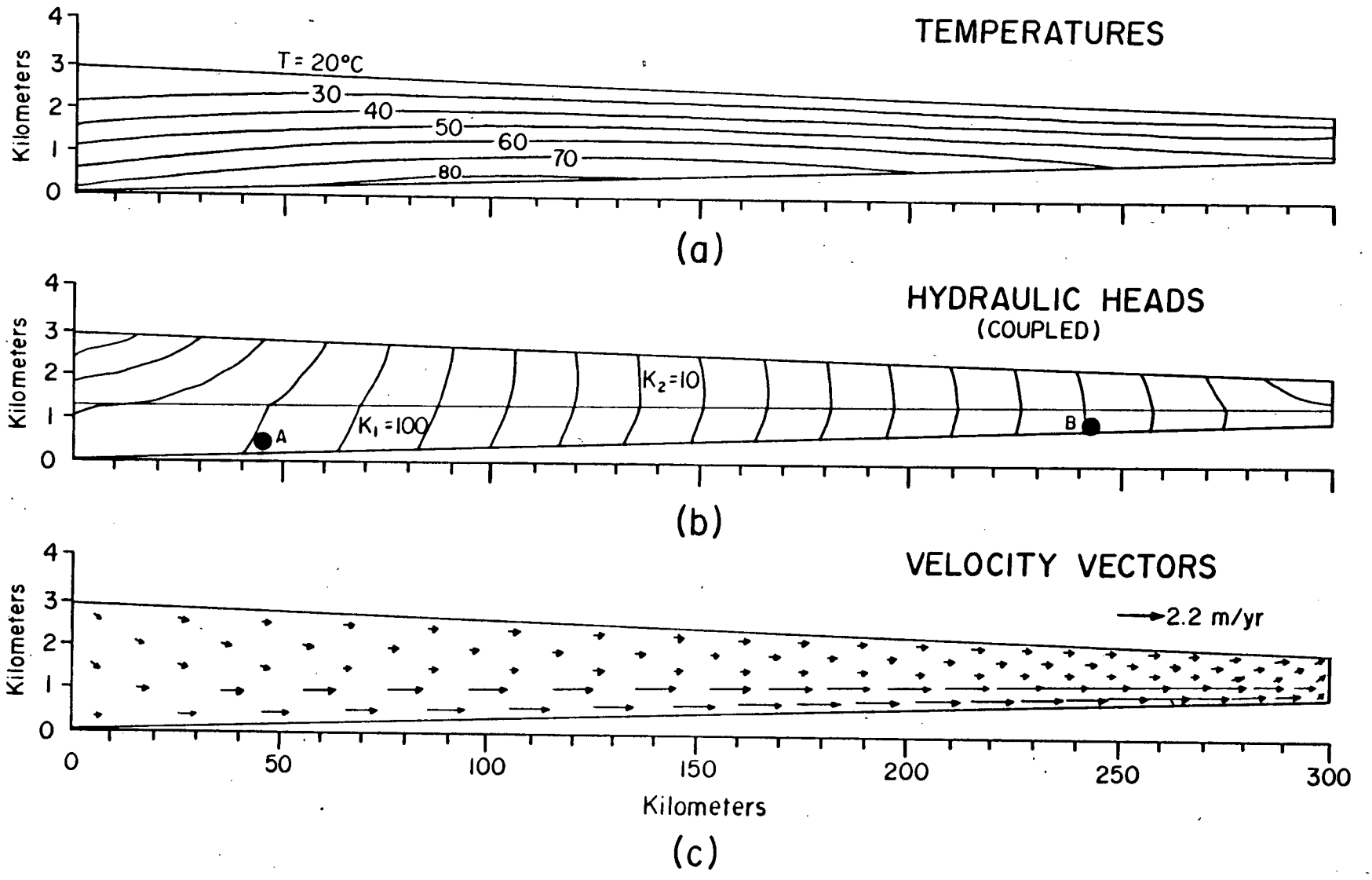

Figure 23. Fluid-flow pattern where density is a function of temperature alone.

conductivity [see Equation (3-5)] of the basal carbonate aquifer is K_{xx} = 100 m/yr, while that of the shale layer is 10 m/yr. Porosities are 0.15 and 0.10 respectively. Both hydrostratigraphic units have an anisotropy ratio of 100:1. It should be pointed out that one can no longer use the rule whereby flow vectors are drawn perpendicular to hydraulic-head contours (e.g. Freeze and Cherry, 1979, Chapter 5), when modeling inhomogeneous fluid flow. For the case of inhomogeneous fluids, the hydraulic-head plot only represents a fresh-water equivalent pressure head, not a true hydraulic potential. However, it will still be a useful variable in the following diagrams for comparison purposes.

The main feature introduced by allowing density to vary with temperature is an upstream bending of the hydraulic-head contours in the aquifer (compare Figures 20a and 23b). Qualitatively, the increase in temperature with depth lowers the fluid density, and thereby increases the upward component of flow. For the marked reference point A in Figure 23b, the downward velocity decreased from 1.0×10^{-3} m/yr in the uncoupled problem (Figure 20a) to 3.2×10^{-4} m/yr for the coupled problem (Figure 23b and 23c). At reference point B in Figure 23b, the average linear velocity changes only slightly from the uncoupled to coupled problem.

Figure 24 gives the results of a model that allows the viscosity of water to vary with temperature alone, while keeping density constant. The temperature effect on viscosity is significant, as could be expected from Figure 10. Warmer temperatures decrease fluid viscosity which in turn creates larger flow rates, relative to the isothermal case at 20°C. Because viscosity effects are introduced into the flow equations as a linear multiplication factor [see Equation (3-8)], it is the magnitude of flow that is affected more so than the flow pattern. This feature is well illustrated by comparing

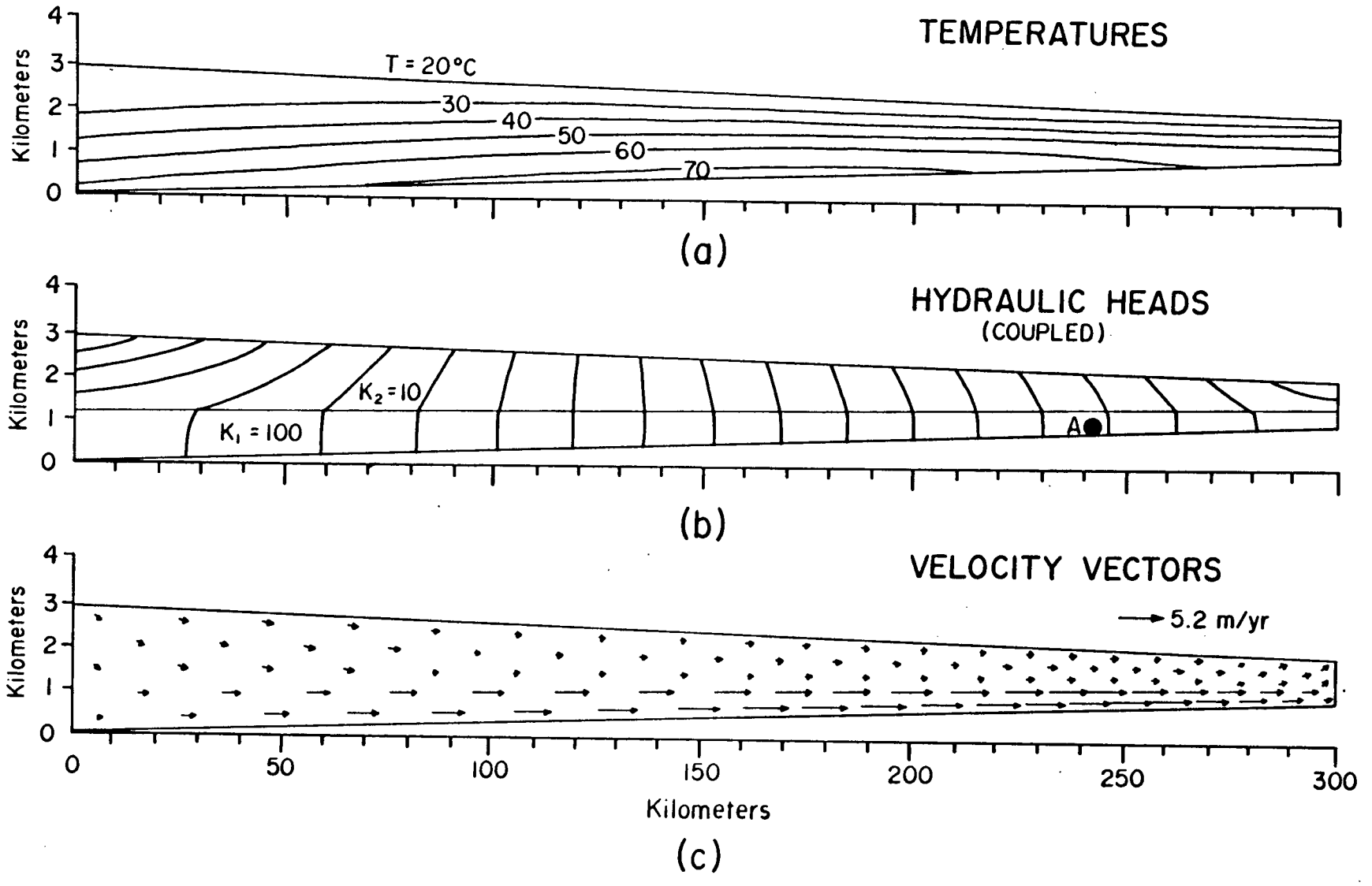

Figure 24. Fluid-flow pattern where viscosity is a function of temperature alone.

Figures 20 and 24. In the coupled-flow problem, the warm temperatures in the basal aquifer cause the system to behave as if the aquifer is more permeable than the uncoupled model (Figure 20). The effect of a lower viscosity is to permit flow velocities of 4.7 m/yr at point A (Figure 24), which is more than double the velocity at the same point in the uncoupled case (Figure 20a). Flow rates double, in fact, along the entire length of the basal aquifer.

Although it is interesting to look at the individual effects of temperature on density and viscosity, in reality the presence of a geothermal gradient affects both fluid properties simultaneously. A simulation showing this phenomena is given in Figure 25. None of the media parameters have been changed from the two previous models. Flow is now influenced by both buoyancy effects and higher velocities in the warmer parts of the basin. At the reference site A (Figure 25b), the horizontal component of velocity is 4.7 m/yr, and the vertical component is 1.9×10^{-2} m/yr, which is greater than the uncoupled vertical velocity of 7.8×10^{-3} m/yr.

Figure 26 summarizes the quantitative results found in modeling the effect of temperature on fluid flow in a large sedimentary basin. The position of the velocity profile is marked by the points Z-Z′ in Figure 25a. The increase in the vertical-velocity component is more subdued in the basal aquifer because of the large horizontal component of flow. With respect to the effect of temperature on viscosity, as illustrated by the horizontal component of flow, the influence is greater in the aquifer than in the shale because of the higher temperatures. Phenomena of these types are obviously important when considering the modeling of basinal-brine flow in ore genesis. In this particular example, the volume of flow in the basal aquifer would be out by a factor of at least 2.0 if the effect of temperature is not included

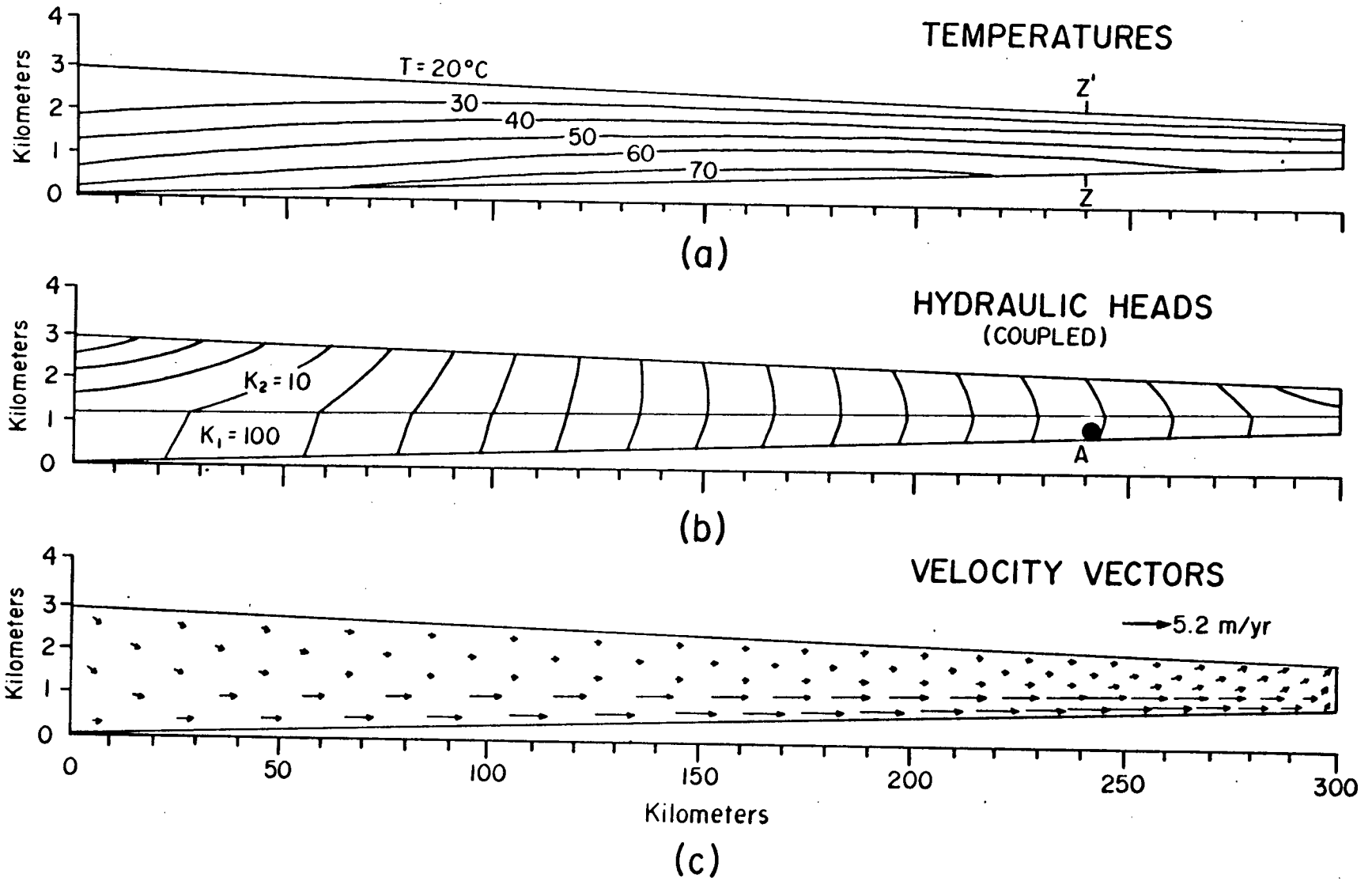

Figure 25. Effect of temperature-dependent fluid properties on regional fluid flow.

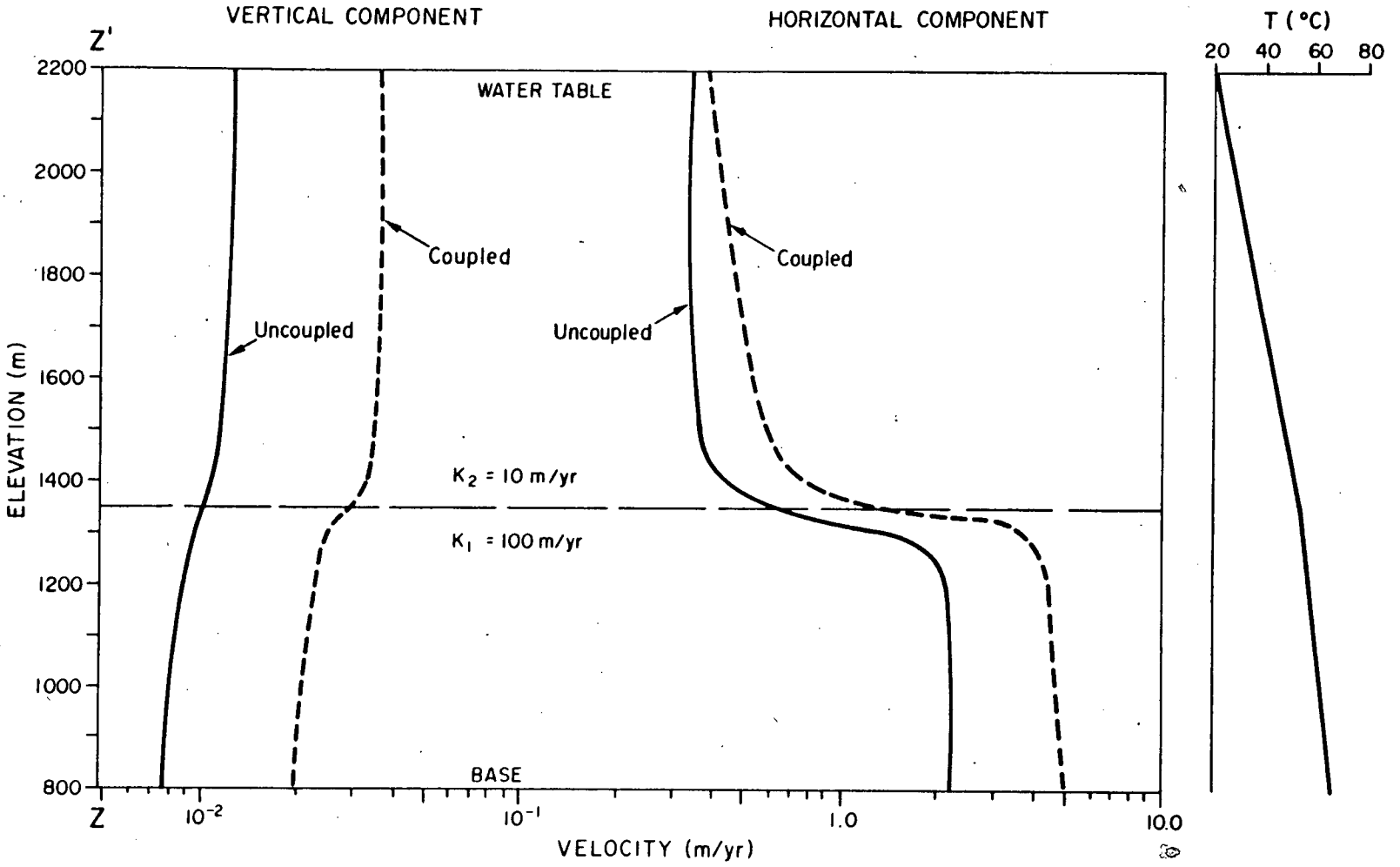

Figure 26. Velocity profile in discharge end of basin showing the effect of temperature-dependent fluid flow.

in the calculation.

The next question to ask would be: what effect does salinity have on the fluid-flow system? Figures 27, 28, 29, and 30 show the results of some numerical experiments that were conducted to help answer this question. All of these models assume there is no temperature gradient present. The two-layer stratigraphy and material properties are the same as in the previous case. The models presented here assume that water above the 2000 m elevation is fresh and therefore is assigned a zero salinity. Below the datum, salinity increases linearly with depth. Salinity is expressed as an equivalent weight percent of sodium chloride (% NaCl). At the deepest point in the model basin (2 km below datum, Figure 27a), a gradient of 0.01 % NaCl/m will produce a salinity of 20% NaCl (about 250,000 mg/liter or 4.3 molal). This salinity gradient is arbitary, but real data could easily be inserted in actual site-specific, field simulations. Temperature is assumed to be constant at 20°C throughout the basin.

Figure 27 is a simulation of the case where density alone is a function of salinity. The salinity distribution is also plotted for reference. By comparing Figures 20a and 27, it can be seen that the most obvious effect of salinity is the change in the hydraulic-head pattern. High salinities in the deeper parts of the basin cause an increase in fluid density which leads to greater buoyancy forces that act downward (Equation 3-8). In order to drive the fluid through the basin, higher gradients in hydraulic head are required than those of the fresh-water-basin model (Figure 20a). At site A in Figure 27b, the vertical velocity increase to 1.5×10^{-3} m/yr relative to the 5.5×10^{-4} m/yr of the fresh-water model. This effect is more subdued in shallower levels of the basin.

The effect of salinity on viscosity alone is shown in Figure 28. As in the case of temperature, viscosity influences flow rates in a linear

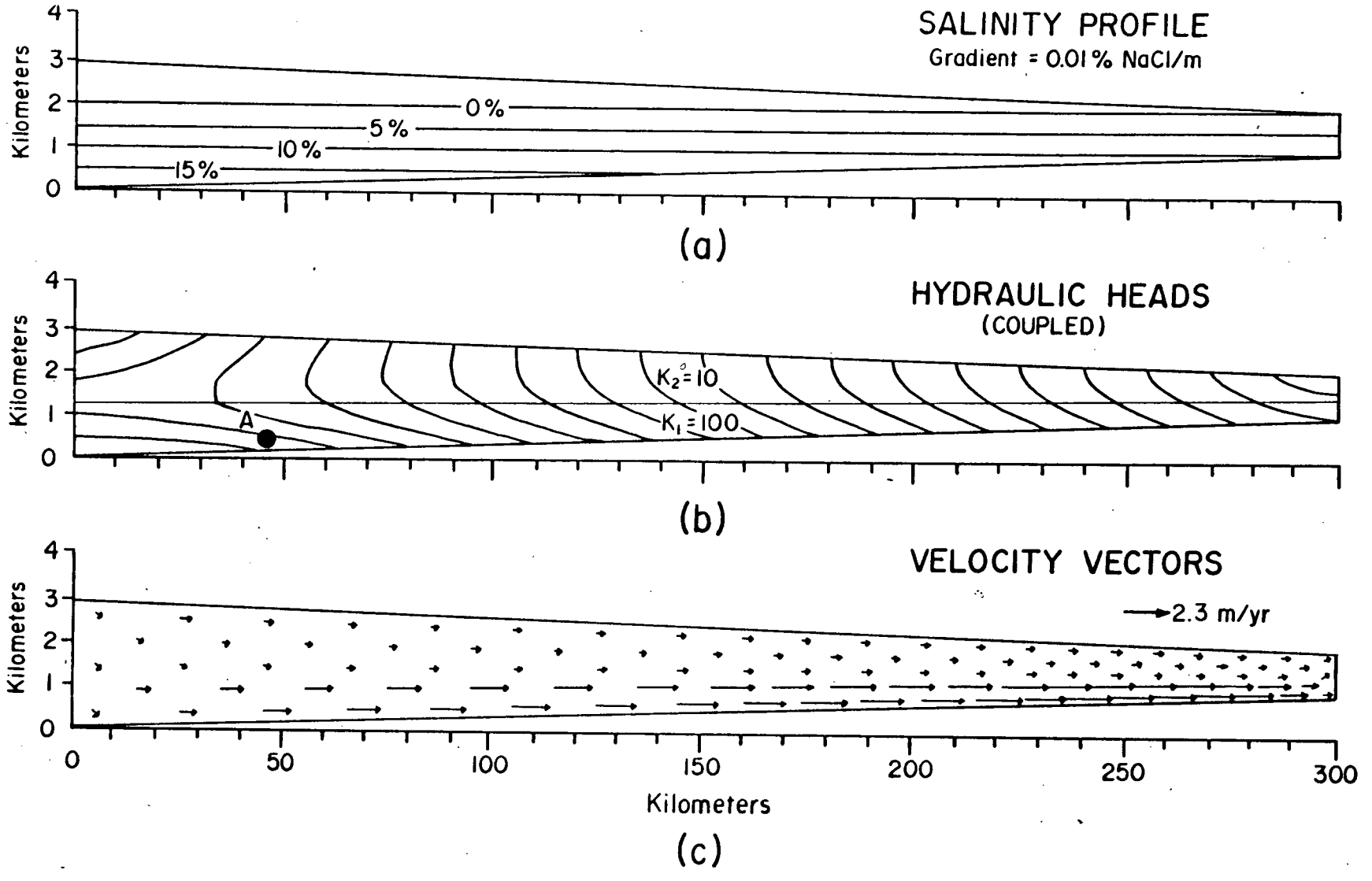

Figure 27. Fluid-flow pattern where density is a function of salinity alone.

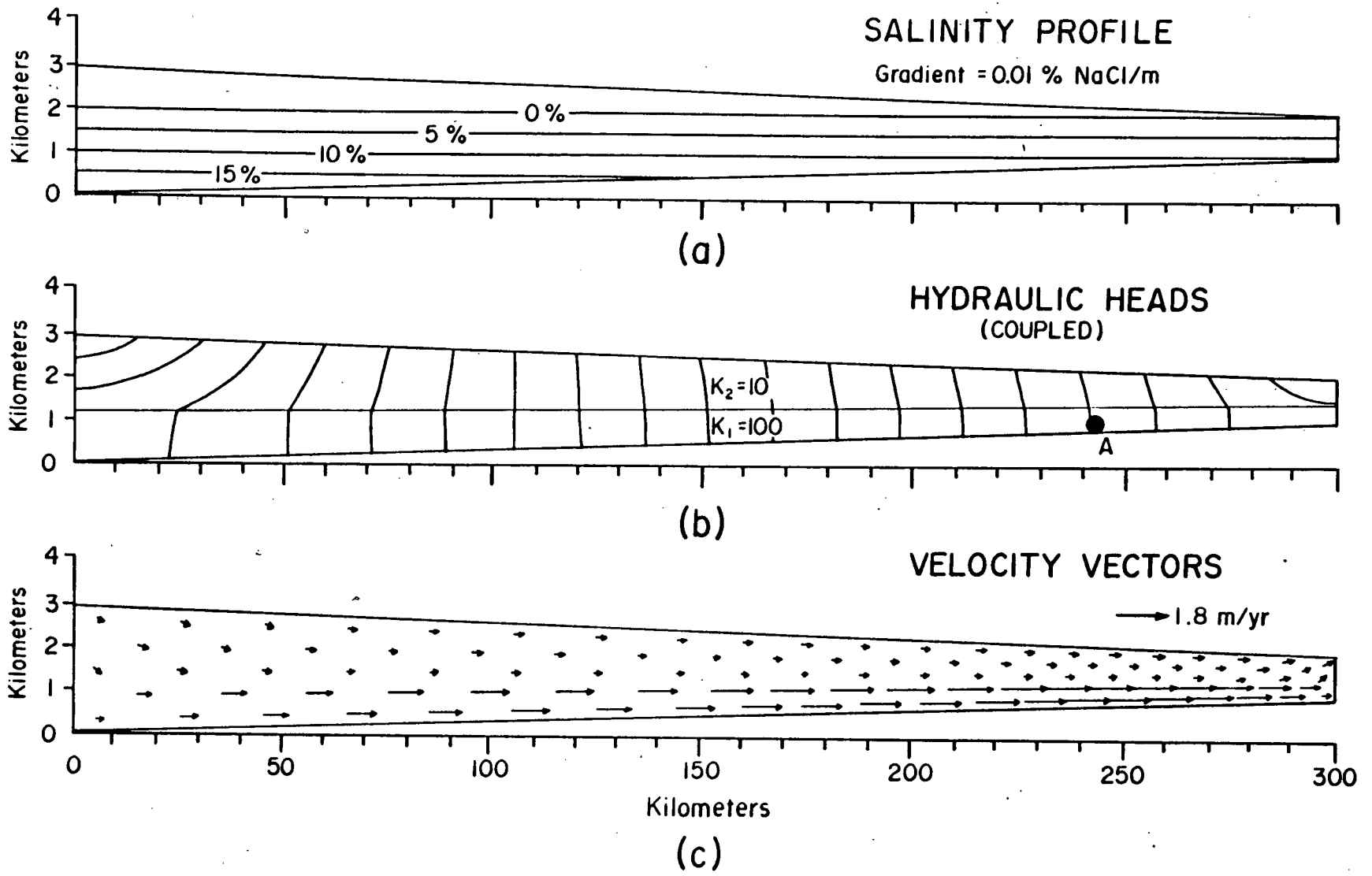

Figure 28. Fluid-flow pattern where viscosity is a function of salinity alone.

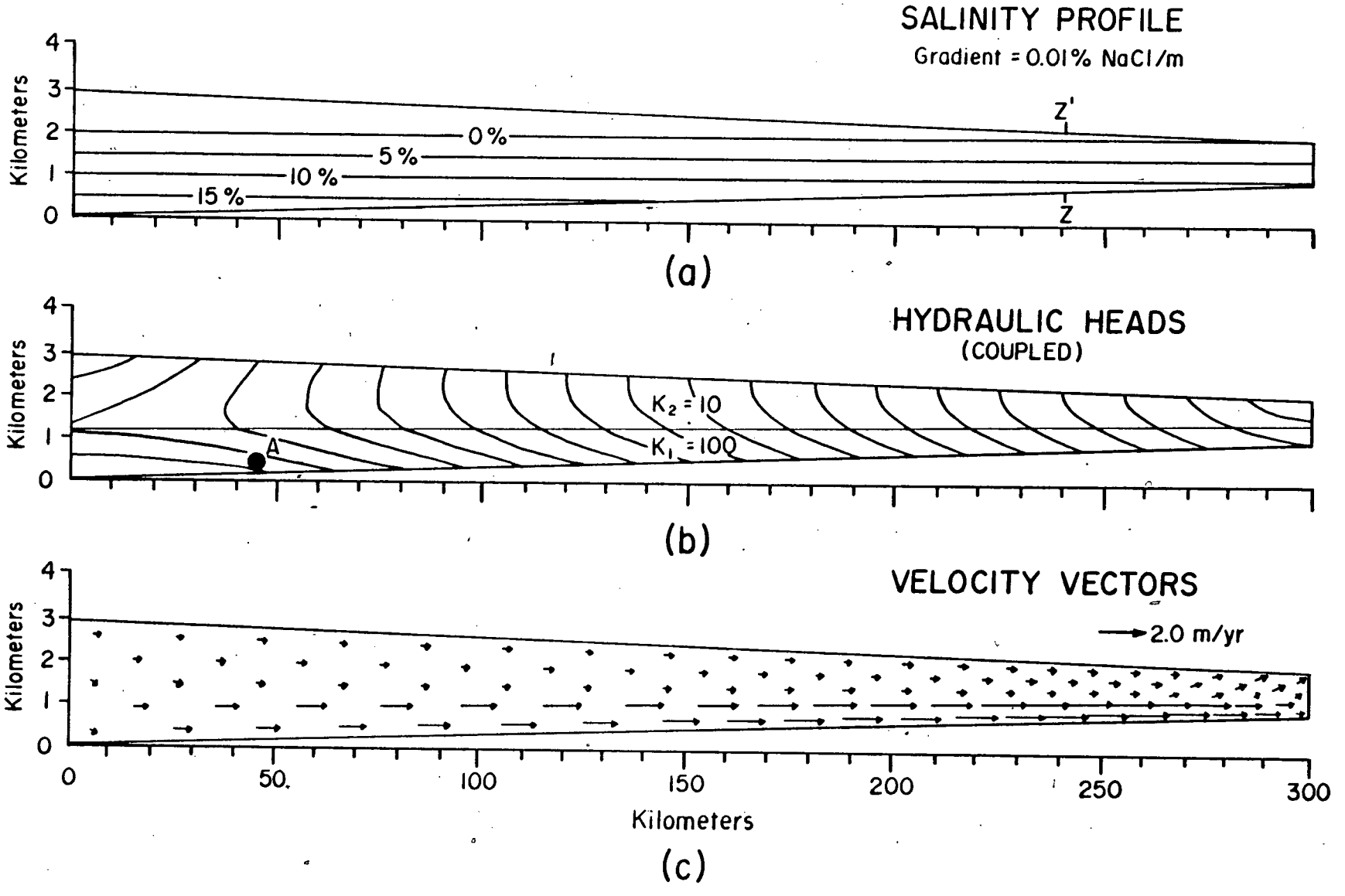

Figure 29. Effect of salinity-dependent fluid properties on regional fluid flow.

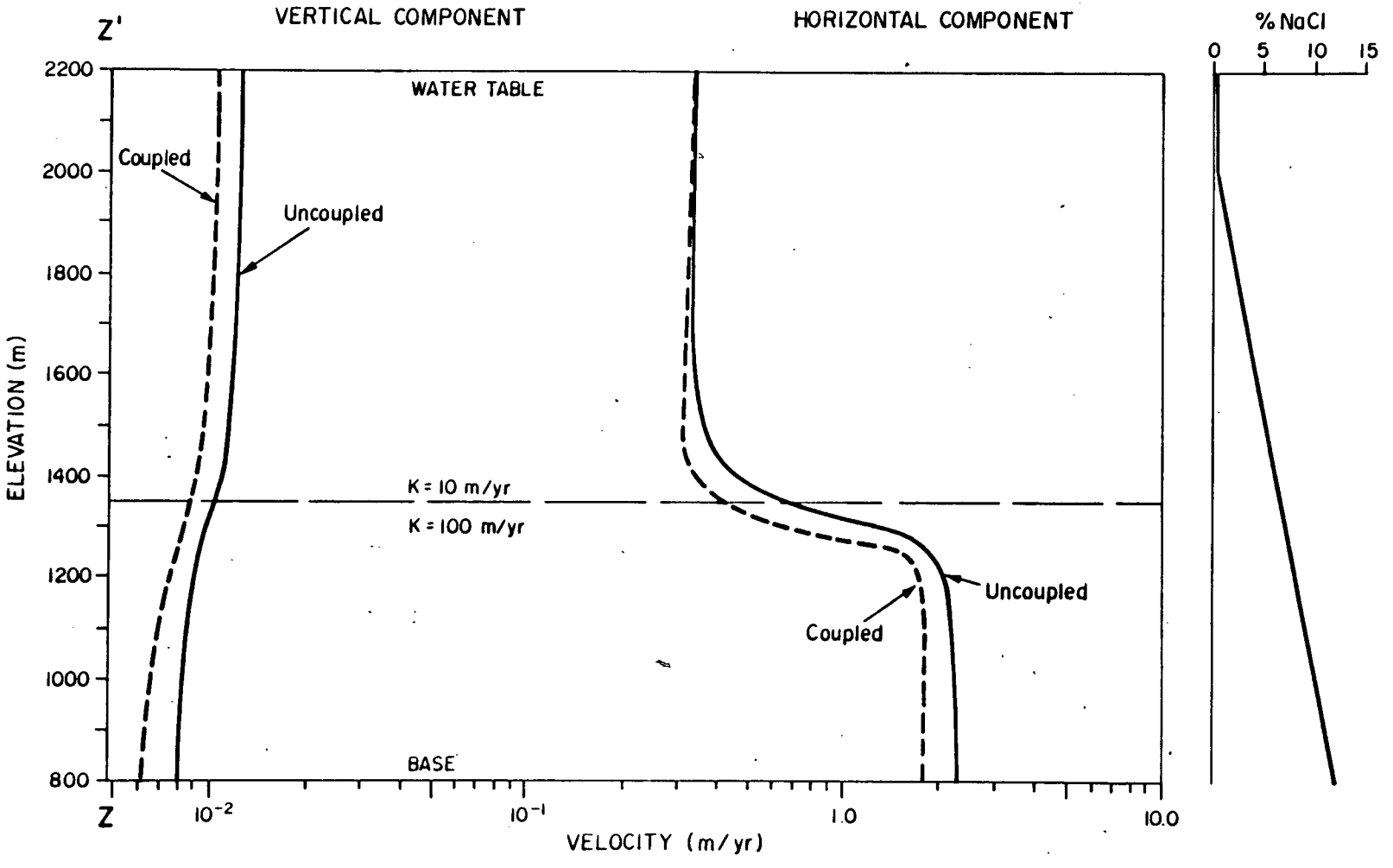

Figure 30. Velocity profile in discharge end of basin showing the effect of salinity-dependent fluid flow.

fashion. At site A in Figure 28b, velocity decreases to 1.8 m/yr, relative to the 2.2 m/yr in the fresh-water case of Figure 20b. The hydraulic-head pattern is not significantly altered by salinity effects on viscosity.

The final set of diagrams in this group are shown in Figures 29 and 30. This simulation includes the effects of both density and viscosity. For reference point A in Figure 29b, the overall response is an increase in the vertical velocity to 1.1×10^{-3} m/yr as compared to the 5.0×10^{-4} m/yr in the fresh-water problem. The effect at the discharge end of the basin is plotted in Figure 30 for the profile line Z-Z′ in Figure 29a. Salinity lowers the volume of flow that passes through a basal aquifer at the basin margin, when compared to a fresh-water (uncoupled) system. It is an important factor, therefore, in the analysis of hydrodynamics in ore formation.

With the individual assessments of temperature and salinity effects on flow completed, we can advance to a more realistic basin model. Figure 31 shows the results of such a model where both temperature and salinity affect the fluid properties. A salinity gradient of 0.01 % NaCl/m is assumed, and the media properties are the same as in the preceding cases. The average linear velocity at the reference site A is 3.8 m/yr. Table 9 compares this velocity value with the previous simulations. It is clear that temperature gradients affect the flow system in a basin to a greater degree than do salinity gradients. However, the salinity effect is significant and it will be included in subsequent models.

The importance of salinity is demonstrated by the effect of different salinity gradients in Figure 32. Gradients of 0.005, 0.010, 0.015, and 0.02 % NaCl/m are modeled. The largest gradient produces a brine with 40% NaCl at the deepest point in the cross section. At the reference point A (Figure 32), the salinity is 6%, 12%, 18%, and 24% for the respective

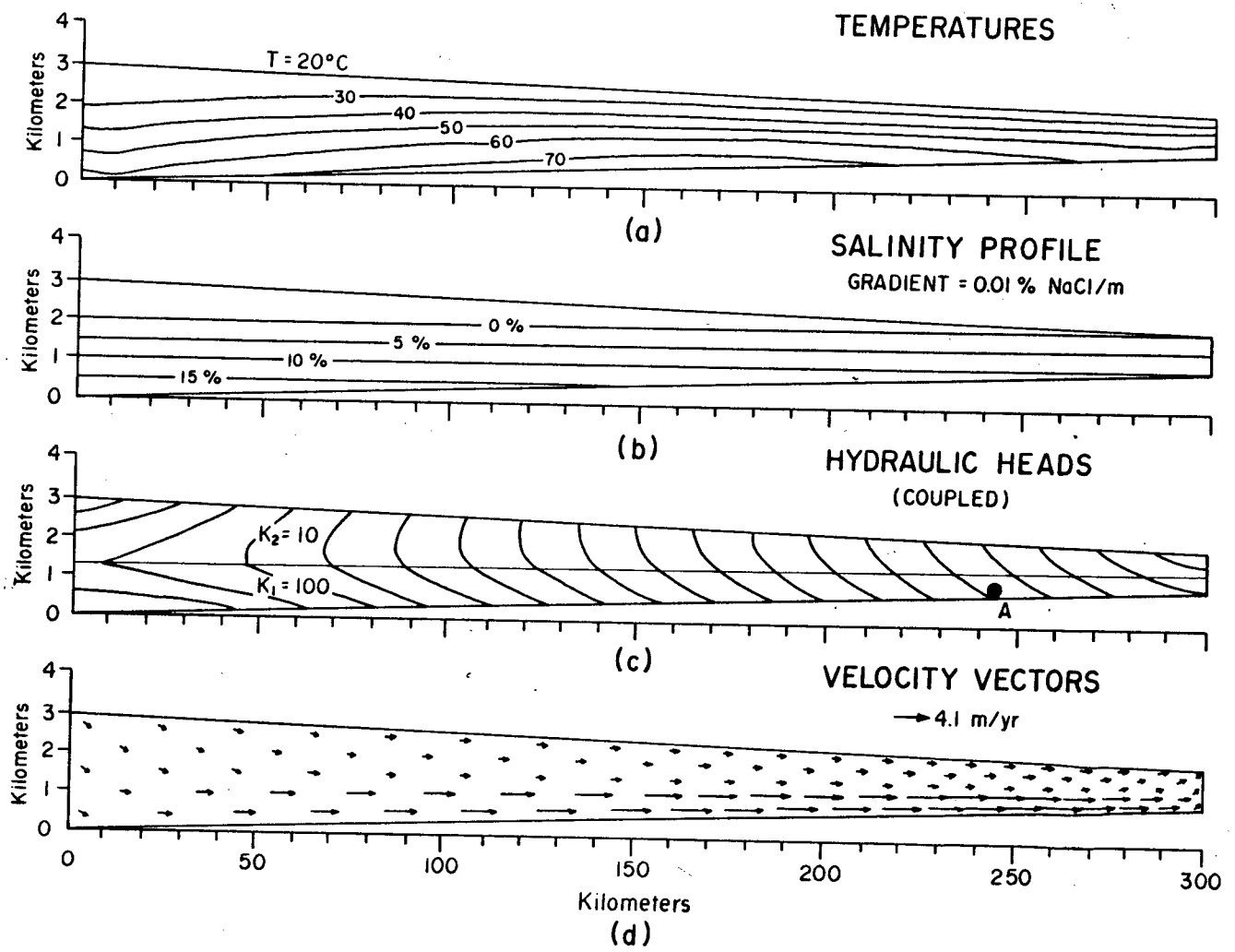

Figure 31. Effect of combined temperature and salinity-dependent fluid properties on regional fluid flow.

Table 9. Summary of the velocity components at the reference site for various temperature-and salinity-dependent flow models

Simulation	Velocity Components at Site A*	
	Horizontal (m/yr)	Vertical (m/yr)
1. No temperature or salinity gradients	2.2	7.8×10^{-3}
2. Temperature gradient only	4.7	1.9×10^{-2}
3. Salinity gradient only	1.8	6.3×10^{-3}
4. Temperature and salinity	3.8	1.5×10^{-2}

* - See Figure 31 for location

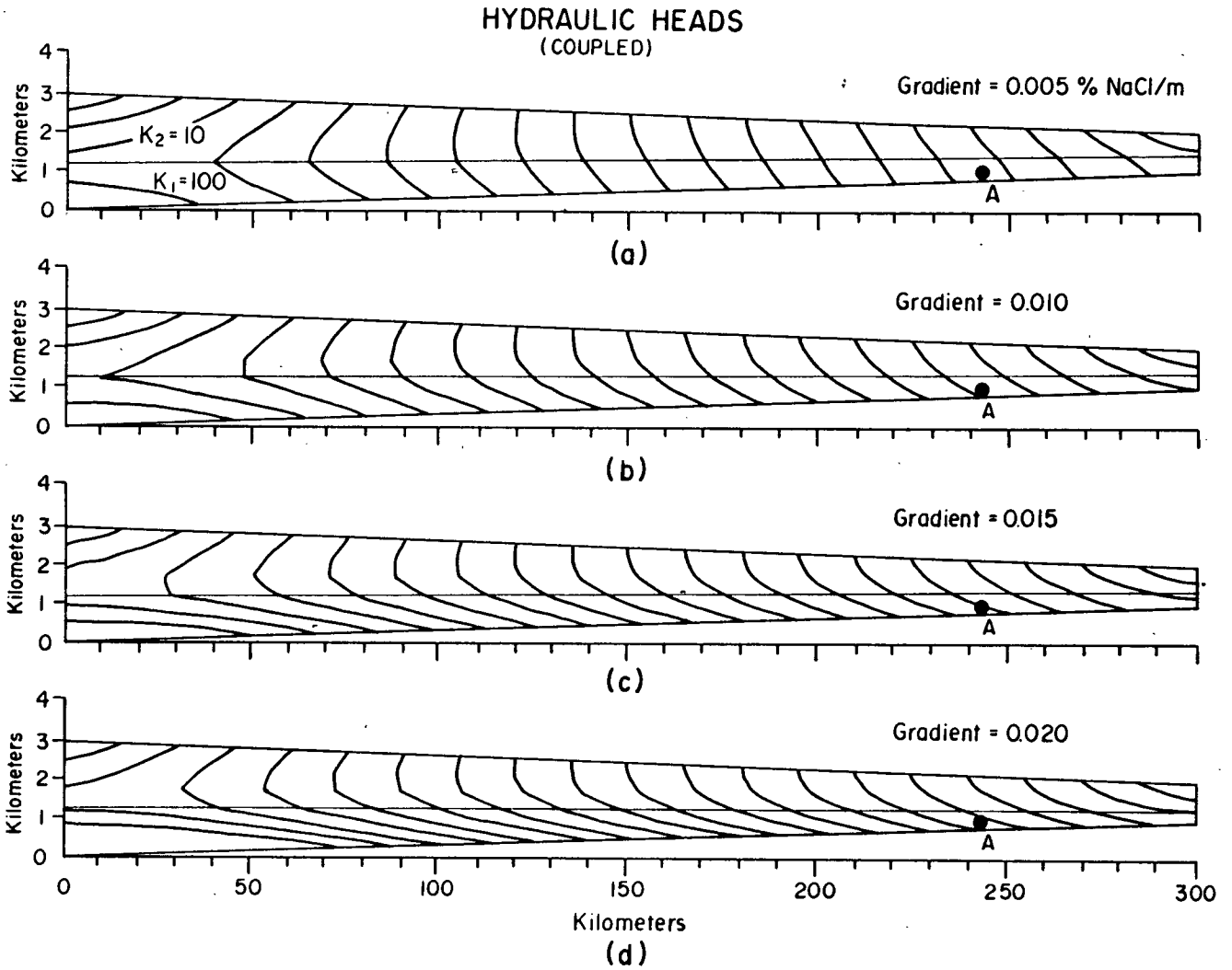

Figure 32. Variation in hydraulic-head patterns and fluid velocity as a function of salinity gradient.

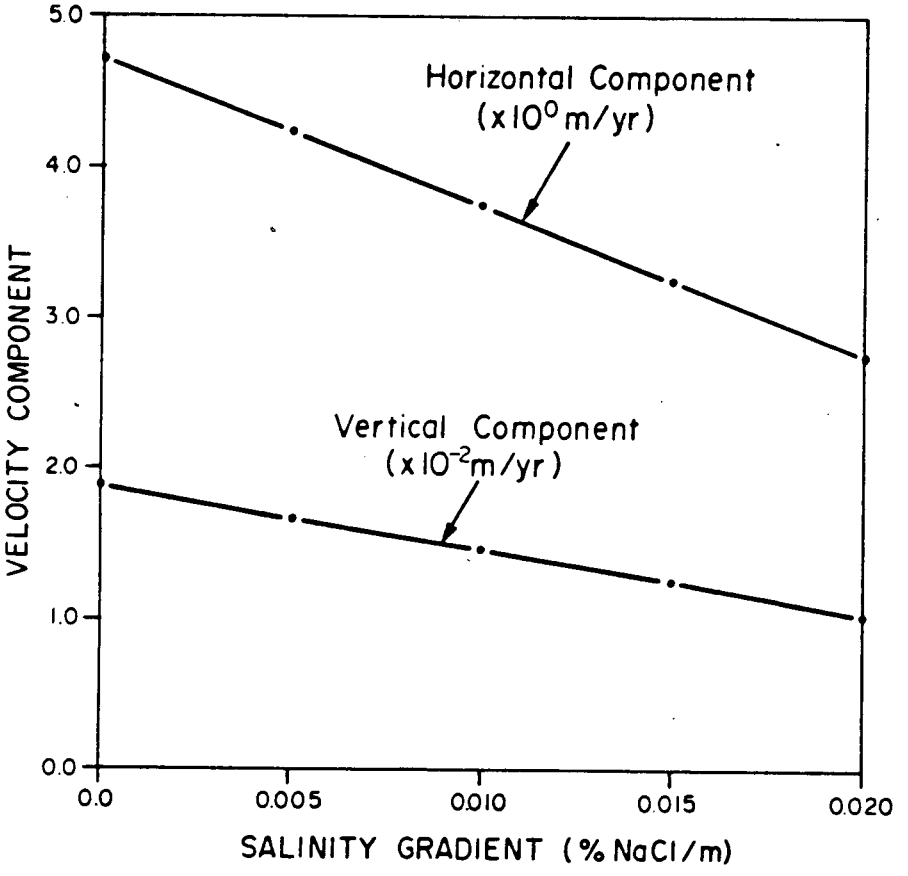

(e)

Figure 32. (Continued)

salinity gradients. Figure 32e shows how the velocity components decrease as higher salinities are assumed. In the simulations to follow, we will employ the 0.01 % NaCl/m gradient as being a representative value for the basin.

Basin Geometry

Fluid-flow simulations can also be conducted to review the influence of basin size, structure, and topography on the groundwater regime. Tóth (1963) and Freeze and Witherspoon (1967) provide a more thorough analysis of the role of these factors than will be presented in this evaluation, but as before, the attention here will be directed to the problem of flow in large sedimentary basins. All of the simulations will model a basin consisting of two layers.

In the preceding simulations the size of the basin was kept a constant 300 km in length and 3 km thick at the thickest point of the wedge. The choice of these dimensions is based on real sedimentary basins, such as those of Figures 2 and 4. It is obvious that basin size may vary: some flow systems may operate over distances of a few kilometers, while others may involve distances of several hundred kilometers. Tóth (1963) and Freeze and Witherspoon (1967) demonstrated with their models that the total continuous length of a regional flow system depends on topographic relief, basin thickness, and subsurface hydraulic conductivities. If the basin is reasonably thick, relief is gentle, and aquifers exist at depth, then continuous flow systems can develop on a basin-wide scale. Numerous field studies have documented the existence of very long, gravity-type flow systems in sedimentary basins (e.g. van Everdingen, 1968; Hitchon, 1969a, 1969b; Bond, 1972; Tóth, 1978).

Figure 33 illustrates the effect of basin size on subsurface flow, over a possible range of dimensions. The length of the basin is 'L' kilometers, and the vertical scale is exaggerated by a factor of 10 in order to illustrate

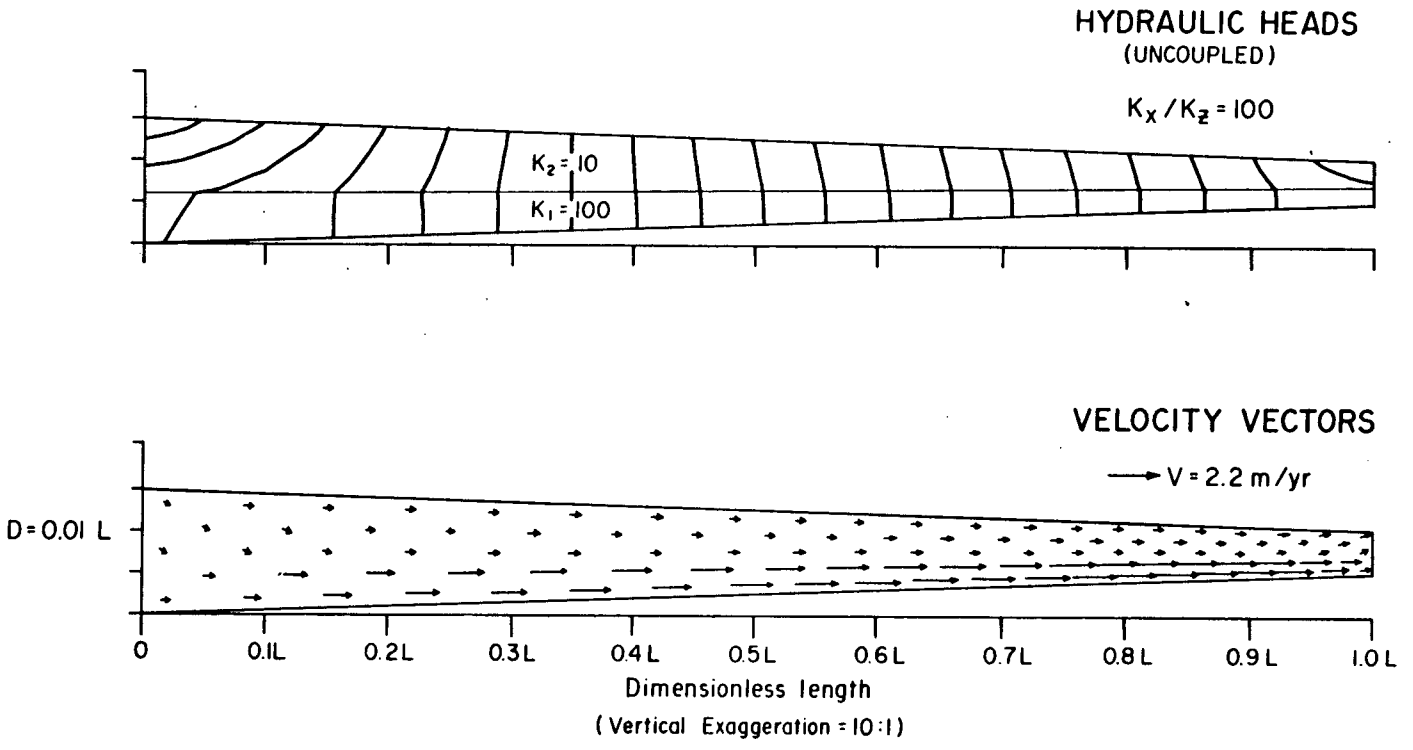

Case 1 : L = 300 km, D = 3 km

Case 2 : L = 150 km, D = 1.5 km

Case 3 : L = 30 km, D = 0.3 km

Figure 33. Dimensionless cross section showing the relationship between regional fluid flow and basin size.

the length-to-depth ratio of 100:1. The slope of the water table is assumed to follow the surface topography with a linear gradient of 0.003. The effect of temperature and salinity are excluded from Figure 33, because it is obvious that a basin 300 m thick will not have the same range of temperature as a basin 3 km thick. The hydraulic-head contours are dimensionless because the length-to-depth ratio, water-table slope, and hydraulic conductivities are the same for each basin size. The contour interval represents 5% of the total potential drop across the basin, which is equivalent to 5 m, 25m and 50 m for basin lengths of L = 30 km, 150 km, and 300 km respectively. Whatever the basin size in the uncoupled case, the flow rates remain the same throughout the basin. These results reflect the mathematical concept of dimensional similitude. This concept recognizes that for similar ratios of controlling parameters, such as topography, geology, and length-to-depth ratio, the quantitative results are similar. Basin similitude allows one to extrapolate modeling results to different system scales under these criteria. Other examples of dimensionless flow nets are shown in Figures 7 and 8.

Although it is mathematically very useful to report modeling results in terms of dimensionless parameters, the data interpretation can become confusing for anyone not experienced in similitude analysis. The subject also becomes very complicated when considering the coupling of heat and mass transport. Dimensionless analysis is not used in this study for these reasons. Further discussions of the general application of similitude theory can be found in Kline (1965), and in Bear (1972) for reference to porous-media problems.

The length-to-depth ratio of a basin has significant influence on fluid-flow patterns. Figure 34 shows the results of three simulations where the ratio L/D is varied as: (a) 10:1, (b) 50:1, and (c) 100:1. Depth is fixed

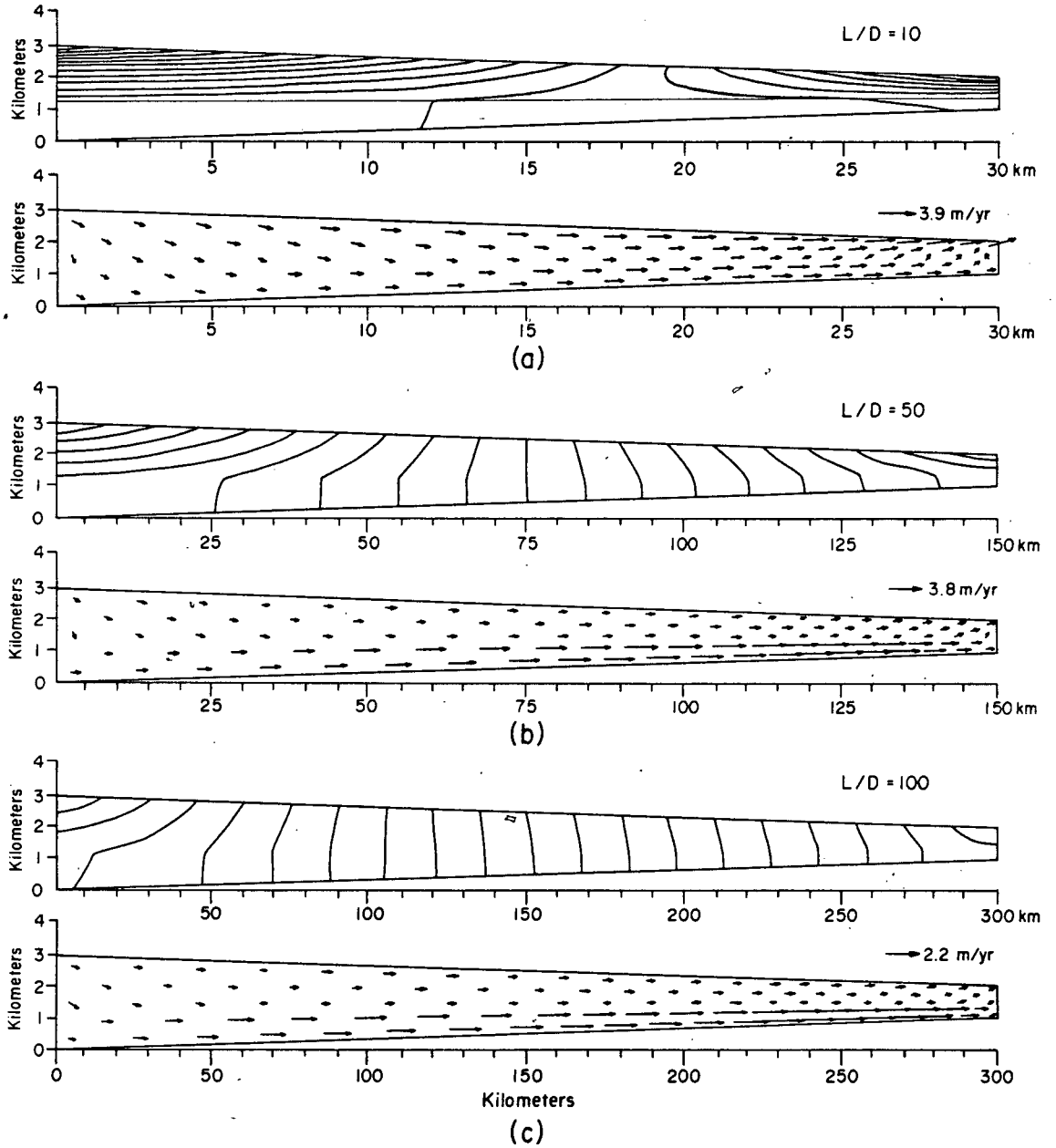

Figure 34. Hydraulic-head patterns as a function of the length-to-depth ratio of a 3 km - thick basin.

at a constant 3 km. The configuration of the water table is linear, with gradients of 0.030, 0.007, and 0.003 for the three cases. Temperature and salinity are excluded from the models. The media properties are as before with $\phi_1 = 0.15$, $\phi_2 = 0.10$, $K_1 = 100$ m/yr, $K_2 = 10$ m/yr, and $K_{xx}/K_{zz} = 100$.

Halving the basin length from 300 km to 150 km (Figure 34b) and doubling the topographic slope increases the hydraulic gradients in the low-permeability unit. Fluid velocities increase throughout the basin, especially in the vertical direction. If the basin length is shortened by a factor of ten (Figure 34a), a considerable amount of energy is required to force fluid flow to the same depth, but over a shorter length. As a result the hydraulic-head equipotentials exhibit large gradients in the shale unit and very low gradients throughout the basal aquifer. Basins with small length-to-depth ratios will be efficient at producing large vertical fluxes over broad areas, but unless moderately high topographic relief exists across the basin, flow rates will be significantly smaller than those basins with larger length-to-depth ratios.

Changing the thickness of a basin of constant length produces similar results, as shown by the hydraulic-head plots in Figure 35. The thicker the basin, the steeper the hydraulic-head gradient becomes in the shale aquitard due to the smaller length-to-depth ratio. Notice that as the maximum thickness (at x = 0 km) is changed from 1.5 km in Figure 35b to 6 km in Figure 35d, the model assumes that the water-table slope changes from 0.0017 to 0.0070. This is purposely done so as to avoid constructing new finite-element meshes for each new model in Figure 35. Cases (a) and (e) are less common examples, but are included for comparison. Flow becomes horizontal in basins of very large length-to-depth ratios (Figure 35a). It is unlikely that such a flow system as depicted here would exist in mature basins because the influence of

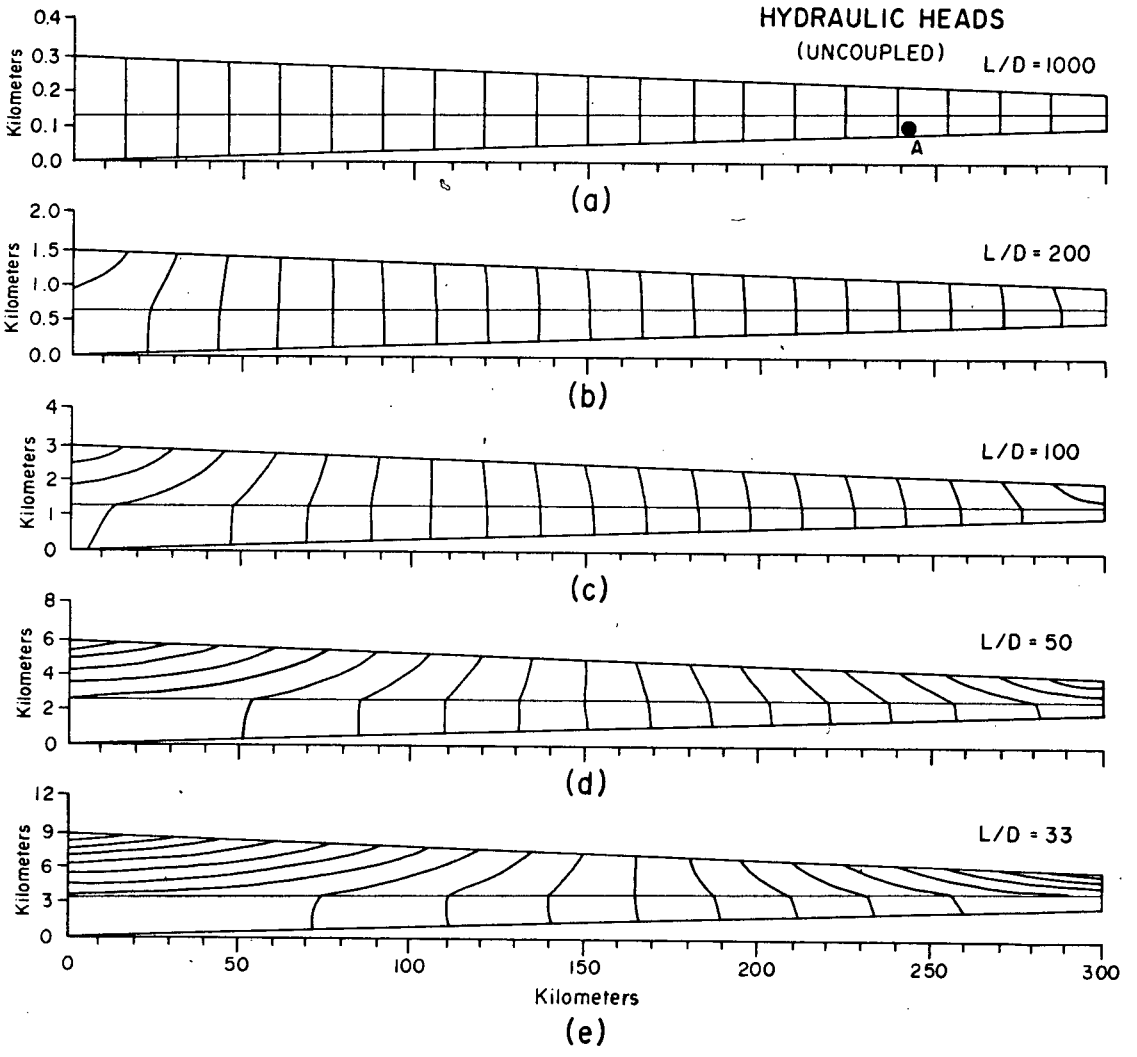

Figure 35. Hydraulic-head patterns and fluid velocity as a function of the length-to-depth ratio of a 300 km long basin.

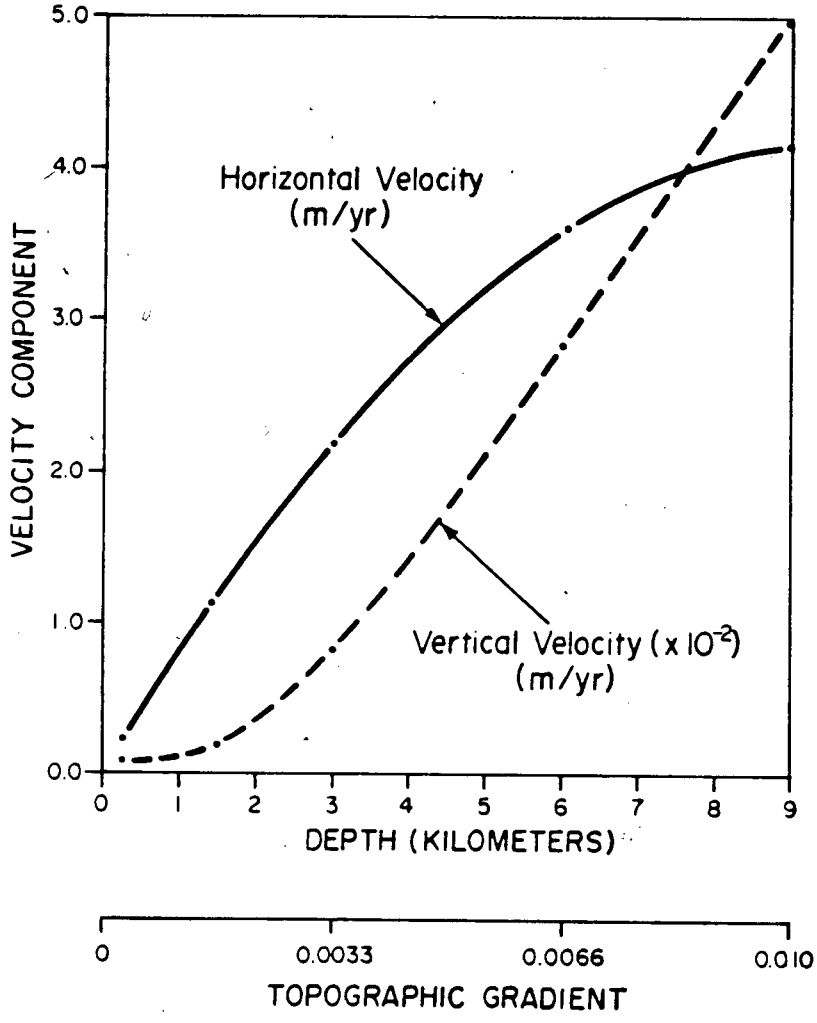

(f)

Figure 35. (Continued)

topography would easily partition the continuous strip into numerous, local flow systems. This type of basin would not be conducive to long-distance transport of metal-bearing brines in ore formation. Figure 32f summarizes the relationship between velocity at reference site A (Figure 35a), basin thickness, and topographic gradient. Most of the velocity change is caused by the change in the water-table slope. Qualitatively, it may prove useful in future studies to consider a suite of steady-state models, such as Figure 35, in assessing the change in flow patterns as a basin evolves to the mature stage.

Few studies have addressed the problem of how basement structure might affect flow patterns and velocities in a basin. Figures 36 and 37 show the effects of a flat-bottom basement and basement arch on the hydrodynamic picture. Comparison of these results can be made with the sloping-bottom basement of Figures 20 and 31. The length-to-depth ratio, water-table slope, and material properties are the same for each case.

Figure 36a illustrates the finite-element mesh used to compute the hydraulic-head patterns in Figures 36b and 36c. The flat basement produces a more symmetric flow pattern than the sloping-basement case. Groundwater recharge occupies the left half of the basin and discharge dominates the right half of the basin. The area of highest flow shifts from the shallow shelf of the basin in the sloping-basement basin (Figure 31) to the central part of the basin in the flat-bottom case (Figure 36d). The effect of a sloping basement is to cause the higher flow rates along the thinning shelf, than would be encountered at the same position in a flat-bottom basin. For the reference site A (Figures 31 and 36), the velocity changes from 3.2 m/yr in the flat-bottom basin to 4.2 m/yr in the sloping-basement model. An accompanying five-fold increase is felt in the vertical velocity component.

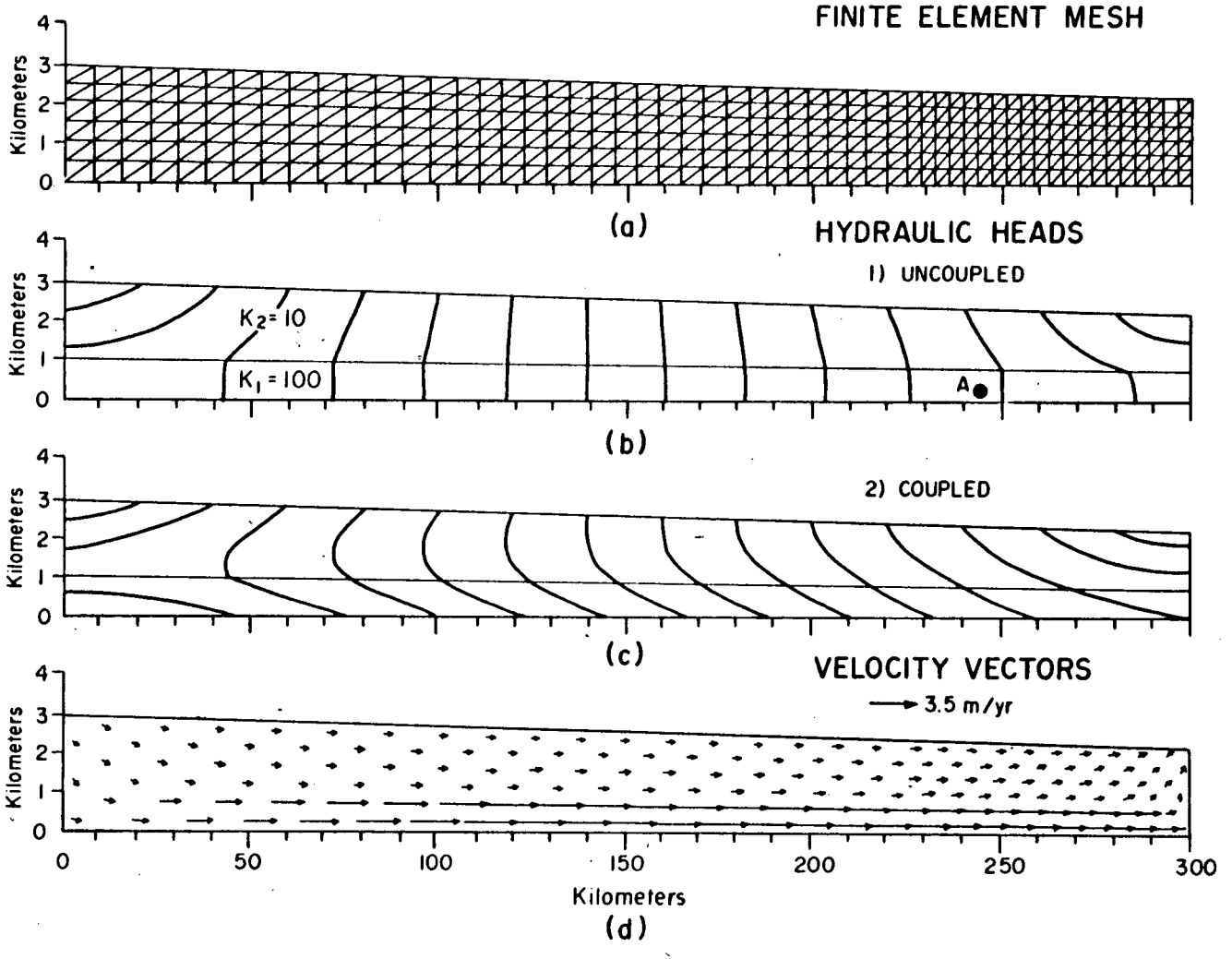

Figure 36. Regional fluid flow in a flat-bottom basin.

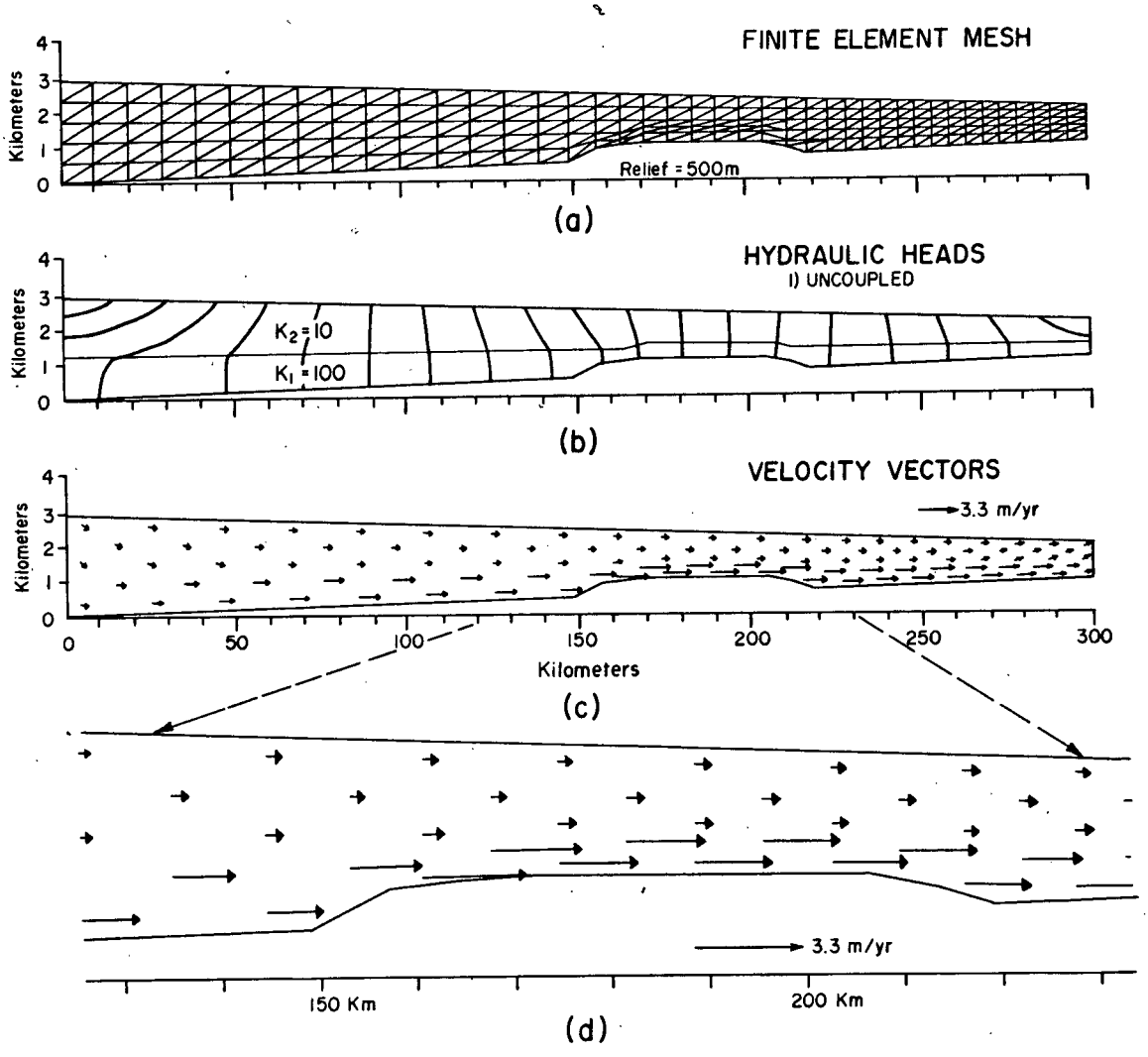

Figure 37. Regional flow patterns in a basin containing a basement arch with a relief of 500 m.

The flow system becomes slightly more complicated when the impermeable bottom surface is perturbed by a large basement high. Figure 37 considers the two-layer case where a basement arch is present in the right-central part of the basin. It is over 50 km in length, and total relief is 500 m. Figure 37 shows how the basement arch forces fluid flow over the high, thereby creating a zone of large flow rate immediately above the structure. Velocity is greatest on the upstream side of the ridge where v_x = 3.3 m/yr and v_z= 4.8×10^{-2} m/yr. The presence of the ridge has created an appreciable vertical flow of fluid in this region.

Increasing the relief of the basement arch has an even greater effect on flow as shown in Figure 38. In this model, the total relief is about 1000 m. Fluid velocity over the ridge reaches a maximum of 3.2 m/yr, which is the highest in the basin. Temperature and salinity effects are accounted for in Figures 38c and 38d. A rather steep salinity gradient of 0.015 % NaCl/m is assumed in this model. Velocities for the coupled simulation reach values of v_x = 5.8 m/yr and v_z = 0.1 m/yr. The accompanying temperature patterns for both Figures 37 and 38 are presented later.

It is apparent from these simple models that the presence of a basement arch impedes the flow of brines moving through basal aquifers to the edge of a basin. On the other hand, phenomena of this type could be important in explaining the genetic association of stratabound ore deposits and basement highs. The conceptual effect of basement structures has been recognized by geologists for a long time, but the simulations given here quantitatively confirm the effect.

Figure 39 summarizes the influence of basement structure on fluid flow, for the four models given here. The velocity distribution in the basal aquifer of each case is plotted as a function of distance along the basin.

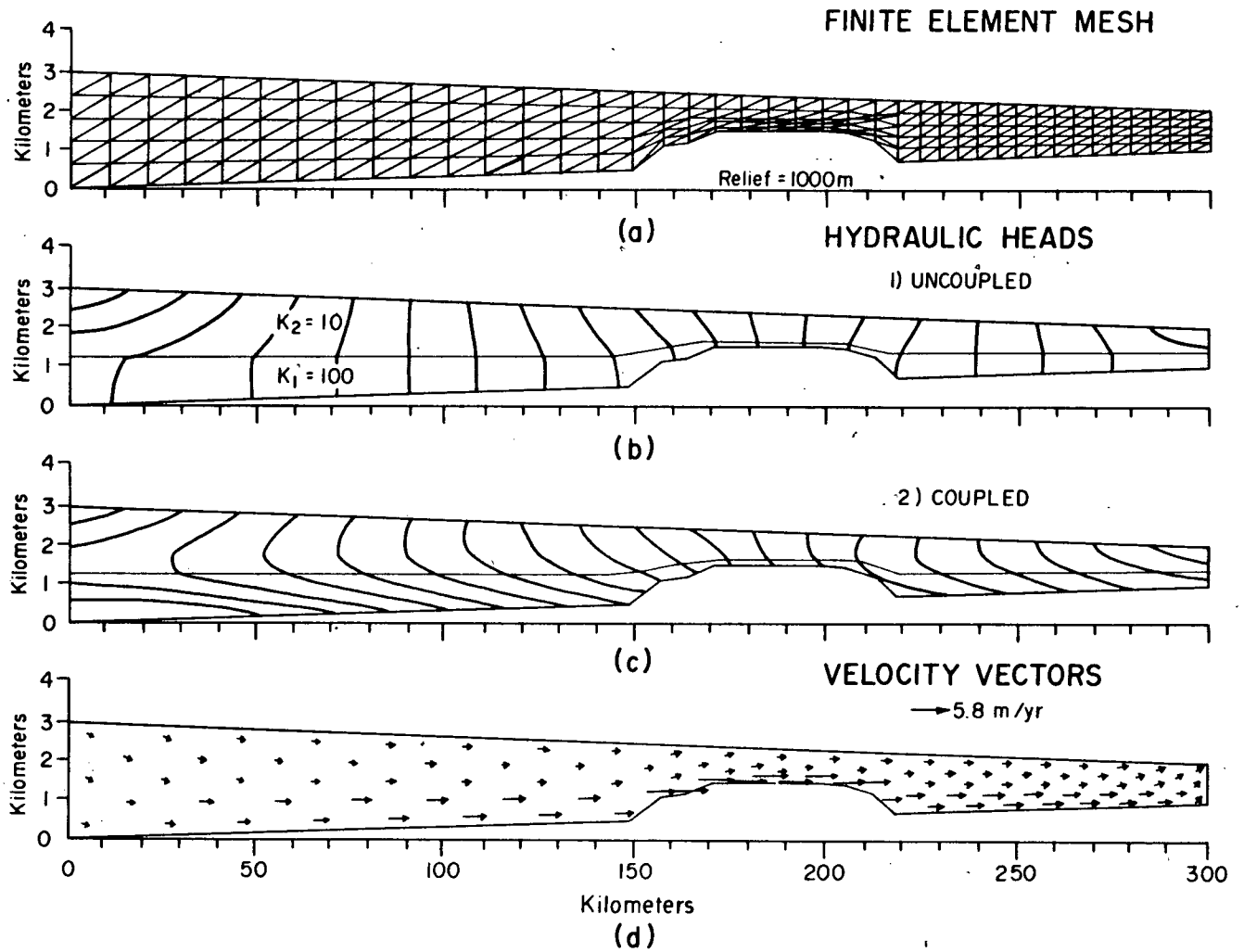

Figure 38. Regional flow patterns in a basin containing a basement arch with a relief of 1000 m.

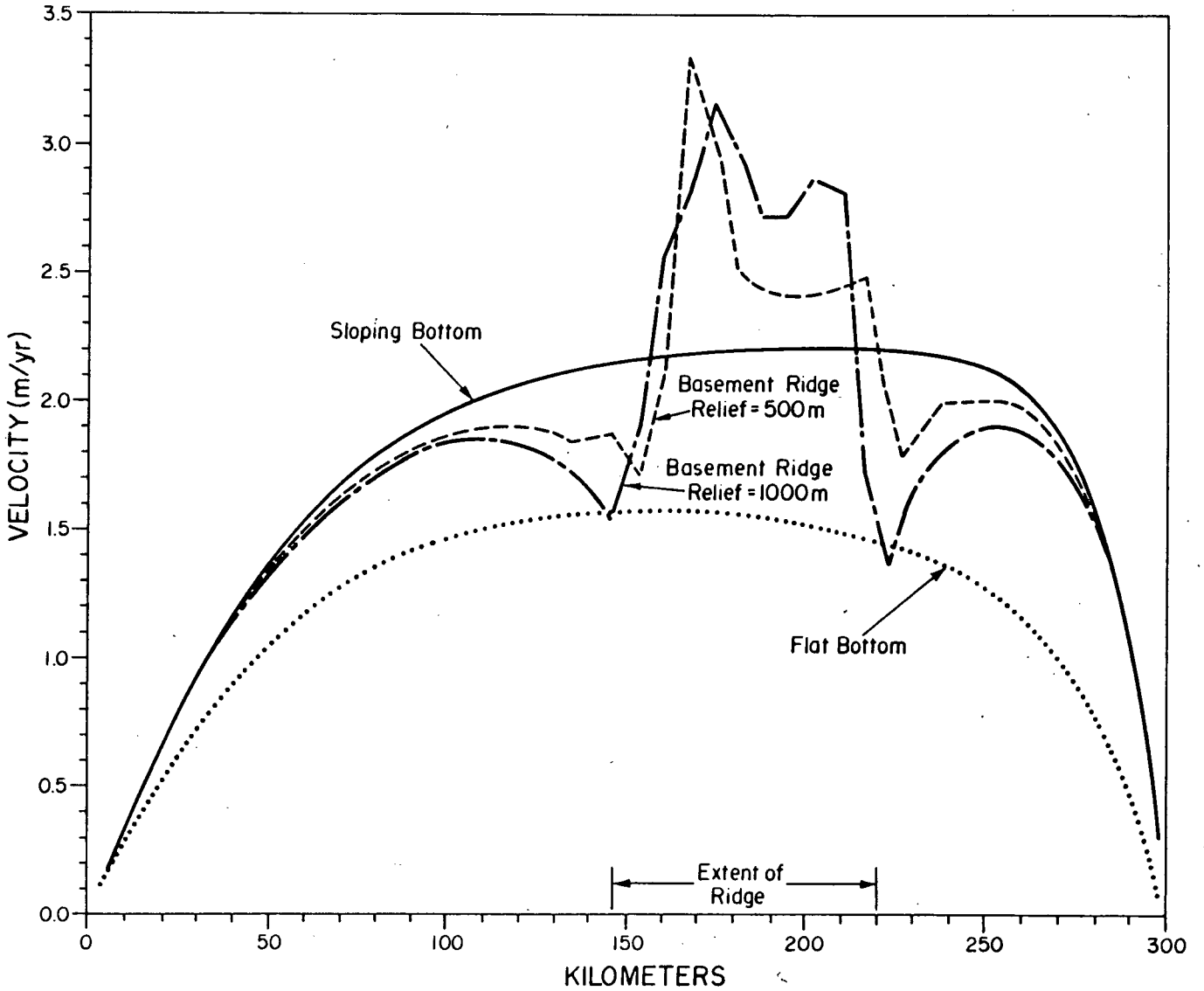

Figure 39. Effect of basement structure on the fluid veolcity in a basal aquifer.

For comparison purposes, all four of the simulations assume there are no temperature or salinity gradients in the basin. Most of the features exhibited in Figure 39 were discussed above and are self-explanatory.

The mechanism responsible for driving the gravity-based flow system is the water-table gradient, which in this study is assumed to be a subdued replica of the topography. As we have seen, the slope of the water-table plays a major role in determining the flow rates in a basin. In this final section on fluid-flow analysis, we will also see that the configuration of the water-table exerts a very strong control on the geometry of flow systems. The influence of this factor has been documented for fresh-water, isothermal basins by Tóth (1963) and Freeze and Witherspoon (1967), as explained in Chapter 2 (see Figures 7 and 8). The simulations that follow review the effect of topography, with respect to flow in large sedimentary basins with temperature and salinity effects included. Once again a simple, two-layer section is studied, and the material properties are kept the same as before.

Figure 40 shows the effect of a change in water-table slope near the basin margin (x = 280 km). The water table now consists of two linear segments, the long part with a regional slope of 3 m/km, and the short part with a slope of 8 m/km. What happens in smaller basins is that a zone of recharge is created directly below the point of slope change (see Figure 7b, Chapter 2). Due to the large length-to-depth ratio of the basin in Figure 40, this recharge feature is not observed. The only influence of the break in slope is to slightly reduce the upward component of flow in the discharge end of the basin. The result is that discharge is better focused near the basin margin, instead of being spread out over a wide area. In Figure 40c, a salinity gradient of 0.015 % NaCl/m is assumed to be present.

The second topographic model, Figure 41, shows the effect of a rise

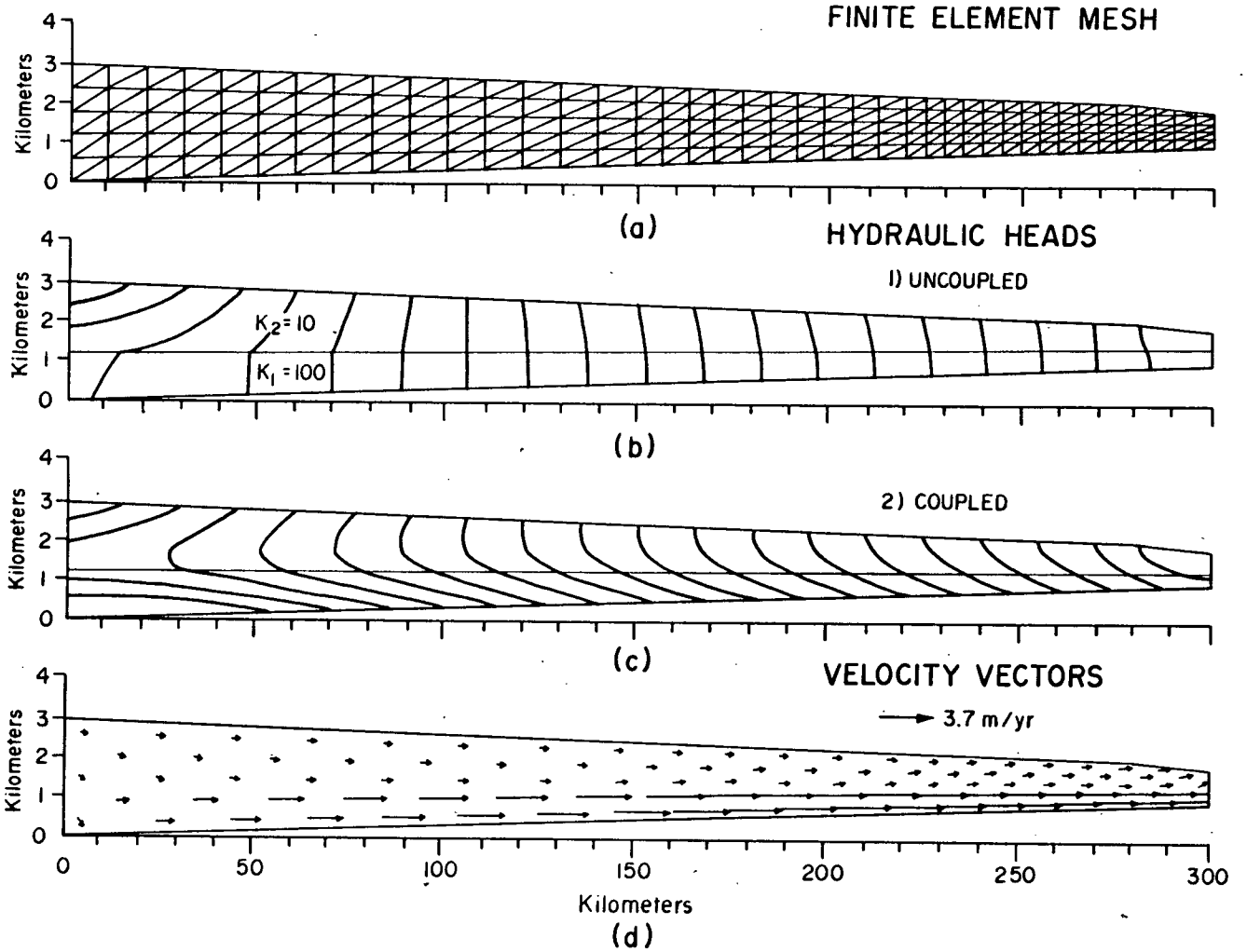

Figure 40. Regional fluid flow with a break in the water-table slope near the basin margin.

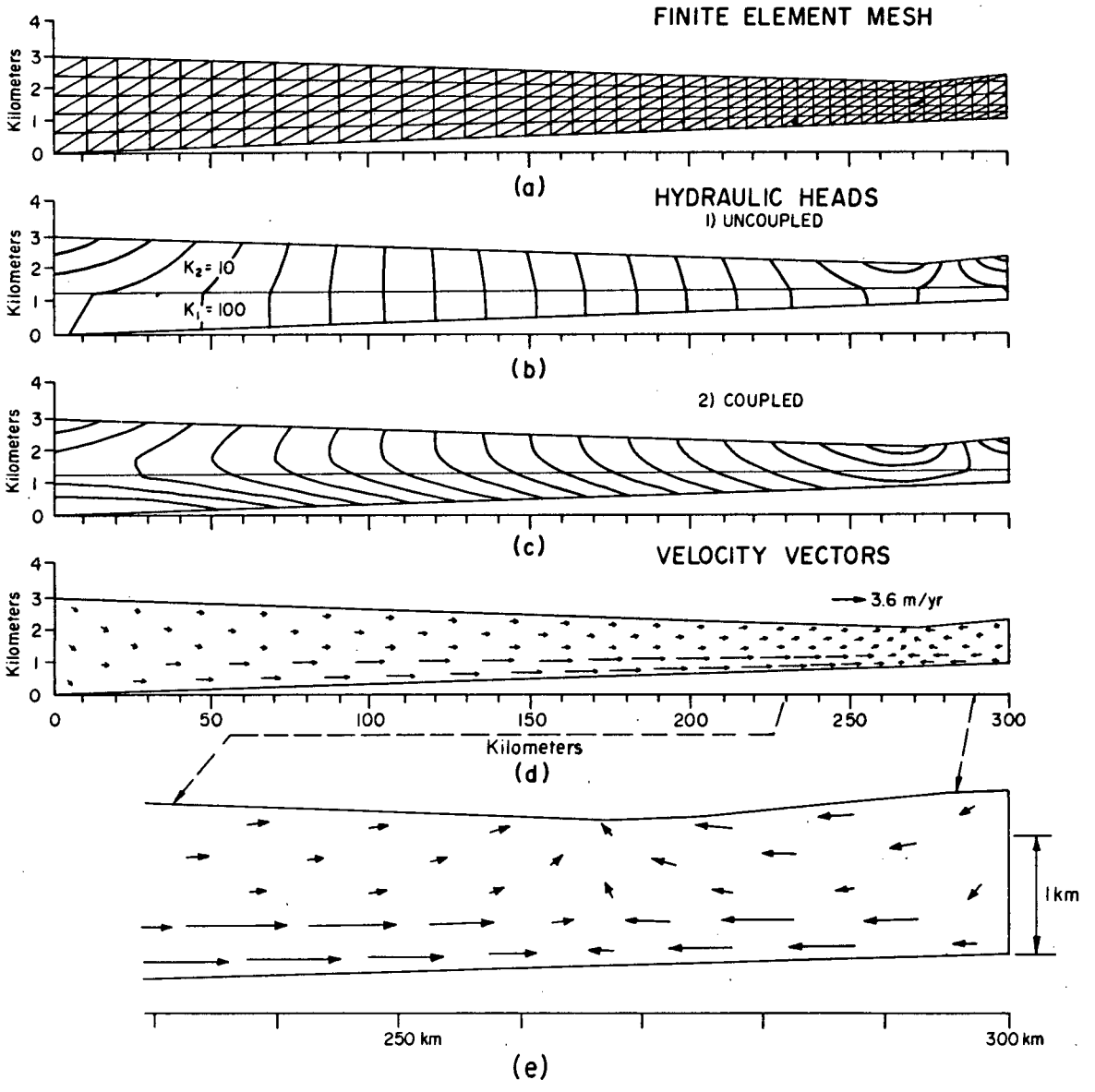

Figure 41. Regional fluid flow with a water-table ridge at the basin margin.

in the water-table elevation at the end of a basin. This ridge has a total relief of about 260 m, as compared to the 800 m relief of the regional slope. Its influence is strong enough to create a local flow system that pushes against the long, regional system, and forms a groundwater divide at the base of the ridge. This type of flow system would be capable of bringing together, for example, metal-bearing brines from the regional flow system and H_2S-bearing fluids from the local system. Mixing would occur over a relatively local area (Figure 41e), provided hydrodynamic dispersion occurs. It will be shown later that the upward discharge in the area also causes the temperature to be elevated over the normal geothermal gradient.

If the water-table ridge is shifted toward the basin interior, a different type of flow system develops, as shown by Figure 42. This ridge causes the development of a local flow system in the shale beds, which serves to recharge the basal aquifer and creates two small discharge zones (Figure 42e), but the direction of flow in the basal aquifer is unchanged. Notice that maximum flow velocities have changed in the basal aquifer from about 3.5 m/yr in the smooth water-table configuration (Figure 40) to about 5.0 m/yr in Figure 42.

The presence of a major valley (water-table depression) in the basin is much more effective at interrupting the flow of brines in a basal aquifer. Figure 43 depicts a depression of the water-table with an approximate depth of 300 m. Fluid flow in the basal aquifer is lateral across most of the basin, until the influence of the valley is reached, and then flow is forced upward to discharge into the depression. Local groundwater flow near the edges of the depression also discharges into the valley, which may dilute the brine flow from greater depths. Fluid velocities in the basal aquifer reach a maximum of 6.7 m/yr below the water-table depression. On the down-

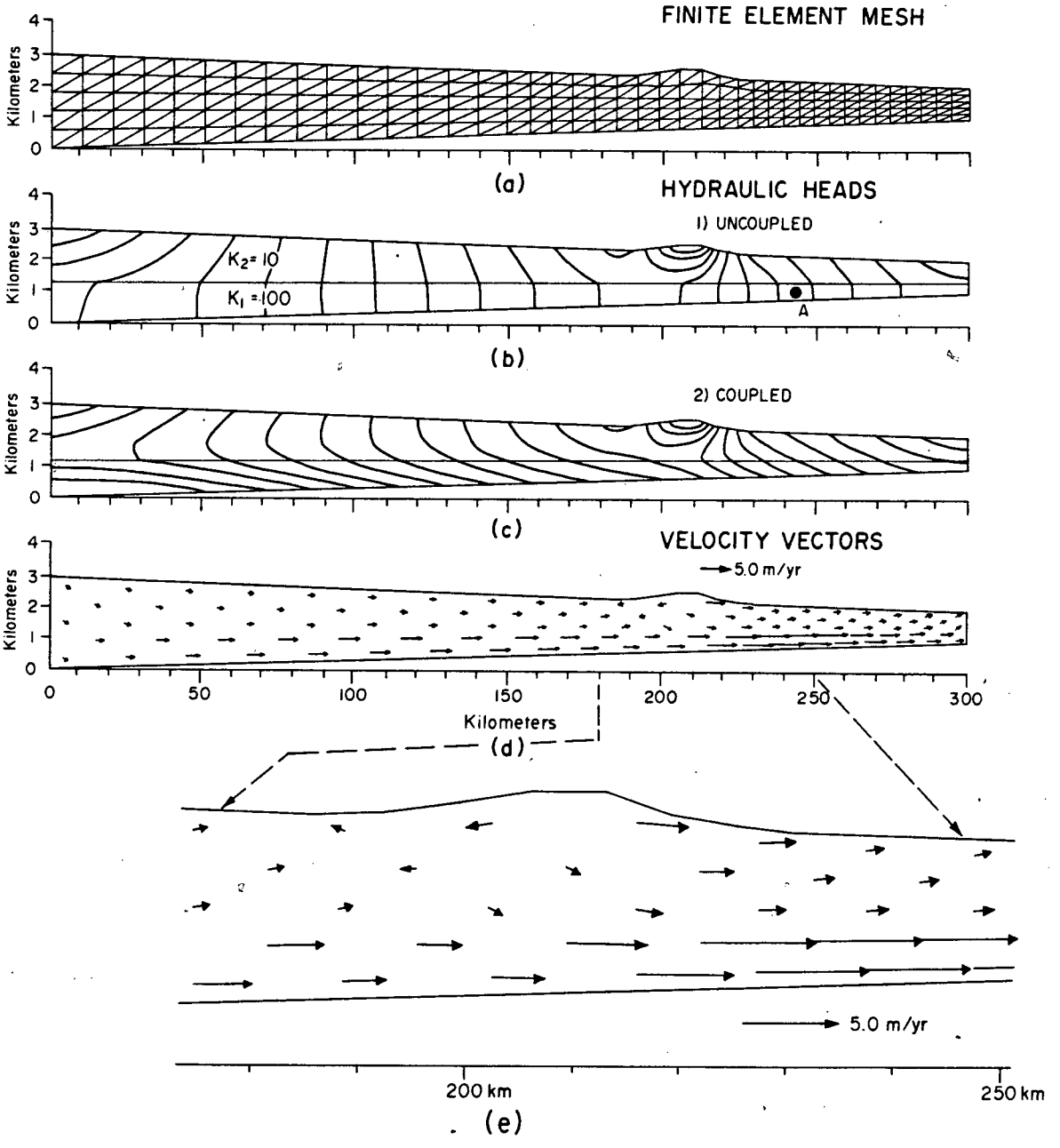

Figure 42. Regional fluid flow with a water-table ridge in the basin interior.

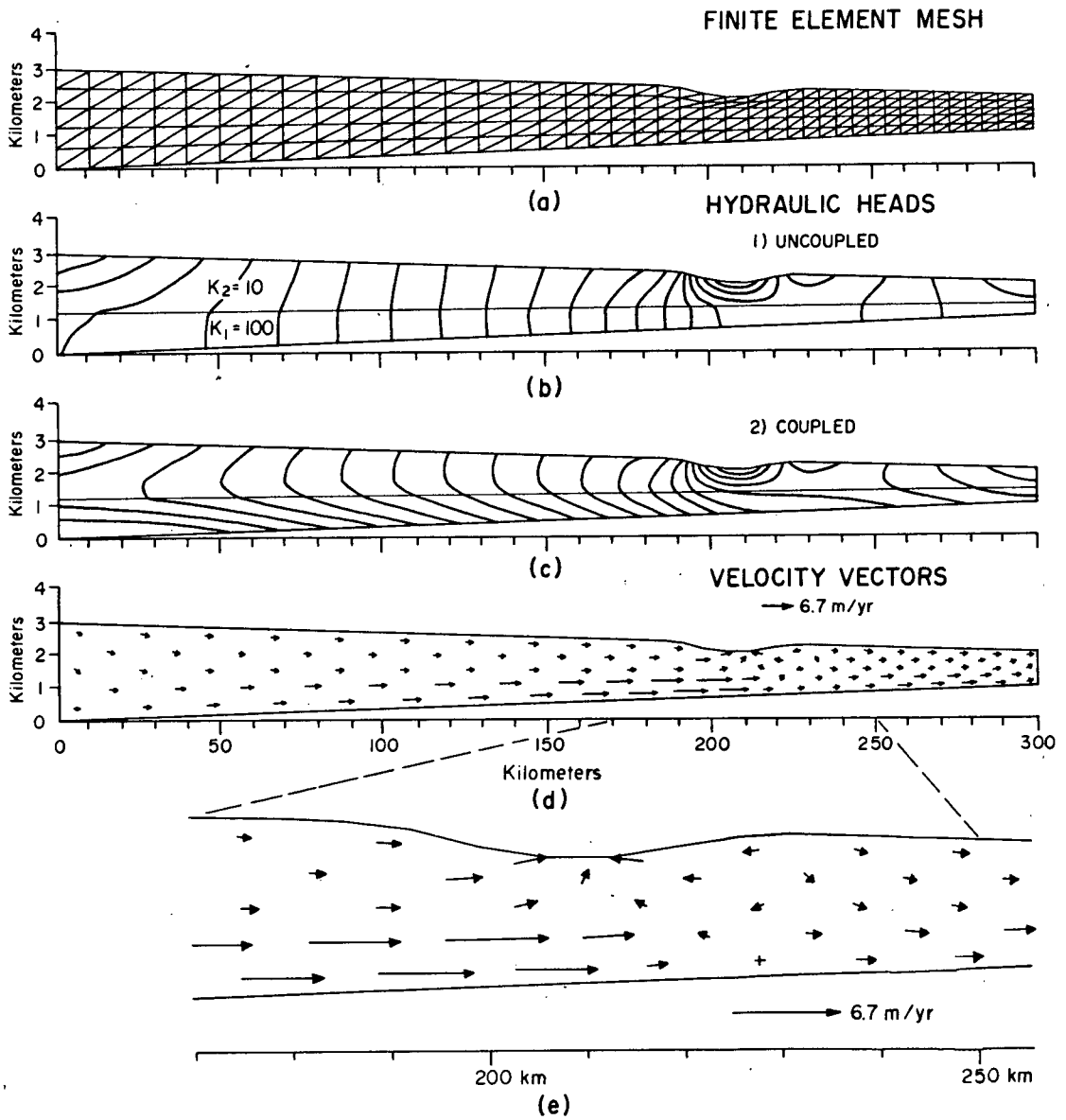

Figure 43. Regional fluid flow with a water-table depression in the basin interior.

stream end of the valley, velocity in the aquifer becomes quite small. The cross-marked velocity vector in Figure 43e (at x = 228 km), denotes an area of flow where the velocity is less than one-hundreth of the maximum recorded velocity (6.7 m/yr).

The final topographic model is presented in Figure 44. It is a model of a basin with an irregular water-table configuration: a gentle, rolling plain in the uplands area and a rugged, hilly set of perturbations in the discharge end of the basin. For the most part, fluid flow is relatively undisturbed in the basal aquifer and flow rates are roughly the same as the model with a linear water-table configuration. Superimposed on the regional system is a set of complex, local flow systems, but their depth of influence is limited to the low-permeability shale unit. The influence of the water-table irregularities would be greater for features of greater relief, or if the hydraulic conductivity contrast between the basal carbonate unit and shale unit was less than the 10:1 ratio assumed here.

Factor Controlling Subsurface Temperatures

Most quantitative modeling of heat transport and fluid flow has been carried out for the purpose of assessing geothermal reservoirs, heat storage in aquifers, radioactive-waste disposal, or the intrusion of plutons. The effect of regional groundwater flow on steady-state temperature patterns has also received study from a number of authors. Stallman (1963) and Bredehoeft and Papadopoulos (1965) show how groundwater velocities can be estimated from observed temperature data. The influence of groundwater flow systems on heat flow in an idealized cross section was investigated mathematically by Domenico and Palciauskas (1973). Parsons (1970) looked at a similar problem using finite-difference models. Both of these studies quantitatively demonstrate that convective heat transport causes geothermal gradients to

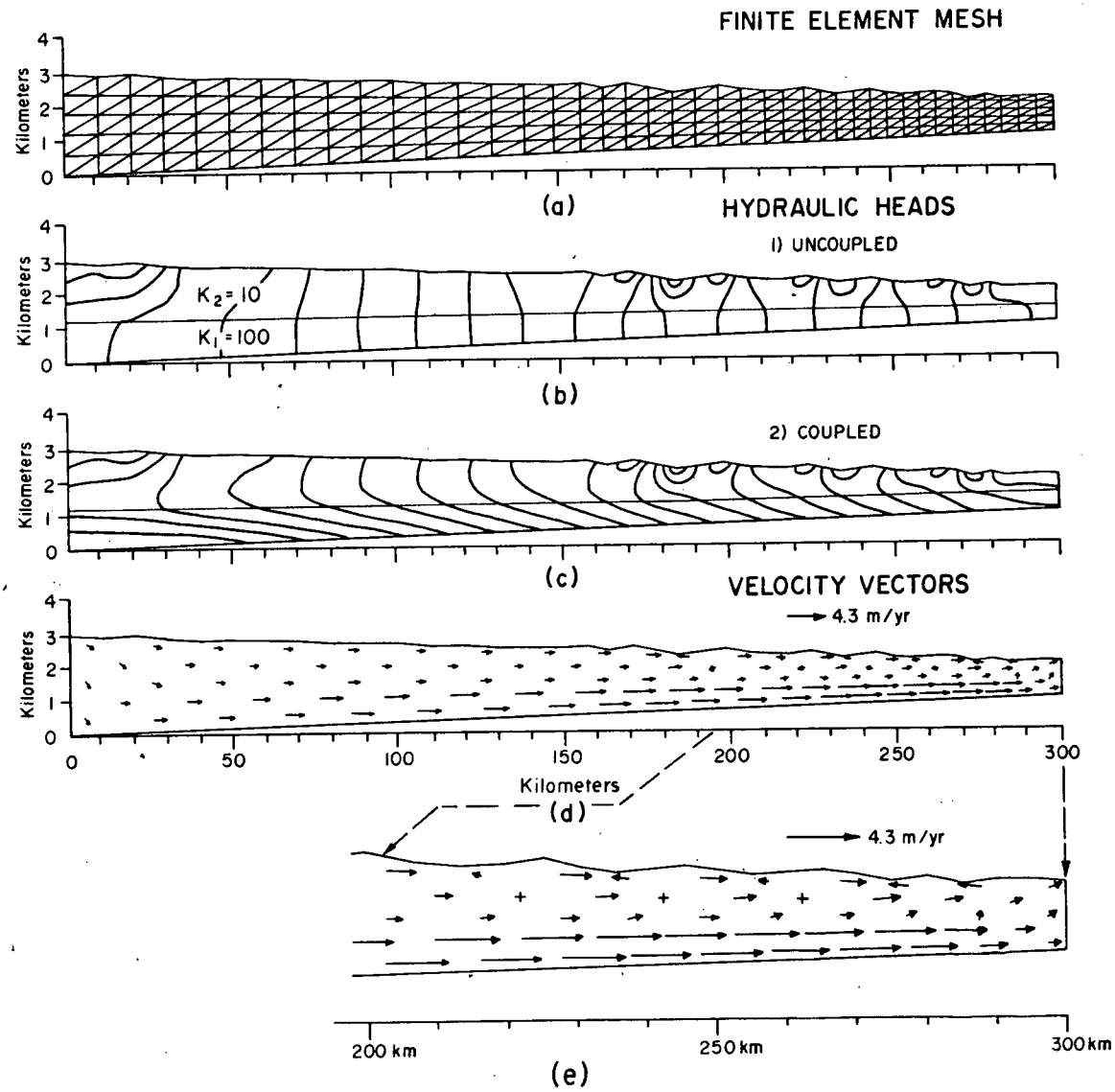

Figure 44. Regional fluid flow with an irregular water-table configuration.

decrease in groundwater areas and increase in discharge areas, relative to the case of pure conduction. Betcher (1977) performs a sensitivity analysis of many of the parameters affecting heat flow in a hypothetical 10 km-long groundwater basin using finite-element models. He presents some of the general relationships between hydraulic and thermal parameters of this basin.

The mathematical analysis of free convection in porous media has also received considerable study. Some of the better-known works are those of Nield (1968), Rubin (1973, 1981), Weber (1975), Tyvand (1977, 1981) and Straus and Schubert (1977). Most of this research is theoretical in nature, and concerns stability criteria for heat and mass transport with fluid flow in single aquifers.

The main purpose of this new assessment is to review some of the controlling factors of heat transport, but on the scale of a large sedimentary basin. Simulations are presented to illustrate the effect of the fluid-flow regime, the boundary conditions, the thermal properties of the porous media, and the basin geometry on the temperature distribution in large basins. Some of the models repeat the general concepts analyzed in previous studies, but their presentation here is justified on the basis of their worth to the specific problem of ore formation and for reasons of completeness. The results are based on the steady-state solution of the coupled fluid and heat-flow equations.

To begin the analysis, let us consider the hydraulic effects on the temperature pattern in the two-layer basins that we have been studying thus far. For example, Figure 31a depicts the typical temperature pattern for the case of the linear water-table slope. It assumes that a constant geothermal heat flux of 60 mW/m^2 occurs along the entire length of the basement boundary.

This heat flow value is representative of continental platform areas. The two lateral boundaries are assumed to be insulated barriers across which there is no heat flow. The water-table surface is an isothermal boundary, where temperature is assigned a value of 20°C to represent the mean air temperature. The lower layer is a dolomite aquifer with a horizontal hydraulic conductivity of 100 m/yr, a porosity of 0.15, an anisotropy ratio of 100 m/yr, and a thermal conductivity of 3.0 W/m°C. A value of 0.63 W/m°C is assumed for the thermal conductivity of the fluid throughout the basin. The upper layer is a shale aquitard with a horizontal hydraulic conductivity of 10 m/yr, a porosity of 0.10, an anisotropy ratio of 100:1, and a thermal conductivity of 2.0 W/m°C. Specific heat capacities of 1005 J/kg°C for the rocks and 4187 J/kg°C for the fluid are assumed to remain constant.

Notice in Figure 31a that the isotherms are not perfectly horizontal nor evenly spaced. The depression of the contours in the recharge end of the basin is caused by fluid flow convecting heat down into the basal aquifer. Upward flow in the downstream end of the basin causes a warping of the isotherms near x = 200 km. Thermal conduction exerts major influence on the temperature field, in spite of the groundwater flow system. This is evident in the near-horizontal character of the isotherms and the spacing control on the isotherms caused by variations in thermal conductivity.

The effect of variable density and viscosity are accounted for in Figure 31a. Some of the earlier simulations given here also considered heat flow in their fluid-flow solutions. In Figure 23a, the viscosity is held constant, but density is allowed to vary with temperature. The temperature field attains a maximum of 83°C near the 100 km-distance marker. If the density is fixed at a constant value, while the viscosity varies with temperature, the change in pattern is pronounced, as shown by Figure 24a.

The effect of viscosity alone is to cause higher rates of groundwater flow in the basal aquifer, and thereby shifting the area of highest temperature up dip in the basin by about 50 km. Temperature in this model is below 75°C.

The point to be emphasized here is that heat-flow patterns in sedimentary basins are the result of two important transport processes: conduction and convection. It is also important that temperature and salinity effects on water density and viscosity be included in the numerical modeling of heat transport, so as to properly account for their influence on convection. With these introductory observations made, we can now turn to an examination of the possible ranges of model parameters, and their control on temperatures in ore-forming environments near basin margins.

Hydraulic Conductivity

Intuitively it makes sense that the process of heat convection will become stronger in a basin as fluid-flow rates increase. Conversely, the effect of thermal conduction dominates the thermal regime if flow rates are small. As we have seen, higher flow rates can be obtained either by increasing the hydraulic conductivity or by increasing the topographic gradient. Coupling fluid flow with a temperature-dependent viscosity (e.g. Figure 24) also provides a means for increasing fluid flow in a basin.

Figure 45 shows the quantitative results of some numerical experiments that were run to demonstrate the effect of hydraulic conductivity on heat flow. To isolate the effects, the thermal conductivities of the two hydrostratigraphic units are set equal to 3.0 W/m°C, and the thermal dispersivities are set equal to zero. The hydraulic conductivity is increased by the same factor in each layer so as to maintain the permeability contrast of 10:1 in each simulation. An anisotropy ratio of 100:1 for hydraulic conductivity is also held constant.

In Figure 45a, the hydraulic conductivity (K_1) is set very low at

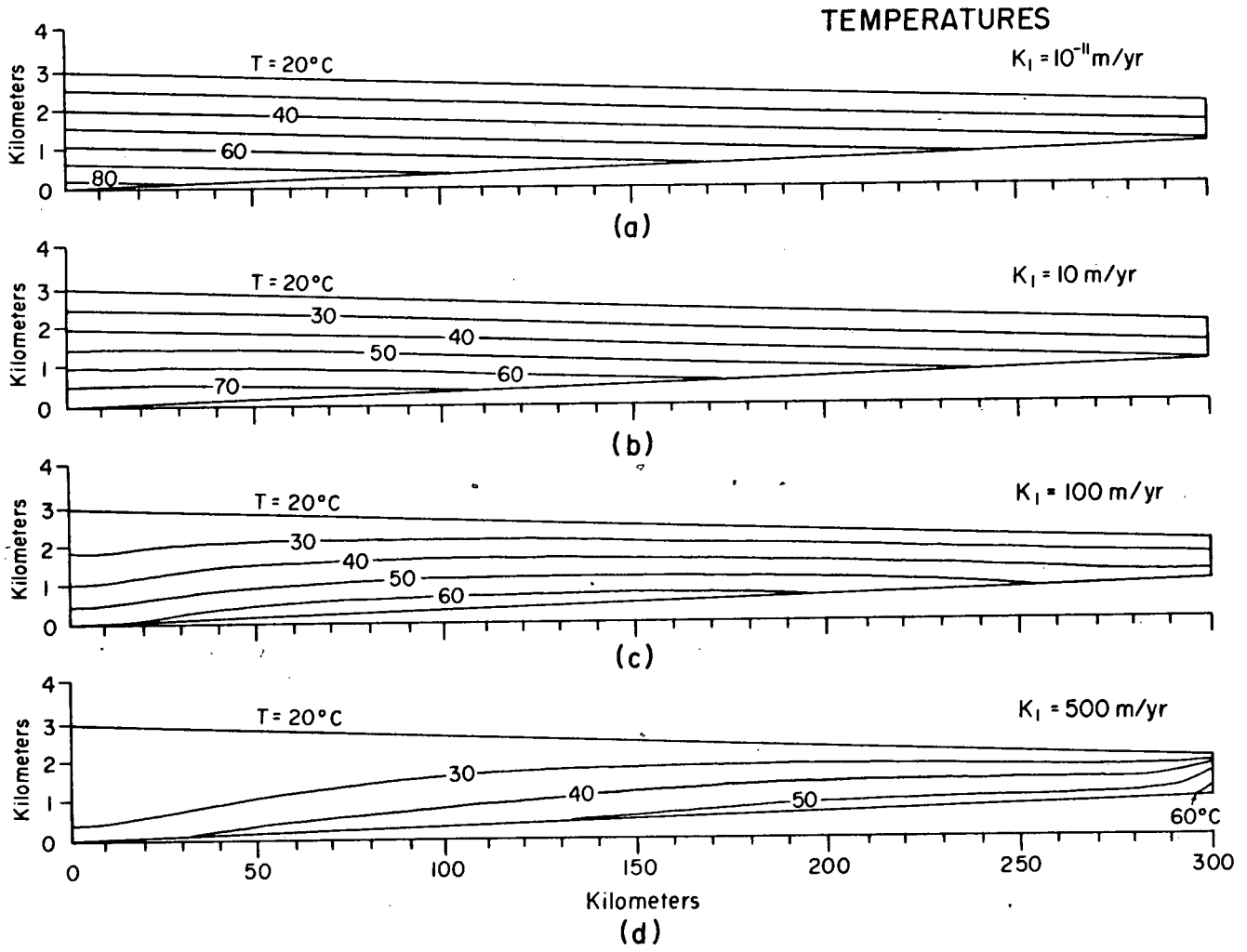

Figure 45. Steady-state temperature patterns showing the effect of convection for various hydraulic conductivities.

10^{-11} m/yr, which ensures that heat transport will be dominated by conduction. Increasing the hydraulic conductivity of the basal unit (K_1) to 10 m/yr and that of the upper unit (K_2) to 1 m/yr (Figure 45b) causes some heat convection, but the temperature pattern change is negligible from case (a). However, when K_1 = 100 m/yr (Figure 45c) the change in the temperature pattern is significant. The temperature contours are now depressed in the recharge end of the basin, but shifted upward in the discharge end of the basin. Notice that the area of highest temperature is no longer in the deepest part of the section as the conduction models, but now is shifted updip in the basin. The last diagram, Figure 45d, shows what happens when the hydraulic conductivity of the basal aquifer is assigned a reasonably high value of 500 m/yr. Convection causes a major depression of subsurface temperature in the recharge end of the basin, while elevating temperatures along the shallow platform. Phenomena of this type may explain the association of high temperatures at shallow depths with the occurrence of carbonate-hosted lead-zinc deposits near a basin margin.

Figure 46 is a plot of average temperature in the basal aquifer as a function of distance along the basin and hydraulic conductivity. These temperature profiles are from the models shown in Figure 45. Isothermal conditions rarely occur in regional aquifers, although this situation may be approached when flow rates are high enough. Higher values of flow reduce the temperature in recharge areas and raise the temperature in discharge areas, relative to the case of conduction alone. Increasing the hydraulic conductivity or flow rates has the effect of shifting the 'hinge point' downstream from point A to point B in Figure 46. If flow rates were unrealistically high, heat transport would be completely dominated by convection, and basin temperatures may become nearly isothermal.

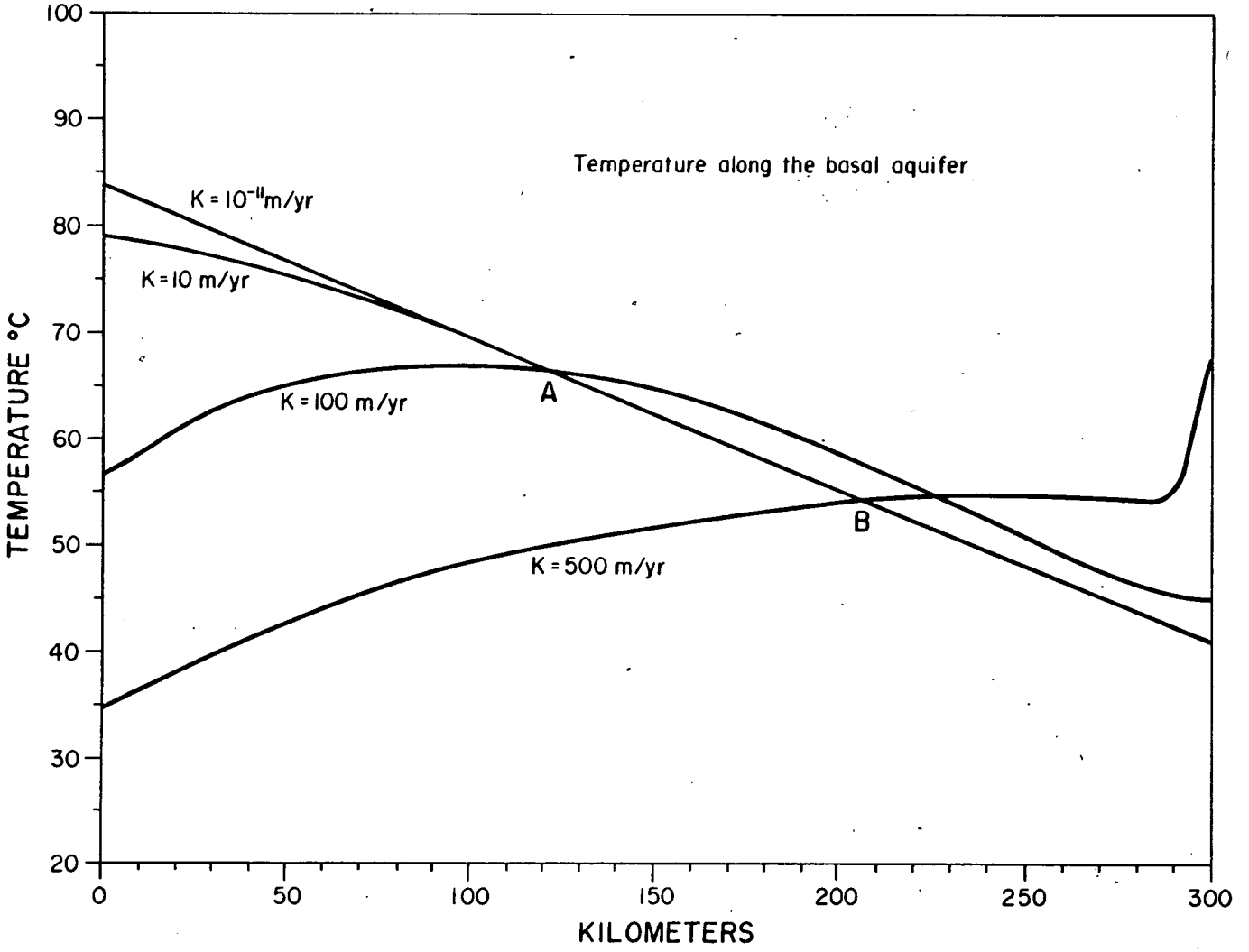

Figure 46. Effect of hydraulic conductivity on the temperature along a basal aquifer.

Thermal Conductivity

In the absence of convection, temperature gradients are controlled by the boundary conditions on the thermal regime, and by the thermal conductivity of the porous media. Table 10 gives the range of thermal conductivities for several types of geologic materials. These have been compiled from the listings of Clark (1966), Kappelmeyer and Haenel (1974), and Sass et al. (1981). Recall from Equation (3-16) that the effective thermal conductivity of the porous medium is a function of the fluid thermal conductivity, the rock thermal conductivity, and the porosity. Temperature also affects the thermal conductivity of rocks and water, but the influence is small for temperatures below 150°C. Porosity is set equal to a constant in the simulations given below, and only the thermal conductivity of the rock is varied.

Figure 47 shows the results of six simulations in which the thermal conductivity of the stratigraphic section is varied between 1.0 and 6.0 W/m°C. The basin is homogeneous with respect to the thermal properties, and a constant geothermal heat flux of 60 mW/m^2 is prescribed on the basement boundary. The hydraulic properties are the same as those of Figure 45c, namely that K_1 = 100 m/yr, K_2 = 10 m/yr, K_{xx}/K_{zz} = 100, ϕ_1 = 0.15, and ϕ_2 = 0.10. Temperatures in the downstream end of the basin appear to meet ore-genesis requirements of T > 50°C for basin thermal conductivities less than 3.0 W/m°C. It is apparent from these simulations and Table 10 that the presence of a thick sequence of shale of limestone is conducive to ore formation at relatively shallow depths.

The effect of a heterogeneous thermal conductivity is displayed in Figure 48. In part (a), the two-layer basin has a top unit with a thermal conductivity κ_2 = 2.0 W/m°C. Temperatures in the basal aquifer reach a maximum of 75°C, which is a 10°C rise over the homogeneous model of Figure 47(c).

Table 10. Thermal conductivity range of geologic materials.

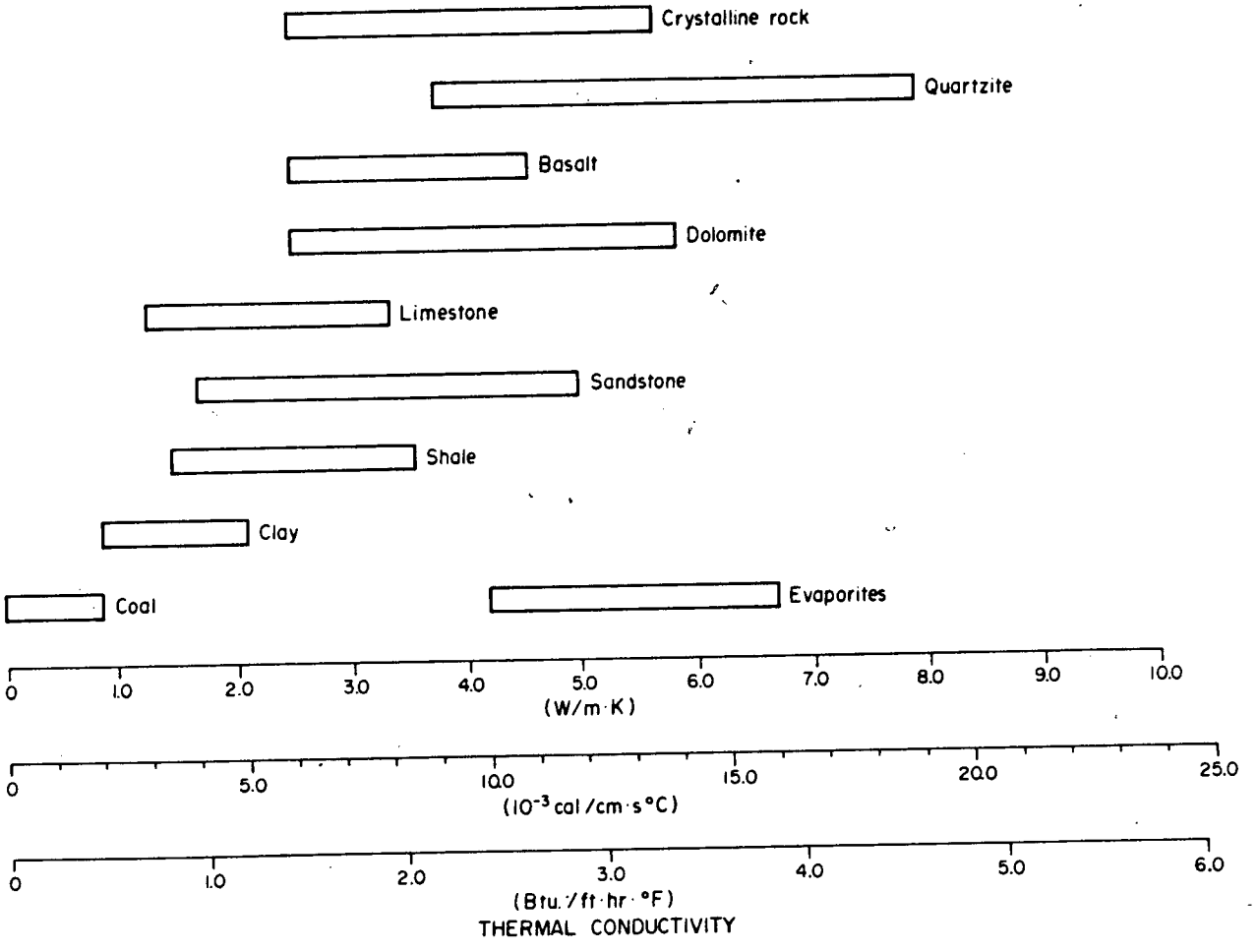

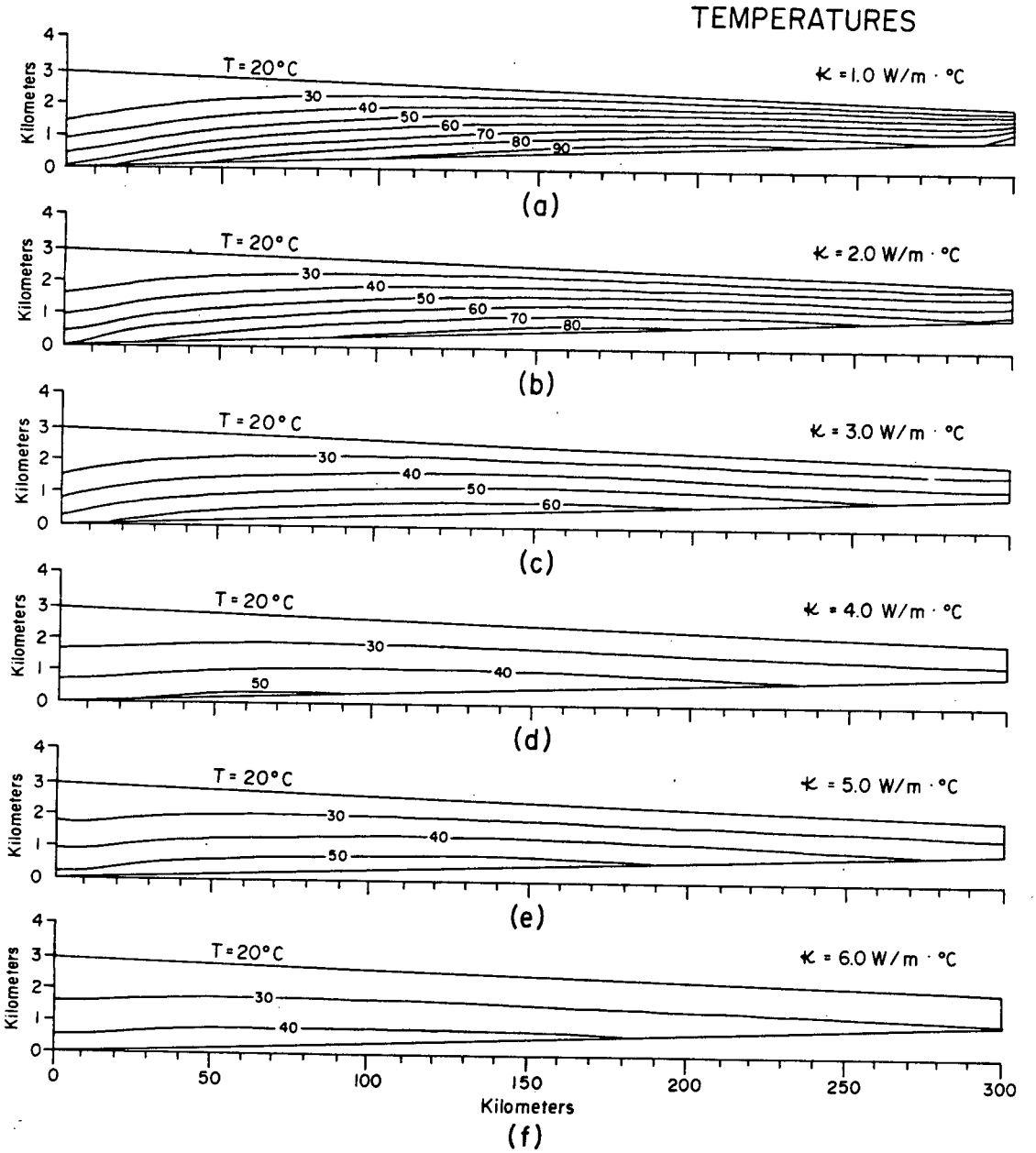

Figure 47. Temperature patterns in a thermally homogeneous basin for various values of thermal conductivities.

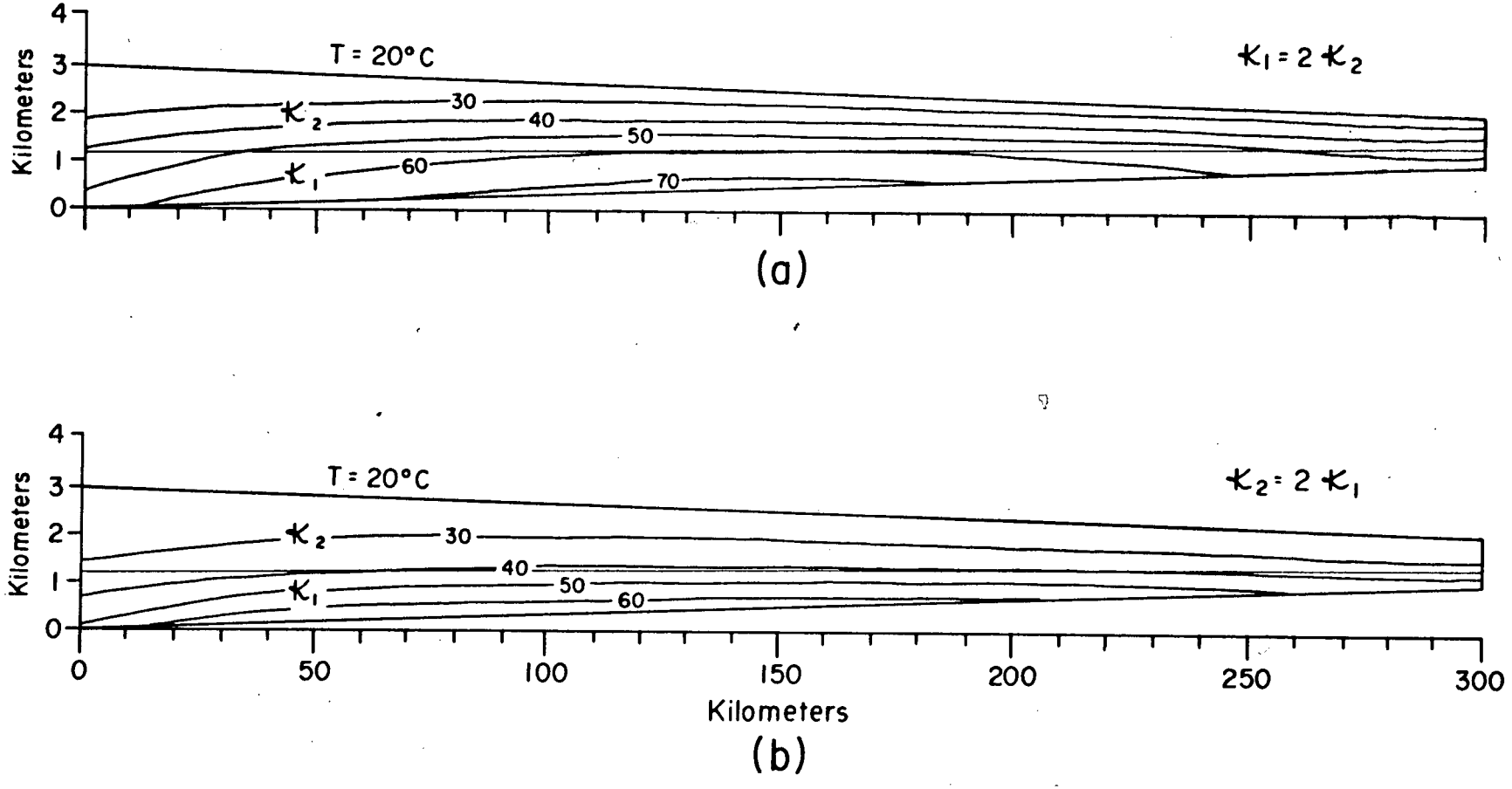

Figure 48. Temperature patterns in a thermally nonhomogeneous basin with two layers.

One would expect even higher temperatures for a basin with a thinner aquifer and thicker shale aquitard.

Reversing the thermal conductivity of the layers, but not the hydraulic properties, produces the temperature pattern in Figure 48b. Now the isotherms are more closely spaced in the basal layer than in the overlying layer. This situation would probably be less common in nature because aquifer lithologies are commonly sandstone or dolomite, both of which are more conductive than low-permeability shale or limestone (Table 10).

Salinity

The effect of a salinity profile on fluid-flow velocities was observed earlier to be relatively small (Figure 30), unless very high salinity gradients were present (Figure 32e). The change in temperature patterns can be expected to be similarly small. To verify this expectation, three simulations were run with salinity gradients of 0.005, 0.010, and 0.015 % NaCl/m in the model basin of Figure 45d. Temperatures were nearly identical in all three simulations, the largest difference being about 1°C in the deepest part of the basin.

One aspect about salinity that may be more important is its effect on the thermal properties of the fluid. Bear (1972, p. 649) reports a thermal conductivity for a 25% NaCl solution that is ten times less than that of fresh water. The presence of very saline brines, therefore, may cause a 20% drop in the effective thermal conductivity of the porous media, relative to the case of less saline water. This type of coupling between the heat equation and salinity profile is not included in the present analysis, but the effect can be estimated qualitatively by comparing the change in temperatures between Figure 47e and 47d.

Thermal Dispersivity

The coefficients of thermal dispersivity, ε_L and ε_T, are the least-known parameters in the heat-transport equation. Thermal dispersion refers to the additional heat transport in a porous medium that is caused by variations in fluid velocity along the flow path. It can be viewed upon as a process of mixing that disperses heat as the fluid packet flows along its tortuous path. The concept is, in fact, borrowed from mass transport theory. Dispersivity data is very scarce, but longitudinal dispersivity ε_L probably ranges between 1 and 500 m and transverse dispersivity ε_T between 0.1 and 50 m, for the regional scale of a sedimentary basin. These numbers are estimated from the compilation given by Anderson (1979).

Figure 49 shows how the extreme magnitudes of the longitudinal dispersivity parameter affect the temperature pattern in a two-layer basin, where K_1 = 100 m/yr and K_2 = 10 m/yr. Transverse dispersivity is assumed a constant value of 1 m in both layers. The longitudinal dispersivity is fixed at 1 m in the shale layer, but is changed from 1 m to 1000 m in the basal aquifer. A heat flux of 60 mW/m^2 is assumed for the bottom boundary, and thermal conductivities of 3.0 W/m$^\circ$C and 2.0 W/m$^\circ$C are assigned for the lower and upper layers. Salinity increases with depth at a gradient of 0.015 % NaCl/m.

It is clear from this simulation that subsurface temperatures are not affected by longitudinal thermal dispersion. This result is not surprising in that the largest component of heat transport is in the vertical plane, which is orthogonal to the main fluid-flow direction in the basin.

Several simulations, however, show that longitudinal dispersivity does help stabilize the coupled fluid flow-heat transport solution. Under conditions of large flow rates, problems arise in the numerical solution of the steady-state system and instabilities (in the numerical solution) cause

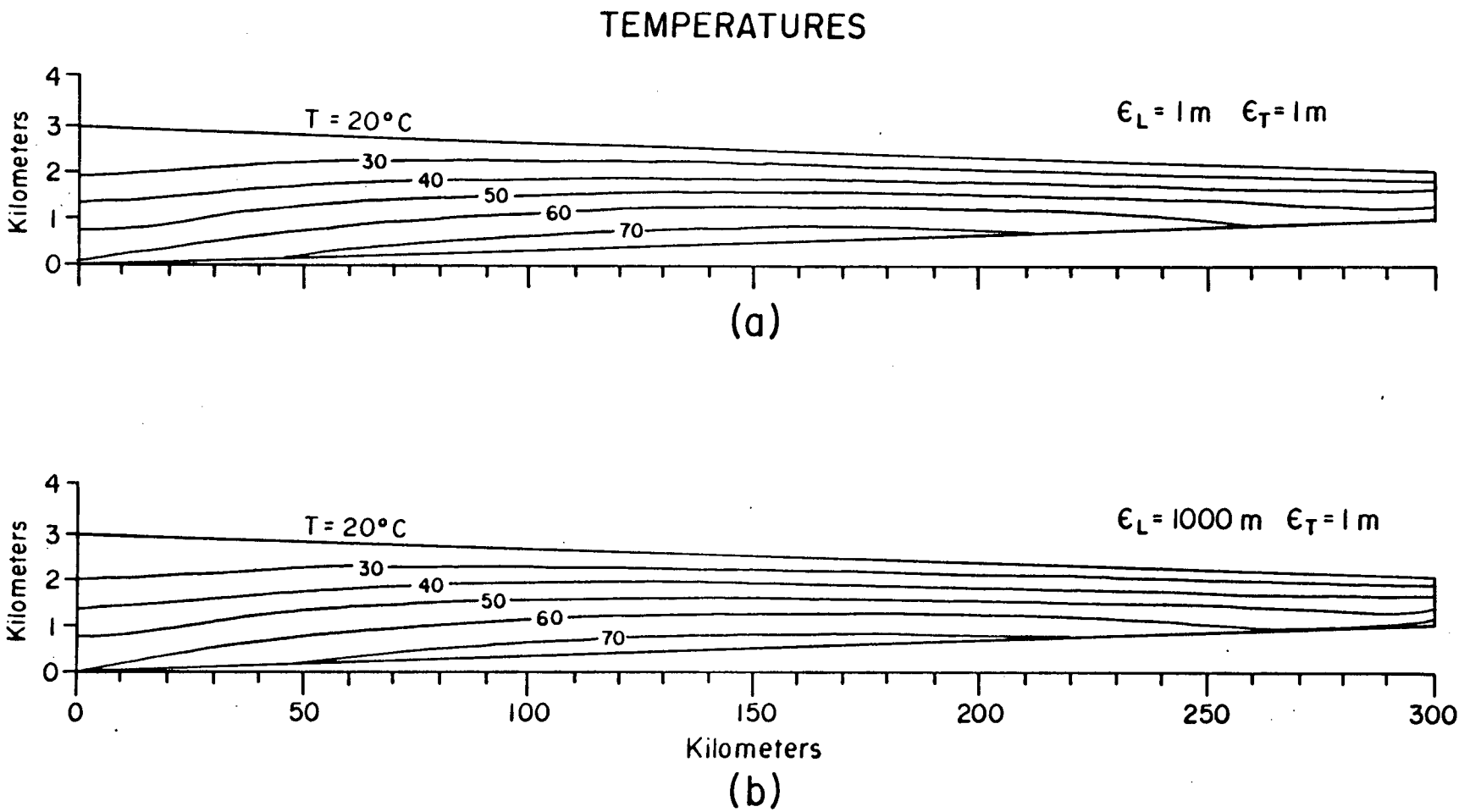

Figure 49. Temperature patterns in a two-layer basin for longitudinal thermal dispersivity values of 1 m and 1000 m.

convergence problems with the simple iterative technique used in this study. Numerical experiments show that the range of stability can be extended when longitudinal thermal dispersivity is set greater than 10 m. Figure 50 gives the results of one experiment where the longitudinal dispersivity of the basal aquifer is set equal to 500 m. The numerical solution converged to a numerically stable temperature field for hydraulic conductivities as high as 1000 m/yr. Previous simulations with longitudinal dispersivity less than 10 m could not achieve a stable solution for hydraulic conductivities above 500 m/yr. The influence of this parameter may be significant where numerical models are designed specifically to simulate heat transport in highly-fractured and karst aquifers.

Although longitudinal dispersivity has a weak influence on temperatures where vertical heat flow is dominant, transverse dispersivity can be a significant parameter. With reference to Figure 51, the transverse dispersivity in both layers is varied over the range of 1 - 50 m. In these particular simulations, K_1 = 200 m/yr, K_2 = 10 m/yr, and the basal heat flux J = 70 mW/m^2. The longitudinal dispersivity is set equal to the transverse dispersivity in all three cases. Notice that as dispersivity is changed to higher values, the amount of thermal dispersion rises, and temperatures are significantly effected. The most pronounced effect occurs in the basal aquifer because fluid-flow velocities are much greater than in the shale.

Geothermal Heat Flow

The simulations presented so far have considered a prescribed basal heat flux of 60 - 70 mW/m^2 as being representative of continental platforms. Field measurements of regional heat flow may vary from about 40 mW/m^2 in stable, granitic shields to over 120 mW/m^2 in tectonically active regions (Sass et al., 1981). Heat flow can exceed 200 mW/m^2 in some geothermal

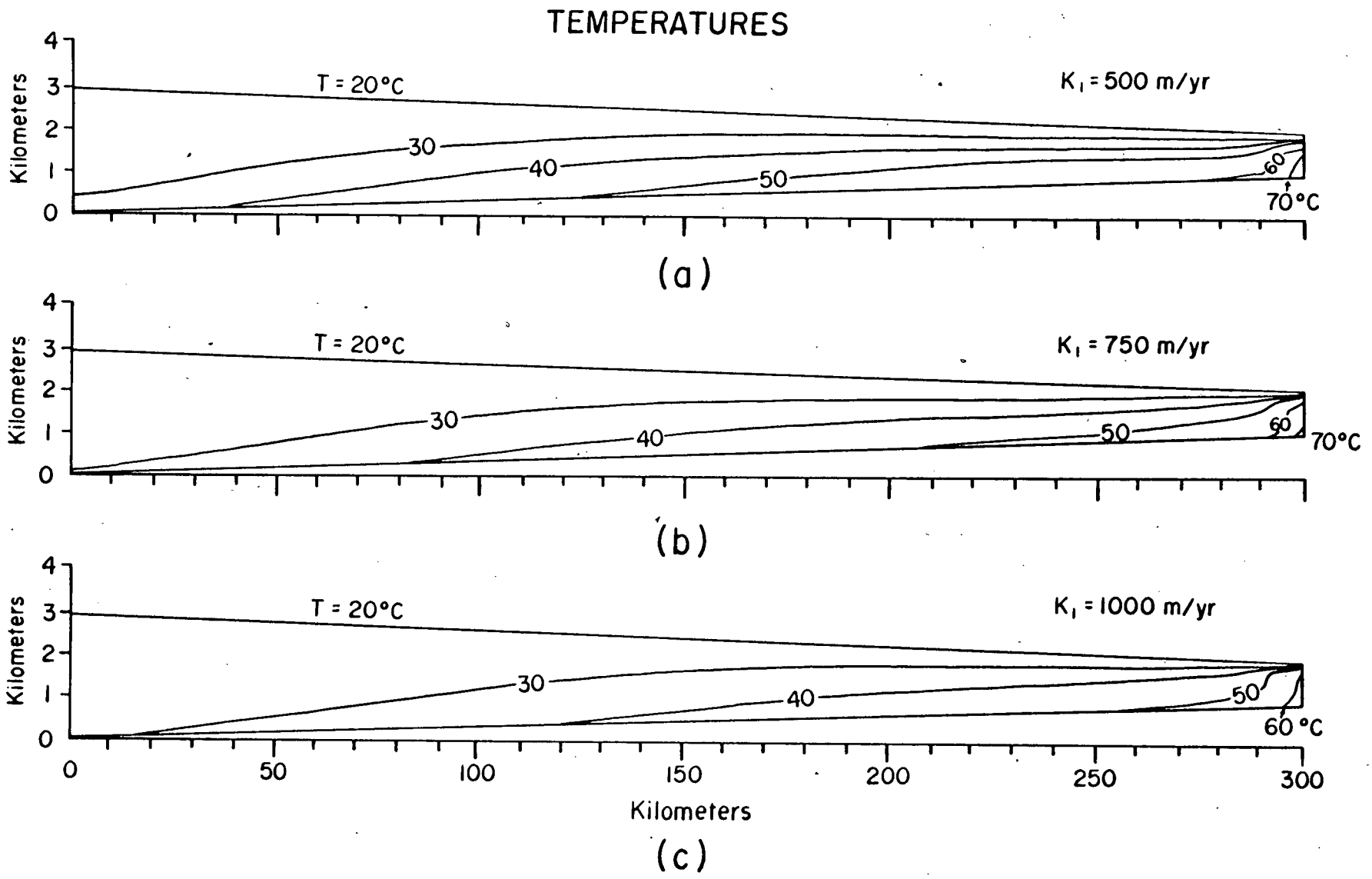

Figure 50. Effect of longitudinal dispersivity on the numerical stability of high-convection regimes.

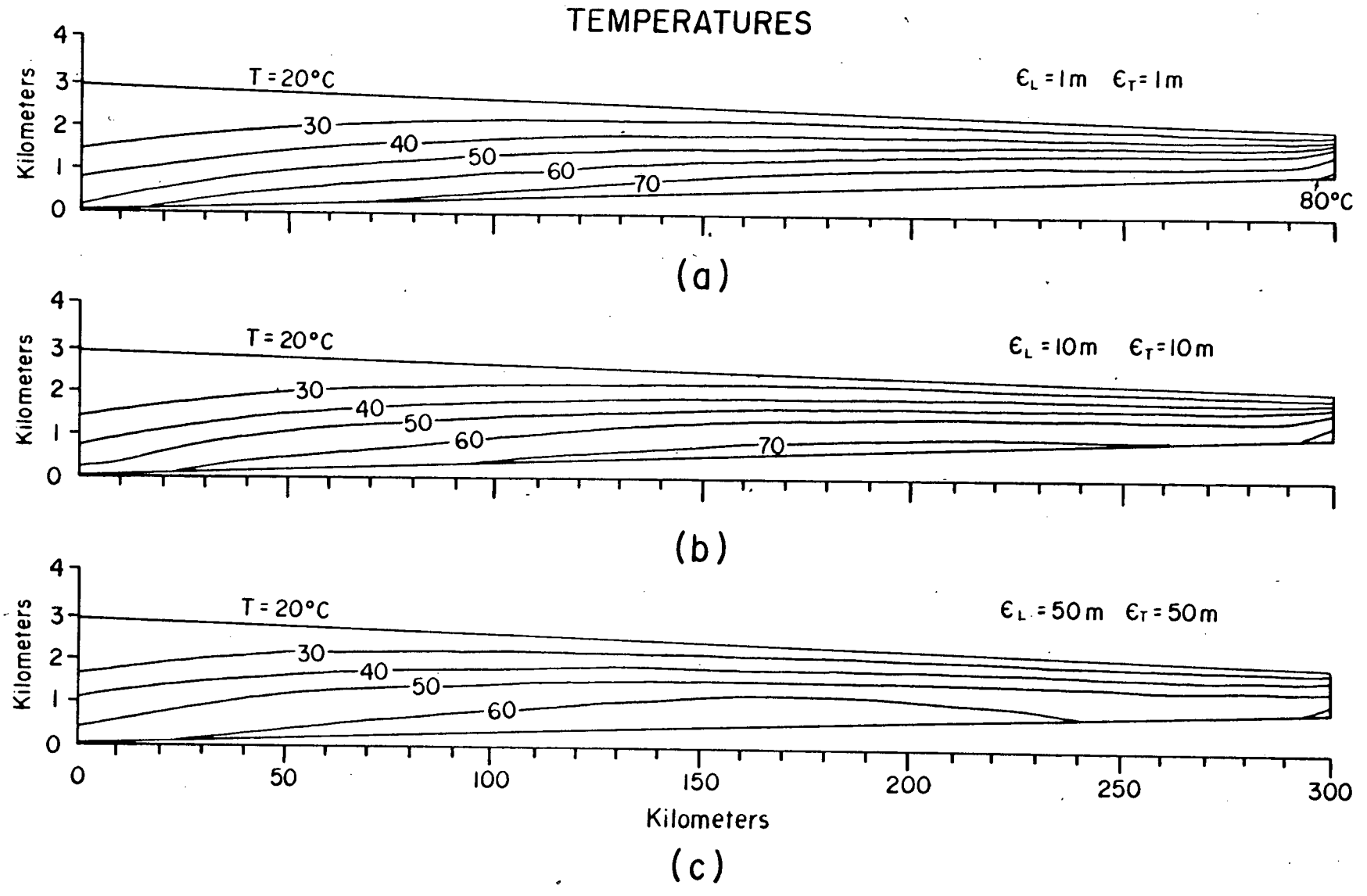

Figure 51. Effect of transverse dispersivity on subsurface temperatures.

environments.

Figure 52 shows the effect of six different values of heat flux on basin temperature patterns. The hydraulic and thermal properties of the two-layer basin are as follows: K_1 = 100 m/yr, K_2 = 10 m/yr, K_{xx}/K_{zz} = 100, ϕ_1 = 0.15, ϕ_2 = 0.10, κ_1 = 3.0 W/m°C, κ_2 = 2.0 W/m°C, and $\varepsilon_L = \varepsilon_T$ = 0.0. A salinity gradient of 0.015 % NaCl/m is also imposed across the section.

In Figure 52a, the basal heat flux is 50 mW/m^2 and the maximum temperature observed is 70°C. Doubling the heat flow to 100 mW/m^2 at the base causes temperatures to rise up to 100°C in the central part of the basin (Figure 52f). The graph of Figure 53 summarizes these results, with the temperature profile along section Z-Z′ (Figure 52b) plotted as a function of depth. Also listed on the diagram are the fluid velocities in the basal aquifer from each of the heat-flux simulations.

Intermediate heat fluxes between 50-100 mW/m^2 are probably the most realistic in stratabound ore-forming systems. The simulations in Figure 52 show that rather high geothermal fluxes would be needed in this basin model to approach the upper temperature range of 150°C, which is observed for some Mississippi Valley-type ore deposits. For lower temperature lead-zinc ores, heat flows of 60 - 80 mW/m^2 appear to be adequate for the size and thickness of the basin in Figure 52. Jessop and Lewis (1978) predicted that the maximum heat flow that a stable, continental region could sustain is about 80 mW/m^2, based on radioactivity considerations alone. This places an upper constraint, therefore, on geologically reasonable values of geothermal flux in our basin model. Unless heat convection is greater than in Figure 52, temperatures will not exceed 80°C near the basin margin (Figure 53).

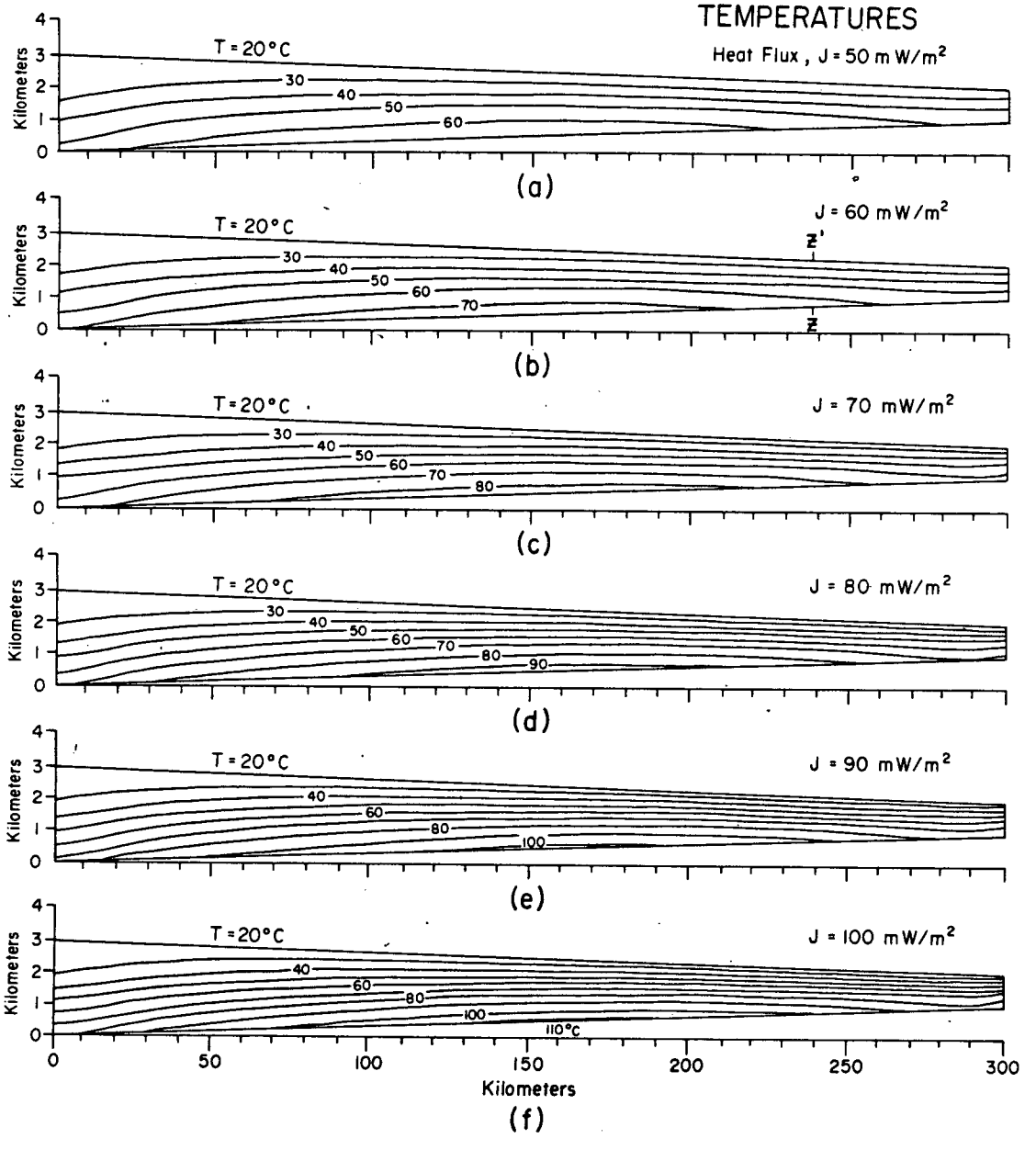

Figure 52. Effect of the geothermal heat flux on subsurface temperature.

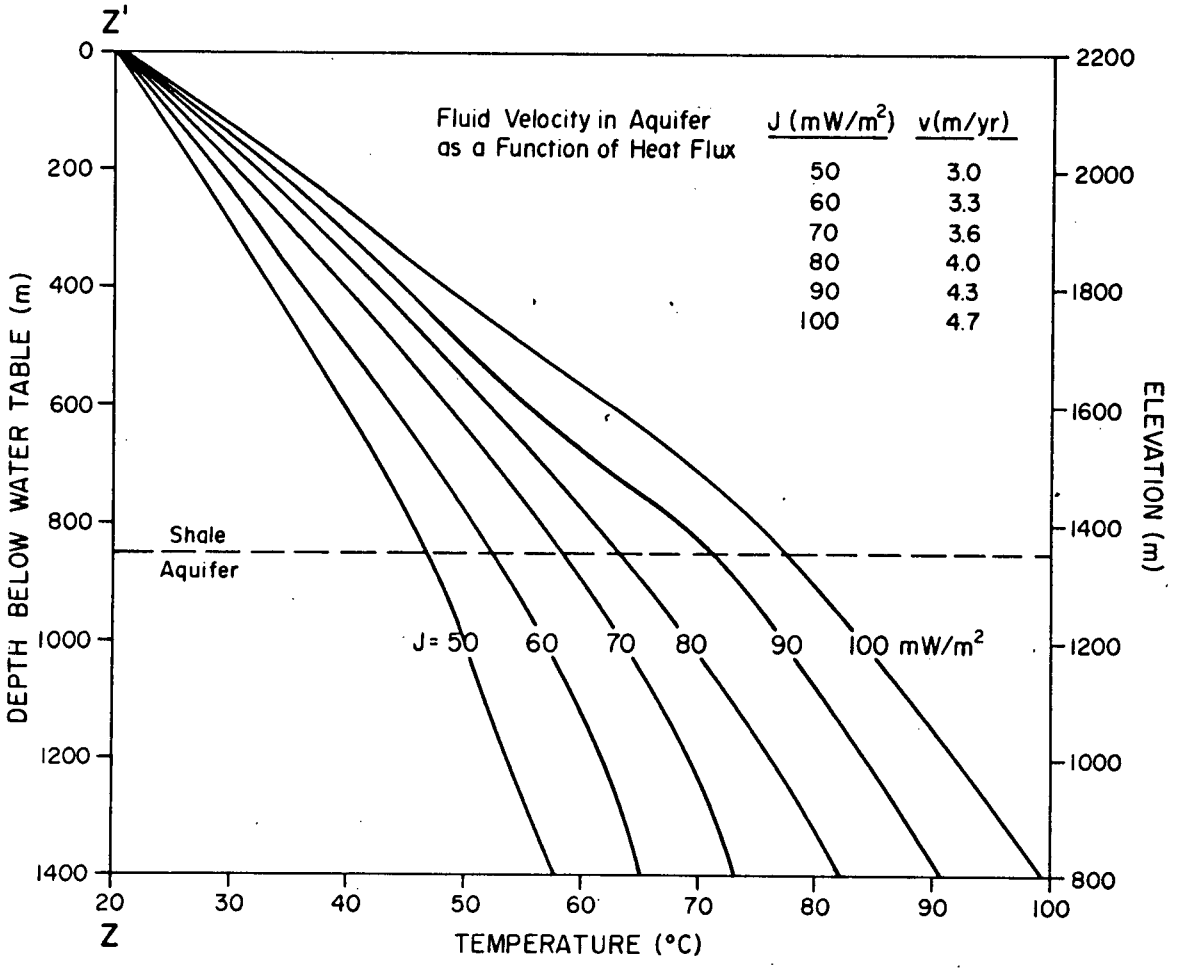

Figure 53. Temperature profile in the shallow end of the basin as a function of the geothermal heat flux.

Climate

Climatic conditions are included in the heat-flow model through the specification of the temperature T_0 on the water-table boundary. For simplicity, the same mean annual surface temperature is prescribed over the entire length of the basin. Figure 54 demonstrates the control of the water-table temperature on the simulated temperature pattern. The geothermal flux is 60 mW/m^2, and other model parameters are the same as the preceding model.

Changing the surface temperature by $10^{\circ}C$ causes a general numerical change in each isotherm by $10^{\circ}C$, although the effect is not perfectly linear. If we are willing to accept a heat flow of 80 mW/m^2 as an upper limit, then the maximum temperature in the basin model ought to range between $85^{\circ}C$ and $105^{\circ}C$ for the surface-temperature range of $10^{\circ}C$ to $30^{\circ}C$. Climatic conditions were apparently favorable for this surface temperature range during Devonian to Tertiary time in the North American continent.

Basin Geometry

In this section, a review of the effects of basin size, structure, and water-table configuration are presented. Some of the temperature plots are obtained from the same simulations that were presented in the preceding section on fluid-flow. Reference to Figures 33 to 44 can be made for the accompanying fluid-flow patterns. A basal geothermal flux of 60 mW/m^2 and a constant surface temperature of $20^{\circ}C$ are assumed in most of the models given below. The hydraulic and thermal properties of the two-layer basin model have not been changed.

The effect of basin size on subsurface temperature is shown in Figure 55. The length-to-depth ratio of each basin is 100:1. Unlike the fluid-flow problem of Figure 33, the velocity field is no longer the same in each basin because of the coupling between temperature, salinity, and the fluid

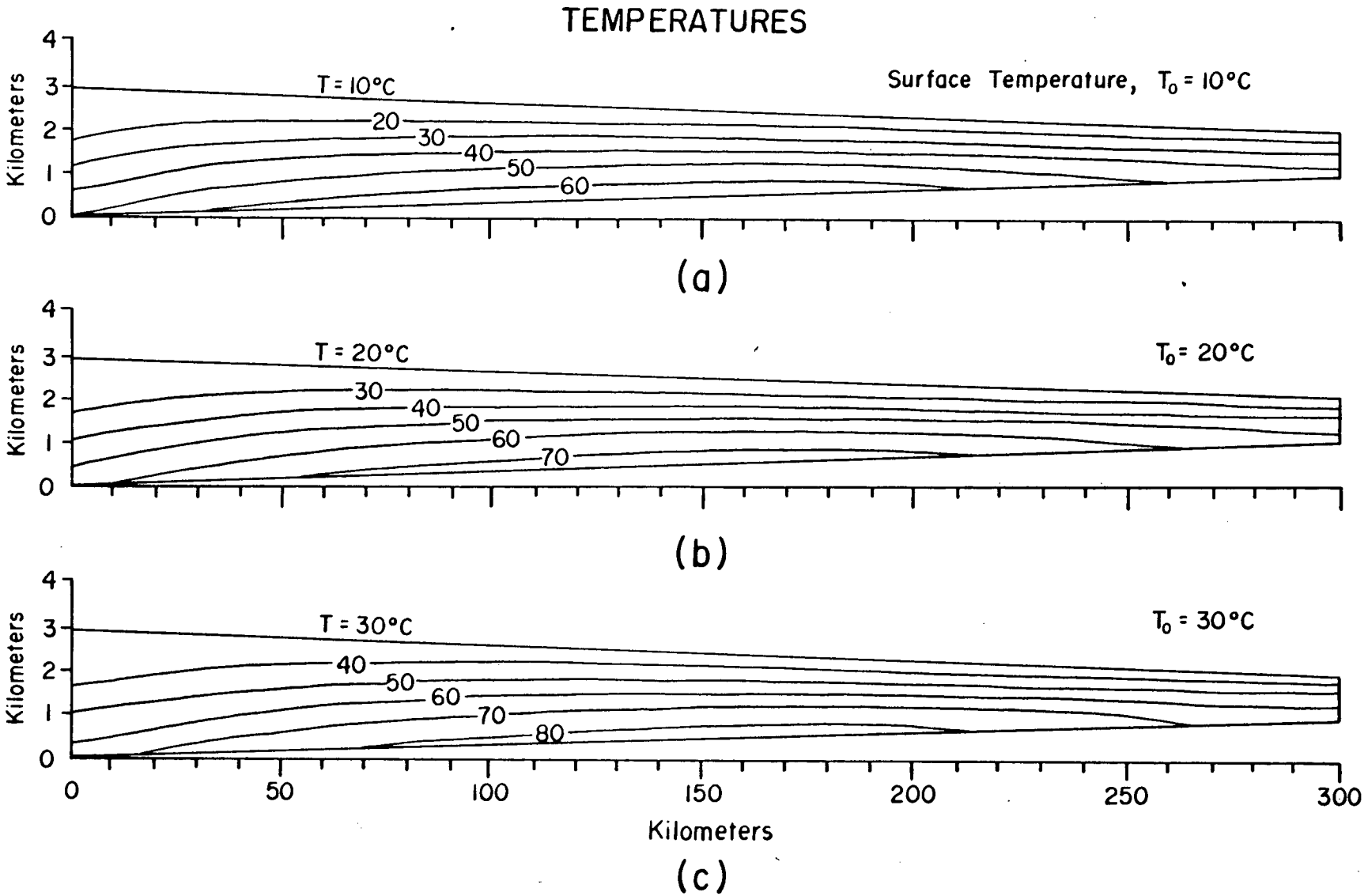

Figure 54. Effect of the prescribed water-table temperature on regional temperatures.

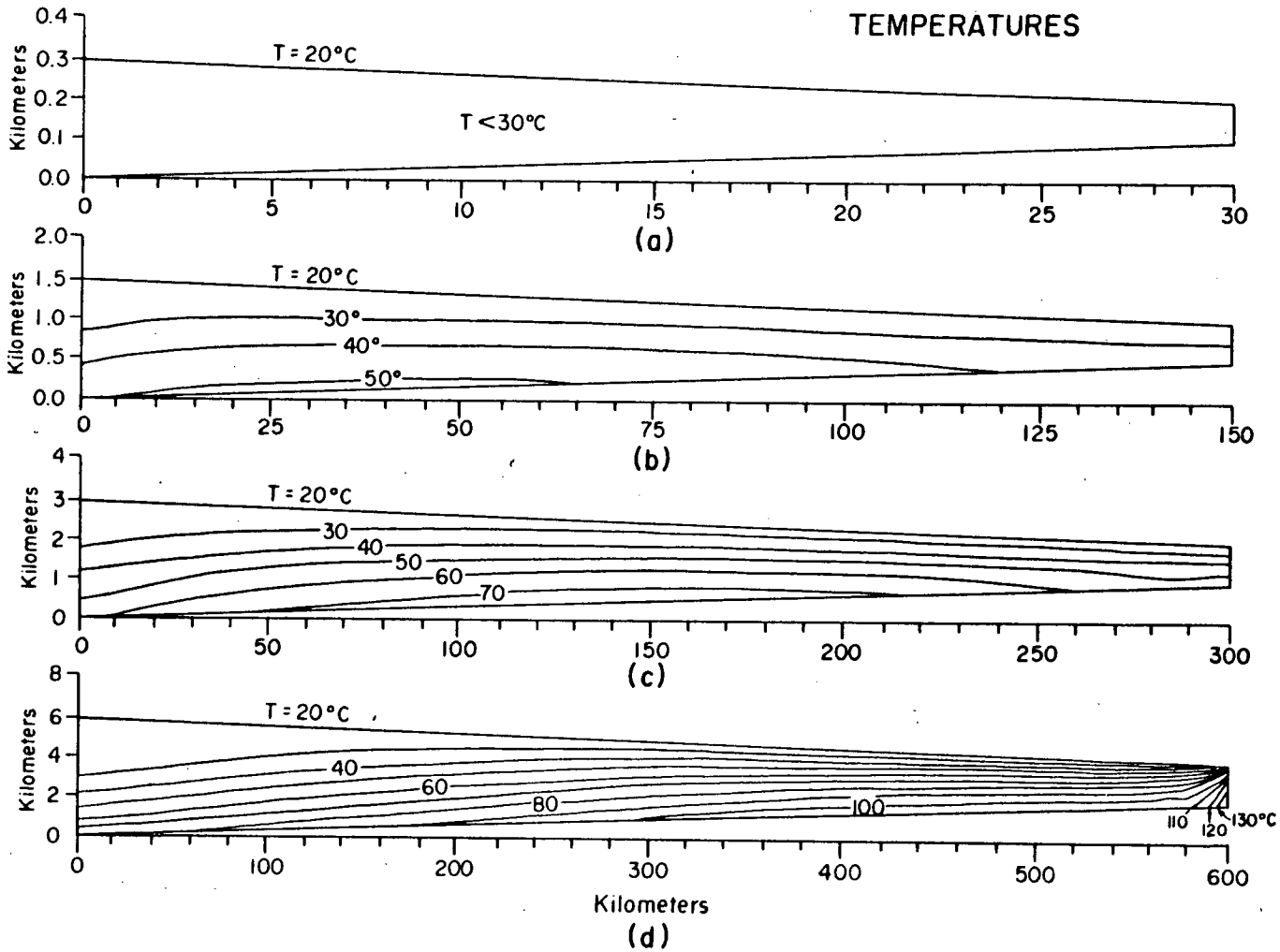

Figure 55. Control of basin size and thickness on subsurface temperatures.

properties. Velocities in the basal aquifer of Figures 55a, 55b, and 55c are all around 2.5 m/yr, but velocities reach values as high as 7.2 m/yr in the 600 km-long basin (Figure 55d). Temperatures easily exceed 100°C at the downstream end of this large basin. Perhaps it is this scale of flow system, with fluid circulation to depths of 6 km, that is responsible for the formation of lead-zinc ores at the high end of their temperature range (100° - 150°C), as in the Mississippi Valley district. A higher geothermal gradient of 80 mW/m^2 and surface temperature of 30°C could push temperatures above 150°C in the discharge end of the basin.

The influence of basement structure on the thermal regime is illustrated in Figure 56. Once again the two-layer basin is used for the demonstration, and the material properties are the same as before. Three cases are modeled; a flat bottom, sloping bottom, and basement arch on a sloping bottom.

Temperatures in the flat-bottom model are much higher at the discharge edge of the basin than the sloping, wedge-shape basin because the stratigraphic section is nearly twice as thick. The presence of a basement arch forces heat to be convected up over the structure, and thereby produces a steep, geothermal gradient on the upstream side of the ridge and a lower gradient on the downstream side. Higher relief on the structure accentuates the thermal anomaly.

All of these features are more clearly illustrated by the graph of Figure 57. It is a plot of temperature in the basal aquifer as a function of distance along the basin. Notice how effective the basement arch is at reducing the convective transport of heat from the thick part of the basin to the thin basin margin. This feature bears out the importance of long, continuous flow systems in the development of adequate temperatures at shallow depths and near the margin of a basin. On the other hand, basement arches

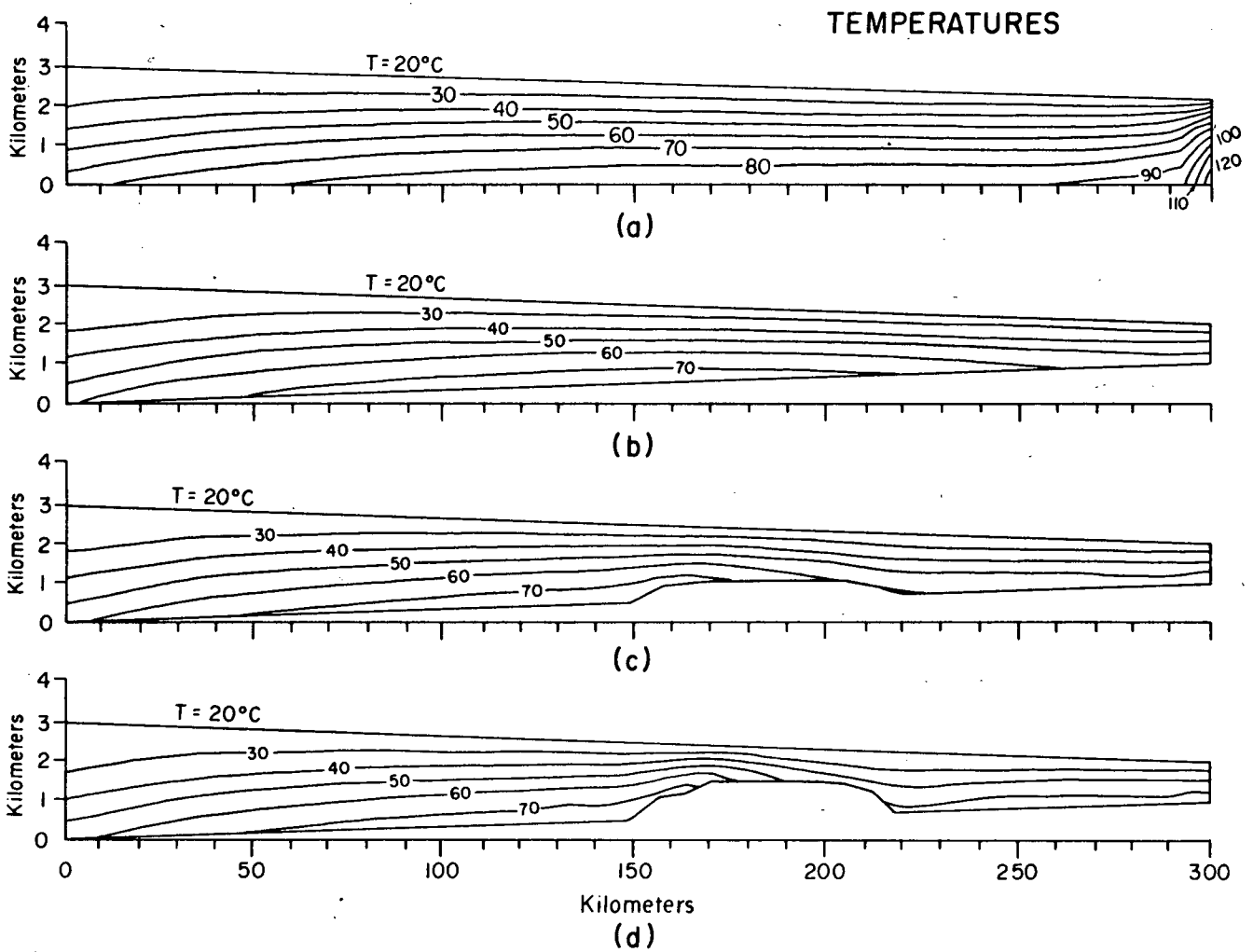

Figure 56. Control of basement structure on subsurface temperature.

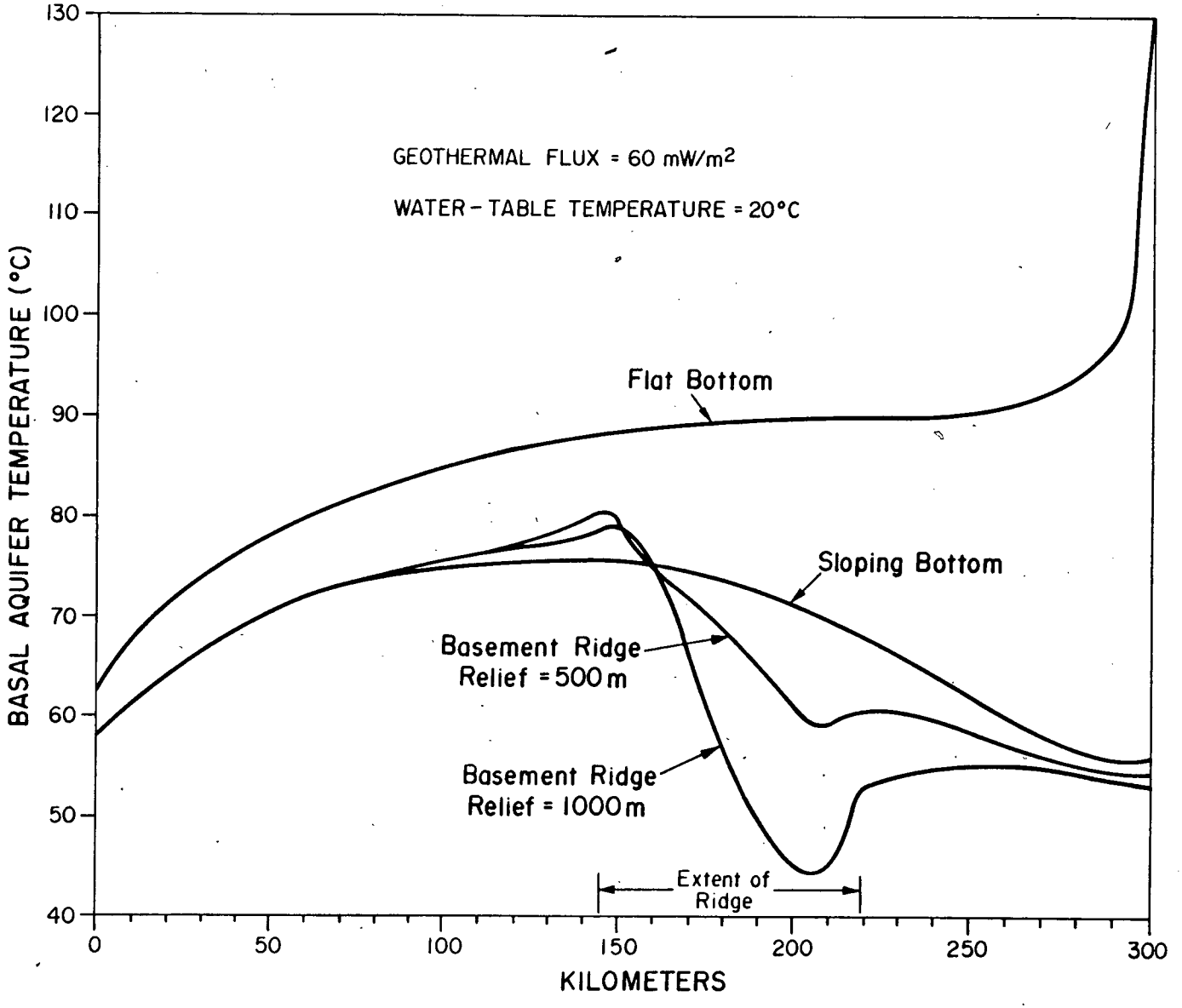

Figure 57. Temperature along the basal aquifer as a function of basement structures.

between major sedimentary basins may themselves serve to form suitable conditions for ore genesis (e.g. Figure 56d). Remember that the absolute temperatures in Figure 57 could be 10°C to 30°C greater, under warmer climatic conditions or higher geothermal heat flow.

Figure 58 displays the effect of topography on temperature patterns in the sloping-bottom basin. The slight break in topographic slope in Figure 58a appears to have little influence on the thermal regime. Introducing a water-table ridge at the end of the basin has a greater effect on bending the isotherms near the topographic depression. Upward discharge of groundwater is well illustrated by the thermal perturbations shown in Figures 58c and 58d. Major topographic lows serve to focus groundwater discharge, which can create anomalously high temperatures at shallow depths. A complicated water-table configuration is reflected by irregular perturbations on the isotherms, as shown in Figure 58e.

It is apparent from these simulations that major topographic features within a basin serve to form zones of downward heat convection in recharge areas and upward heat convection in discharge areas. As in the case of fluid flow, the heat-transport system can be weakly or strongly modified, depending on topographic relief, basin size and structure, and material properties of the hydrostratigraphic units. The genetic association between anomalously high temperatures and lead-zinc ores is clearly linked to groundwater-discharge features.

Factors Controlling Mass Transport

As a metal-bearing brine flows through a basin the concentration will vary along the flow path. This variation can be caused by a number of geochemical and hydraulic processes. In the absence of mixing or geochemical reactions, the solute will travel at a rate equal to the average linear

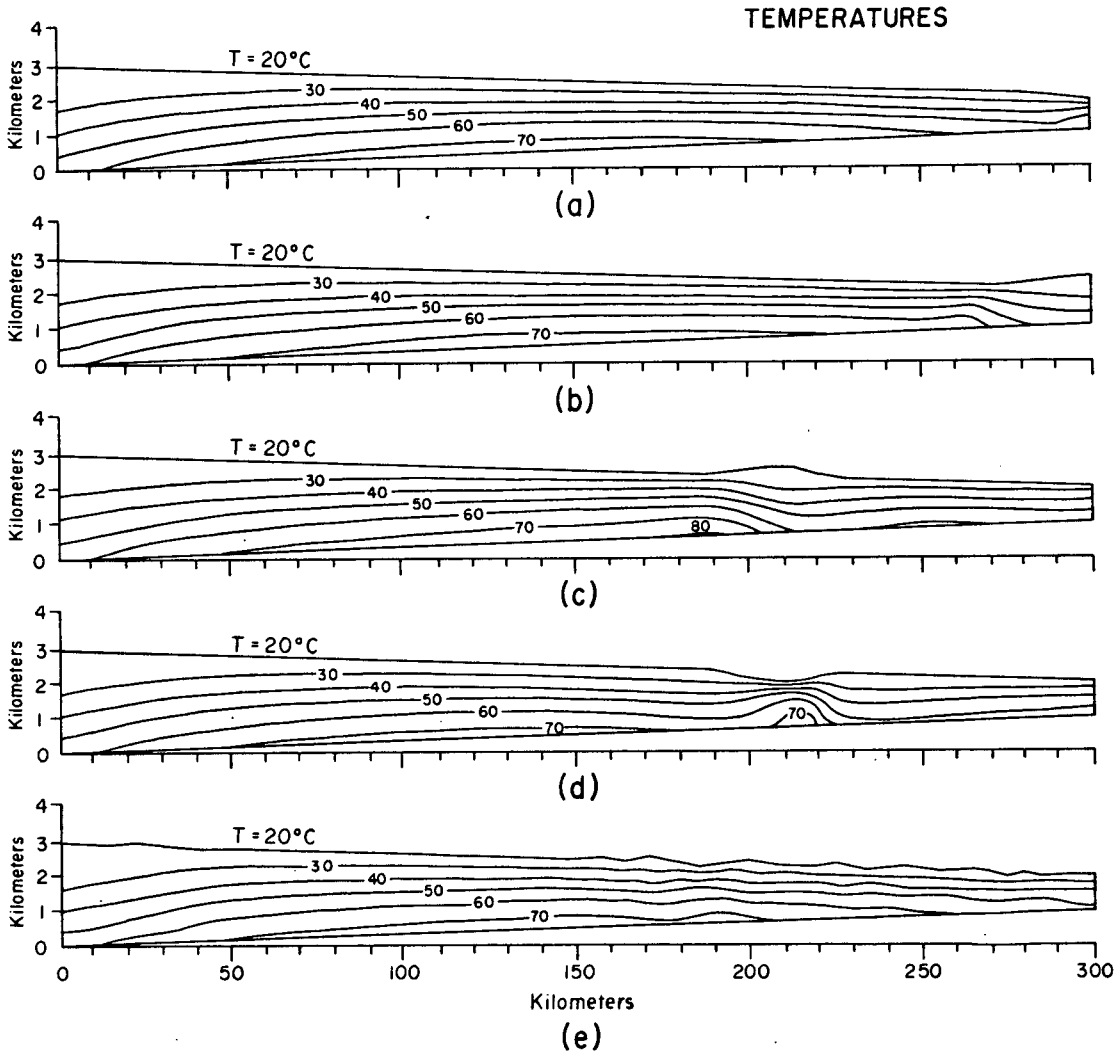

Figure 58. Control of water-table configuration on subsurface temperature.

velocity of the groundwater and the concentration will remain unchanged. Solute transport in porous media is not, however, this simple. Even in a nonreactive medium, the processes of mechanical mixing and molecular diffusion casue the solute to spread away from the flow path and decrease the original concentration of the aqueous component. This spreading phenomena is better known as hydrodynamic dispersion, which was mathematically described in previous chapters.

This study is not the first to consider the general factors affecting mass transport in groundwater-flow systems. Pickens and Lennox (1976), Schwartz (1977), and others have established the importance of dispersion through sensitivity analyses of modeling parameters.

The simulation results given here provide a review of the factors affecting mass transport, but on the scale of a large sedimentary basin and in relation to ore genesis rather than groundwater contamination. Many of the concepts, which are directly dependent on the advection patterns of mass, are already self-evident from the fluid-flow patterns presented earlier. For this analysis, attention is directed to the specific problem of understanding how the concentration of an ore-forming component reaching a depositional site depends on the original concentration in the source-bed area, the length of the flow path, the rate of flow, and the degree of dilution caused by dispersion along the flow path. This type of information is needed when making reasonable estimates of the metal concentrations in a brine passing through an ore-forming site.

The transport models given here do not simulate the geochemical process of releasing metals from source bed to the fluids. Instead, they simply assume that a certain metal concentration exists at a specified location and initial time. The goal is to follow the path of a metal-bearing

fluid packet as it travels through the basin to a discharge area, and show how the concentration is affected by the fluid-flow system. Although when reference is made to the solute it is usually meant to describe a metal species, the modeling results are equally valid for any aqueous species, including sulfide.

All of the simulations previously shown are, in one way or another, useful to the understanding of mass transport in sedimentary basins. The flow patterns tell us how metal species would be advected through the basin, and therefore place constraints on where an ore deposit could form or from what source beds an aquifer could 'drain' an adequate supply of metals. The possible combination of fluid-flow factors affecting the advection of a solute are numerous. Figures 7 and 8, and 16 through 44 give a wide selection of the types of flow patterns that can exist in sedimentary basins, and how they can regulate the possible locations of ore deposition. The flow velocities from these simulations add quantitative criteria to the assessment by determining travel times, mass-flux rates, and the time required to deposit a large ore body for a given concentration value.

In this section, the emphasis is placed upon the quantitative aspects of mass transport. Three controlling factors are examined in detail: hydraulic conductivity, permeability contrasts in layered basins, and dispersion.

Hydraulic Conductivity

Consider the simple, two-layer basin with a sloping basement and linear water-table slope. The fluid-flow and heat-flow solutions were given in Figure 31. Groundwater flow is directed downward across the shale beds in the elevated end of the basin; it flows laterally through the basal aquifer and shale aquitard in the mid-section of the basin; and it is forced

upward across the shale unit near the basin margin. The flow pattern remains nearly the same for any fixed contrast in the hydraulic conductivities between the layers, but the fluid velocity depends on the actual value of the hydraulic conductivities and the size of the basin, as shown earlier.

The effect of hydraulic conductivity on transport times and concentration patterns is easily determined. Figures 59 and 60 summarize the results of some simulations designed for this purpose. For the model shown in Figure 59 the parameter values used are as follows: the carbonate aquifer - K_1 = 80 m/yr, ϕ_1 = 0.15, K_{xx}/K_{zz} = 100, κ_1 = 3.0 W/m^{o}C, ε_L = 10 m, ε_T = 1 m, α_L = 10 m, α_T = 1 m, and the shale aquitard - K_2 = 4 m/yr, ϕ_2 = 0.10, K_{xx}/K_{zz} = 100, κ_2 = 2.0 W/m^{o}C, ε_L = 10 m, ε_T = 1 m, α_L = 1 m, α_T = 1 m. A salinity gradient of 0.10 % NaCl/m is also present. A surface temperature of 10°C is placed on the water-table and a geothermal flux of 70 mW/m^2 is prescribed on the bottom boundary. The dispersivity coefficients α_L and α_T also affect mass transport, but the effects of these parameters are reserved for later consideration.

Only the relative solute concentrations at four-different time steps and the steady-state velocity-vector field are shown in Figure 59. The relative concentration values of 5%, 10%, and 15% of the source are represented by the contours in Figure 59b. That part of the plume with relative concentrations greater than 15% of the source value is shaded. The units of concentration are arbitrary. At the source location, a pulse of metal species is introduced so as to produce an initial concentraion of C_0 in the brine at time t = 0. The position and concentration pattern of the pulse is shown at times of 50,000, 75,000, and 100,000 yr. By t = 200,000 yr, most of the original mass released has been transported through the basin, and it has been discharged to the land surface.

It should be emphasized that Figure 59 represents a single <u>numerical</u>

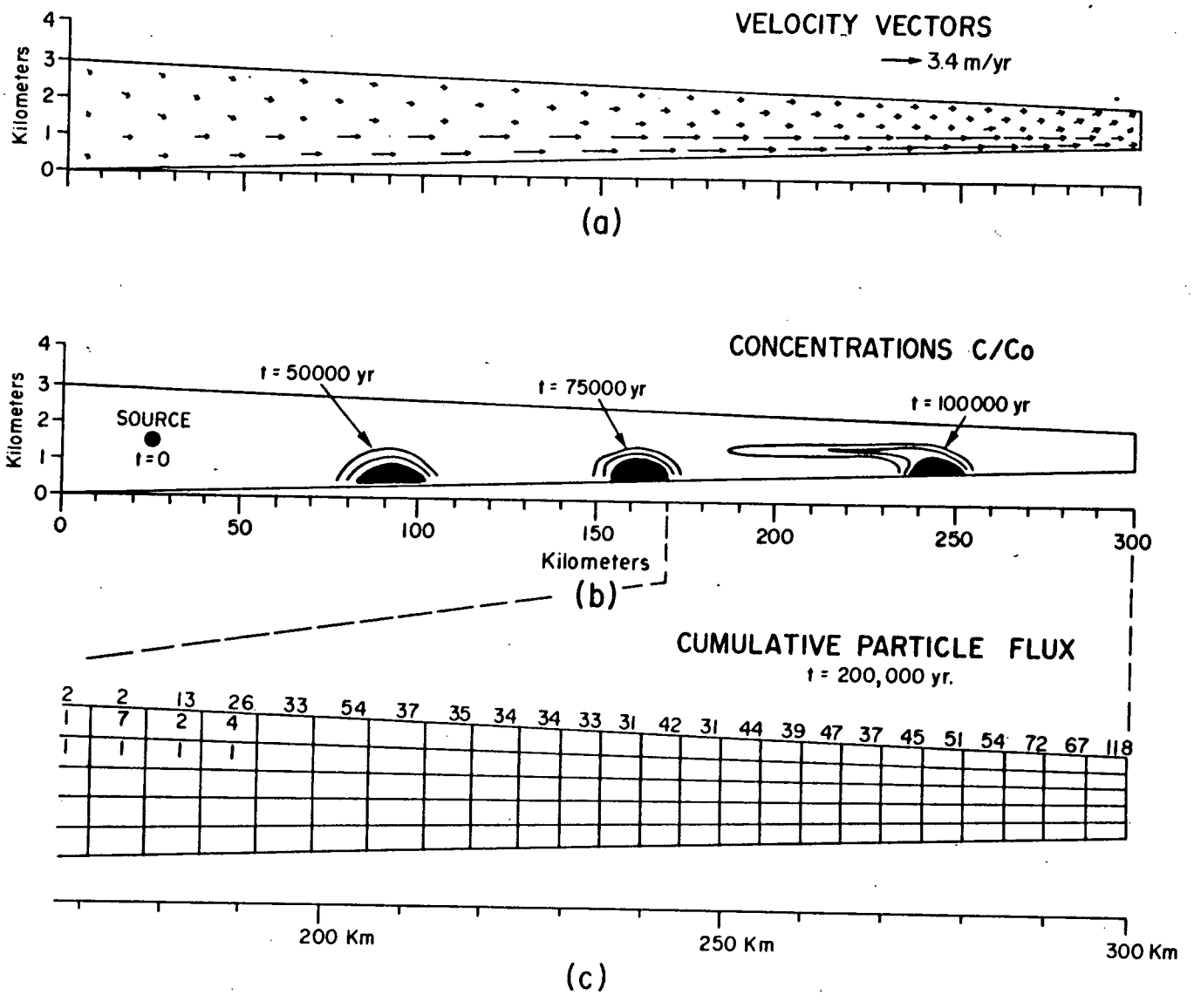

Figure 59. Mass transport pattern in a two-layer basin.

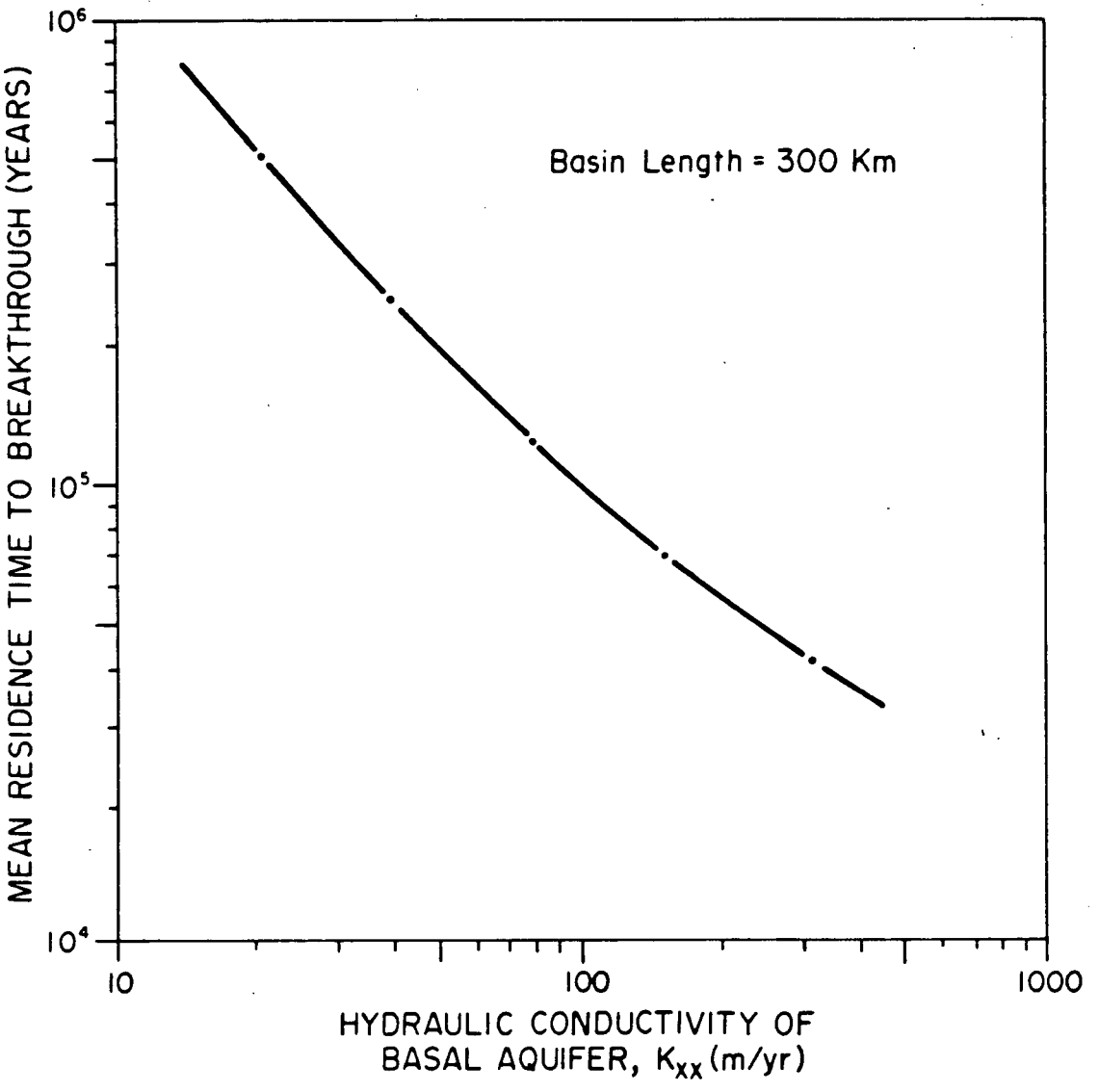

Figure 60. Relationship between the average basin-residence time for a metal-bearing pulse and the hydraulic conductivity of the basal aquifer, in a two-layer basin.

event of metals entering the flow system and being transported through the basin. This is not to imply that ore formation is the results of a single pulse of metal-bearing brine, or even a set of discrete pulses. The representation in Figure 59 is simply a mathematical device for estimating the concentration levels in a fluid as it continuously flows through the basin.

As fluid passes through the shale bed and into the basal aquifer, in the recharge end of the basin, a substantial amount of mixing occurs. After 50,000 yr, the pulse has travelled nearly one-third of the basin length, mostly through the aquifer. The maximum concentration in the pulse C_{max} is now only about 40% of the source concentration C_0. The pulse is at a mid-position in the basin at 75,000 yr, and C_{max}/C_0 has dropped to about 35%. As the brine moves updip toward the shallow end of the basin, upward fluid discharge begins to influence concentrations. This is marked by the trailing 'tail' of the pulse at t = 100,000 yr. Leakage of mass up into the low-permeability shale is responsible for this feature. Mass in the shale unit moves much slower than in the aquifer (Figure 59a) and as a result the concentration plume takes on a stretched-out appearance. However, a large portion of the mass continues its route through the permeable aquifer and eventually is forced to surface at the end of the basin. The leakage of mass into the overlying shale produces a dispersed zone of mass discharge between x = 200 km and x = 300 km.

The nature of the discharge distribution is best documented by Figure 59c, which expands the view of the discharge end of the basin at t = 200,000 yr. As explained in the last chapter, the numbers plotted on the top of the water table represent the cumulative particle flow leaving the mesh through the upper row of cells. This cumulative particle distribution is obtained by tallying the location of the particle as it is naturally

ejected from the mesh in the moving-particle random-walk numerical procedure. Much of the particle flux from the cells between x = 250 km and x = 300 km are transported mainly through the aquifer and are discharged relatively early, as compared to the rest of the particle distribution, which arrived much later because of its longer path through the shale aquitard. Although the time distribution of particle flux is not shown, the cumulative distribution does produce a type of spatial histogram that shows how mass is discharged at the basin margin.

Keeping other parameters constant while varying hydraulic conductivity causes transport times to increase or decrease according to the direction of change in the hydraulic conductivity. Doubling the permeability means that the transit time of a pulse will be halved. Figure 60 shows the nearly linear relationship obtained for the two-layer basin model. Hydraulic conductivity is plotted against the observed time needed for the center of mass of the pulse to break through to the water-table surface at the downstream end of the basin.

Concentrations in the metal-bearing pulse decrease along the flow path (Figure 59b). Higher flow rates should lead to greater dispersion in a flow system, but little change is observed in the mass-transport pattern when hydraulic conductivity is varied over the range shown in Figure 60. Figure 61 displays the results of several simulations from which the maximum pulse concentration in the basal aquifer C_{max}/C_0 is plotted as a function of distance. The solid curve is drawn to indicate the general trend of the solute concentration in a schematic form. It is obvious that dispersion can significantly reduce the amount of metal reaching an ore-forming site near the edge of a basin. In the two-layer basin, about 20% of the source-bed concentration is present in the fluid as it passes through the aquifer at

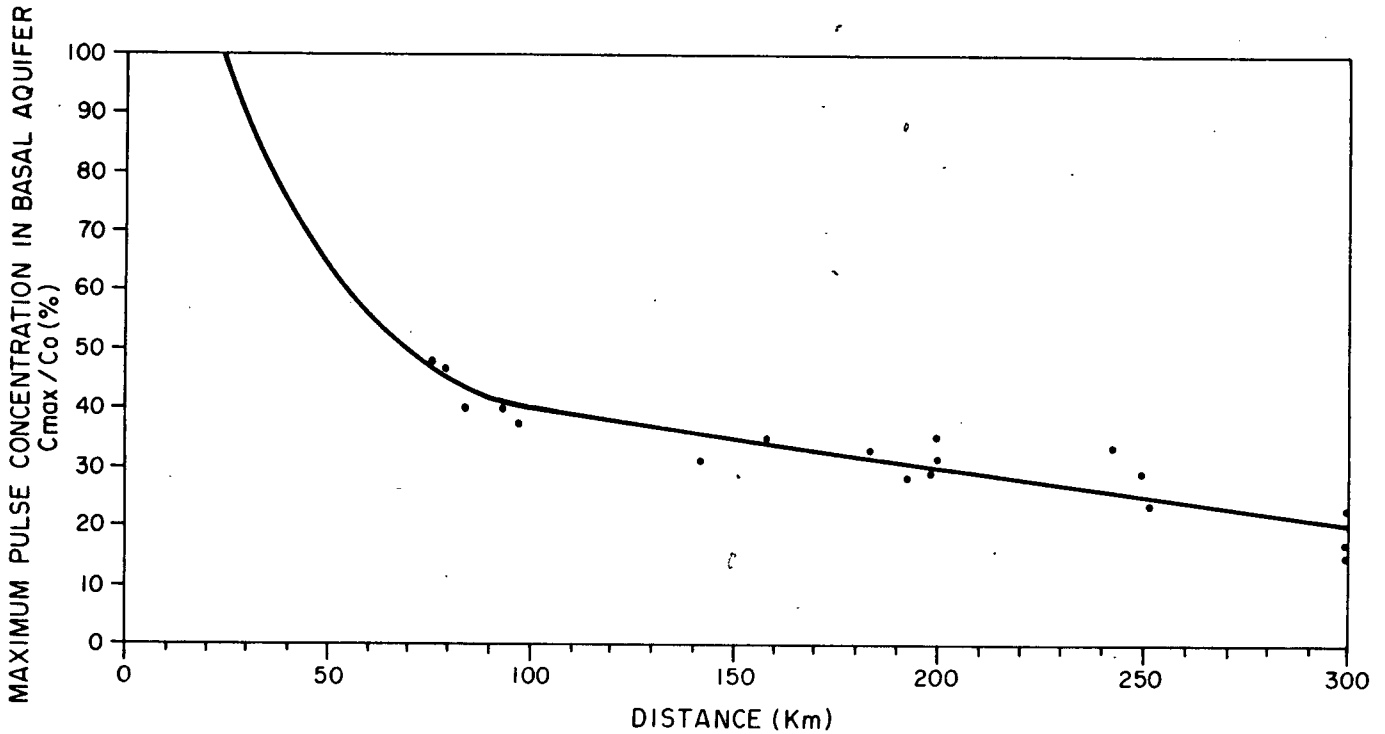

Figure 61. Maximum solute concentration in the basal aquifer as a function of transport distance.

the basin margin.

The degree of hydraulic-conductivity contrast between the layers determines the vertical flow rates and the area over which cross-formation flow occurs, as shown earlier in Figure 20. One would expect in an aquifer-aquitard system, with a high ratio of hydraulic conductivity contrast K_1/K_2, that the discharge of mass would be spread over a narrow area at the downstream end of a basin because of the enhanced focusing of flow into the aquifer. Figure 62 shows some simulation results that demonstrate the sensitivity of the mass-discharge pattern to the hydraulic-conductivity ratio K_1/K_2. These histograms are constructed from the type of particle-flux distribution given in Figure 59c. The particle mass counted at the water table is simply expressed as a percentage of the total mass of the original pulse. High K_1/K_2 ratios appear to limit the area of mass discharge, relative to low ratios, but the influence is not strong. In Figure 62c, the mass is more evenly distributed in the discharge-half of the basin than in the cases of lower ratios (Figure 62a and 62b). Leakage of mass into the overlying shale is less in the low-ratio cases because the component of upward flow is smaller.

It is difficult to assess the importance of the mass-discharge distribution in controlling ore-precipitation patterns in carbonate-hosted lead-zinc deposits, mainly because ore occurrence is commonly confined to karstic aquifers. However, modeling of this type may have application in other types of stratabound ore deposits. As an example, Figure 63 is a schematic cross section through the Lake Superior basin at the time of formation of the White Pine copper deposit. The geology and copper content of the Nonesuch Shale are obtained from the study by White (1971). The conceptualized fluid-flow pattern is based on an interpretation of the gravity-driven groundwater model proposed by White (1971) to explain copper mineralization in the Nonesuch

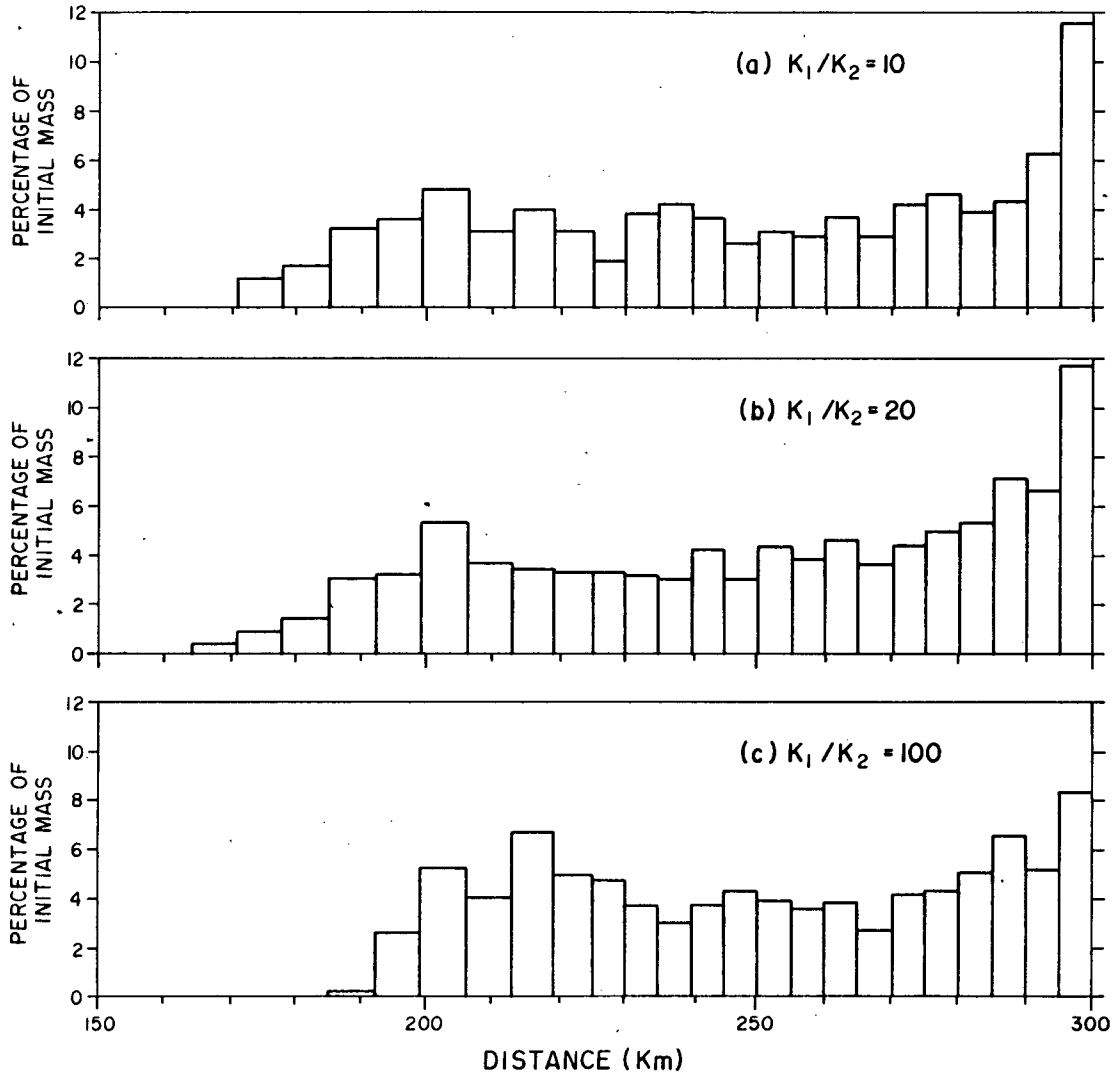

Figure 62. Effect of hydraulic conductivity contrast between aquifer K_1 and aquitard K_2 on the mass-discharge pattern at the water table.

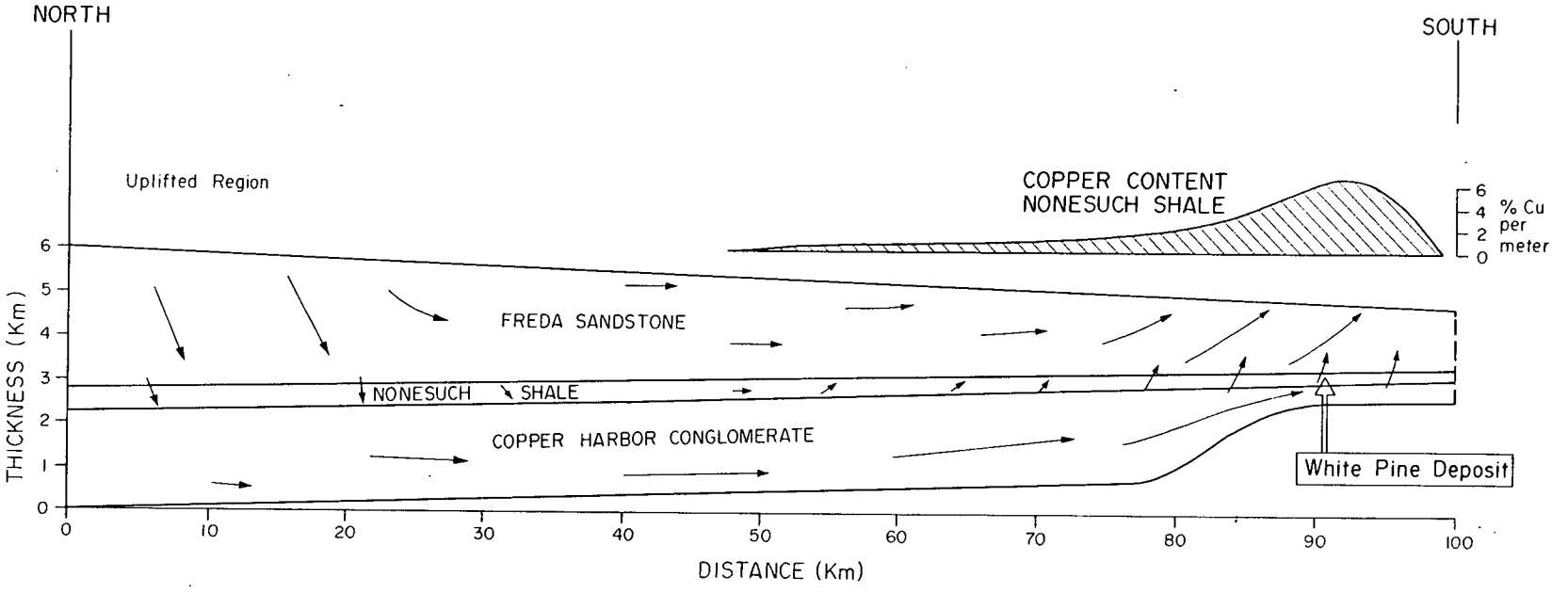

Figure 63. Copper content of the Nonesuch Shale and conceptual model of fluid flow in the Lake Superior basin at the time of formation of the White Pine copper deposit (modified after White, 1971).

Shale at White Pine, Michigan. Copper-bearing fluids flowed through the basal conglomerate aquifer toward the edge of the Lake Superior basin, and were eventually forced upward and through the shale beds. Copper precipitation was caused by replacement of pre-existing iron-sulfide minerals in the shale (Brown, 1971). Notice that the copper-content profile (Figure 63) is comparable to the mass-discharge patterns of Figure 62. The presence of a widespread reactant (i.e. pyrite) allows the development of a well-defined mineralization pattern, with maximum deposition where upward flow rates were probably the greatest. The localization at White Pine may be due to the presence of the basement arch, which served to focus upward discharge, as in Figures 37 and 38. It could also be argued that the wide spread of the copper mineralization may indicate that the hydraulic conductivity contrast between the two main hydrostratigraphic units in the basin, the Copper Harbor Conglomerate and the Freda Sandstone, was not great.

Dispersivity

Dispersion is a mixing process that results in the spreading of a solute in both a longitudinal and lateral direction with respect to a flow path. It is caused by the combined action of molecular diffusion, microscopic variations in fluid velocity, and changes in velocity from bed to bed. In geologic systems such as large sedimentary basins, it is the large-scale dispersive processes that are most significant. The mathematical expression for dispersion lumps all of these processes together as two coefficients: the longitudinal dispersion coefficient D_L and the transverse dispersion coefficient D_T. Equation (4-21) shows how each coefficient consists of two components, a term representing the medium dispersivity times the velocity, and a term representing the effective molecular diffusivity. The dispersivity is a

function of the medium and the aqueous species.

Diffusion coefficients for aqueous species commonly range from 10^{-9} to 10^{-12} m^2/s in porous media (Freeze and Cherry, 1979). Compared to mechanical dispersion, diffusion is several orders of magnitude smaller. Its effect on mass transport is relatively small, unless hydraulic conductivity is very low. A constant value of diffusivity of 10^{-10} m^2/s is used in this study, but in all cases its effect is negligible.

In preceding simulations, a longitudinal dispersivity α_L of 10 m and a transverse dispersivity α_T of 1 m are assumed for the aquifer layer. Dispersivity is set at a constant 1 m for both components in the overlying shale. These numbers are assumed to be representative of this basin. Unfortunately, there is little data available on dispersivity coefficients in natural environments. Observed and model-calibrated data collected to date indicate a dispersivity range of 0.01 to 100 m (Anderson, 1979). The actual value of dispersivity chosen usually reflects the nature and scale of heterogeneities in the flow system. Representative values for the basin being modeled in this study are thought to range between 10 m and 500 m for the longitudinal coefficient. The transverse dispersivity is expected to be lower in value by a factor of 1 to 100. Further details on dispersion in porous media can be found in Anderson (1979). Table 11 summarizes her findings for the range of dispersivity of common geologic materials.

To test the sensitivity of the two-layer basin to the dispersivity parameters, a series of simulations have been run where these coefficients are varied. All other parameters are kept constant. The basal aquifer is assumed to have a horizontal hydraulic conductivity of 200 m/yr and a porosity of 0.15. The overlying aquitard has a horizontal hydraulic conductivity of 10 m/yr and a porosity of 0.10. An anisotropy ratio of horizontal to

Table 11. Longitudinal dispersivity range of geologic materials.

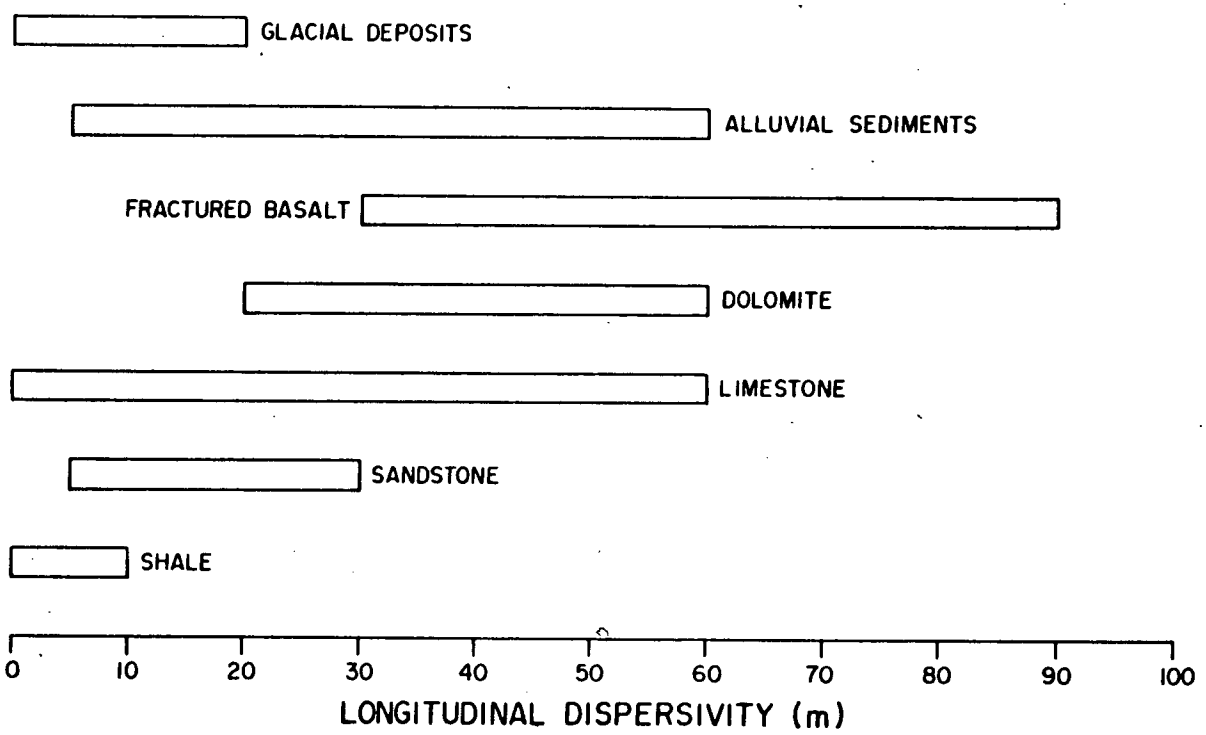

vertical hydraulic conductivity of 100:1 is once again assumed for both hydrostratigraphic units.

The first set of simulations consider the homogeneous and isotropic dispersivity case where the dispersivity is constant throughout the basin. Mass is instantaneously released from source beds at a point deep in the recharge end of the basin. Figure 64 shows the position and shape of the concentration plumes at t = 20,000 yr and t = 40,000 yr. Four separate simulations are given in Figure 64, with dispersivity values of 1 m, 5 m, 10 m, and 50 m respectively. Concentration contours of 5%, 10%, and 15% C/C_0 have been plotted.

If there is little dispersion in a flow system, a dissolved metal species will move along a flow path as plug-type flow with little change in concentration between the points of entrance and exit. In Figure 64b, the maximum concentration of the pulse averages nearly 35% C_{max}/C_0 at t = 40,000 yr. Increasing the dispersivity causes further dilution of the solute. The C_{max}/C_0 values decrease to about 15%, 10%, and 5% for α = 5 m, 10 m, and 50 m. Clearly the chance of having a concentrated metal-bearing brine reach an ore-forming site near the end of a basin is unlikely if transport involves long distances in a highly dispersive flow system.

A more realistic field situation occurs when the transverse dispersivity is much less than the longitudinal dispersivity. Figure 65 shows some of the modeling results from a series of simulations designed to examine the effect of the α_L/α_T ratio. In the shale unit $\alpha_L = \alpha_T$ = 1 m, and in the aquifer α_T = 1 m, but α_L is varied. The hydraulic properties and velocity-vector diagram are the same as Figure 64a.

The results show that increasing the longitudinal dispersivity in the aquifer causes the concentration contours to stretch out along the flow

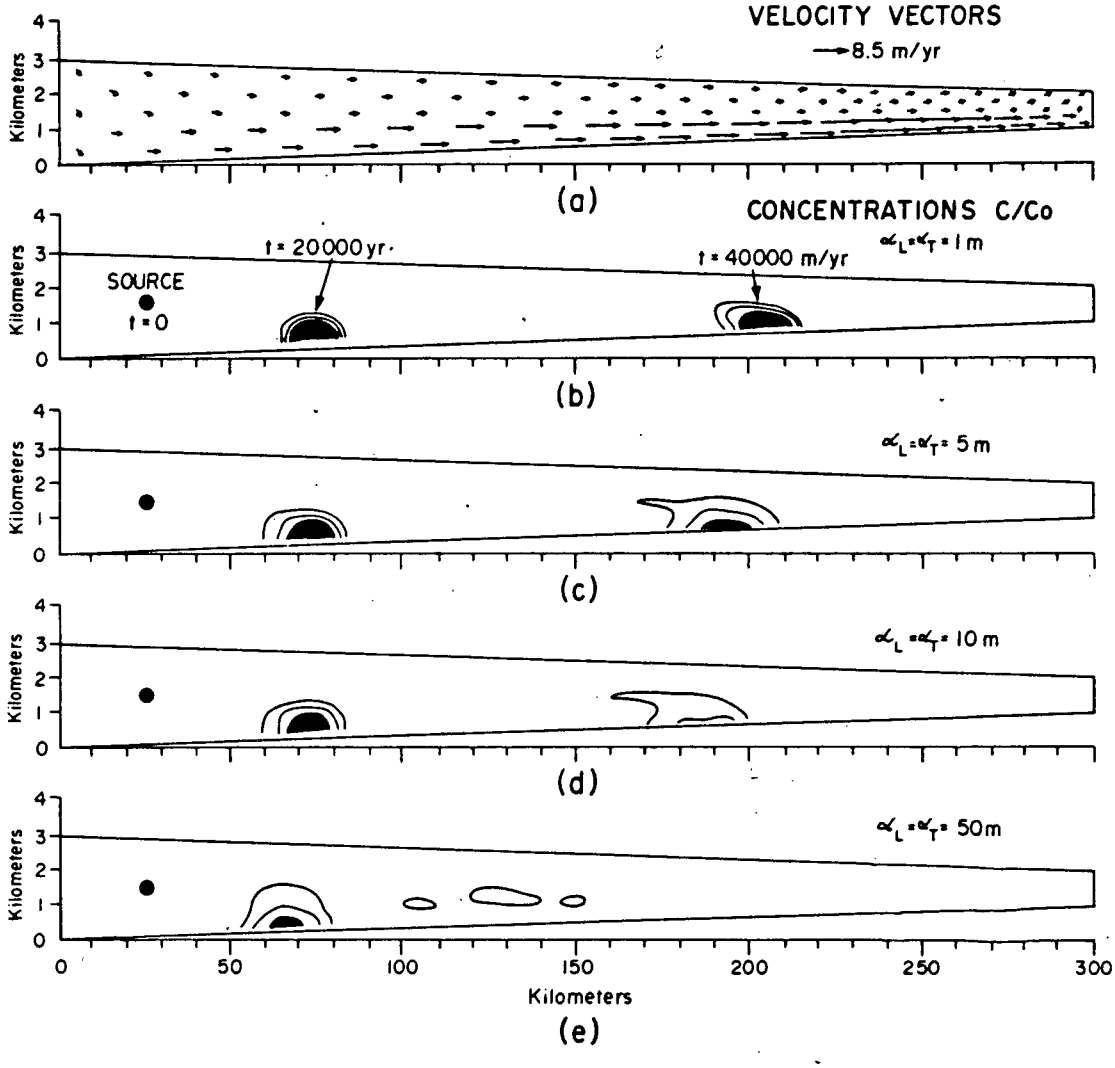

Figure 64. Effect of isotropic and homogeneous dispersivity on the mass-transport patterns in a two-layer basin.

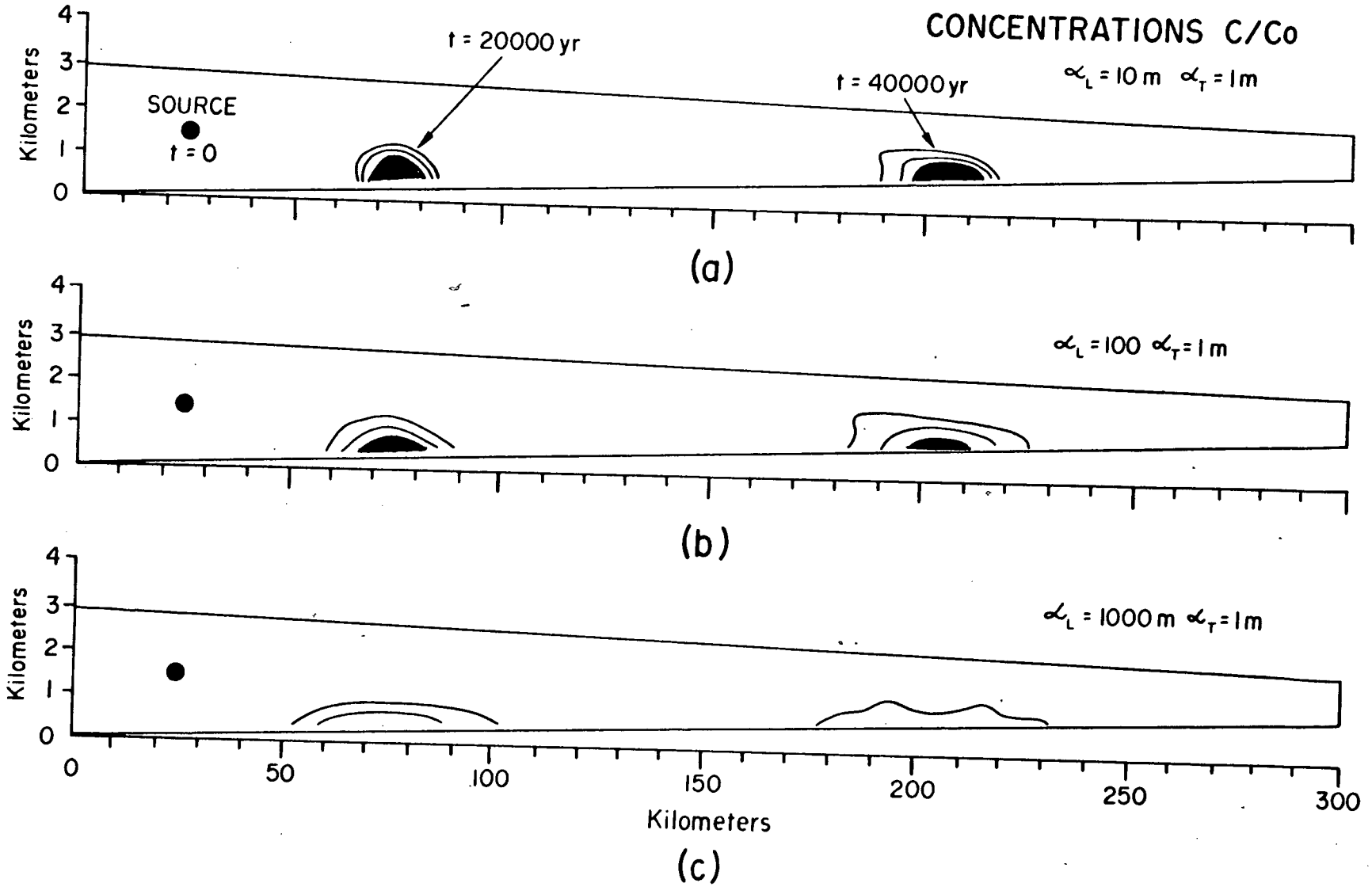

Figure 65. Effect of longitudinal dispersivity on mass transport patterns.

path. Passing from α_L = 10 m to α_L = 1000 m produces a nearly three-fold expansion of the plume at t = 40,000 yr. Comparison of Figures 64d and 65a illustrates the effect of transverse dispersivity on the 'height' of the mass-transport plume.

The increased mixing by systems with larger α_L coefficients is shown in Figure 66. For the same time t = 40,000 yr, an α_L = 10 m reduces the pulse concentration to about 30% of C_0, while an α_L = 1000 m causes the concentration to drop to about 5% C/C_0. Existing field data support longitudinal dispersivity coefficients of 10 m to 100 m for regional-scale problems. The amount of hydrodynamic dilution that can occur between source beds and possible depositonal sites can be estimated from Figure 66. Based on the modeling results, a maximum of about 20-30% of the source concentration level would be present in a metal-bearing brine that has travelled over 250 km to an ore-forming site. If a geochemical model requires a minimum concentration of 3 mg/kg•H_2O Zn to precipitate enough sphalerite at the ore site, then the original concentration of zinc in the source-bed area would have to be at least 10 to 15 mg/kg•H_2O. Although this transport model is greatly simplified because it does not account for the gain or loss of zinc through reactions along the flow path, it does provide a better model of the role of fluid flow in ore formation than a simpler plug-flow calculation.

Geology

A variety of geologic configurations and structures in a basin may control the formation and position of stratabound ore deposits. So far we have seen the effects of some simple basin structures and water-table configurations on fluid-flow patterns. The two-layer basin has fit the needs of this preliminary analysis of an ore-forming system by splitting the geology into its simplest components of aquifer and aquitard lithologies. Numerous

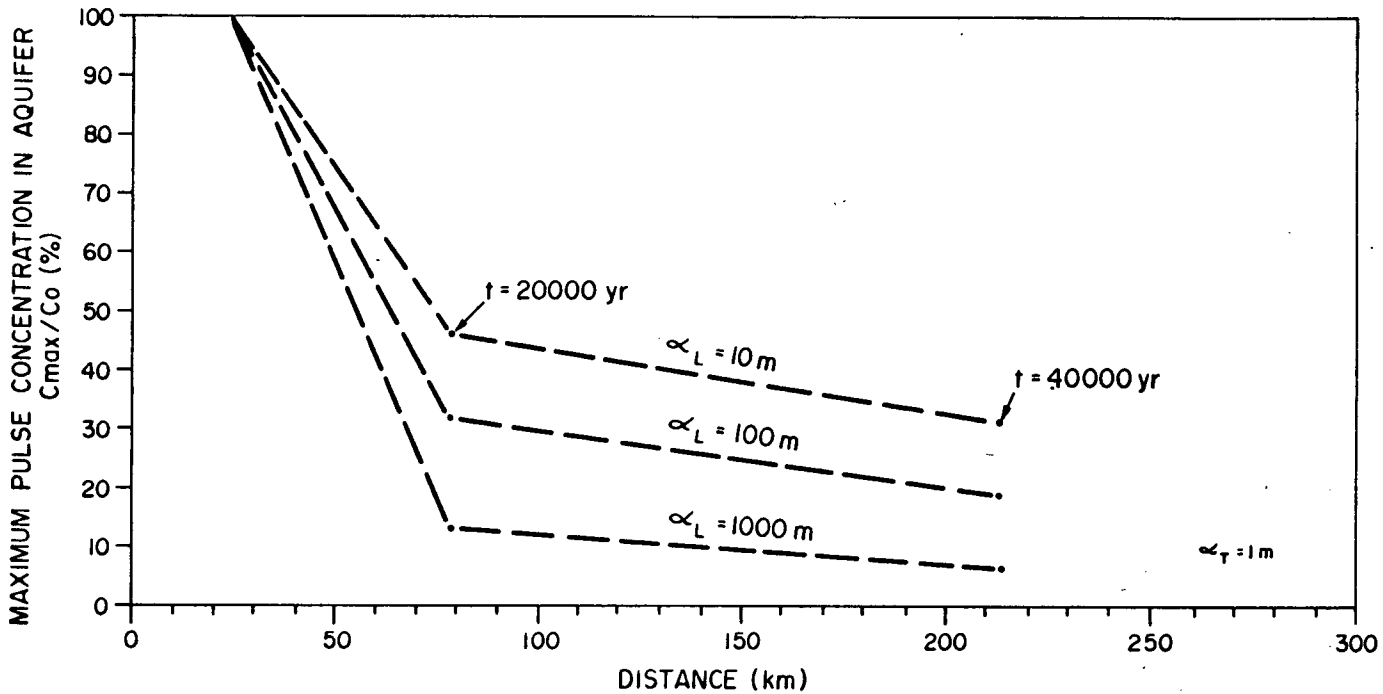

Figure 66. Maximum concentration in the basal aquifer as a function of longitudinal dispersivity.

modifications of this simple configuration are possible. Whatever the nature of the stratigraphy, however, aquifers serve to focus flow such that fluids will follow the route of least energy loss. From this point of view, the two-layer basin analysis is justified in order to understand the role of the controlling factors at their simplest level.

It would be impractical to cover all the possible geologic configurations of interest in ore formation, even in an idealized format. However, over twenty transport simulations have been conducted on specialized geologic configurations with a variety of stratigraphic and structural features. Each of these models displays a unique set of fluid-flow patterns, subsurface temperature distribution, and concentration patterns that arise from the specific geologic configuration. Figure 67 considers some of the hypothetical configurations that are modeled. The existence of discontinuous aquifers generally causes an upward movement of flow near the margin of the aquifer, whether or not the pinchout is due to a facies change, faulting, basement structures, or unconformities (Figures 67a, 67b, 67c, and 67d). Upward flow also brings with it higher temperatures at these pinchout locations. The effect of a broadly-warped basin (Figure 67d) is not much different from an undeformed basin of the same size. Figure 67f shows the configuration of a high-permeability carbonate-reef structure resting near the top of a basal sandstone aquifer. The upper unit surrounding the reef consists of shale and limestone. In this model, fluid flow is mostly through the basal aquifer, although the presence of the high-permeability reef also focuses downward flow from the shale beds into the reef, much as in the manner shown in Figure 22.

Space does not permit the presentation of all these modeling results, but one example will be shown. Figure 68 is an idealized section of a basin with a basal carbonate aquifer (Unit 1) overlain by a thick sequence of

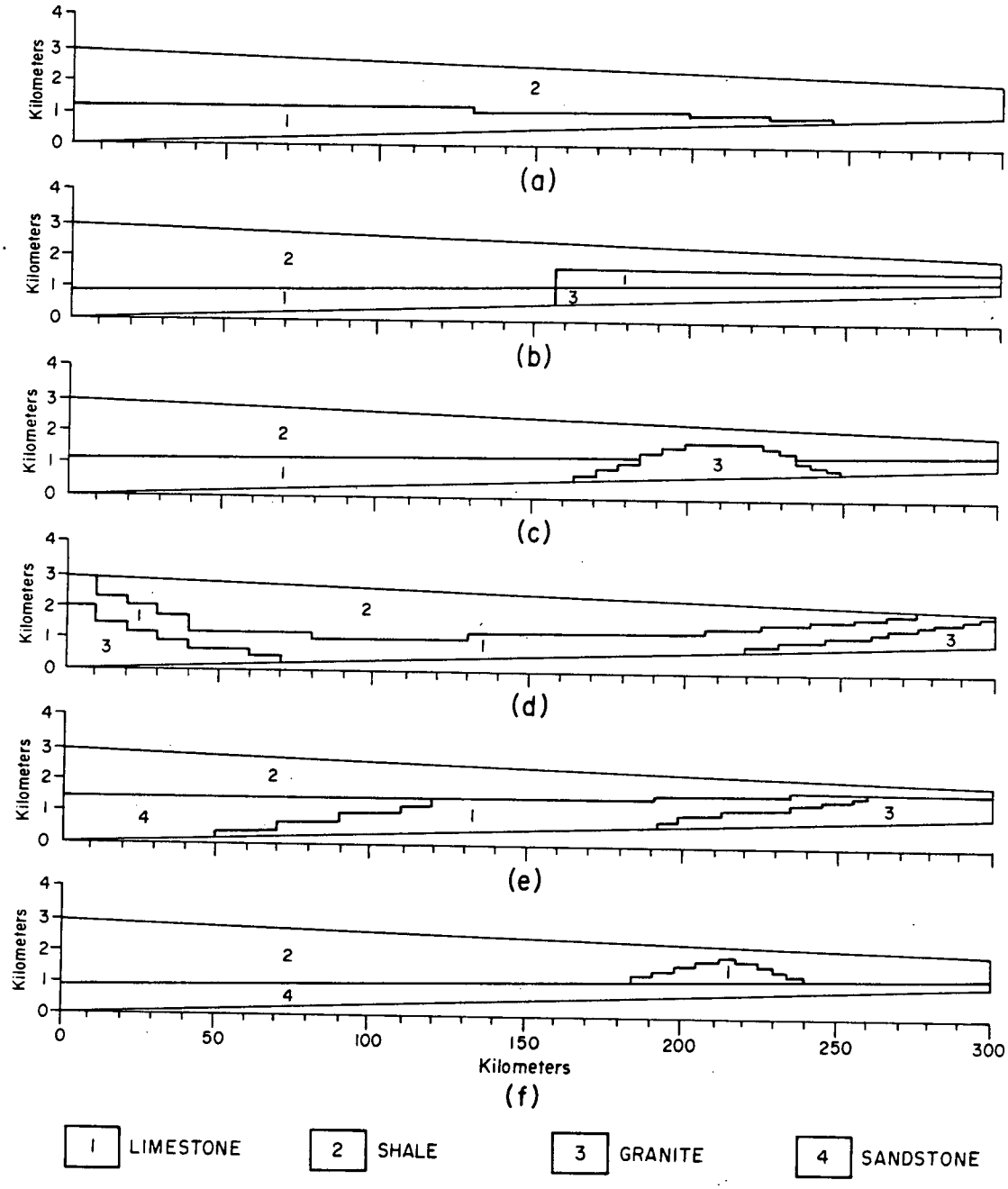

Figure 67. Idealized cross sections of several geologic configurations of possible importance to stratabound ore formation.

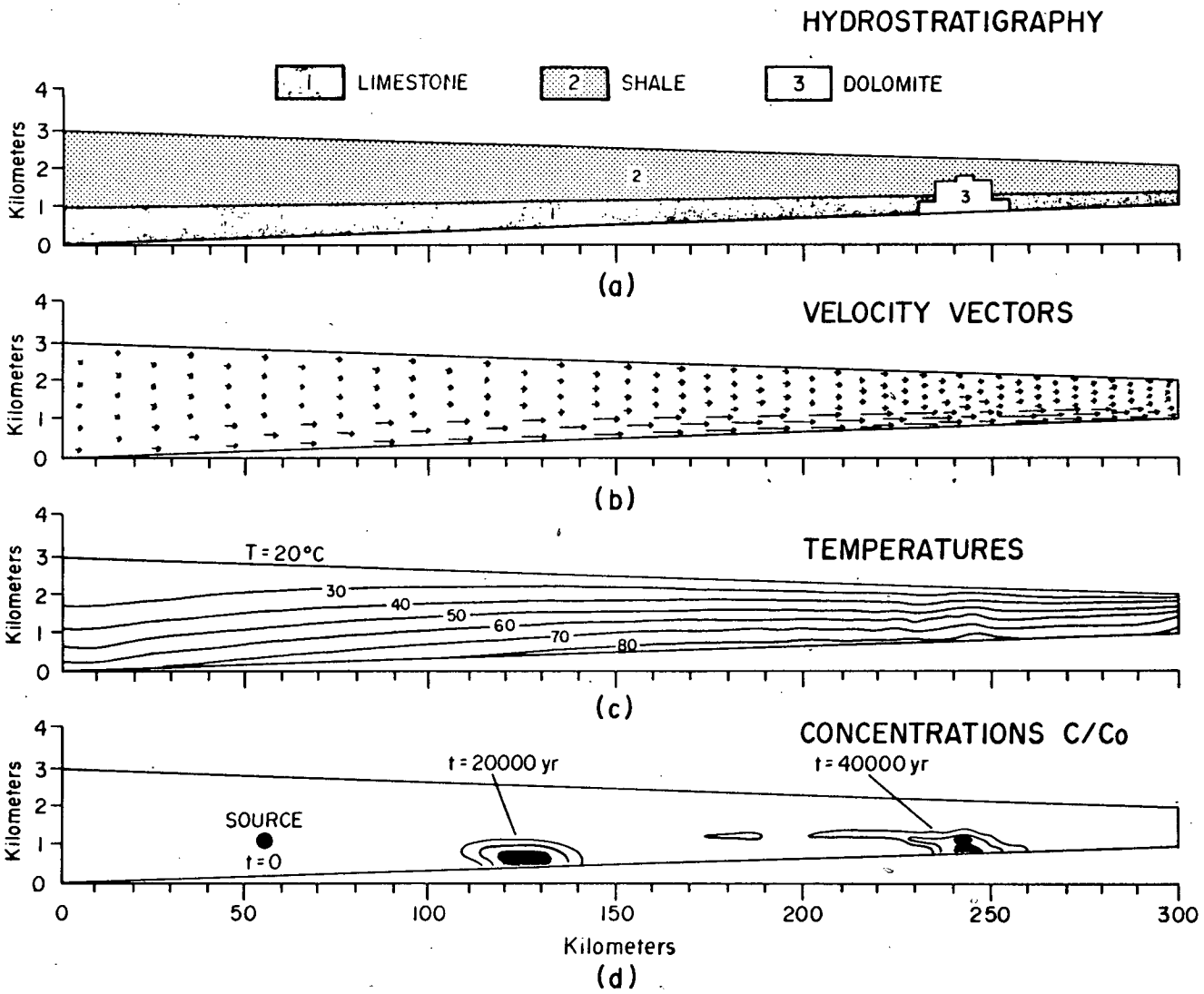

Figure 68. Transport simulation showing the influence of a reef structure at depth.

Table 12. Model parameter data for simulation problem of a reef structure at depth

Parameter	Symbol	Hydrostratigraphic Unit 1	2	3	Units
Fluid Flow					
Porosity	ϕ	0.20	0.10	0.30	(fraction)
Horizontal hydraulic conductivity	K_{xx}	200.0	10.0	500.0	m/yr
Vertical hydraulic conductivity	K_{zz}	2.0	0.1	5.0	m/yr
Salinity gradient	-	0.010 (all units)			%NaCl/m
Heat Transport					
Thermal conductivity of rock	κ_s	3.0	2.0	3.0	W/m^oC
Longitudinal thermal dispersivity	ε_L	100.0	1.0	100.0	m
Transverse thermal dispersivity	ε_T	1.0	1.0	1.0	m
Geothermal heat flux at base	$J = 70.00$				mW/m^2
Temperature at water table	$T_0 = 20.0$				^oC
Mass Transport					
Longitudinal dispersivity	α_L	100.	1.0	100.0	m
Transverse dispersivity	α_T	1.0	1.0	1.0	m
Apparent diffusion coefficient	D_d	3.0×10^{-3} (all units)			m^2/yr

mudstones (Unit 2). Near the basin margin, a karstic-reef feature (Unit 3) is present, which is fifty-times more permeable than the shale beds and twenty-times more permeable than the carbonate aquifer. Table 12 lists some of the set of parameter values assumed in the simulation.

The karst-reef structure does not create major alterations in the regional flow pattern of the two-layer basin model. It has the main effect of causing lateral flow over a larger area of the basin, and limits the zone of upward discharge to that part of the basin updip from the structure. Fluid velocities are the highest in the basal part of the reef at 9.0 m/yr. These high flow rates are also responsible for maintaining a nearly constant temperature along the basal aquifer unit. The strong influence of convection on the thermal regime is marked by the parallelism of the isotherms with the basement slope. Subsurface temperatures do not exceed 85°C in the reef structure. Figure 68d shows the mass-transport solutions at t = 20,000 yr and t = 40,000 yr for a pulse of mass released just above the carbonate aquifer in the recharge end of the basin. Only the 5%, 10%, and 15% C/C_0 concentration levels are contoured. Approximately 20% of the source-bed concentration level reaches the karst-reef structure at the other end of the basin.

Geochemical Models of Transport and Precipitation

Of all the processes effecting ore genesis in sedimentary basins, the geochemical factors that control metal solubilities and ore precipitation have received the most quantitative research. With reference to the carbonate-hosted lead-zinc deposits, recent studies that review the general theories include Anderson (1978), Anderson and Macqueen (1982), Giordano and Barnes (1981), and Sverjensky (1981). Some of these concepts have been introduced earlier in Chapter 2. Table 13 contains a summary of the three basic geochemical models proposed in the literature.

Table 13. Geochemical models for stratabound ore genesis (after Anderson, 1978 and Sverjensky, 1981)

Transport Model	Reasons for Deposition
I. Metals transported in low-sulfur fluid	a) Mixing with H_2S-bearing solutions b) Replacement of iron sulfides c) Thermal degradation of organics
II. Metals transported in sulfate-bearing fluid	a) Sulfate reduction by bacterial destruction of organics to produce H_2S b) Sulfate reduction by non-bacterial destruction of organics to produce elemental sulfur c) Sulfate reduction internally due to methane d) Sulfate reduction externally on encountering petroleum e) Sulfate reduction due to reaction with iron-bearing minerals
III. Metals and sulfide transported together in the same fluid	a) Reaction with host rock and rise in pH b) Temperature drop c) Decreased stability of chloride complexes due to mixing

The purpose of this section is to provide a quantitative analysis of two of the most likely geochemical models, through the use of reaction-path modeling with EQ3/EQ6. First to be considered are basinal-brine models that support metal transport in a sulfate-type fluid (II, Table 13). Secondly, the geochemical conditions necessary for simultaneous transport of metal and sulfide in the same fluid (III, Table 13) are examined and possible precipitation mechanisms tested.

Mixing-type models that assume transport of metal in one fluid and sulfide in another are not explicitly assessed in this evaluation. We have already seen from the fluid-flow and mass-transport modeling that the transport of two immiscible fluids, without mixing through dispersion, is highly unlikely in long-distance brine transport. On the other hand, some hydrogeologic conditions are capable of supplying to mixing areas one or the other ore-forming components from different parts of the basin. This is accomplished through the development of local flow systems, which are superimposed on regional systems (e.g. Figures 22 and 41). The possibility of a mixing-type model is still open, provided field evidence can be found to clearly support it over the simpler hydrodynamic situation of a single, ore-forming fluid.

Metal-Sulfate Brine Models

Consider the model of a metal-bearing brine containing sulfate SO_4^{2-}. If it reaches an area where organic material is present, then the possibility exists for the reduction of sulfate to sulfide, and precipitation of the metals from solution. Several mechanisms are available in sedimentary basins for the reduction of sulfate to reduced sulfide (H_2S or HS^-) in solution, as listed in Table 13. Organic material is abundant in many carbonate-hosted lead-zinc deposit environments, and its destruction through bacterial-reduction

processes is a primary source of H_2S at temperatures less than 80°C.

Table 14 outlines the composition of a hypothetical 2.0 m (molal) NaCl brine at a temperature of 75°C. The concentration values are chosen to be representative of a deep, basinal brine in equilibrium with carbonate aquifers. Comparison can be made with present-day oil-field brines and fluid-inclusion analyses for data of this type. Numerous compilations have been published that list brine compositions, including White (1968), Hitchon, Billings and Klovan (1971), Carpenter, Trout, and Pickett (1974), and Land and Prezbindowski (1981). The actual range of compositions that could be modeled is wide, but Table 14 is suitable for this study.

Perhaps the most sensitive parameter in Table 14, and the poorest known, is the pH. The value chosen is critical to mineral and aqueous species stabilities, yet the natural range of pH in brines can be wide. Anderson (1973, 1975) demonstrated that the minimum pH of an ore-forming fluid is about 5.7 at 100°C, assuming a partial pressure of CO_2 of 1 bar and equilibrium with calcite and dolomite. Sverjensky (1981) has estimated, however, that the pH of basinal brines can be as low as 4.3, and still be within two log units of neutrality. At temperatures of 50°C and 100°C, neutrality occurs at pH = 6.63 and 6.12, respectively. He assumed a maximum concentration of dissolved CO_2 [as H_2CO_3 and CO_2(aq)] of 0.05 molal, and reported that McLimans (1977) measured 0.02 to 0.14 m CO_2 in fluid inclusions from ores in the Upper Mississippi Valley district (see Figure 1 for location). Hitchon (1981) has studied modern oil-field brines in Alberta, and has found partial pressures of CO_2 as high as 6.5 bars. In this study, a maximum dissolved CO_2 (as H_2CO_3) of 0.04 m is assumed, and pH is allowed to range between 5.0 and 6.8.

There appears to be little doubt from experimental data and field

Table 14. Initial conditions for the metal-sulfate brine model

T = 75°C

pH = 5.0

$f_{O2} = 10^{-50}$ f_{CO2} = 5 bars

(Eh = + 0.014 volts)

Component	Concentration Totals (moles/kg)	Concentration Totals (mg/kg)
Na	1.46	30,030
K	5.0×10^{-2}	1,746
[1]Ca	2.4×10^{-1}	8,710
[2]Mg	9.2×10^{-3}	200
SiO_2(aq)	2.0×10^{-4}	5
Cl	2.0	63,330
SO_4	5.0×10^{-3}	145
[3]H_2CO_3(app)	4.2×10^{-2}	2,160
Fe	5.0×10^{-9}	2.5×10^{-4}
[4]Zn	1.0×10^{-4}	6.0
Pb	1.0×10^{-6}	0.2

1. Calcite saturation
2. Dolomite saturation
3. $H_2CO_3(app) = CO_2(aq) + H_2CO_3(aq)$
4. Total zinc content = $Zn^{++} + ZnCl^{+} + ZnCl_2 + ZnCl_3^{-} + ZnCl_4^{2-}$

observations that metal transport in brines is accomplished mainly through chloride complexing (Helgeson, 1964). Fluid-inclusion studies by Roedder (1967) have also shown that the bulk of ore-forming brines, in carbonate-hosted lead-zinc ore environments, were sodium-calcium-chloride fluids, the reduced-sulfur content was low, and the salinity ranged between 1.0 m and 5.0 NaCl (10% to 30% NaCl by weight), but averaged around 2.0 m NaCl. Other types of complexing, such as bisulfide and organic, may have been important in certain systems (Giordano and Barnes, 1981). For the purpose of this study, only chloride complexing is considered.

The solubility of galena or sphalerite in brines is a function of the reduced sulfur content, salinity, and temperature. If reduced sulfur (H_2S or HS^-) is low, metal transport is easily accomplished. In fresh water, solubilities are less than 1 ppm (parts per million), but chloride complexing can allow concentrations up to thousands of parts per million (Anderson, 1978). Factors controlling the solubilities of sphalerite and galena have been studied with both experimental and theoretical approaches (see Barnes, 1979). We will briefly review some of these factors below.

Figure 69 illustrates the stability fields of the sulfur species as a function of the solution pH and the oxidation state, which is represented by the oxygen gas fugacity. The temperature is 100°C, and the brine has a salinity of 3.0 m NaCl. Total sulfur content of sulfate and sulfide is set at 10^{-2} m, which is thought to be representative of precipitation conditions in the Mississippi Valley-type deposits (Anderson, 1973). Also plotted on the graph are the 10^{-5} m concentration curves of total zinc and lead in equilibrium with sphalerite and galena. Reference to these curves are made later in the chapter.

At a pH of 5.0 to 6.0, the dominant sulfur species is either SO_4^{2-}

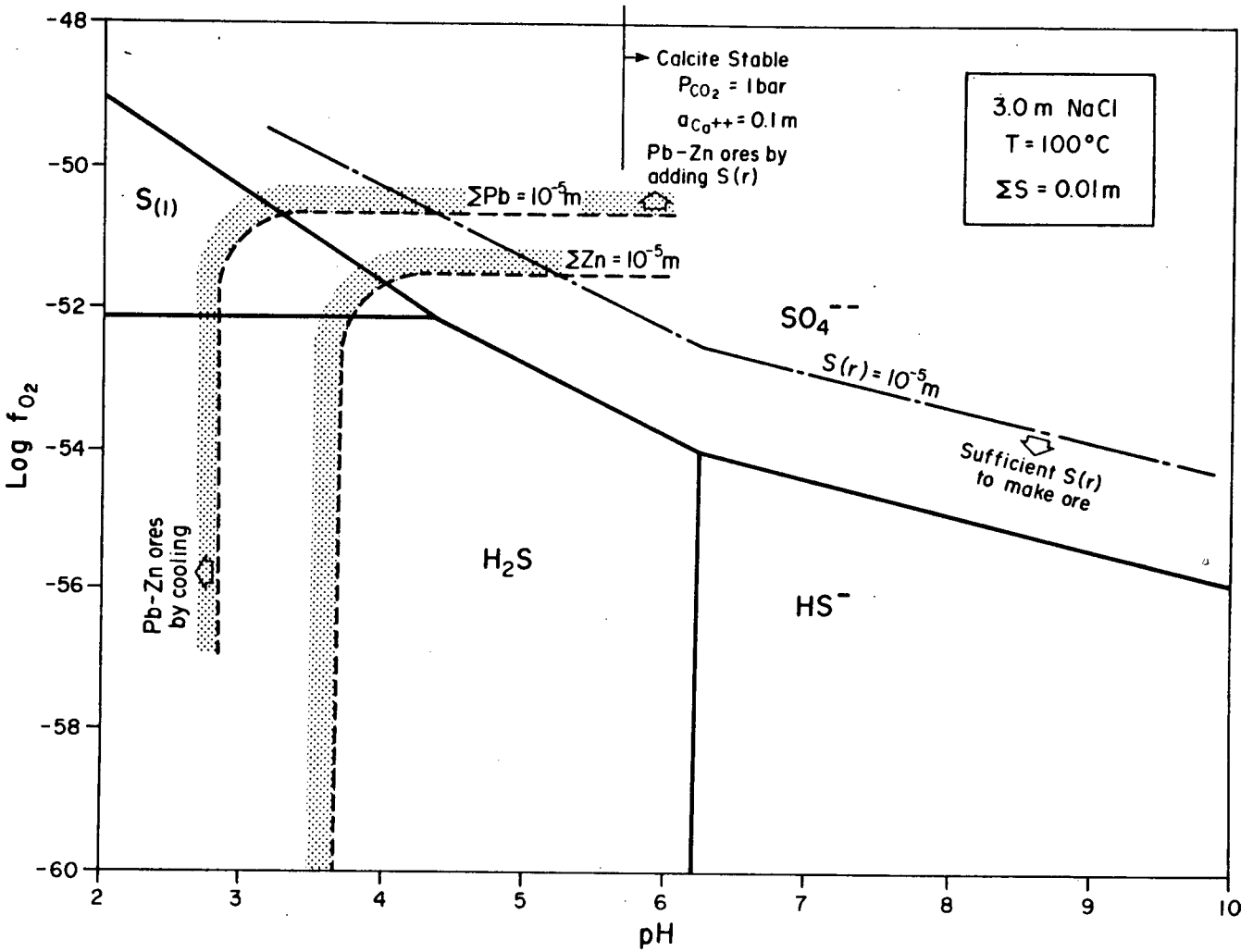

Figure 69. Stability fields of sulfur species as a function of pH and oxidation state f_{O_2} (after Anderson, 1978).

or $H_2S(aq)$, depending on the reducing conditions (Figure 69) and temperature Helgeson (1969) calculated the concentration ratio of sulfate to sulfide as a function of oxygen fugacity, temperature, and pH. Figure 70 charts this relationship for a fixed pH = 5.0. Sulfate-bearing brines tend to occur at temperatures less than 100°C, at least for $f_{O_2} > 10^{-55}$. Higher temperatures or more reducing conditions will generally favor sulfide-bearing brines. For example, approximately ten times more sulfide exists at 150°C than at 100°C. The temperature regime of a sedimentary basin, therefore, will place strong constraints on the type of sulfate species involved in metal transport.

The effects of reduced sulfur concentration on the concentrations of lead and zinc are shown in Figure 71. The temperature is 100°C and the brine is a 3.0 m NaCl solution. Three sets of curves are plotted for each metal at pH = 4.0, 5.0, and 6.0. Notice that metal concentrations can easily exceed 10^{-5}m (2 ppm Pb, 1 ppm Zn) in brines where reduced sulfur is less than 10^{-5} m (0.3 ppm H_2S). Decreasing the pH from 5.0 to 4.0 has a strong influence on metal concentrations, causing an increase by a factor of ten in stoichiometric solutions.

Salinity also exerts a significant control on the solubility of metal sulfides. Figure 72 demonstrates the change in zinc concentration due to a rise in salinity from 1.0 m to 3.0 m NaCl (5 - 15% wt. equiv. NaCl). Curves for pH = 4.0 and 6.0 are plotted and temperature is 100°C. The 3.0 m NaCl curves are from Anderson (1973, Figure 2), and the 1.0 m NaCl curves are from Barnes (1979, Figure 8.10). At a pH ≅ 4.0, the change in salinity from 1.0 m to 3.0 m NaCl causes the concentration of zinc in equilibrium with sphalerite to rise from about 2 ppm to 15 ppm (Figure 72). The metal content of brines in this range of salinity is almost entirely due to chloride complexes. The species $PbCl_4^{2-}$ and $ZnCl_4^{2-}$ dominate in the temperature range of 50°C to 150°C

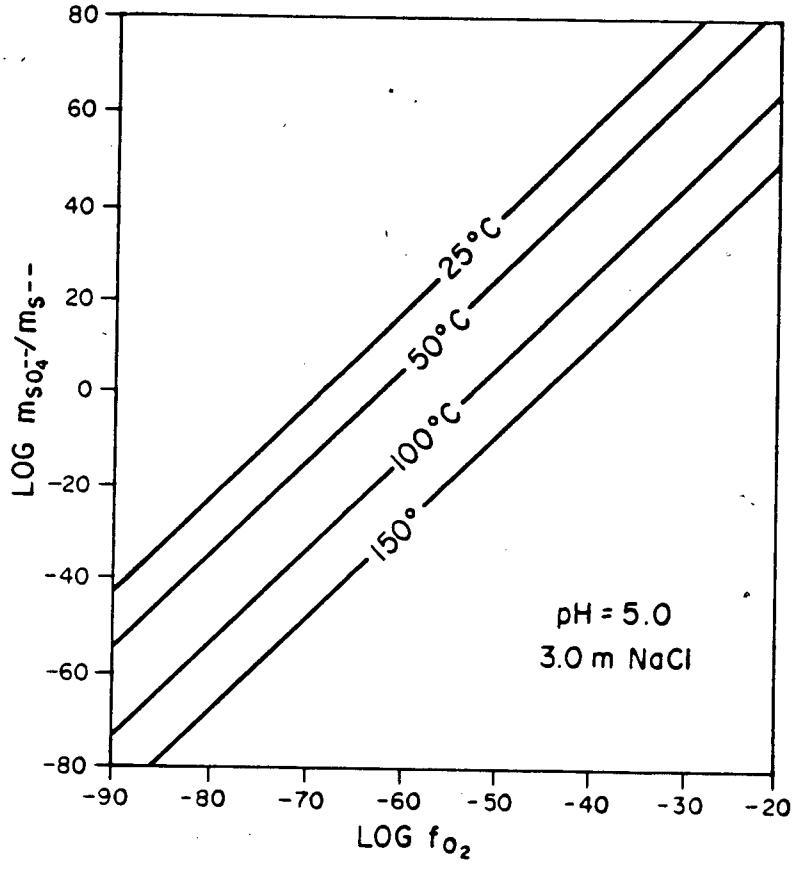

Figure 70. Sulfate-sulfide concentration relationship as a function of oxygen fugacity and temperature (after Helgeson, 1969).

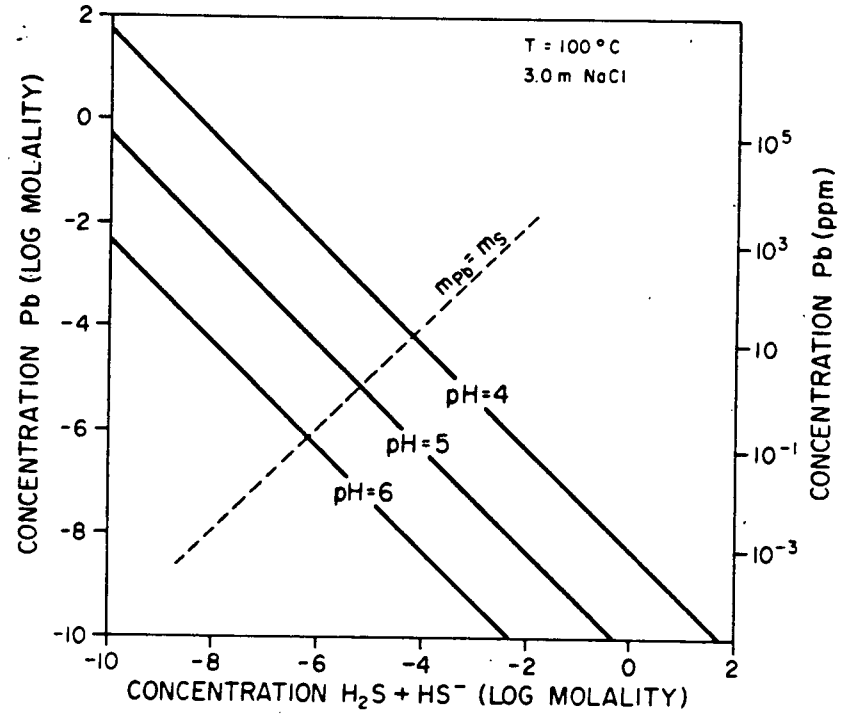

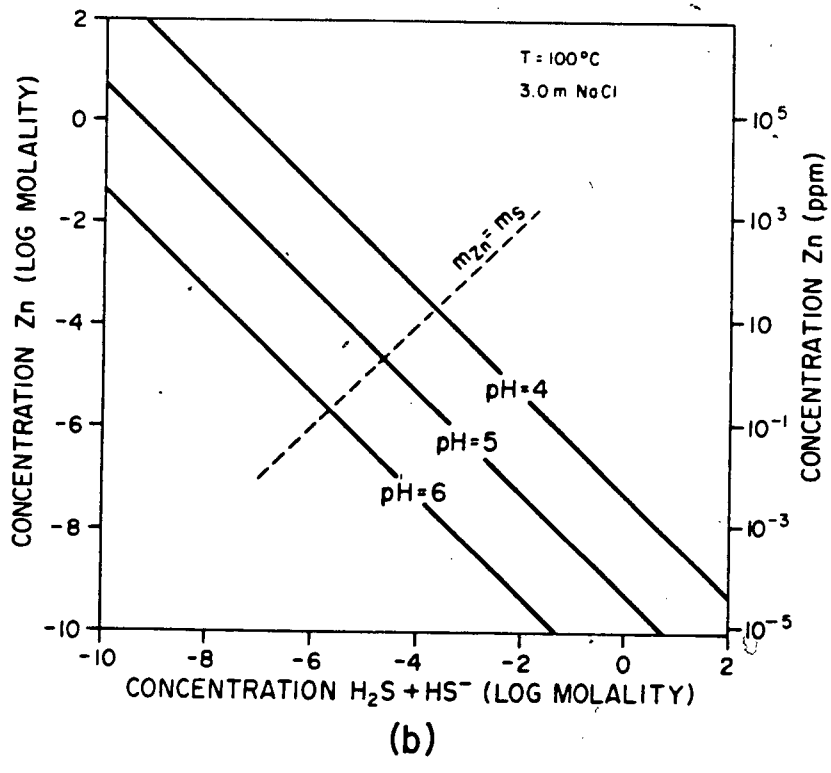

Figure 71. Lead and zinc concentrations in a 3.0 m NaCl brine as a function of sulfide concentration and pH (after Anderson, 1973).

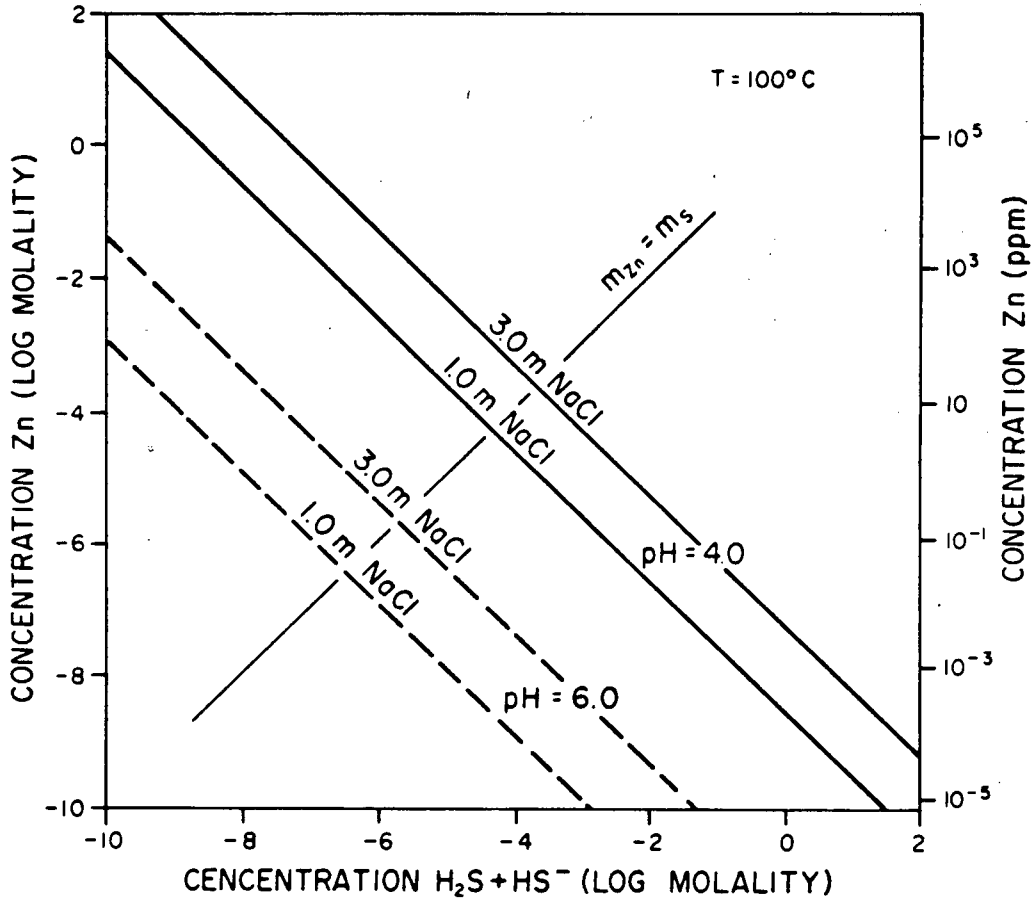

Figure 72. Effect of salinity on zinc concentration (after Anderson, 1973 and Barnes, 1979).

(Helgeson, 1969, Figure 15).

Higher temperatures enhance the effect of the chloride complexes on metal solubility, as shown in Figure 73, for a 3.0 m NaCl solution at pH = 5.0. Total zinc concentration in equilibrium with sphalerite is expressed in ppm (mg/kg • H_2O) and plotted as a function of temperature (^{o}C). At 50°C the sphalerite solubility is about 0.2 ppm, but this increases to 5.5 ppm at 150°C. This data is roughly estimated from the original diagram given by Anderson (1973) by dividing the numbers at pH = 4.0 by a factor of ten (Anderson, 1973).

The minimum concentration of Pb or Zn needed to form a major ore deposit is uncertain, but a range of 10^{-5} m to 10^{-4} m is commonly stated in the literature (Anderson, 1973; Barnes, 1979). Natural concentrations of base metals in brines vary from less than one to several-hundred mg/kg • H_2O (Anderson and Macqueen, 1982). Chemical analyses of fluid inclusions indicate a concentration range of 10^{-5} m to 10^{-2} m for ores of the Mississippi Valley region (Sverjensky, 1981). Although metal concentrations do not commonly exceed a few mg/kg • H_2O in present-day basinal brines, Anderson (1978) believes these brines are well qualified as examples of the ore-forming fluids of the past.

The sulfate content of subsurface brines is variable, but concentrations of at least a few hundred ppm are common (e.g. Hitchon, 1977). Total dissolved sulfur contents of fluid inclusions range in their maximum values from 1000 ppm (Roedder, 1976) to 4000 ppm (McLimans, 1977). Most brines appear to contain more than enough sulfur as sulfate (10^{-2} m) to precipitate sulfide minerals, provided some form of mechanism is available to reduce the sulfate at the ore-forming site.

Hydrogen sulfide gas is a common constituent of many oil-field brines, but unfortunately the concentration range of $H_2S(aq)$ is not well documented. Reasonable concentration values probably range between 10^{-4} and 10^{-2} m,

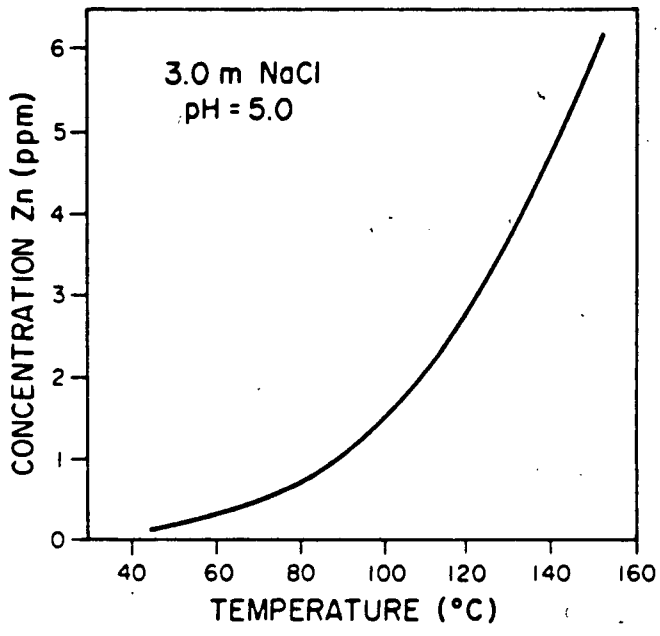

Figure 73. Effect of temperature on sphalerite solubility (modified after Anderson, 1973).

according to Anderson (1977). Field data reported by Giordano and Barnes (1981) places H_2S concentrations in the range from 10^{-5} m to 10^{-2} m for oil-field brines in Mississippi. Hitchon (1981) reports partial pressures of H_2S as high as 15 bars or about 0.6 m H_2S in natural gas reservoirs in Alberta. The problem with known sulfide-type brines, with respect to ore genesis, is that those containing even a small amount of H_2S are usually very low in metal content (Anderson and Macqueen, 1982).

It is evident from the above discussion that a wide variety of geochemical conditions will allow a metal-sulfate brine to carry sufficient lead or zinc to form a major ore deposit, provided some sort of sulfate-reduction process occurs. Three reaction-path simulations are now presented to demonstrate some of the possibilities.

The first experiment to be considered involves the addition of H_2S to the model brine of Table 14. It is assumed that sulfate in the fluid has been reduced at the ore site to H_2S. The actual process of sulfate reduction is not simulated, only that a source of H_2S is suddenly available. Sulfate reduction can be accomplished through the anaerobic-bacterial decay of organic matter, or the internal reduction due to the presence of methane (Table 13). The amounts of lead and zinc chosen here are 10^{-6} m Pb and 10^{-4} m Zn. These numbers are not meant to simulate a metal ratio from any particular known ore environment, but are simply assumed as reasonable concentrations, based on the solubility data given above.

Figure 74 shows the results of a reaction-path simulation with EQ3/EQ6 where 10^{-3} moles/kg $\cdot$ H_2O (34 mg/kg) of $H_2S(g)$ are dissolved into the metal-sulfate brine. Only a selected group of aqueous species are plotted in the speciation diagram. The brine is assumed to be initially in equilibrium with dolomite and limestoneat a temperature of 75°C. As H_2S dissolves, the

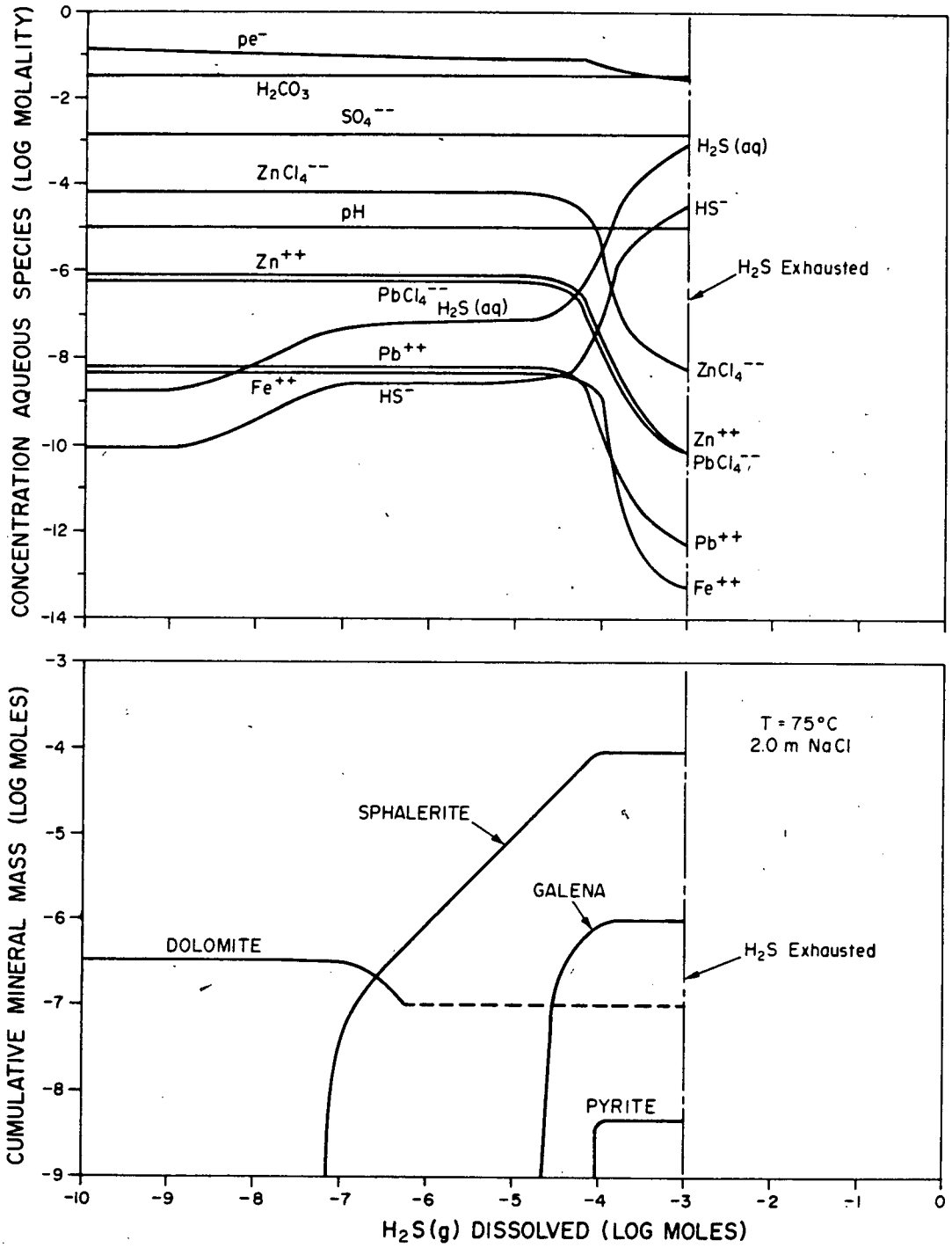

Figure 74. EQ3/EQ6 simulation of the reaction of a metal-sulfate brine with H_2S.

aqueous sulfide species gradually become more concentrated. Dolomite is the first mineral phase to precipitate, but later begins to dissolve with further addition of H_2S and precipitation of sphalerite. The pH remains constant throughout the reaction process, while the oxygen fugacity drops from 10^{-50} to 10^{-57}. Precipitation of the sulfide minerals is also reflected in the change in concentrations of the free-metal species and metal-chloride. Most of the metal content of the fluid is exhausted by the point at which 10^{-4} moles of H_2S have been dissolved. Galena is the next mineral to precipitate after sphalerite, and pyrite is deposited last. Approximately 10^{-4} moles (10 mg) of sphalerite, 10^{-6} moles (0.3 mg) of galena, and 10^{-8} moles (0.001 mg) of pyrite are precipitated per kg of H_2O. These figures can be compared to the simulation example given in the previous chapter (Figure 16), in which the brine is at a pH = 6.8 and the zinc concentration is an order of magnitude lower. Reacting a basic type of sulfate brine with H_2S produced about twenty times more dolomite dissolution than the example of Figure 74.

The addition of other strong reducing agents, such as methane or hydrogen gas, to a metal-bearing brine can also cause sulfide mineral precitation. Methane is a common component of basinal brines, and fluid inclusion data indicate that substantial amounts of methane occurred in ore-forming fluids, even as high as 800 mg/kg • H_2O (Roedder, 1976). Figure 75 shows the effects when the brine of Table 14 encounters methane along its flow path.

In this example, 10^{-3} moles (16 mg) per kg • H_2O is permitted to react with the metal-bearing fluid. Addition of 10^{-7} moles of methane causes an abrupt drop in the oxidation state of the fluid, as marked by the pe^- curve (Figure 75). The shift to a more reducing environment changes the sulfate to sulfide ratio (Figure 70), as noticed in the sudden increase in $H_2S(aq)$ and HS^- concentrations. Toward the end of sphalerite precipitation, dolomite

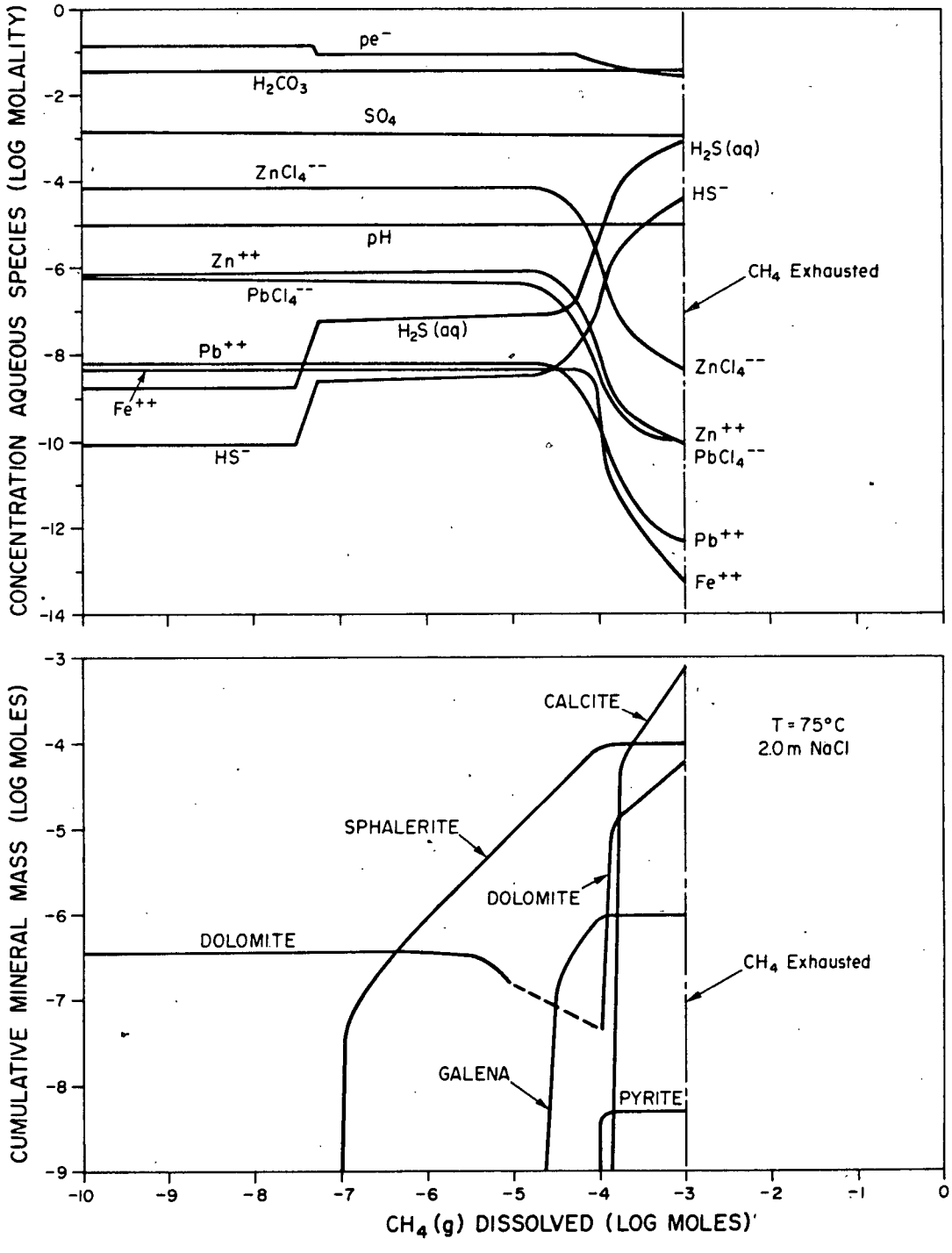

Figure 75. EQ3/EQ6 simulation of the reaction of a metal-sulfate brine with CH_4.

that was precipitated earlier begins to dissolve. As the zinc concentrations drop off, the addition of more methane causes galena to precipitate, and then pyrite. Sulfide precipitation ceases after 10^{-4} moles of CH_4 has dissolved, but further addition of methane causes the oxidation state to drop further and large amounts of calcite and dolomite to precipitate. Late-stage carbonate mineralization is a common feature of many lead-zinc ore deposits. In this particular model, the same amounts of sulfide minerals precipitated as in the H_2S model, but about 75 mg of calcite and 10 mg of dolomite are deposited per kg • H_2O.

Dissolved methane may also reduce sulfate in brines internally, but the rate of reaction is thought to be too slow for ore-genesis (Barton, 1967). On the other hand, this feature could allow CH_4 to be carried metastably in solution for long distances, perhaps to an ore-forming site where bacteria could enhance the reaction rate (Skinner, 1979).

Another possibility of reducing a sulfate-bearing brine is through replacement-type reactions with pre-existing sulfide minerals. Figure 76 considers the case where the model brine of Table 13, containing 10^{-4} m Zn and 10^{-6} m Pb, passes through a pyrite-bearing carbonate bed. The amount of pyrite (FeS_2) available for reaction is 10^{-3} moles (120 mg). Compared to the preceding models, the reaction with pyrite appears to be a less efficient mechanism for ore precipitation at these metal concentrations. Only 10^{-6} moles (0.1 mg) of sphalerite is precipitated in this model before the pyrite comes to equilibrium with the brine. Subsequent simulations showed that greater amounts of ore will precipitate if the initial zinc and lead concentrations are higher than those of Table 14. For example, using a zinc concentration of 10^{-3} moles/kg • H_2O resulted in the precipitation of 38 mg of sphalerite per kg of water. Approximately 2 x 10^{-4} moles (27 mg) of

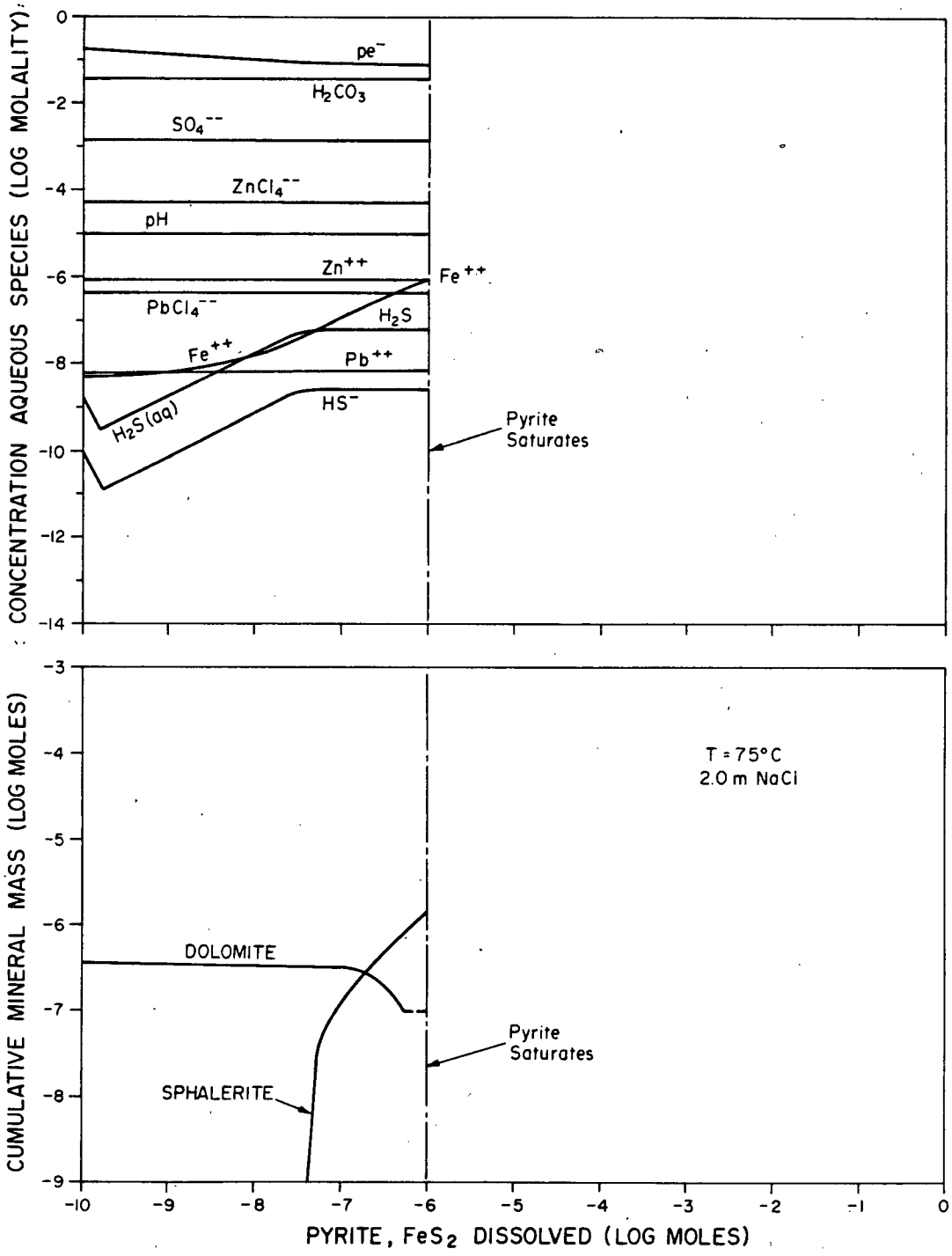

Figure 76. EQ3/EQ6 simulation of the reaction of a metal-sulfate brine with pyrite.

pyrite is destroyed before pyrite saturates with respect to the brine.

All three of the reducing models given above have shown the viability of a metal-sulfate brine to produce ore mineralization when H_2S is added to the fluid or the oxidation state is modified. Geologic evidence as to the relative importance of the various sulfate-reduction mechanisms has not been clearly established. It is known that bacteria-assisted reduction is unlikely in ore environments where temperatures are above 80°C; however, the inorganic mechanism suggested by Orr (1974) is apparently adequate for systems of 80°C to 120°C in organic-rich strata. Reactions with methane or pyrite are equally reasonable from geologic evidence.

Mineral textures commonly show evidence to support the geochemical model of H_2S addition to brines. At Pine Point, for example, sulfide minerals demonstrate clearly that relatively rapid precipitation took place, which supports H_2S addition (Beales, 1975). Anderson and Macqueen (1982) point out, however, that slow addition of H_2S to a brine may as easily produce mineral textures that usually are thought to be characteristic of deposition from a metal-bearing sulfide-type fluid.

Metal-Sulfide Brine Models

We have seen that sulfate-reduction mechanisms allow a wide variety of geochemical conditions for the brine carrying the metal to a depositional site. Lead and zinc concentrations can easily exceed 10^{-4} moles/kg • H_2O, even at pH values greater than 5.0, so long as reduced sulfur activities are low (Figure 71). In a brine transporting both metal and aqueous sulfide, the geochemical conditions are much more restrictive, especially in regard to the amount of metal that can be carried in solution with an equal amount of sulfide. Figures 71 and 72 show that about 10^{-5} m is the maximum concentration of metal sulfide that can be carried in the same solution, at a pH of 5.0 and a

temperature of 100°C. Slightly higher concentrations can be achieved in more acidic brines, depending on the salinity (Figure 72).

Two simulation results are now presented to demonstrate the relative importance of two-different precipitation mechanisms. In the first simulation, a metal-sulfide brine is saturated with respect to sphalerite and galena. Precipitation of sulfide minerals occurs when the brine encounters a dolomite bed. In the second simulation, a drop in temperature causes sulfide precipitation from a brine originally in equilibrium with sphalerite, galena, and quartz.

Consider the model-brine composition of Table 15. The solution is in equilibrium with quartz, sphalerite, and galena at a temperature of 100°C. Besides the higher temperature and more reducing conditions, the fluid is otherwise of similar composition to Table 14. In this particular model, the sphalerite solubility gives a zinc concentration of 6.0×10^{-6} moles/kg • H_2O in a 2.0 m NaCl solution. An equal amount of reduced sulfur is also present. The fluid is undersaturated with respect to calcite and dolomite.

Figure 77 shows the results of an EQ3/EQ6 simulation in which the metal-sulfide brine encounters a dolomite bed. About 1.0 mole (185 g) of dolomite is allowed to react with the fluid. An increase in pH from 5.0 to 5.3 causes the brine to become saturated with respect to sphalerite first, and then later with galena. This is accompanied by an increase in concentration of the carbonate-type aqueous species, and a decrease in metal and sulfide concentrations. The solution eventually becomes saturated with respect to dolomite, after about 6×10^{-4} moles (115 mg) have dissolved. The total quantity of sphalerite precipitated is 3.1×10^{-6} moles (0.3 mg), and the quantity of galena precipitated is 4.6×10^{-8} moles (0.01 mg), all per kg • H_2O.

Varying the salinity or the temperature of the brine will alter the

Table 15. Initial conditions for the metal-sulfide brine model

T = 100°C

pH = 5.0

f_{O_2} = 10^{-55} f_{CO_2} = 5 bars

(Eh = - 0.168 volts)

Component	Concentration Totals (moles/kg)	Concentration Totals (mg/kg)
Na	1.85	38,000
K	5.0×10^{-2}	1,745
Ca	5.0×10^{-2}	1,790
Mg	1.0×10^{-3}	20
SiO_2(aq)	8.0×10^{-4}	20
Cl	2.0	63,330
[1] SO_4	1.7×10^{-10}	1.5×10
H_2CO_3(app)	$2.8 \times 10-^{2}$	1,585
Fe	5.0×10^{-9}	2.5×10^{-8}
[2] Zn	6.0×10^{-6}	0.36
[3] Pb	1.0×10^{-7}	0.02
[4] $S_{(r)}$	6.0×10^{-6}	0.20

1. Quartz saturation

2. Sphalerite saturation

3. Galena saturation

4. Total reduced sulfur $S_{(r)} = H_2S(aq) + HS^-$

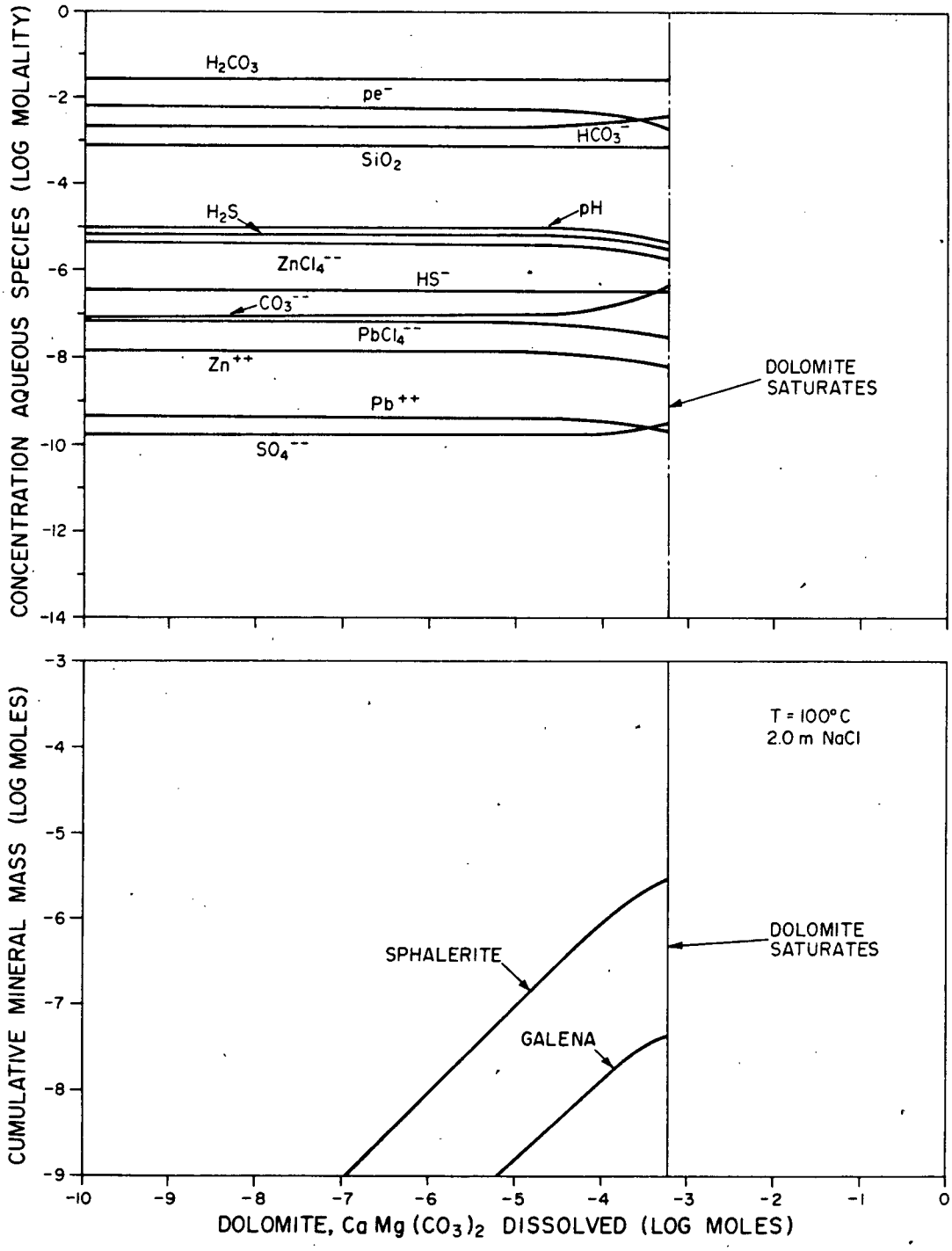

Figure 77. EQ3/EQ6 simulation of the reaction of a metal-sulfide brine with dolomite.

the solubility of sphalerite and galena, and therefore the amount of ore precipitation due to the pH shift. Table 16 lists the results of six EQ3/EQ6 simulations in which the NaCl concentration was varied. As expected, maximum deposition occurs from the most saline case. The effect of temperature on the amount of sphalerite formed is shown in Table 17. Increasing the temperature from 100°C to 150°C creates a tenfold increase in the amount of metal depositied, for a pH shift from 5.0 to 5.3. It is clear that high temperatures and salinities enable the metal-sulfide brine model to produce greater amounts of ore for a given pH change.

The second reaction mechanism to be tested is the effect of cooling. Figure 78 charts the mass-transfer results in which the model brine of Table 15 is cooled from 100°C to 60°C. The solution is initially saturated with respect to quartz, sphalerite, and galena. Over the 40°C temperature drop, about 5.0×10^{-6} moles (0.46 mg) of sphalerite, 9.0×10^{-8} moles (0.021 mg) of galena, and 5.0×10^{-4} moles (29.4 mg) of quartz are precipitated per kg $\cdot$ H_2O. The temperature drop also caused the oxygen fugacity to vary from 10^{-55} to 10^{-65} bars, while pH is slightly modified from 5.0 to 4.9. Precipitation of the secondary minerals forces an accompanying decrease in the concentration of most of the metal-chloride complexes, sulfide species, and aqueous silica. The change in temperature and oxidation state are very effective at shifting the sulfate to sulfide ratio of the solution, as witnessed by the SO_4^{2-} decrease (Figure 78).

Within the first 10°C of cooling, about 35% of the final mineral masses have precipitated. It takes roughly 30°C drop in temperature to achieve a recovery of at least 85% of the sulfide minerals. Further observations of this type are listed in Table 18. Whether or not a cooling of 40°C is geologically reasonable is debatable. To localize enough ore

Table 16. Mass of sphalerite precipitated in reaction with dolomite as a function of salt concentration

Case *	NaCl Concentration	Mass Precipitated	
	(molality)	(moles/kg)	(mg/kg)
A	1.0	3×10^{-7}	0.03
B	2.0	3×10^{-6}	0.30
C	3.0	4×10^{-6}	0.35
D	4.0	5×10^{-6}	0.50
E	5.0	8×10^{-6}	0.75
F	6.0	1×10^{-5}	1.10

(* - T = 100°C, pH = 5.0

Table 17. Mass of sphalerite precipitated in reaction with dolomite as a function of temperature

Case *	Temperature	Mass Precipitated	
	(°C)	(moles/kg)	(mg/kg)
A	25	3×10^{-7}	0.03
B	50	6×10^{-7}	0.06
C	75	8×10^{-7}	0.07
D	100	3×10^{-6}	0.30
E	125	1×10^{-5}	1.00
F	150	3×10^{-5}	3.00

(* - 2.0 m NaCl, pH = 5.0)

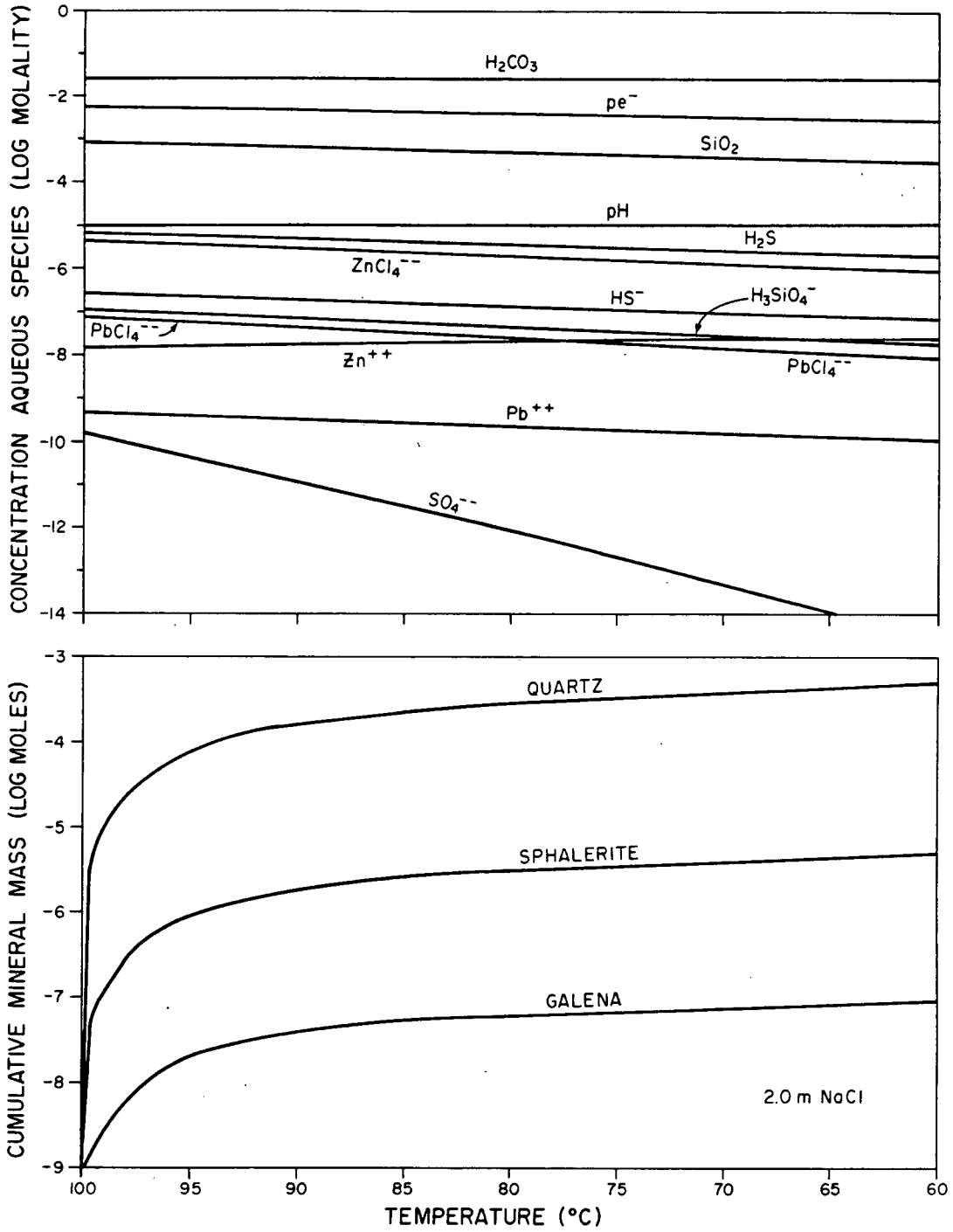

Figure 78. EQ3/EQ6 simulation showing the effect of cooling the metal-sulfide brine from 100°C to 60°C.

Table 18. Relative masses of minerals precipitated in cooling from 100°C to 60°C (per kg H_2O)

Temperature Drop (from 100°C)	Product Minerals *		
	Galena	Sphalerite	Quartz
10°C	43%	37%	32%
20°C	71%	65%	59%
30°C	89%	85%	81%
40°C	100%	100%	100%
	(0.021 mg)	(0.46 mg)	(29.4 mg)

(* - Mineral masses at T = 60°C are defined as 100% reference points.)

through this size of temperature change would require extremely high geothermal gradients. Based on the heat-transport results, modest changes in temperature of $10^{\circ}C$ are more likely to occur. The results of Figure 78 indicate that even if large changes in temperature do occur, large flow rates and long periods of time are needed to form a major ore deposit by the cooling mechanism.

Different geochemical conditions than assumed here will change the effectiveness of pH shift and cooling in ore precipitation. Anderson (1977, 1975) also evaluated the effect of pH shift and cooling on the precipitation of galena and sphalerite. Figure 69 summarizes some of his results in which the solubility contours of 10^{-5} m of Pb, Zn, and reduced sulfur $S_{(r)}$ are superimposed over the sulfur speciation field. Anderson's papers demonstrated that both processes can deposit appreciable quantities of metal if the fluid is acidic. As one example, a pH change from 4.0 to 4.3 can produce about 7 mg/kg H_2O galena, while a temperature change from $100^{\circ}C$ to $90^{\circ}C$ can result in about 4 mg/kg H_2O galena. The range of conditions over which these mechanisms are effective, however, are limited in the case of lead to brine with pH less than 4.0 and f_{O_2} of 10^{-50} to 10^{-51} bars (Figure 69). Anderson suggests this acidity level is not common in basinal brines, and therefore concluded that transport of both metal and sulfide in the same fluid is not geologically important in the formation of Mississippi Valley-type deposits.

Sverjensky (1981) has recently found a possible exception to Anderson's conclusion. Sulfur-and lead-isotope data from the Viburnum Trend of southeast Missouri support a transport model where sulfur is carried with metal to the site of deposition (Sverjensky, Rye, and Doe, 1979). Various lines of geologic and geochemical evidence led Sverjensky (1981) to conclude that sulfate reduction could not have been an important mechanism in this region. He recalculated the solubilities of galena and sphalerite using new

thermodynamic data, and found that concentrations could be greater than those of Figure 71. As one example, Sverjensky computes solubilities of 6×10^{-6} m (1.2 ppm) for lead and 4×10^{-5} m (2.6 ppm) for zinc, at a pH = 5.0 and a temperature of 100°C. This data suggests that the sulfide-type brine model may be an important factor in stratabound ore genesis. Large flow rates would still be required, however, if changes in pH and temperature are responsible for ore precipitation.

A Preliminary Application to the Pine Point Deposits

Up to now we have seen the numerical results for a wide variety of idealized geologic configurations. These models can provide much insight into the factors controlling fluid velocities, subsurface temperatures, metal concentrations in brines, and possible scenarios of sulfide precipitation at the ore-forming site. The ultimate practical use of the models, however, is to assess ore-genesis theories of gravity-driven flow in specific basins and ore districts.

The object of this final section is to demonstrate the significance of the modeling results with a quantitative analysis of a field example. For this purpose, the Pine Point lead-zinc ore district is examined in relation to regional paleoflow systems in the Western Canada sedimentary basin of Alberta and the Northwest Territories. The treatment is relatively brief at this stage. Emphasis is first placed on understanding the possible role of ancient transport processes on a regional scale, not the actual prediction of local ore distribution at the depositional site. More stratigraphic and hydrologic detail is needed before a reasonable thorough assessment can emerge. The results given below are preliminary in nature and should be regarded as such.

The first step in constructing a quantitative model of fluid flow is

to identify the geometry and geologic configuration of the basin. The general geology of Pine Point and its structural setting in the Western Canada sedimentary basin was introduced in Chapter 2 (see Figures 3 and 4). Figure 79 shows further details of the regional setting of Pine Point, the Keg River barrier (Middle Devonian), and the accompanying structural features in the Great Slave Lake region. Two cross-section lines are marked on the map: section A-A′ crosses the basin in a northwest-southeast direction that is transverse to the barrier complex, and section B-B′ crosses the basin in a southwest-northeast direction that is parallel to the barrier complex. The terms barrier complex or Keg River barrier are synonymous for the carbonate strata of Middle Devonian age that extend from the Keg River Formation to the Slave Point Formation inclusive, as defined by Williams (1981).

The stratigraphy along section A-A′ is shown in Figure 80, and the stratigraphy along section B-B′ is shown in Figure 81. Lithological facies are represented in a simplified form in both sections, particularly for the long profile B-B′. Detailed descriptions of these stratigraphic units appear in several publications, the most recent of which are Williams (1978, 1981). In general, the subsurface succession includes: a basal unit of Middle Devonian carbonates and evaporites, a thick sequence of Upper Devonian shales, more shales and carbonates of Mississippian age, and shales and sandstones of Cretaceous age which overlie the older strata unconformably.

A gravity-driven fluid-flow model requires a topographic gradient to develop basinal flow systems. Geologic evidence suggests that the western margin of the Western Canada basin has been topographically higher than the eastern platform of the basin since the early Mesozoic. This was due to a gradual orogenic uplift in the Cordillera, which culminated with the formation of the Rocky Mountains in Eocene time (McCrossan and Glaister, 1964). Tóth

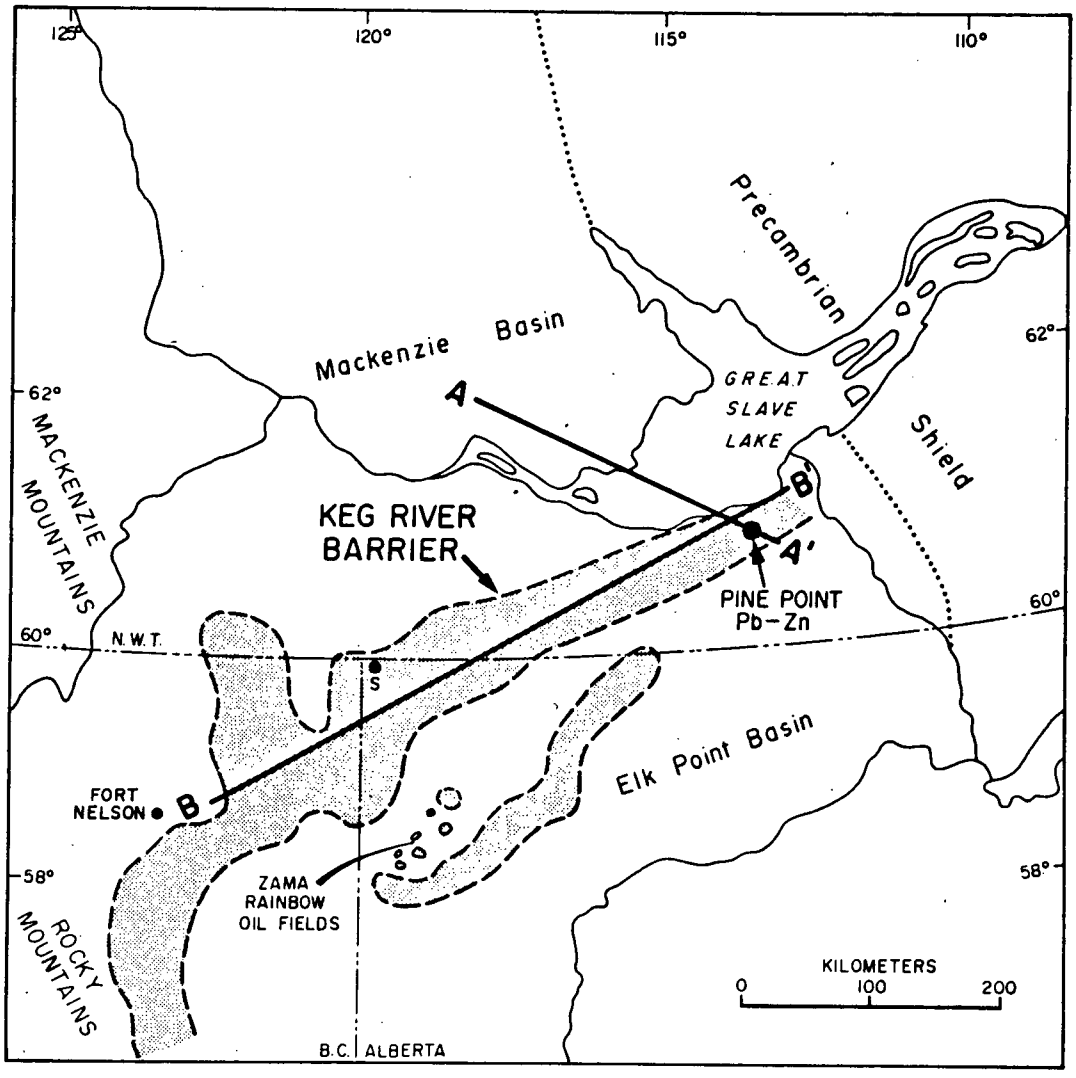

Figure 79. Map of the Great Slave Lake region showing the location of Pine Point, the Keg River barrier, and the section lines A-A′ and B-B′. Geology is after Law (1971).

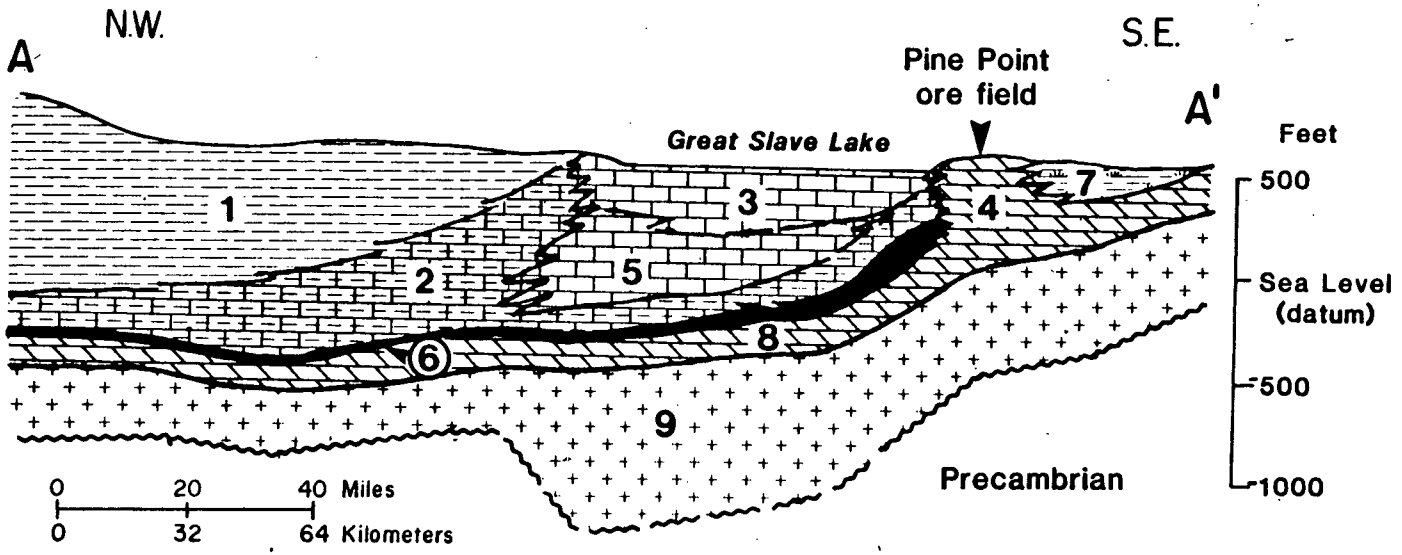

LEGEND

1 Hay River Formation, shale
2 Horn River Formation, limestone & shale
3 Slave Point, Sulphur Point Formations, Limestone
4 Middle Devonian carbonate barrier complex
5 Pine Point Formation, limestone
6 Bituminous Member
7 Muskeg Formation, evaporites
8 Lonely Bay Formation, dolomite (Keg River Fm.)
9 Chinchaga Formation and older Devonian evaporites

Figure 80. Cross section A-A′, transverse to the barrier complex (after Macqueen et al., 1975).

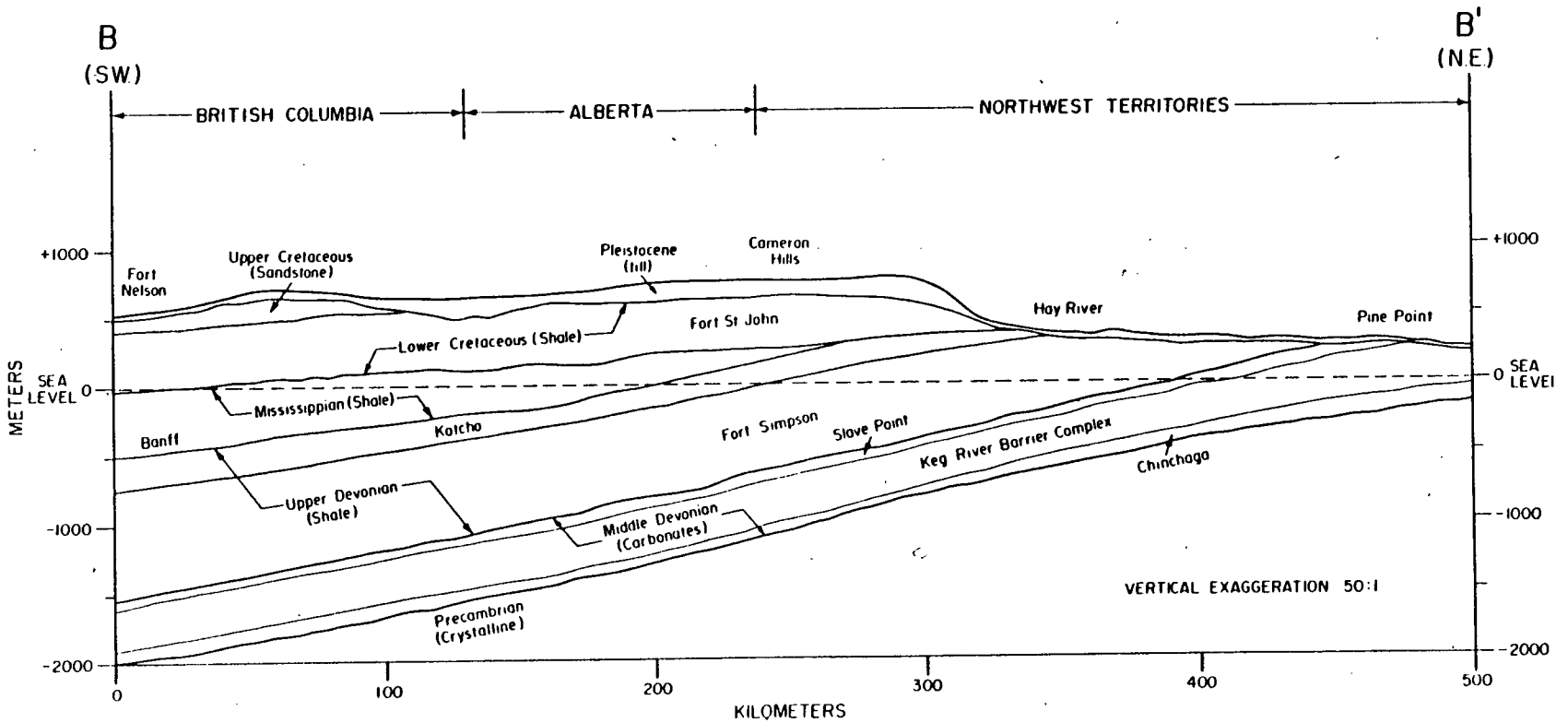

Figure 81. Cross section B-B′, longitudinal to the barrier comples from Fort Nelson, B.C. to Pine Point, N.W.T.

(1978) has studied paleoflow systems in a large area of northern Alberta, and he found that the existing flow patterns of the basinal brines owe their origin to Pliocene topography. Furthermore, Tóth contends that much of northern Alberta became geologically and topographically mature in the period between Late Mississippian and Early Cretaceous, a period of about 175 million years. A well-developed, topography-controlled gravity flow system operated during this time interval, with major fluid flow from southwest to northeast across the emerging basin (see Tóth, 1978). The present-day existence of large flow systems from the Rocky Mountains to the Canadian Shield is also documented in other studies, including those of van Everdingen (1968) and Hitchon (1969a, 1969b).

Based upon the discussion above, we can reasonably assume that the major direction of fluid flow through the Keg River barrier was likely to the northeast (parallel to section B-B′) for much of the Mesozoic and Cenozoic eras. According to Kyle (1980), there is no geologic evidence to constrain the date of lead-zinc mineralization at Pine Point, except that it is post Devonian. The cross section in Figure 81 can be used to form a hydrogeologic configuration for a two-dimensional representation of the basin. This will provide a good approximation of the flow field because of the very long dimension of the Western Canada basin in the northwest-southeast direction (Figure 3). Hitchon (1971) has mapped the present-day hydraulic-head distribution in the barrier complex, and he found that the flow pattern is mostly longitudinal to the barrier, with fluid flow updip toward the northeast and Pine Point.

Figure 82 shows an example of one of the hydrogeologic simulations that have been performed along section B-B′. In Figure 82a, the geologic configuration of Figure 81 is simplified to four major hydrostratigraphic

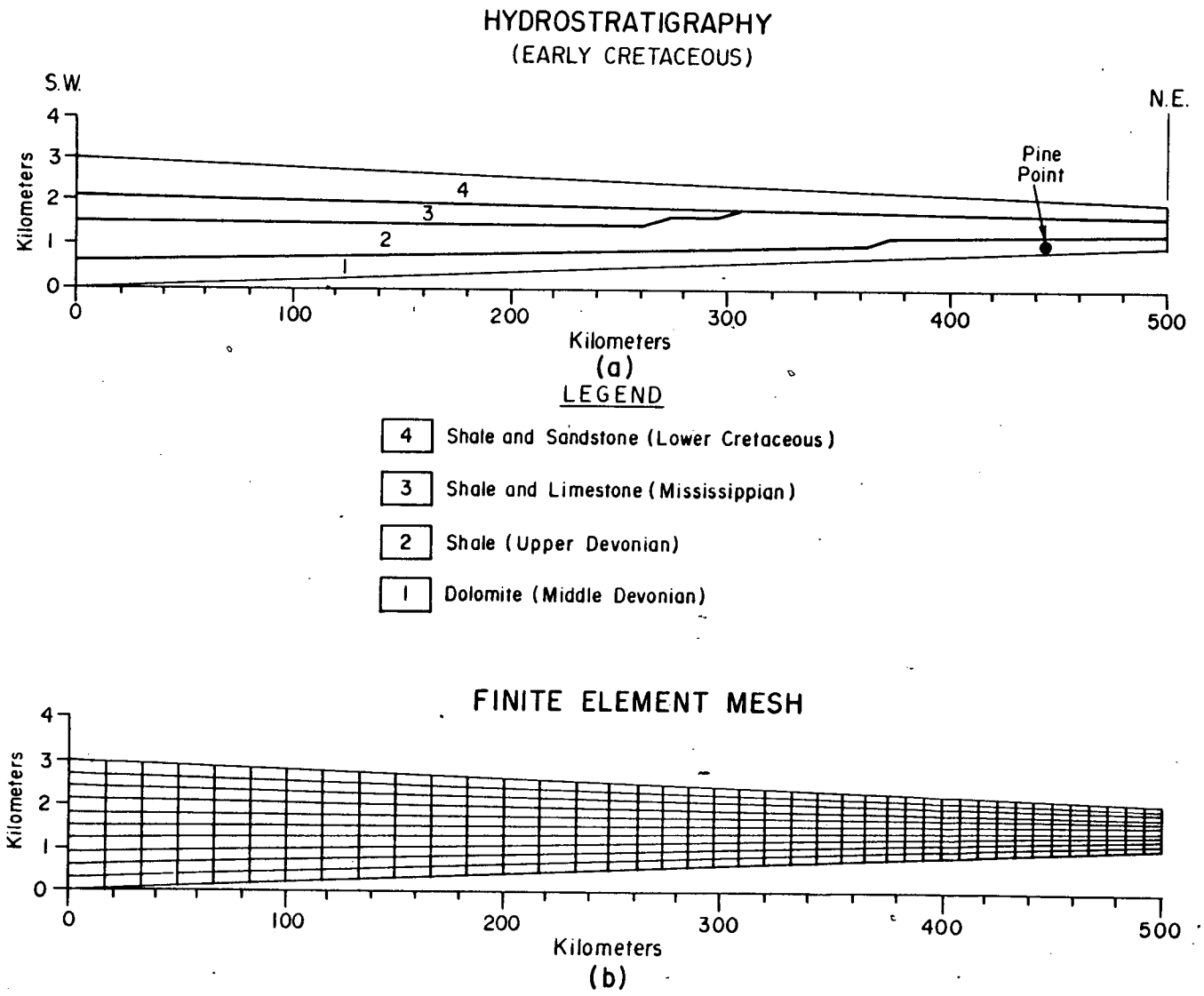

Figure 82. Pine Point model.

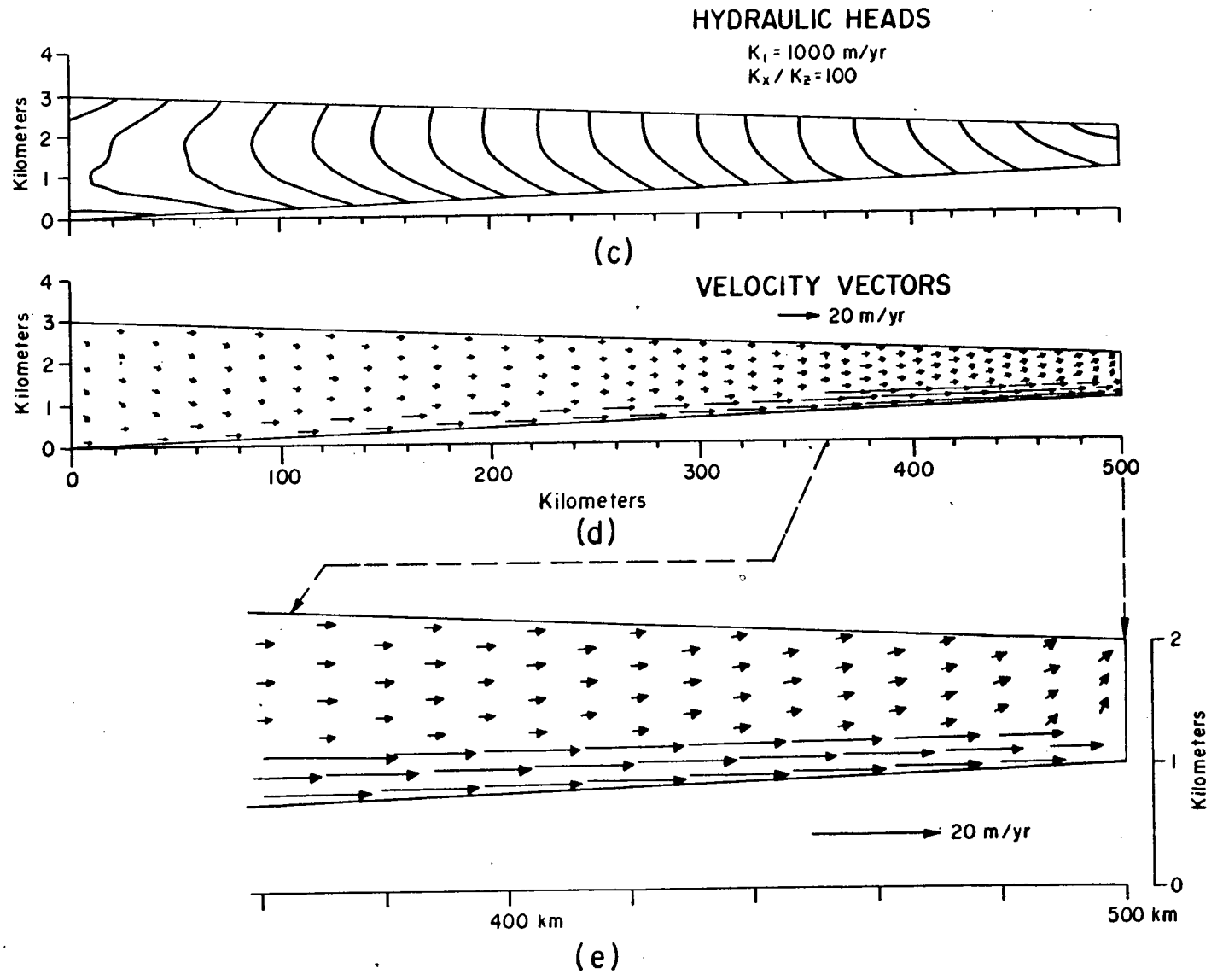

Figure 82. Pine Point model. (Continued)

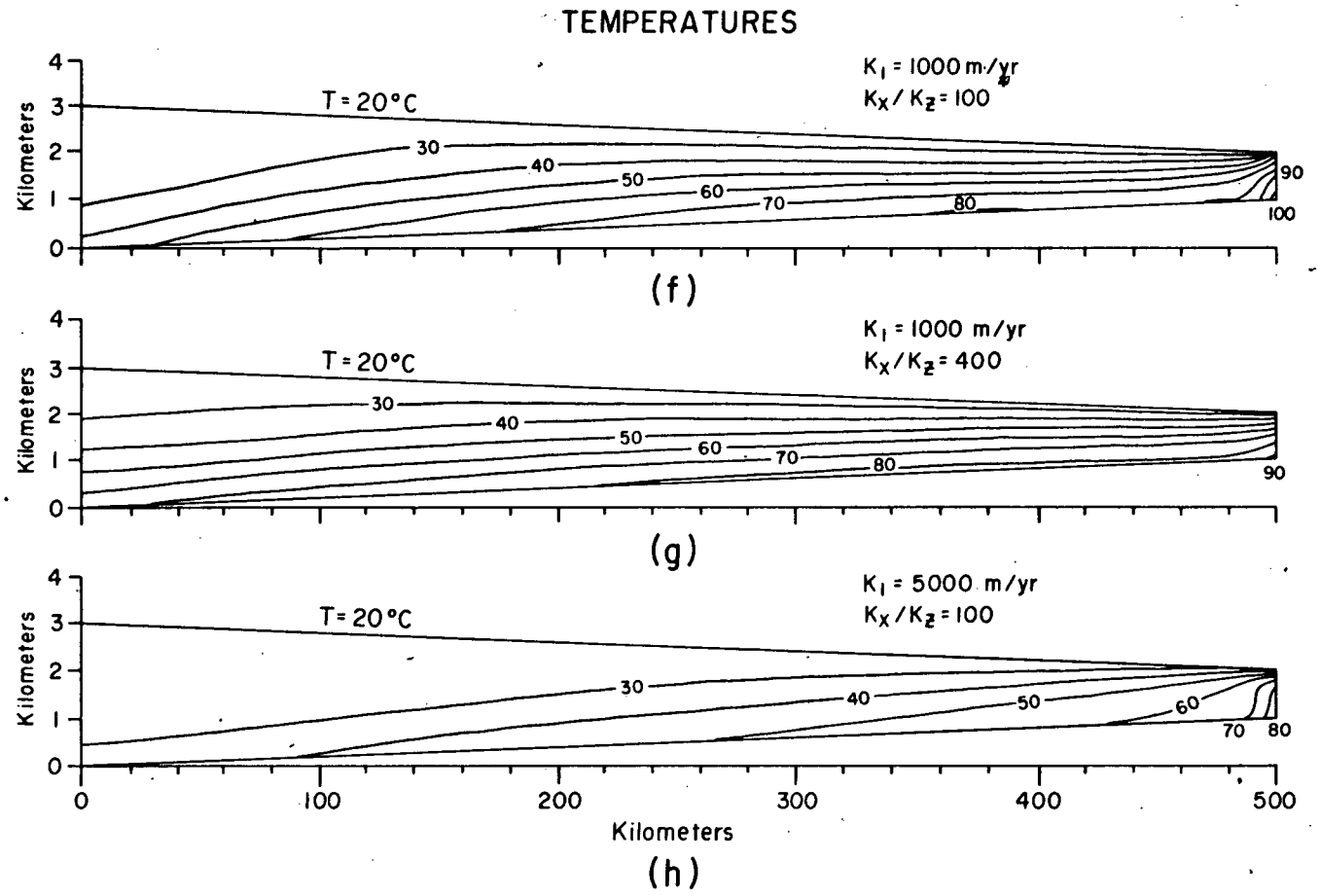

Figure 82. Pine Point model. (Continued)

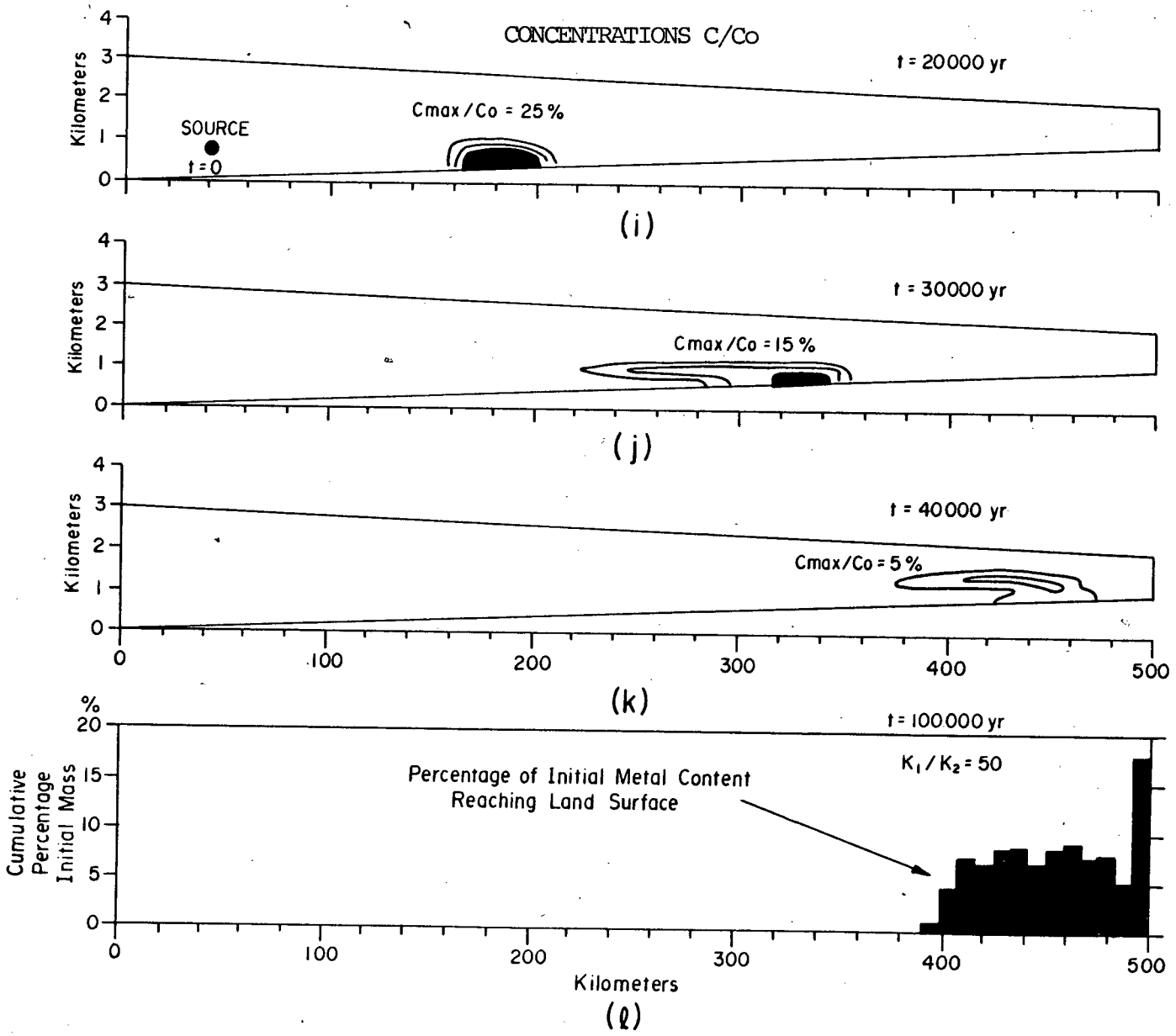

Figure 82. Pine Point model. (Continued)

units. The basin is 500 km in length, and varies in thickness along the wedge from 3000 m at x = 0 km to 1000 m at the groundwater divide at x = 500 km. A low topographic relief is reflected in a gentle water-table gradient of 2 m/km. The lower boundary represents the base of the deepest permeable formation, which in this case is the Keg River barrier complex (Figure 81). The hydraulic conductivity and porosity of evaporites are very low (Tables 7 and 8), therefore, the top of the Chinchaga Formation makes a convenient place to site the impermeable base of the model. This impermeable boundary has a gentle slope, which rises 2 m/km toward the northeast. In the east, a groundwater-flow divide is arbitrarily selected at a distance of 50 km east of the existing location of Pine Point (Figure 82a). The formations probably thinned to a feather edge somewhere beyond this region. The western flow divide is located in an area to the east of Fort Nelson (Figure 79), near the edge of the present-day Foothills of the Rocky Mountains. The stratigraphic section thickens considerably (∿ 6 km maximum) toward the thrusted section of the basin, west of the modeled section.

Figure 82a is meant to depict the geologic setting of the basin in the Early Cretaceous, about 125 million years ago. At this period in time the basin was geologically mature and gravity-flow systems were probably well developed, due to uplift in the Rocky Mountain region. The exact thickness of the rocks overlying the Pine Point site at this time are unknown, mainly because the later Paleozoic and Mesozoic strata are now absent in the region. Williams (1979) estimates that a maximum of 750 m of Upper Devonian shale, 300 m of Carboniferous strata, and 0-1500 m of Jurassic-Cretaceous clastics may have overlain the Pine Point area, but are now missing because of erosion. These observations are consistent with the burial history made by Deroo et al. (1977) for Devonian rocks in Alberta. They concluded that the

maximum depth of burial was probaly less than 1500 m on the eastern shelf of the Western Canada sedimentary basin. Based on coal-rank studies, they also estimated that approximately 1800 m of sediments were eroded from the basin, after the uplift of the Rocky Mountains in the Eocene. It is probable, therefore, that the Pine Point area was covered by at least 1000 m of strata over the period from the Permian to the Tertiary.

For the purpose of this model (Figure 82a), 500 m of Upper Devonian shale (Unit 2) are assumed to be present at Pine Point, which are unconformably overlain by about 400 m of Jurassic-Cretaceous clastics (Unit 4). Over 300 m of Mississippian strata are truncated further west in the basin. Approximately 350 m of Middle Devonian carbonates (Keg River Fm. to Slave Point Fm. inclusive) are represented at the Pine Point site. All four of the hydrostratigraphic units thicken downdip in the basin.

Table 19 lists the set of material properties and model parameters used in the Pine Point simulation. Porosity data are estimated from Table 8 and the values compiled by Hitchon (1968). Representative values of hydraulic conductivity are chosen from Table 7 and the results from the preceding sensitivity simulations. Tóth (1978) has analyzed the present-day permeability data for a large area of study about 300 km south of Pine Point. His data, which was compiled from drillstem tests and core analyses, can also be used as a guide for selecting the possible range of hydraulic conductivities in this model. In terms of ore formation, the most critical permeability parameter is the value of hydraulic conductivity assumed for the barrier complex. A value of 1000 m/yr (about 3 darcy) is chosen in Table 19 for the principal hydraulic conductivity in the x-direction. It is a conservative number for a karst-type aquifer, but probably representative of an aquifer in the deep subsurface. Vogwill (1976) has performed extensive aquifer tests on the

Table 19. Pine Point Simulation : input parameters data

Parameter	Symbol	Hydrostratigraphic Unit 1	2	3	4	Units
Fluid Flow						
Porosity	ϕ	0.25	0.10	0.10	0.15	fraction
*Horizontal hydraulic conductivity	K_{xx}	1000.00	20.00	50.00	25.00	m/yr
*Vertical hydraulic conductivity	K_{zz}	10.00	0.20	0.50	0.25	m/yr
Reference fluid density	ρ_0	998.2	(all units)			kg/m^3
Reference fluid viscosity	μ_0	1.0×10^{-3}	(all units)			Pa • S
*Salinity gradient	-	0.01	(all units)			%NaCl/m
Heat Transport						
Thermal conductivity of fluid	κ_f	0.63	(all units)			W/m • K
Thermal conductivity of rock solids	κ_s	3.0	1.9	2.5	2.0	W/m • K
Specific heat capacity of fluid	C_{vf}	4187.0	(all units)			J/kg • K
Specific heat capacity of rock solids	C_{vs}	1005.0	(all units)			J/kg • K
Longitudinal thermal dispersivity	ε_L	50.0	10.0	10.0	10.0	m
Transverse thermal dispersivity	ε_T	1.0	1.0	1.0	1.0	m
*Geothermal heat flux at base	J	70.0	(constant)			mWm^{-2}
*Temperature at water table	T_0	20.0	(constant)			^oC
Mass Transport						
*Longitudinal dispersivity	α_L	50.0	10.0	10.0	10.0	m
Transverse dispersivity	α_T	50.0	1.0	1.0	1.0	m
Apparent diffusion coefficient	D_d	3×10^{-3}	(all units)			m^2/yr

(* - Parameters varied for different simulations.)

barrier-complex rocks at Pine Point, and based on his data, the present-day hydraulic conductivity reaches a maximum of about 5000 m/yr.

A salinity gradient of 0.010 % NaCl/m is assumed to have existed at this stage in geologic time. It produces a salinity of about 10% NaCl (2.0 molal) at the Pine Point site and a maximum salinity of 20% NaCl (4.3 molal) at the western end of the basin. Increasing the proposed salinity profile will decrease fluid velocity (Figure 32 e), but for an increase to 15% NaCl (at the ore-forming site) the change will be small. Several field studies support this assumed salinity range. For example, fluid-inclusion studies by Roedder (1968) indicate that brine salinity at Pine Point was between 10% and 25% NaCl. Present-day salinity variations in the Devonian strata of western Canada range from 100,000 to 200,000 mg/liter as total dissolved solids (Hitchon and Horn, in press). Formational fluids in contact with the Chinchaga evaporites commonly exceed 200,000 mg/liter total solids. Brine samples from the Keg River barrier have been analyzed by Billings, Kesler, and Jackson (1969), at the point marked 'S' in Figure 79. They found that total dissolved solids average around 140,000 mg/liter, which also supports the modeled salinity gradient.

All of the heat and mass-trasnport coefficients are chosen as representative values, based on the simulations presented earlier and the type of lithologies involved. Thermal conductivities are obtained from Table 10, and the dispersivity coefficients are based on the range given in Table 11. The geothermal heat flux of 70 mW/m^2 and assumed surface temperature of $20^{\circ}C$ are also defensible as geologically reasonable. The thermal conductivities and heat flow are comparable to present-day data reported by Majorowicz and Jessop (1981) for western Canada.

The finite-element mesh for the Pine Point model is shown in

Figure 82b. It is of similar shape to the mesh used in the sensitivity analysis (Figure 17), but now it contains twice as many elements. This provides a greater degree of accuracy, which is needed when progressing from simple basins to more realistic and complicated geologic configurations. Because so many elements are present, only the quadrilateral cells, and not the triangular elements, are drawn. Also notice that the vertical exaggeration of the sections in Figure 82 are now 20:1, which is double the exaggeration used in the sensitivity analysis.

The hydraulic-head distribution and resulting flow pattern are shown in Figures 82c, 82d, and 82e. Maximum fluid-flow velocities of 20 m/yr occur in the barrier-complex unit, near the downstream end of the basin. This karstic aquifer is fifty-times more permeable than the overlying shales of Unit 2 (Fort Simpson Fm.), and because of the high contrast it has the greatest influence on the basin flow systems. Fluid flow is directed down across the less-permeable beds in the recharge end of the basin and upward in the discharge end of the basin. Cross-formational flow could easily provide a mechanism for the transport of metals into the Keg River barrier in the recharge part of the flow system. Fluid flow in the midsections of the basin is essentially lateral and updip. Comparison can be made with some of the simulations given in the sensitivity analysis to conceptualize how the flow pattern in Figure 82d would be different for other configurations of topography, basement structure, or hydraulic-conductivity structure.

Let us digress from Figure 82 for a moment and examine Figure 83. The purpose of showing this diagram is to demonstrate the correlation between the flow systems generated by the numerical model and actual flow systems observed in real sedimentary basins. The upper diagram of Figure 83 shows the present day hydraulic-head distribution along a west-east cross section

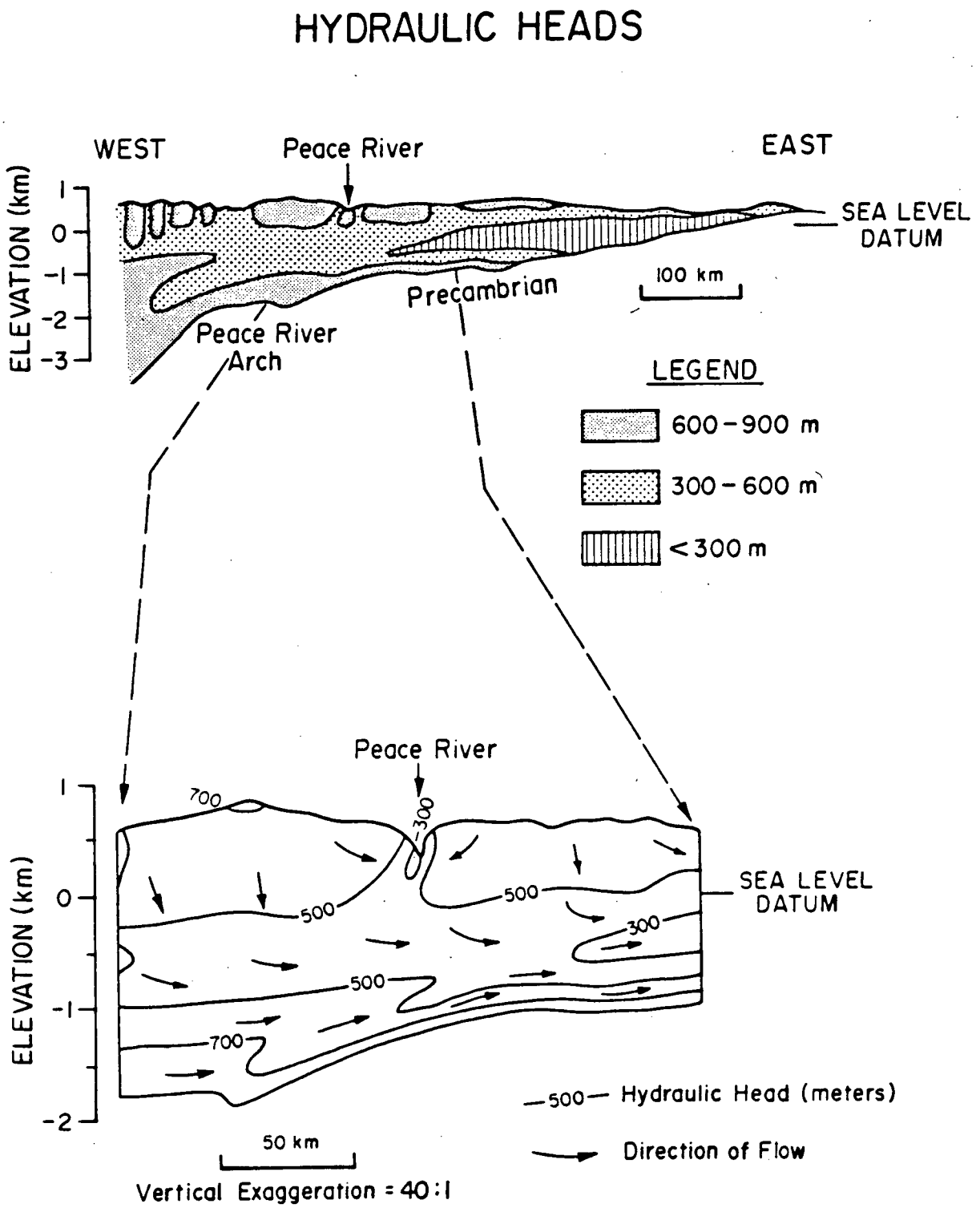

Figure 83. Hydraulic-head pattern in north-central Alberta (after Hitchon 1969a, 1974).

through north-central Alberta, as mapped by Hitchon (1969a). The lower diagram is a more detailed and contour expansion of the flow regime, which is modified from Hitchon (1974). The location and geology of this cross section can be found in Figures 3 and 4, where it is marked as section B-B′. The zones of low hydraulic head coincide with major topographic lows and in the highly permeable reef carbonates in the Upper Devonian strata. The presence of this high-permeability layer causes the focusing of fluid flow that is shown in Figure 83. Besides the influence of an irregular topography, many similarities exist between the present-day hydraulic heads and the flow patterns from the theoretical model of Figure 82d. One point of special interest is the increase in hydraulic head with depth in the recharge end of the basin (Figure 82c). This feature was shown earlier to be caused by the salinity effect on fluid density (Figure 27). Future studies of hydrodynamics of real sedimentary basins will have to consider this phenomena in order not to misinterpret the true fluid-flow directions.

The simulated temperature pattern for the Pine Point basin model is given in Figure 82f. It shows that temperatures of at least 80°C are possible, at the depth of the assumed Pine Point deposit (see Figure 82a). Remember from the sensitivity models that this maximum temperature value is highly dependent on the prescribed boundary conditions, among other factors. A higher geothermal flux or higher surface temperature will yield even greater subsurface temperatures than the 80°C - 100°C range shown here. Fluid flow causes the geothermal gradient to be depressed where the Keg River barrier is recharged, and the gradient is elevated in the discharge end of the flow system. Figures 82g and 82h illustrate the temperature changes that are possible if the hydraulic conductivity of the formations are modified. In Figure 82g, the anisotropy ratio of horizontal to vertical hydraulic conducti-

vity is increased to 400 : 1. This allows less vertical flow of water, which in turn allows a smaller amount of vertical thermal convection, relative to the 100 : 1 ratio of Figure 82f. The results is a less disturbed temperature field in the recharge and discharge ends of the basin.

A second example of the effect of convection is shown in Figure 82h. In this simulation, the hydraulic conductivity of the barrier complex is increased to 5000 m/yr, which causes a five-fold increase in the velocities of Figure 82d. Convective heat transfer is now quite large, the result being that temperatures are substantially lowered at the proposed depositional site to about 60°C. On the other hand, if flow rates are too low, thermal convection will not be sufficient to carry enough heat from the deeper parts of the basin up into the thinner shelf. Nor would the flow volumes be adequate to form a major ore deposit over a reasonable period of time.

Figure 84 presents the relationship between the horizontal hydraulic conductivity of the barrier-complex aquifer and the resulting average linear velocity and temperature. The curves are plotted for the reference site of Pine Point (Figure 82a), which is at a depth of about 1200 m below the water-table. The heat flow on the basal boundary is held at a constant 70 mW/m^2, and the temperature at the water table is 20°C. It is clear that a sacrifice in fluid velocity is required to maintain a warm temperature, or vice versa. Velocities up to 25 m/yr are possible in this model, with accompanying temperatures above 70°C.

Fluid-inclusion work by Roedder (1968) and Kyle (1977) indicates that the ore-forming fluids at Pine Point ranged in temperature from 51°C to 99°C. The thermal models given above are therefore consistent with the field data. Geothermal gradients in these simulations (Figure 82f, g, and h) are as low as 20°C/km in the recharge end of the basin, and generally increase to about

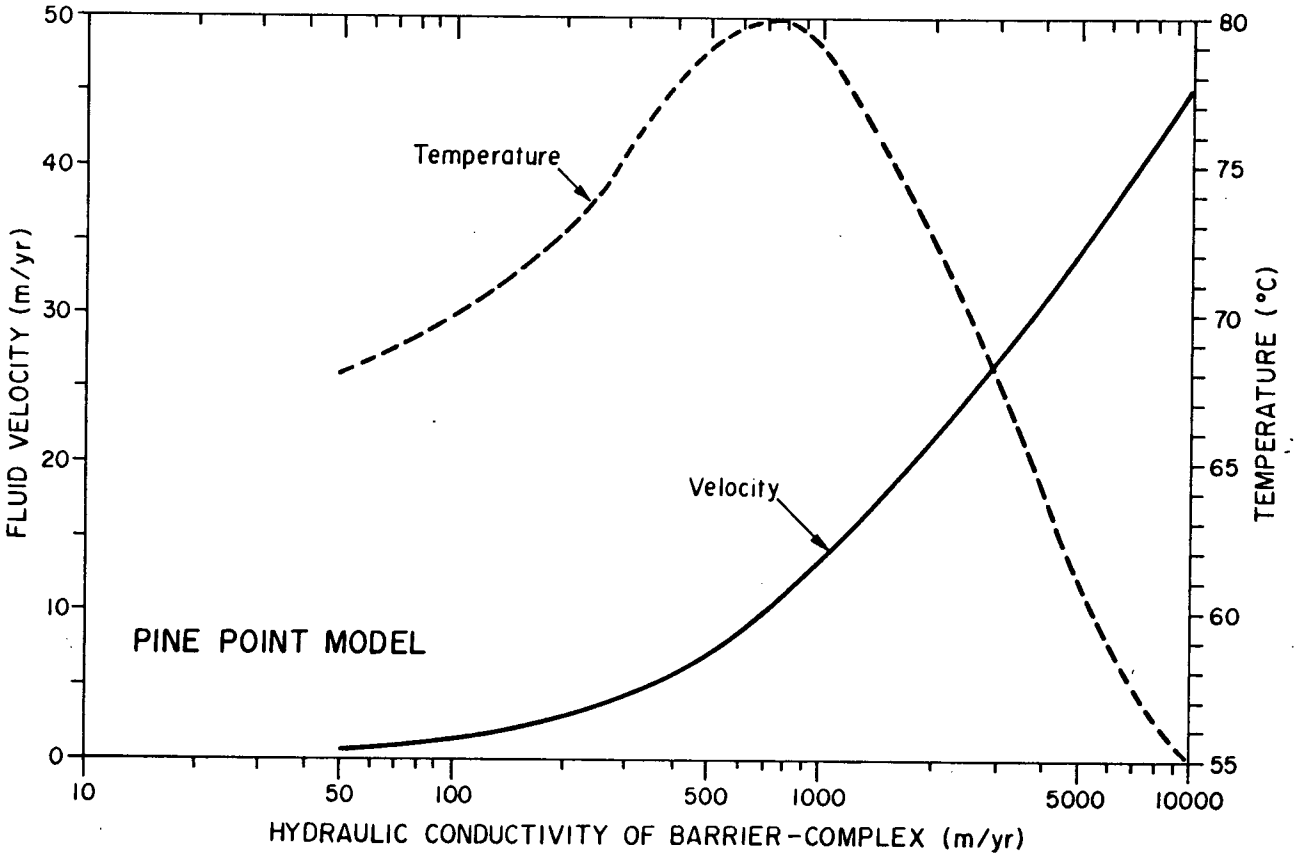

Figure 84. Fluid velocity and temperature at the Pine Point site as a function of the horizontal hydraulic conductivity of the barrier complex.

60°C/km in the downstream section of the basin. Very high gradients of 80°C/km or more are possible near fluid-flow divides.

Present geothermal gradients in the Western Canada sedimentary basin range from less than 25°C/km to over 50°C/km, and heat flow varies between 50 mW/m^2 and 100 mW/m^2 (Majorowicz and Jessop, 1981). Figure 85 is a map of central Alberta from Deroo et al. (1977) that shows a trend of increasing geothermal gradient across the basin, from less than 30°C/km in the Foothills region of the Rocky Mountains to over 50°C/km near the mid-section of the basin. This pattern is probably the result of downward fluid flow into the basal carbonate strata, and northeasterly movement of fluids updip, as in Figure 83. Several closed-contour highs and lows are also present on the geothermal gradient map, and they appear to be related to topography-induced convection between major river valleys, much as in the manner depicted in Figure 58d. Present-day temperature data in the barrier complex itself are scarce. Majorowicz and Jessop (1981) report very high values of heat flow (100 mW/m^2) in the northeast corner of British Columbia (see Figure 79), and they also report temperatures in excess of 90°C for basement rocks below the barrier complex. It is safe to conclude from the discussion above that existing geothermal data in western Canada support the theoretical heat-flow interpretations.

Figures 82i - 82ℓ show the results of a mass-transport simulation for the Pine Point model. The purpose of this simulation is to document the influence of dispersion on diluting the metal concentration of a brine flowing through source beds in the western side of the basin to the eastern-platform edge. The fluid-flow pattern is that of Figure 82d. Contours representing 5%, 10%, and 15% of the initial concentration Co have been plotted. Also plotted above the plume in each time diagram is the approximate maximum

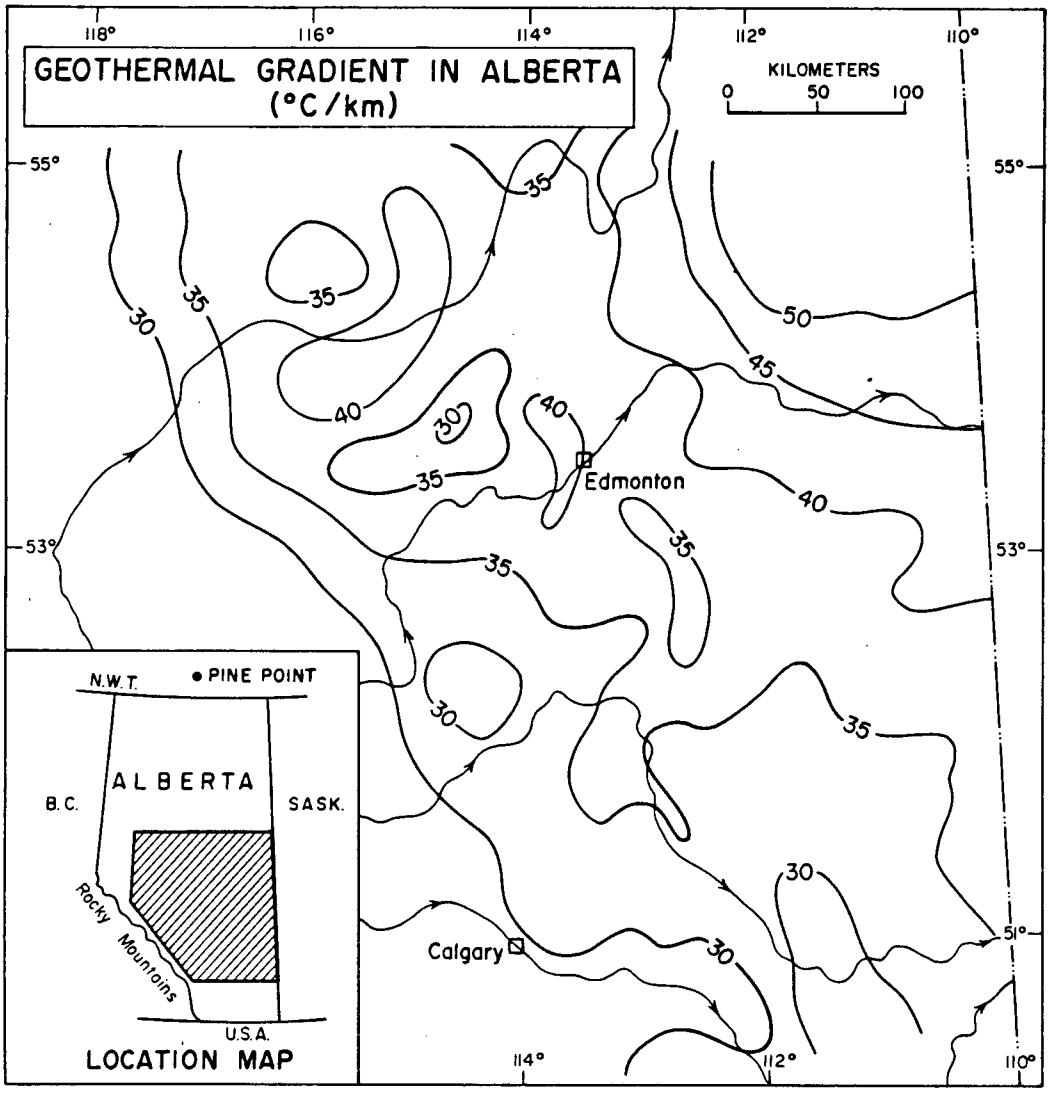

Figure 85. Geothermal gradient in central Alberta showing the effects of regional fluid flow (after Deroo et al., 1977).

concentration predicted in the Keg River barrier. Areas with relative concentrations greater than 15% C/Co are shaded. A lateral dispersivity of 50 m is assumed for the karstic aquifer (Unit 1), and a value of 10 m is assigned to the overlying strata. Transverse dispersivity is a constant 1 m in all four layers (Table 19).

By time t = 30,000 yr, the mass has travelled about 300 km and only 15% of the source-bed concentration level is present in the basal aquifer. Mass is also starting to be advected upward into the Devonian shales at this stage. At t = 40,000 yr, the center of mass of the metal-bearing pulse has just passed the proposed Pine Point location. Based on this simulation result, it appears that 5 - 10% of the metal concentration leaving the source beds deep in the basin would reach the Pine Point site. Nearly all of the mass is discharged upward in the basin beyond x = 400 km, as shown by the particle-distribution histogram of Figure 82ℓ. The last bar in this histogram represents the fraction of mass that passed through the entire length of the aquifer, while the later arriving, bell-shaped section of the histogram represents the mass that is discharged up into the shale beds relatively early.

We have seen that metal concentrations are dependent on the amount of dissolved sulfide, salinity, and temperature. If aqueous sulfide is low, then substantial metal concentrations can exist. To deposit ore, however, requires that either sulfide is provided externally at the site, or that accompanying sulfate is reduced to sulfide at the site. Small amounts of metal and sulfide can be carried together in equilibrium, but the pH must be slightly acidic and the temperature should be greater than about 100°C. Unless both metal and sulfide are continually added to the fluid along the flow path, long-distance transport can be effectively ruled out for this transport model because of the

diluting effects caused by dispersion. It was also shown that even if dispersion is small, the precipitation mechanisms of pH shift and cooling require that large flow rates occur over a long period of time to form a major ore deposit.

The metal concentrations of the brines that passed through Pine Point and the precipitation mechanism causing ore deposition are not known. Geologic evidence appears to indicate that the addition of H_2S to a metal-bearing brine at the site caused ore deposition. Jackson and Beales (1967) proposed that destruction of abundant organic matter in the barrier-complex rocks by sulfate-reducing bacteria was a probable source of H_2S. Bacterial degradation of organic matter can also generate large volumes of methane through anaerobic fermentation, which could have acted as an important reducing agent. It is also noted, however, that hydrogen sulfide is more abundant when the organic matter is rich in sulfur, as is often the case with carbonate-evaporite sequences (Tissot and Welte, 1978).

Abundant organic matter, heavy oil, and bitumen occur within the barrier complex at Pine Point (Macqueen and Powell, in press). Hitchon (1977) and Macqueen et al. (1975) have also shown that many of the shales, carbonates, and evaporites in the Keg River barrier region are relatively rich in metals, particularly zinc. Present-day brines in the barrier complex are noted to be metal-rich. Billings, Kesler, and Jackson (1969) report an average zinc concentration of 19 mg/liter for brine samples taken downdip in the barrier, about 350 km southwest of Pine Point (at point 'S' in Figure 79). Hitchon (1981) reports an average zinc concentration of 1.4 mg/liter in Alberta formation waters from Devonian strata, but also reports that up to 91 mg/liter have been found in some locations. The likely range of metal concentrations in ancient ore-forming brines is debated. Ranges of 10 - 1000 mg/kg • H_2O are

commonly defended (Sverjensky, 1981), but maximum concentrations were probably less than a few hundred mg/kg • H_2O (Anderson, 1978). Based on the present-day brine data, a maximum level of 50 - 100 mg/kg • H_2O seems reasonable for the Western Canada sedimentary basin.

Macqueen and Powell (in press) conclude that the exact genetic relationship between lead-zinc mineralization and indigenous organic matter remains unclear at Pine Point. They also conclude, however, that in-situ generation of H_2S by sulfate reduction was probably the primary mechanism for ore precipitation. They suggest that sulfate-type brines could have reacted with small amounts of pre-existing H_2S in the barrier to produce elemental sulfur, which in turn reacted with organic matter to produce more H_2S. This abiogenic reduction mechanism has an advantage over bacterial reduction through its ability to operate at temperatures above 80°C. Whatever type of sulfate reduction took place, the continued supply of H_2S was apparently sufficient to deposit about 100 million tons of 9% lead-zinc ore (Kyle, 1980).

Although the Pine Point model of Figure 82 is preliminary in nature, it can be used to estimate the possible duration of mineralization required to account for the known ore reserves. We will assume that the ore-forming fluid leached sufficient amounts of metal from the shale bed area deep in the basin (Figure 82i). As a first estimate, a zinc concentration of about 20 mg/kg • H_2O is assumed to exist in the source beds. Figure 82k shows that only about 5 - 10% of this initial concentration or 1 - 2 mg/kg • H_2O would be present near the end of the flow system, because of dispersion along the flow path. This ore-forming concentration is in the range of minimum values suggested by Anderson (1975) and Barnes (1979). The amount of metal precipitated per kg of brine will of course depend on the local geochemical environment and how conditions varied through time. Relatively rapid deposition is indicated at Pine Point (Anderson,

1978; and others), and therefore it is likely that almost all of the metal in solution was deposited on encountering H_2S, as in Figure 74. The general paragenetic sequence of sphalerite followed by galena is observed, and both carbonate precipitation and dissolution are common in the mineralization process (Kyle, 1980).

Figure 84 can be used to estimate the possible flow rates involved in ore deposition. To convert these average linear velocities to volume-flow rates (i.e. specific discharge), the velocity is multiplied by the porosity value (0.25) of the barrier aquifer. Knowing the total cross-sectional area of flow, one can then compute the total volume of brine flowing through the barrier per unit time. The barrier complex is at least 50 km wide (Figure 79) and approximately 300 m thick (Figures 80, 81). According to Kyle (1980, 1981), the most permeable sections at Pine Point occurred in the dolomite facies of the Pine Point Group, which is over 10 km wide. The forty-some ore bodies are scattered over a stratigraphic interval of 200 m. Based on these dimensions, a conservative estimate of the effective cross-sectional flow area would be 10 km wide by 100 m thick, or 1.0×10^6 m^2. For an average velocity of 20 m/yr (Figure 84), the temperature is about 75°C and the specific discharge rate is 5.0 $m^3/m^2 \cdot yr$. Total discharge parallel to the barrier, therefore is about 5.0×10^6 m^3/yr. If only 1 mg Zn is transported per kg of brine (density = 1050 kg/m^3), then the zinc mass-flux rate is about 5250 kg/yr (5.8 tons/yr). To deposit the total zinc content of 5 million tons at Pine Point (Kyle, 1981) would require approximately 865,000 years.

Figure 86 summarizes the relationship between specific discharge, zinc precipitated, and time for deposition of 5 million tons in the Pine Point model. The style of the graph is based on a design first presented by Roedder (1960). The boxed-in region represents what are believed to be the most representative

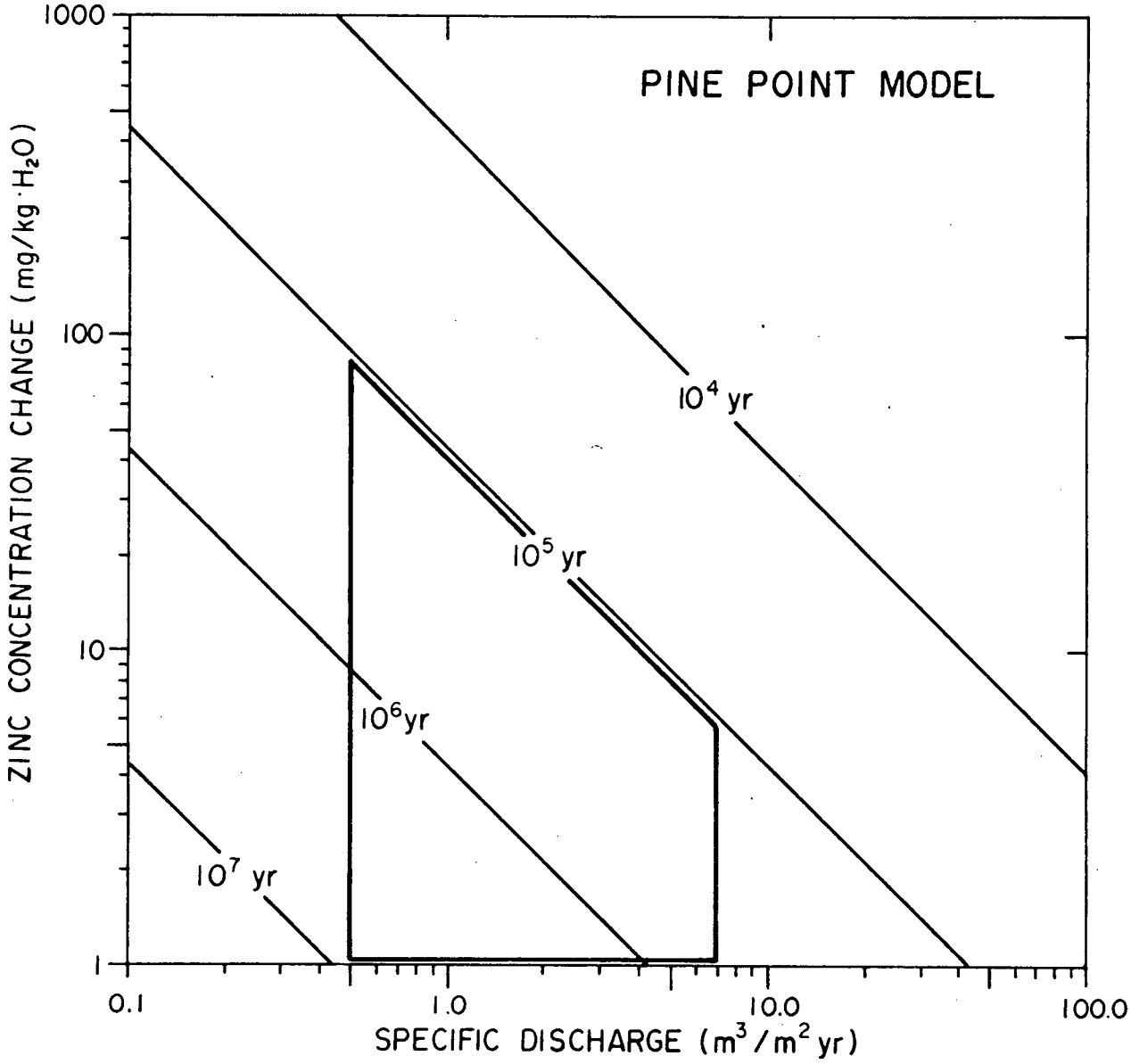

Figure 86. Relationship of specific discharge, zinc precipitated, and duration of mineralization for the Pine Point deposit.

range of variables that could have led to the formation of Pine Point. With specific discharges of 0.5-7.0 $m^3/m^2 \cdot yr$ and zinc precipitation of 1 - 100 mg/kg $\cdot H_2O$, the duration of mineralization would range from 10^5 to 10^7 yr. In the case of long-distance transport, zinc concentrations would not likely have exceeded 5 mg/kg $\cdot H_2O$. For this range of zinc precipitated, the ore deposits at Pine Point would have formed in 0.5 to 5.0 million years, based on flow rates of 1.0 to 5.0 $m^3/m^2 \cdot yr$. Comparable time spans have been estimated for other stratabound ore deposits (e.g. White, 1971; Sverjensky, 1981). The main conclusion to be drawn from this preliminary analysis of Pine Point, however, is that gravity-driven groundwater flow systems are quantitatively capable of forming large ore deposits in sedimentary basins.

CHAPTER 6

SUMMARY AND CONCLUSIONS

Analysis confirms what simple common sense teaches us, namely, the correctness of judgments is as much more probable as the judges are more numerous and more enlightened.

Laplace, 1820.

The origin of stratabound ore formation is known to be dependent on the flow of fluids through porous media. Carbonate-hosted lead-zinc deposits have received the largest amount of geologic research of any of the stratabound ores, and yet the fundamental role of fluid-flow systems has been poorly understood. On the other side, groundwater hydrologists have only recently become aware of the potential applications of modern fluid-flow theory and modeling techniques in addressing geologic processes of this type.

A quantitative model that simulates the role of groundwater flow in the formation of stratabound ore deposits has been presented. The numerical modeling has been used to assess the role of gravity-driven flow systems. The various factors effecting fluid-flow patterns, subsurface temperatures, mass-transport patterns, and ore precipitation have been studied, and generic modeling of hypothetical sedimentary basins has been used to establish the relative importance of various model parameters and geologic environments.

The findings of this quantitative study are summarized below.

Geologic Considerations

1. Lead-zinc deposits of the Mississippi Valley type belong to a group of low-temperature ores that are classified as stratabound and epigenetic in

origin. Although they were deposited sometime after the sediments were lithified, stratabound ores are now considered to be genetically related to the normal evolution of a sedimentary basin. Only the carbonate-hosted lead-zinc ores are discussed in this study.

2. These deposits generally occur in flat-lying dolomite strata, which are commonly associated with porous, barrier-reef complexes and adjacent facies. On a regional scale, carbonate-hosted lead-zinc deposits are found near the margins of large sedimentary basins, and are presently at shallow depths. Because many of the deposits are hosted by Paleozoic strata, the configuration of the Precambrian basement can bear some influence on ore location. More important, however, is the role of large, extensive aquifers. In southeast Missouri, an extensive basal sandstone probably served as a paleo-aquifer, while at Pine Point, N.W.T., the presence of a karstic barrier played a major role in ore formation. Dolomitization and karstification were also important processes in the development of permeable conduits in many ore districts.

3. Mineralogy is dominated by various combinations of galena, sphalerite, pyrite, barite, dolomite, calcite, and quartz. Secondary in abundance are fluorite, celestite, chalcopyrite, native sulfur, and bitumen. Ore mineralization is principally due to precipitation of sulfides in small, pore-space openings, but solution features typically localize the ore into high-grade zones. Fluid-inclusion studies provide significant data concerning the nature of the mineralizing fluids, which were mainly Na-Ca-Cl brines. Temperatures of 50° - 150°C and salinities of 10% - 30% NaCl are indicated by the fluid-inclusion studies. Furthermore, the geochemical character of these ore-forming fluids is comparable to present-day oil-field brines.

4. Disagreement exists as to the origin of the driving mechanism for fluid flow. Although the concept of lateral secretion is generally agreed upon, the

relative importance of basin compaction as compared to gravity-driven flow systems is uncertain. It is likely that compaction and gravity-based flow are both important as end members in the hydrodynamic evolution of a basin. The computer models designed in this study are specifically built to test the gravity-driven flow mechanism in a mature sedimentary basin.

5. The geochemical environments of metal transport and ore precipitation are well known, but widely debated. Geologic evidence in some ore districts support a geochemical model where both metal and sulfide species are transported in the same solution, and ore precipitation is caused by cooling or pH change. Other ore districts indicate that only metal is transported in the brine, and accompanying sulfate is reduced at the ore site to deposit the sulfide minerals. It has also been suggested that the ore deposits could represent sites at which two-different fluids mixed. The implications that can be drawn from this study with respect to these various theories of ore genesis are summarized later.

The Numerical Models

1. The transport of fluid, heat, and chemical components through porous media can be described mathematically, according to physical laws of fluid flow, heat and mass transport, and thermodynamics. The resulting set of governing equations can take on various levels of complexity depending on the nature of the problem and the degree of coupling between the processes being studied.

2. For the purposes of modeling fluid-flow, temperature, and metal transport and precipitation, a number of assumptions and simplifications must be made. Many of these simplifications are necessary in order to find a practical method for the numerical solution of the equations. This is especially true when it comes to modeling fluid flow in chemically reactive porous media.

3. The model developed here is for a two-dimensional vertical cross-section through a basin, in which the configuration of the topography and geology are assumed to remain relatively constant over a period of at least a few million years. The basin is assumed to be fully saturated and rigid, and fluid salinity is a prescribed function of depth.

4. The equations of fluid flow and heat transport are coupled through the fluid density and viscosity, and are solved iteratively. Both equations are represented in their steady-state forms,and are solved with the finite-element technique. The movement and concentration of a metal component in the brine is modeled with the moving-particle random-walk solution to the transient mass-transport equation. Multicomponent modeling with this technique is theoretically possible, but the computer time needed for such simulations is currently impractical. For these reasons, only a single component is tracked through the basin in any given simulation. A wide variety of basin shapes, topographic expressions, and geologic configurations can be modeled. Output is in the form of the contoured steady-state hydraulic-head field, the temperature field, and the velocity-vector field. Concentration patterns are also contoured on the profiles, and plots can be generated for any specified time.

5. Geochemical speciation and reaction-path computations are made externally to the transport models with the EQ3/EQ6 code written by Wolery (1978, 1979a). Given the bulk composition of a fluid, it calculates the complete distribution of species and then predicts the consequences of allowing reactants to be dissolved into the modeled fluid. Newton-Raphson iteration in conjunction with finite-difference methods are used to solve the highly non-linear equations governing chemical equilibrium. Output is in the form of species concentrations and masses of minerals produced or destroyed per kg of

H_2O. The code can model through-flow systems, closed systems, and allows temperature to vary as a function of reaction progress.

6. Unfortunately, the computer time required to perform geochemical calculations in one cell of a finite-element mesh is approximately equal to the total computational time required for the fluid-flow, the heat transport, and the mass-transport simulations combined. The cost of running a fully-transient transport model with geochemical reactions is therefore impractical with current computer capacities. Nevertheless, the reaction-path technique is very useful in predicting metal concentrations and scenarios of sulfide precipitation at possible ore-forming sites.

Modeling Results

Fluid Flow

1. The factors effecting steady-state fluid-flow patterns in sedimentary basins are well known in the field of groundwater hydrology. Variations in subsurface permeabilities, basin geometry, and water-table configuration are the main controlling factors. Fluid velocities are determined by the hydraulic gradient imposed on the basin by the water-table slope.

2. The presence of a basal aquifer in a basin causes groundwater flow to be focused down into the aquifer in the higher-elevation recharge areas, and focused upward out of the aquifer in the lower-elevation discharge areas. The hydraulic-conductivity contrast between the aquifer and overlying strata controls the degree of focusing into the aquifer. Contrast ratios as small as 10:1 are sufficient to allow significant cross-formational flow from shale beds into major aquifers. Lateral variations in hydraulic conductivity can cause profound disruptions in a regional flow system, the effects of which in some cases can create local flow systems. These local flow paths conceivable could provide a mechanism for the gradual supply of a component such as aqueous H_2S

to a metal-bearing brine flowing through a regional aquifer.

3. Geothermal gradients are coupled to fluid-flow patterns and flow velocities through their influence on fluid density and viscosity. Higher temperatures cause greater flow rates by lowering the viscosity of a basinal fluid. Near the lateral edge of a basin, this effect could cause fluid velocities calculated with an uncoupled analysis to be too small by a factor of two. Higher temperatures also cause the density to decrease with depth, thereby leading to upward buoyancy forces. This can increase vertical fluid velocities by a factor of about three.

4. The pronounced effect of salinity on fluid flow can be observed in field-measured hydraulic-head patterns. With an increase in salinity with depth, the hydraulic head may actually increase at deeper levels in the recharge end of a basin, rather than decrease as it does in fresh-water flow systems. Higher salinity increases the density and viscosity of a basinal fluid, which generally reduces both horizontal and vertical components of the velocity vector. Near the less saline edge of a basin, the salinity effect on fluid velocity is relatively small, causing a decrease of about 20% over a computed fresh-water model.

5. The effects of temperature and salinity do not cancel each other out. Although thermal effects are greater, both factors should be taken into account when modeling fluid flow in sedimentary basins.

6. The length of a flow system in a basin depend on topographic relief, basin thickness, and permeability variations. If the basin is a few kilometers thick, relief is gentle, and aquifer exist at depth, then continuous flow systems can develop over distances of several-hundred kilometers. Major valleys, however, can interrupt the flow paths by focusing fluid flow into the valley bottom. Paleotopography, therefore, can have an important influence on the

location of ore formation.

7. In this study, most of the sensitivity simulations are carried out in a wedge-shape basin that is 300 km in length and varies in thickness from 3000 m in the higher-elevation recharge end to 1000 m in the lower-elevation discharge end. The basement surface is assumed to slope at a rate of 3 m/km updip to the basin margin. In a wedge-shape basin, fluid velocities in a basal aquifer are at a maximum near the shallow, updip end of the basin. Basement structure also effects flow patterns and velocities in other types of basins. For basins of relatively constant thickness (i.e. flat bottom), the flow pattern is more symmetric and velocity is highest near the mid-section of the basin. Major basement arches can restrict fluid flow to a thin stratigraphic interval, which will concentrate upward discharge and high flow rates above the arch. This feature may explain the association of some ore deposits with basement highs.

Heat Transport

1. All of the factors that effect fluid flow also effect subsurface temperature because flow rates determine the amount of heat convection in a porous medium. Both conduction and convection are equally important processes in the thermal regime. Under conditions of relatively slow fluid-flow rates, thermal conduction is the dominant mechanism of heat transport. In a two-layer basin with a hydraulic conductivity ratio between layers of 10:1 and an anisotropy ratio of 100:1 in both layers, the effects of convection begin to appear in the temperature pattern when the hydraulic conductivity of the basal layer approaches a value of 10m/yr.

2. Fluid flow in a sedimentary basin causes temperature to be lowered in recharge areas and raised in discharge areas. The differing gradients are causes by the convection of heat away from the deeper parts of the basin and

updip to the discharge area of the regional fluid-flow system near the basin margin. Depending on the hydraulic conductivity and its anisotropy, temperature can be raised as much as 30°C in discharge areas, over the temperatures expected under conduction alone.

3. On the basis of the effects of their thermal conductivities on heat and fluid-flow patterns, it can be shown that the presence of overlying sequences of shale and limestone is conducive to the development of temperatures in a basal aquifer that is characteristic of ore-forming environments.

4. Thermal dispersion has a weak influence on the temperature pattern in a basin. Transverse dispersivities greater than about 50 m are needed before temperatures are affected by more than 10°C in large, fluid-flow systems. However, the coefficient of transverse dispersivity is normally less than 10 m.

5. Based on the representative range of continental heat flows of 50 - 80 mW/m^2 and surface temperatures of 10° - 30°C, maximum temperatures near the shallow edge of a 300 km long, wedge-shape basin can range from about 50°C to 95°C at a depth of less than 1000 m. Temperatures of 100°C to 150°C are possible in larger basins with dimensions of several kilometers maximum thickness by several-hundred kilometers long. There is no need, therefore, to invoke deep-seated heat sources or sudden pulses of hot brine from depth to explain the occurrence of warm temperatures in stratabound ore formation.

6. Groundwater discharge zones, whether they are caused by stratigraphic pinchouts, topographic expressions, or basement arches, can significantly perturb the subsurface temperature pattern. In some cases, the high geothermal gradients locally created by these features may play a role in localizing ore precipitation through cooling.

Mass Transport

1. In the absence of geochemical reactions and hydrodynamic dispersion between source beds and depositional sites, the transport of an aqueous metal is solely governed by the fluid-flow regime. Mass that is released from a source bed will travel as an undisturbed plug along the flowline and with the average linear velocity of the groundwater. This type of mass transport, however, rarely occurs in nature.

2. Hydrodynamic dispersion includes the processes of mechanical dispersion and molecular diffusion. Mechanical dispersion is a mixing process that results in the spreading of a solute in both a longitudinal and lateral direction with respect to the flow path. Molecular diffusion in a porous medium also results in the reduction of concentration gradients, but its effects are usually several orders of magnitude smaller than mechanical dispersion.

3. The influence of dispersion on long-distance transport of metals is severe. For transport distances of 300 km, dispersion can dilute the metal concentration of a fluid to a value that is 10 - 20% of the original concentration of the fluid in the source-bed area. If 1 mg/kg • H_2O is taken as the minimum metal concentration needed to form ore at the depositional site, then approximately 5 - 10 mg/kg • H_2O must be present in the source-bed area, again for transport distances of 300 km. This assumes there are no other sources or sinks for the metal along the flow path.

4. On a regional scale, the gradual increase in upward flow beyond the mid-point of the basin causes mass to spread out of a basal aquifer. The area over which this occurs depends on the hydraulic-conductivity ratio between the aquifer and surrounding strata and the configuration of the water table.

5. A variety of geologic configurations, such as pinchouts and the like, can create local flow systems that lead to the convergence of flow paths from

different stratigraphic levels. It is unlikely, in the presence of dispersion, that mixing of two-different fluids would occur over a small-enough area to localize an ore deposit, unless flow is restricted to discrete fracture zones.

Geochemical Transport and Ore Precipitation

1. The main factors effecting the solubilities of galena and sphalerite in basinal brines include the temperature, the salinity, and the pH and oxidation state. Concentrations of several hundred mg/kg • H_2O are possible, provided that the sulfide content of the brine is very low. Sulfide can be supplied at the ore-forming site, either through reduction of sulfate in the metal-bearing brine, or by addition of H_2S through reactions with the surrounding rocks. Other reducing agents such as methane or pre-existing iron-sulfide minerals can also cause ore deposition. When sulfide is supplied at the site of deposition, the composition of the metal-bearing brine can be of many possibilities.

2. Metal and aqueous sulfide can be carried in the same solution at equilibrium, but a combination of high salinity, high temperature, and acidic conditions (pH = 3 -5) is required to achieve concentrations of even a few mg/kg • H_2O. Precipitation of ore can be accomplished through a pH shift or cooling. The pH change is usually assumed to come from the dissolution of carbonates. However, neither of these mechanisms are very effective at depositing sulfides when the pH is greater than 5.0, the temperature is less than 80°C, and the salinity is below 3.0 m NaCl. Furthermore, a rather narrow range of pH and oxygen fugacity conditions restrict the possible composition range of a solution carrying metal and sulfide through carbonate rocks.

3. The relative importance of these two geochemical models may vary from one basin environment to another. Geologic evidence from some ore districts indicate a sulfate-reducing mechanism for ore precipitation, while other

districts support a model with transport of metal and sulfide together.

4. Long-distance transport of metal and sulfide in solution is ruled out because the dilution effect of dispersion would reduce these small concentrations even lower. Continuous addition of both metal and sulfide along the flow path, or much higher initial concentrations due to organic complexing may overcome the dilution problem. Large flow rates and long periods of time would still be required if changes in pH and temperature are responsible for ore precipitation.

Pine Point Model

1. The ability of a gravity-driven fluid-flow system to produce a major ore deposit can be quantitatively verified by studying known ore districts. For this purpose, a preliminary cross-section model along the Keg River barrier complex provides insight into the formation of lead-zinc mineralization at Pine Point.

2. The age of mineralization at Pine Point is unknown, except that it occurred in post-Devonian time. Southwest to northeast gravity-driven flow systems could have operated in the Western Canada sedimentary basin over much of the 175 million-year period between the Late Mississippian and the Tertiary. About 1000 m of sedimentary cover would have overlain the Pint Point area in the Early Cretaceous.

3. Reasonable estimates of the model parameters needed for studying Pine Point can be made through geologic considerations, the results of the sensitivity analysis, and the present-day data on hydraulic conductivity, heat flow, and brine geochemistry in the basin.

4. The modeling results show that the barrier-complex aquifer was the major factor in focusing fluid flow across the Upper Devonian shales in the thick, western part of the section, and in discharging metal-bearing brines

updip to the basin margin in the east. Average linear velocities probably reached the range of 4.0 - 20.0 m/yr in the basin margin area, which leads to specific-discharge rates of about 1.0 - 5.0 $m^3/m^2 \cdot yr$ through the barrier rocks at Pine Point.

5. Temperatures probably averaged around 80°C at the assumed 1000 m depth of the Pine Point site. Depending on flow rates and geothermal parameters, temperatures could have ranged from 60°C to 100°C. These predictions are consistent with temperature estimates made from fluid-inclusion data.

6. Geologic and hydrodynamic criteria support a sulfate-reduction model for the deposition of ore at Pine Point. Metal was brought to the ore-forming site in a sulfate-type brine, and the action of sulfate-reducing bacteria, aided by abiogenic reaction with H_2S, caused ore precipitation in the more permeable, karstic sections of the barrier. It is also possible that lateral-permeability changes downdip or topographic effects near the end of the basin caused local flow systems to develop, which in turn assisted in the supply of H_2S through reduction of sulfate at shallow depth with flow down into the karst aquifer.

7. If transport of metals was from shales deep in the basin, then minimum metal concentrations of about 20 mg/kg $\cdot$ H_2O near the source were needed to sustain a concentration of at least 1 mg/kg $\cdot$ H_2O near the basin margin. Closer source beds or addition of metal along the flow path would not require the same initial concentration, because the dilution caused by dispersion would be less.

8. An estimated time period of 0.5 to 5.0 million years is necessary to account for the metal tonnage at Pine Point, based on a probable precipitation range of 1 - 5 mg/kg $\cdot$ H_2O and flow rates of 1.0 - 5.0 $m^3/m^2 \cdot yr$.

This study has shown that gravity-driven groundwater flow systems are capable of forming large ore deposits over relatively short intervals of geologic time. Numerical modeling provides a powerful tool for testing ore-genesis hypotheses and for developing an understanding of the conditions necessary for ore deposition in sedimentary basins. As it stands, hydrogeologic modeling can be used to refine exploration models of sedimentary basins or specific ore districts, but on a regional scale. Attempts to extend the method into the prediction of ore formation on a local scale will probably face data limitations that will be difficult to surmount in the foreseeable future.

The quantitative assessment of transport processes in ore genesis can be improved in a number of directions. Future studies should consider three-dimensional modeling; they should include compaction and erosion processes; and they should examine the genetic relationship between present-day flow patterns in basins and paleoflow systems. One of the primary reasearch needs is the development of new numerical approaches for integrating spatial and temporal geochemical calculations in mass-transport modeling. It is hoped that the work begun in this study will encourage future hydrogeologic research in these directions.

REFERENCES

Adler, H. H., 1976, Concepts of uranium-ore formation in reducing environments in sandstones and other sediments : International Atomic Energy-Proceedings Paper IAES-SM-183/43, p.14-168.

Ahlstrom, S. W., 1975, Modeling the transport of selected radionuclides in subsurface water systems using the discrete-parcel random-walk approach : Trans. Amer. Geophys. Union, v.56, p.979.

Ahlstrom, S. W., H. P. Foote, R. C. Arnett, C. R. Cole, and R. J. Serne, 1977, Multicomponent mass transport model : theory and numerical implementation : Battelle, Pacific Northwest Laboratories, Report 2127, Richland Washington.

Anderson, G. M., 1973, The hydrothermal transport and deposition of galena and sphalerite near 100°C : Econ. Geol., v.69, p.480-492.

_____, 1975, Precipitation of Mississippi Valley-type ores : Econ. Geol., v.70, p.937-942.

_____, 1977, Thermodynamics and sulfide solubilities; in Short course in application of thermodynamics to petrology and ore deposits : Min. Assoc. Canada, p.136-150, Vancouver.

_____, 1978, Basinal brines and Mississippi Valley-type ores : Episodes, v.1978, No.2, p.15-19.

Anderson, G. M. and R. W. Macqueen, 1982- in press, Ore deposit models - 6. Mississippi Valley-type lead-zinc deposits : Geoscience Canada.

Anderson, M. P., 1979, Using models to simulate the movement of contaminants through groundwater flow systems: CRC Critical Reviews in Environmental Control, v.9, p.97-156.

Barnes, H. L., 1979, Solubilities of ore minerals:in Geochemistry of Hydrothermal Ore Deposits, 2nd ed., edited by H. L. Barnes, p.404-460, John Wiley and Sons, Inc.

Barnes, H. L. and G. K. Czamanske, 1967, Solubilities and transport of ore minerals : in Geochemistry of Hydrothermal Ore Deposits, 1st ed., edited by H. L. Barnes, p.334-381, Holt, Rinehart, and Winston, New York.

Barton, P. B., Jr., 1967, Possible role of organic matter in the precipitation of the Mississippi Valley ores : Econ. Geol., Monograph 3, p.371-378.

Bassett, H. G., and J. G. Stout, 1967, Devonian of western Canada : in International Symposium on the Devonian System, edited by D. H. Oswald, p.717-752, Calgary.

Bathe, K. J., and E. L. Wilson, 1976, Numerical Methods in Finite Element Analysis : Prentice-Hall, New Jersey.

Beales, F. W., 1975, Precipitation mechanisms for Mississippi Valley-type deposits : Econ. Geol., v.70, p.943-948.

Beales, F. W. and S. A. Jackson, 1966, Precipitation of lead-zinc ores in carbonate reservoirs as illustrated by Pine Point ore field, Canada : Inst. Mining Metallurgy Trans., v.75, sec.B, p.B278-B285.

Bear, J., 1969, Hydrodynamic dispersion; in Flow Through Porous Media : edited by R. J. M. De Wiest, p.108-199., Academic Press, New York.

_____, 1972, Dynamics of Fluids in Porous Media : 764 pp., Elsevier, New York.

Bennison, A. P., 1978, Geological Highway Map of the Great Lakes Region : Amer. Assoc. Petrol. Geologists, Map No.11, Tulsa, Oklahoma.

Betcher, R. N., 1977, Temperature distribution in deep groundwater flow systems - a finite element model : Unpub. M.Sc. thesis, Univ. of Waterloo.

Billings, G. K., S. E. Kesler, and S. A. Jackson, 1969, Relation of zinc-rich formation waters, northern Alberta, to the Pine Point ore deposit : Econ. Geol., v.64, p.385-391.

Bird, R. B., W. E. Stewart and E. N. Lightfoot, 1960, Transport Phenomena : John Wiley and Sons Inc., New York.

Bischoff, J. L., A. S. Radtke and R. J. Rosenbauer, 1981, Hydrothermal alteration of graywacke by brine and seawater : roles of alteration and chloride complexing on metal solubilization at 200° and 350°C : Econ. Geol., v.76, p.695-676.

Bond, D. C., 1972, Hydrodynamics in deep aquifers of the Illinois basin : Circ. 470, Ill. State Geol. Surv., 51 p., Urbana.

Bredehoeft, J. D., C. R. Blyth, W. A. White and G. B. Maxey, 1963, Possible mechanism for concentration of brines in subsurface formations : Bull. Amer. Assoc. Petrol. Geol., v.47, p.257-269.

Bredehoeft, J. D. and I. S. Papadopoulos, 1965, Rates of vertical groundwater movement estimated from the earth's thermal profile : Water Resour. Res. v.1, p.325-328.

Bedehoeft, J. D. and G. F. Pinder, 1973, Mass transport in flowing groundwater : Water Resour. Res., v.9, p.194-209.

Brown, A. C., 1971, Zoning in the White Pine copper deposit, Ontonagon County, Michigan : Econ. Geol., v.66, p.543-573.

Brown, T. H., 1977, Water-rock interactions : An introduction to mass transfer; in Short course in application of thermodynamics to petrology and ore deposits : Min. Assoc. Canada, p.151-159, Vancouver.

Butler, A. P., Jr., 1969, Groundwater as related to the origin and search for uranium deposits in sandstone, Laramie, Wyoming : Contributions to Geology, v.8, No.2, part 1, p.81-86.

Campbell, N., 1967, Tectonics, reefs, and stratiform lead-zinc deposits of the Pine Point area, Canada : Econ. Geol., Monograph 3, p.59-70.

Carnahan, B. H., H. A. Luther and J. O. Wilkes, 1969, Applied Numerical Methods : Wiley, New York, 604 p.

Carnahan, C. L., 1975, Non-equilibrium thermodynamic treatment of transport processes in ground-water flow : Technical Report Series, Hydrology and Water Resources, No.24, Desert Research Institute, Univ. of Nevada, Reno.

Carpenter, A. B., M. L. Trout and E. E. Pickett, 1974, Preliminary report on the origin and evolution of lead-and zinc-rich oil field brines in central Mississippi : Econ. Geol., v.69, p.1191-1206.

Carslaw, H. S. and J. C. Jaeger, 1959, Conduction of Heat in Solids : Oxford University Press, London, 510 p.

Chapman, B. M., 1982, Numerical simulation of the transport and speciation of nonconservative chemical reactants in rivers : Water Resour. Res., v.18, p.155-167.

Clark, S. P., Jr., 1966, Thermal conductivity; in Handbook of Physical Constants : edited by S. P. Clark, Jr., p.459-473, Geol. Soc. Amer., Memoir 97, Section 21.

Cox, G. H., 1911, Origin of the lead and zinc ores in the upper Mississippi Valley district : Econ. Geol., v.6, p.427-603.

Dagan, G., 1972, Some aspects of heat and mass transfer in porous media : in Fundamentals of Transport Phenomena in Porous Media, Developments in Soil Science, v.2, p.55-64, Elsevier, New York.

Daubrée, A., 1887, Les eaux sauterraines, aux epoques anciennes et a l'epoque actuelle : Paris, Dunod, 3 vol.

Davis, J. H., 1977, Genesis of the southeast Missouri lead deposits : Econ. Geol., v.72, p.443-450.

Davis, S. N., 1969, Porosity and permeability of natural materials : in Flow Through Porous Media, edited by R. J. M. De Wiest : p.54-89, Academic Press, New York.

de Josselin de Jong, G., 1960, Singularity distributions for the analysis of multiple fluid flow through porous media : Jour. Geophys. Res. v.65, p.3739-3758.

_____, 1969, Generating functions in the theory of flow through porous media, in Flow Through Porous Media : edited by R. J. M. De Wiest, p.376-400, Academic Press, New York.

Deroo, G., T. G. Powell, B. Tissot and R. G. McCrossan with contributions by P. A. Hacquebard, 1977, The origin and migration of petroleum in the Western Canada sedimentary basin, Alberta : A geochemical and thermal maturation study : Geological Survey of Canada, Bull. 262, 136 p.

Domenico, P. A., 1977, Transport phenomena in chemical rate processes in sediments : Ann. Rev. Earth Planet Sci., v.5, p.287-317.

Domenico, P. A. and V. V. Palciauskas, 1973, Theoretical analysis of forced convective heat transfer in regional groundwater flow : Geol. Soc. Amer. Bull., v.84, p.3803-3814.

Douglas, R. J. W., et al., 1973, Geology of the Trout River area, and Great Slave Lake area, District of Mackenzie, Northwest Territories : Geol. Surv. Canada, Map Series 1370A, 1371A, 1 : 500,000, Surveys and Mapping Branch, Ottawa.

Dozy, J. J., 1970, A geologic model for the genesis of the lead-zinc ores of the Mississippi Valley, USA : Inst. Mining Metallurgy Trans., Sec. B., v.79, p.163-170.

Ellis, A. J., 1968, Natural hydrothermal systems and experimental hot water/rock interaction : reactions with NaCl solutions and trace metal extraction : Geochim. Cosmochim. Acta. v.32, p.1313-1363.

Evenson, D. E. and M. D. Dettinger, 1979, Dispersive processes in models of regional radionuclide migration - a technical memorandum : Camp Dresser and McKee Inc. for Lawrence Livermore Laboratory, University of California.

Faust, C. R. and J. W. Mercer, 1979, Geothermal reservoir simulation : 1. Models for liquid-dominated and vapour-dominated hydrothermal systems : Water Resour. Res., v.15, p.23-30.

Feller, W., 1961, An Introduction to Probability Theory and Its Applications (2nd ed.) : John Wiley and Sons, New York.

Fischer, R. P., 1968, The uranium and vanadium deposits of the Colorado Plateau region : in Ore Deposits of the United States, 1933-1967, edited by J. D. Ridge, p.735-746, v.1, Amer. Inst. Min. Metall. and Petrol. Eng., New York.

_____, 1970, Similarities, differences, and some genetic problems of the Wyoming and Colorado Plateau types of uranium deposits in sandstone : Econ. Geol., v.65, p.778-784.

Fletcher, R. C. and R. J. Vidale, 1975, A finite difference model for diffusion and combined diffusion - inflitration metasomatism in a multicomponent system : Annual Report of the Geophysical Laboratory, Carnegie Institution Year Book, 1974, p.424-428.

Freeze, R. A., 1969, Regional groundwater flow - Old Wives Lake Drainage basin, Saskatchewan : Can. Inland Waters Branch, Sci. Series, No.5, 245 p.

_____, 1978, Mathematical models of hillslope hydrology : in Hillslope Hydrology, (Chapter 6) : edited by M. J. Kirkby, p.177-225, Wiley-Interscience, New York.

Freeze, R. A. and J. A. Cherry, 1979, Groundwater : Prentice Hall, New Jersey, 604 p.

Freeze, R. A. and P. A. Witherspoon, 1966, Theoretical analysis of regional groundwater flow : 1. Analytical and numerical solutions to the mathematical model : Water Resources Res., v.2, p.641-656.

_____, 1967, Theoretical analysis of regional groundwater flow : 2. Effect of water-table configuration and subsurface permeability variation : Water Resources Res., v.3, p.623-634.

_____, 1968, Theoretical analysis of regional groundwater flow : 3. Quantitative interpretations : Water Resources Res., v.4, p.581-590.

Frind, E. O., 1980, Seawater intrusion in continuous coastal aquifer-aquitard systems : Proc. Third Intern. Conf. on Finite Elements in Water Resources, Univ. Miss., Oxford.

Garder, A. O., Jr., 1964, Numerical calculation of multidimension miscible displacement by the method of characteristics : Soc. Petrol. Eng. Jour., v.4, p.26-36.

Garrels, R. M. and C. L. Christ, 1965, Solutions, Minerals and Equilibria : Harper and Row, New York 450 p.

Gerdemann, P. E. and H. E. Myers, 1972, Relationships of carbonate facies patterns to ore distribution and to ore genesis in the southeast Missouri lead district : Econ. Geol., v.67, p.426-433.

Giordano, T. H. and H. L. Barnes, 1981, Lead transport in Mississippi Valley-type ore solutions : Econ. Geol., v.76, p.2200-2211.

Gussow, W. M. C., 1962, Regional geological cross-sections of the Western Canada sedimentary cover : Alberta Soc. Petrol. Geologists, Calgary.

Haas, J. L., Jr., 1976, Physical properties of the coexisting phases and thermodynamic properties of the H_2O component in boiling NaCl solutions : U.S. Geological Survey, Bull. 1421-A and 1421-B.

Haji-Sheikh, A. and E. M. Sparrow, 1966, The floating random walk and its applications to Monte Carlo solutions of heat equations : Jour. SIAM Appl. Math., v.14, p.370-389.

Hanor, J. S., 1979, The sedimentary genesis of hydrothermal fluids : in Geochemistry of Hydrothermal Ore Deposits, 2nd ed., edited by H. L. Barnes, p.137-172, John Wiley and Son, New York.

Helgeson, H. C., 1964, Complexing and Hydrothermal Ore Deposition : Macmillan, New York, 128 p.

_____, 1968, Evaluation of irreversible reactions in geochemical processes involving minerals and aqueous solutions - I. Thermodynamic relations : Geochim. Cosmochim. Acta, v.32, p.853-877.

Helgeson, H. C., 1969, Thermodynamics of hydrothermal systems at elevated temperatures and pressures : Amer. Jour. Sci., v.267, p.729-804.

_____, 1979, Mass transfer among minerals and hydrothermal solutions : in Geochemistry of Hydrothermal Ore Deposits, 2nd e., edited by H. L. Barnes, p.568-610, John Wiley and Sons, Inc.

Helgeson, H. C., T. H. Brown, A. Nigrini and T. A. Jones, 1970, Calculation of mass transfer in geochemical processes involving aqueous solutions : Geochim. Cosmochim. Acta., v.34, p.569-592.

Helgeson, H. C. and D. H. Kirkham, 1974a, Theoretical prediction of the thermodynamic behavior of aqueous electrolytes at high pressures and temperatures. I. Summary of the thermodynamic/electrostatic properties of the solvent : Amer. Jour. Sci., v.274, p.1089-1198.

_____, 1974b, Theoretical prediction of the thermodynamic behavior of aqueous electrolytes at high pressures and temperatures. II. Debye-Huckel parameters for activity coefficients and relative partial molal properties : Amer. Jour. Sci., v.274, p.1199-1261.

Hill, A. D., 1978, Flow with simultaneous heterogeneous reactions in porous media : Ph.D. thesis, Univ. of Texas, Austin, 143 p.

Hitchon, B., 1968, Rock volume and pore volume data for plains region of Western Canada sedimentary basin between latitudes 49° and 60° N : Amer. Assoc. Petrol. Geologists Bull., v.52, p.2318-2323.

_____, 1969a, Fluid flow in the Western Canada sedimentary basin : 1. Effect of topography : Water Resour. res., v.5, p.186-195.

_____, 1969b, Fluid flow in the Western Canada sedimentary basin : 2. Effect of geology : Water Resour. Res., v.5, p.460-469.

_____, 1971, Origin of oil : geological and geochemical constraints : Origin and Refinery of Petroleum, Advances in Chemistry Series, No. 103, Amer. Chem. Soc., p.30-66, Washington.

_____, 1974, Application of geochemistry to the search for crude oil and natural gas, in Introduction to Exploration Geochemistry : edited by A. A. Levinson, p.509-545, Applied Publishing Ltd., Calgary.

_____, 1976, Hydrogeochemical aspects of mineral deposits in sedimentary rocks, in Handbook of Strata-Bound and Stratiform Ore Deposits : edited by K. H. Wolf, p.53-66, Elsevier, New York.

_____, 1977, Geochemical links between oil fields and ore deposits in sedimentary rocks : in Proc. Forum on Oil and Ore in Sediments, p.1-37, P. Garrard, ed., Imperial College, London.

_____, 1981, Genetic Links between shales, formation fluids and ore deposits - example for zinc from Alberta, Canada : Geol. Soc. Amer., Annual Meeting, Cincinnati, Ohio, Abstracts, p.473.

Hitchon, B., G. K. Billings and J. E. Klovan, 1971, Geochemistry and origin of formation waters in the Western Canada sedimentary basin : III. Factors controlling chemical composition : Geochim. Cosmochim. Acta, v.35, p.567-598.

Hitchon, B. and M. K. Horn, in press, Petroleum occurrence indicators in formation waters from Alberta, Canada : Amer. Assoc. Petrol. Geologists Bull.

Hubbert, M. K., 1940, The theory of ground-water motion : Jour. Geol., v.48, p.785-944.

Huyakorn, P. S. and G. F. Pinder, 1977, A pressure-enthalpy finite element model for simulating hydrothermal reservoirs : in Advances in Computer Methods for Partial Differential Equations II : edited by R. Vichnevetsky, IMACS (AICA), p.284-293.

Jackson, S. A. and F. W. Beales, 1967, An aspect of sedimentary basin evolution : the concentration of Mississippi Valley-type ores during the late stages of diagenesis : Bull. Can. Petrol. Geol., v.15, p.393-433.

Jessop, A. M. and T. L. Lewis, 1978, Heat flow and heat generation in the Superior Province of the Canadian Shield : Tectonophysics, v.50, p.55-77.

Kappelmeyer, O. and R. Haenal, 1974, Geothermics-with Special Reference to Application : Borntraeger, Berlin-Stuttgart.

Kestin, J., H. E. Khalifa, Y. Abe, C. E. Grimes, H. Sookiazian and W. A. Wakeham, 1978, The effect of pressure on the viscosity of aqueous NaCl solutions in the temperature range 20-150°C, Jour. Chem. Eng. Data, v.23, p.328-336.

Kestin, J., H. E. Khalifa and R. J. Correia, 1981, Tables of the dynamic and kinematic viscosity of aqueous NaCl solutions in the temperature range of 20-150°C and the pressure range 0.1-35 MPa : Jour. Phys. Chem. Ref. Data, v.10, p.71-87.

Kline, S. J., 1965, Similitude and Approximation Theory, McGraw-Hill, New York.

Konikow, L. F. and D. B. Grove, 1977, Derivation of equations describing solute transport in ground water : U.S. Geological Survey, Water Resources Investigations, Paper 77-19, 30 p.

Kyle, J. R., 1977, Development of sulfide-hosting structures and mineralization, Pine Point, Northwest Territories : Ph.D. thesis, Univ. Western Ontario, London, 226 p.

_____, 1980, Controls of lead-zinc mineralization, Pine Point district, Northwest Territories, Canada : Mining Engineering, Nov., p.1617-1626.

_____, 1981, Geology of the Pine Point lead-zinc district : in Handbook of Strata-Bound and Stratiform Ore Deposits, edited by K. H. Wolf, Regional studies and specific deposits, v.9, p.643-741, Elsevier, Amsterdam.

Land, L. S. and D. R. Prezbindowski, 1981, The origin and evolution of saline formation water, Lower Cretaceous carbonates, south-central Texas, U.S.A. : Jour. Hydrol., v.54, p.51-74.

Law, J., 1971, Regional Devonian geology and oil and gas possibilities, upper Mackenzie River area : Bull. Can. Petrol. Geol., v.19, p.437-486.

Levorsen, A. I., 1967, Geology of Petroleum, (2nd ed.) : W. H. Freeman and Co., San Francisco, 724 p.

Li, T. M. C., 1980, Axisymmetric numerical simulation of hydrothermal systems including changes in porosity and permeability due to quartz-water reaction : Unpub. Ph.D. thesis, Pennsylvania State University 240 p.

Lusczynski, N. J., 1961, Head and flow of groundwater of variable density : Jour. Geophys. Res., v.66, p.4247-4256.

Majorowicz, J. A. and A. M. Jessop, 1981, Regional heat flow patterns in the Western Canada sedimentary basin : Tectonophysics, v.74, p.209-238.

Macqueen, R. W., 1976, Sediments, zinc and lead, Rocky Mountain Belt, Canadian Cordillera : Geoscience Canada, v.3, p.71-81.

Macqueen, R. W. G. K. Williams, R. R. Barefoot, and A. E. Foscolos, 1975, Devonian metalliferous shales, Pine Point region, District of Mackenzie : Geol. Surv. Can., Report of Activities, Paper 75-1, Part A, p.553-556.

Macqueen, R. W. and T. G. Powell, in press, Organic geochemistry of the Pine Point lead-zinc ore field and region, Northwest Territories, Canada : Econ. Geol.

McCrossan, R. G. and R. P. Glaister, (Eds.), 1964, Geological History of Western Canada : Alberta Soc. Petrol. Geologists, Calgary, Alberta.

McLimans, R. K., 1977, Geologic fluid inclusion and stable isotope studies of the Upper Mississippi Valley zinc-lead district, southwest Wisconsin : Ph.D. thesis, Pennsylvania State Univ., 175 p.

Mercer, J. W., and C. R. Faust, 1981, Ground-Water Modeling : National Water Well Association, Worthington, Ohio, 60 p.

Mercer, J. W. and G. F. Pinder, 1974, Finite element analysis of hydrothermal systems, in Finite Elements in Fluid Flow : edited by J. T. Oden, p.401-414, Univ. of Alabama Press, Huntsville.

Naymik, T. G. and M. J. Barcelona, 1981, Characterization of a contaminant plume in groundwater, Meredosia, Illinois : Ground Water, v.19, p.517-526.

Neuman, S. P., 1973, Saturated-unsaturated seepage by finite elements : Jour. Hydraulic Division, Proc. Amer. Soc. Civil Engineers, v.99, No.HY12, p.2233-2250.

Nield, D. A., 1968, Onset of thermohaline convection in porous media : Water Resour. Res., v.4, p.553-560.

Noble, E. A., 1963, Formation of ore deposits by water of compaction : Econ. Geol., v.58, p.1145-1156.

Nordstrom, D. K., et al., 1979, A comparison of computerized chemical models for equilibrium calculations in aqueous systems, in Chemical Modeling in Aqueous Systems : edited by E. A. Jenne, p.857-892, Amer. Chem. Soc. Symp. Series, 93, American Chemical Society, Washington, D.C.

Norris, A. W., 1965, Stratigraphy of Middle Devonian and older Paleozoic rocks of the Great Slave Lake region, Northwest Territories : Geol. Surv. Can., Memoir 322.

Norton, D. and L. M. Cathles, 1979, Thermal aspects of ore deposition; in Geochemistry of Hydrothermal Ore Deposits (2nd ed.), edited by H. L. Barnes, p.611-631, John Wiley and Sons, New York.

Norton, D. and H. P. Taylor, Jr., 1979, Quantitative simulation of the hydrothermal systems of crystallizing magmas on the basis of transport theory and oxygen isotope data : An analysis of the Skaergaard Intrusion : Jour. Petrology, v.20, p.421-486.

Oetking, P., D.E. Feray and H. B. Renfro, 1966, Geological Highway Map of the Mid-Continent Region : Amer. Assoc. Petrol. Geologists, Map No. 1, Tulsa, Oklahoma.

Ohle, E. L., 1959, Some considerations in determining the origin of ore deposits of the Mississippi Valley type : Econ. Geol., v.54, p.769-789.

_____, 1980, Some considerations in determining the origin of ore deposits of the Mississippi Valley type - part II : Econ. Geol., v.75, p.161-172.

Orr, W. L., 1974, Changes in sulfur content and isotopic ratios of sulfur during petroleum maturation-study of Big Horn Basin Paleozoic oils : Amer. Assoc. Petrol. Geol. Bull., v.50, p.2295-2318.

Ortiz, N. V., J. A. Ferentchak, F. G. Ethridge, H. C. Granger, and D. K. Sunada, 1980, Ground-water flow and uranium in Colorado Plateau : Ground Water, v.18, p.596-606.

Parsons, M. L., 1970, Groundwater thermal regime in a glacial complex : Water Resour. Res., v.6, p.1701-1720.

Perry, R. H. and C. H. Chilton, 1973, Chemical Engineers' Handbook, 5th ed., McGraw-Hill, New York, p.3-246.

Pickens, J. F. and W. C. Lennox, 1976, Numerical simulation of waste movement in steady groundwater flow systems : Water Resour. Res., v.12, p.171-180.

Pickens, J. F. and G. E. Grisak, 1979, Finite-element analysis of liquid flow, heat transport and solute transport in a ground-water flow system: 1. Governing equations and model formulation : Report on Hydrogeologic Research Activities 1978/79, Contaminant Hydrogeology Section, Environment Canada, for A.E.C.L., Whiteshell Nuclear Research Establishment, Pinawa, Manitoba.

Pinder, G. F., 1973, A Galerkin-finite-element simulation of groundwater contamination on Long Island, New York : Water Resour. Res., v.9, p.1657-1669.

Pinder, G. F. and H. H. Cooper, Jr., 1970, A numerical techniques for calculating the transient position of the saltwater front : Water Resours. Res., v.6, p.875-882.

Pinder, G. F. and W. G. Gray, 1977, Finite Element Simulation in Surface and Subsurface Hydrology : Academic Press, New York, 295 p.

Pipes, L. A. and L. R. Harvill, 1970, Applied Mathematics for Engineers and Physicists : p.573-577, McGraw-Hill, New York.

Plummer, L. N. and W. Back, 1980, The mass balance approach : Application to interpreting the chemical evolution of hydrologic systems : Amer. Jour. Sci., v.280, p.130-142.

Poreh, M., 1965, The dispersivity tensor in isotropic and axisymmetric mediums : Jour. Geophys. Res., v.70, p.3909-3913.

Prickett, T. A., T. G. Naymik and C. G. Lonnquist, 1981, A 'random-walk' solute transport model for selected groundwater quality evaluations : Illinois State Water Survey, Bull. 65, Champaign, 103 p.

Reddell, D. L. and D. K. Sunada, 1970, Numerical simulation of dispersion in groundwater aquifers : Hydrology Paper No. 41, Colorado State University, Fort Collins, 79 p.

Ridge, J. D., 1976, Origin, development, and changes in concepts of syngenetic ore deposits as seen by North American geologists : in Handbook of Strata-Bound and Stratiform Ore Deposits, edited by K. H. Wolf, Classification and historical studies, v.1, p.183-294, Elsevier, Amsterdam.

Robie, R. A. and D. R. Waldbaum, 1968, Thermodynamic properties of minerals and related substances at 298.15 K (25.0°C) and one atmosphere (1.013 Bars) pressure and at higher temperatures. U.S. Geological Survey, Bull, 1259, 256 p.

Roedder, E., 1960, Fluid inclusions as samples of the ore-forming fluids : Intern. Geol. Congr., Proc. Sec. 16, Copenhagen, p.218-229.

_____, Environment of deposition of stratiform (Mississippi Valley-type) ore deposits, from studies of fluid inclusions : Econ. Geol., Monograph 3, p.349-362.

Roedder, E., 1968, Temperature, salinity, and origin of the ore-forming fluids at Pine Point, Northwest Territories, Canada, from fluid inclusion studies : Econ. Geol., v.63, p.439-450.

_____, 1976, Fluid inclusion evidence in the genesis of ores in sedimentary and volcanic rocks : in Handbook of Strata-Bound and Stratiform Ore Deposits, edited by K. H. Wolf, v.4, p.67-110, Elsevier, Amsterdam.

Rowe, A. M. Jr. and J. C. S. Chou, 1970, Pressure-volume-temperature-concentration relation of aqueous NaCl solutions : Jour. Chem. Eng. Data, v.15, p.61-66.

Rubin, H., 1973, Effect of solute dispersion on thermal convection in a porous medium layer : Water Resour. Res., v.9, p.968-974.

_____, 1974, Heat dispersion effect on thermal convection in a porous medium layer : Jour. Hydrol., v.21, p.173-185.

_____, 1981, Thermal convection in a nonhomogeneous aquifer : Jour. Hydrol., v.50, p.317-331.

Rumer, R. R., Jr., 1972, One the derivation of the convection-dispersion equation by spatial averaging : in Fundamentals of Transport Phenomena in Porous Media : Developments in Soil Science 2, p.268-275, IAHR, Elsevier, Amsterdam.

Sanford, R. F., 1982, Preliminary model of regional Mesozoic groundwater flow and uranium deposition in the Colorado Plateau : Geology, v.10, p.348-352.

Sass, J. H., D. D. Blackwell, D. S. Chapman, J. K. Costain, E. R. Decker, L. A. Lawver and C. A. Swanberg, 1981, Heat flow from the crust of the United States : in Physical Properties of Rocks and Minerals : edited by Y. S. Touloukian, W. R. Judd and R. F. Roy, p.503-548, McGraw-Hill, New York.

Schwartz, F. W., 1975, A prababilistic mass transfer model : Canadian Hydrology Symp. - 75 Proc., Winnipeg, p.407-412.

_____, 1977, Macroscopic dispersion in porous media : The controlling factors : Water Resour. Res., v.13, p.743-752.

_____, 1978, Applications of probabilistic - deterministic modeling to problems of mass transfer in groundwater systems : Third Intern. Hydrol. Symp., p.281-296, Fort Collins, Colorado.

Schwartz, F. W. and P. A. Domenico, 1973, Simulation of hydrochemical patterns in regional groundwater flow : Water Resour. Res., v.9, p.707-720.

Schwartz, F. W. and A. Crowe, 1980, A deterministic-probabilistic model for contaminant transport, report prepared for U.S. Nuclear Regulatory Commission, Washington, D. C., by CGS, Inc., Urbana, Illinois, 158 p.

Segol, G. and G. F. Pinder, 1976, Transient simulation of saltwater intrusion in southeastern Florida : Water Resour. Res., v.12, p.65-70.

Sharp, J. M., Jr., 1978, Energy and momentum transport model of the Ouachita basin and its possible impact on formation of economic mineral deposits : Econ. Geol., v.73, p.1057-1068.

Siebenthal, C. E., 1915, Origin of the zinc and lead deposits of the Joplin region, Missouri, Kansas, and Oklahoma : U.S. Geological Survey, Bull. 606.

Skall, H., 1975, The paleoenvironment of the Pine Point lead-zinc district : Econ. Geol., v.70, p.22-45.

Skinner, B. J., 1979, The many origins of hydrothermal mineral deposits: in Geochemistry of Hydrothermal Ore Deposits (2nd ed.), edited by H. L. Barnes, p.1-21, John Wiley and Sons, New York.

Slattery, J. C., 1972, Momentum, Energy, and Mass Transfer in Continua : McGraw-Hill, New York, 679 p.

Smith, L. and F. W. Schwartz, 1980, Mass transport. 1. A stochastic analysis of macroscopic dispersion : Water Resour. Res., v.16, p.303-313.

Snyder, F. G., 1968, Geology and minerals deposits, midcontinent United States : in Ore Deposits of the United States, 1933-1967, edited by John D. Ridge, v.1, p.257-284, Amer. Inst. Min., Metall., and Petrol. Eng., New York.

Snyder, F. G. and P. E. Gerdemann, 1968, Geology of the Southeast Missouri lead district : in Ore Deposits of the United States, 1933-1967, edited by John D. Ridge, v.1, p.326-358, Amer. Inst. Min., Metall., and Petrol. Eng., New York.

Sorey, M. L., 1978, Numerical modeling of liquid geothermal systems : U.S. Geological Survey Professional Paper 1044-D, 25 p.

Stallman, R. W., 1963, Computation of groundwater velocity from temperature data, in Methods of collecting and interpreting groundwater data, edited by R. Bentall, U.S. Geological Survey, Water Supply Paper 1554-H, p.36-46.

Stanton, R. L., 1972, Ore Petrology : McGraw-Hill, New York.

Straus, J. M. and G. Schubert, 1977, Thermal convection of water in a porous medium : effects of temperature-and pressure-dependent thermodynamic and transport properties : Jour. Geophys. Res., v.82, p.325-333.

Sverjensky, D. A., 1981, The origin of a Mississippi Valley-type deposit in the Viburnum trend, southeast Missouri : Econ. Geol., v.76, p.1848-1872.

Sverjensky, D. A., D. M. Rye and B. R. Doe, 1979, The lead and sulfur isotopic compositions of galena from a Mississippi Valley-type deposit in the New Lead Belt, southeast Missouri : Econ. Geol., v.74, p.149-153.

Tissot, B. P. and D. H. Welte, 1978, Petroleum Formation and Occurrence : Springer-Verlag, Berlin, 538 p.

Tóth, J., 1962, A theory of groundwater motion in small drainage basins in central Alberta : Jour. Geophys. Res., v.67, p.4375-4387.

_____, 1963, A theoretical analysis of groundwater flow in small drainage basins : Jour. Geophys. Res., v.68, p.4795-4812.

_____, 1978, Gravity-induced cross-formational flow of formational fluids, Red Earth region, Alberta, Canada : Analysis, patterns, and evolution : Water Resour. Res., v.14, p.805-843.

_____, 1980, Cross-formational gravity-flow of groundwater : A mechamism of transport and accumulation of petroleum (the generalized hydraulic theory of petroleum migration) : in Problems of Petroleum Migration, edited by W. H. Roberts, III, and R. J. Cordell, Amer. Assoc. Petrol. Geol., Studies in Geology No.10, p.121-167.

Tyvand, P. A., 1977, Heat dispersion effect on thermal convection in anisotropic porous media : Jour. Hydrol., v.34, p.335-342.

_____, 1981, Influence of heat dispersion on steady convection in anisotropic porous media : Jour. Hydrol., v.52, p.13-23.

van Everdingen, R. O., 1968, Studies of formation waters in Western Canada : Geochemistry and hydrodynamics : Can. Jour. Earth Sci., v.5, p.523-543.

Van Zeggeren, F. and S. H. Storey, 1970, The Computation of Chemical Equilibria : Cambridge University Press, 176 p.

Vogwill, R. I. J., 1976, Some practical aspects of open-pit dewatering at Pine Point : Bull. Can. Inst. Min. and Metall., v.69, p.76-88.

Walters, L. J., Jr. and T. J. Wolery, 1975, A monotone-sequences algorithm and FORTRAN IV program for calculation of equilibrium distributions of chemical species : Computers and Geosciences, v.1, p.57-63.

Wang, H. F. and M. P. Anderson, 1982, Introduction to Groundwater Modeling - Finite Difference and Finite Element Methods : W. H. Freeman and Co., San Francisco, 237 p.

Weber, J. E., 1975, Dispersion effect on buoyancy-driven convection in stratified flows through porous media : Jour. Hydrol., v.25, p.59-70.

White, D. E., 1968, Environments of generation of some base-metal ore deposits : Econ. Geol., v.63, p.301-335.

_____, 1974, Diverse origins of hydrothermal ore fluids : Econ. Geol., v.69, p.954-973.

White, W. S., 1971, A paleohydrologic model for mineralization of the White Pine copper deposit, northern Michigan : Econ. Geol., v.66, p.1-13.

Williams, G. K., 1978, An update of subsurface information, Cretaceous rocks, Trout Lake area, southern Northwest Territories : in Current Research Part A, Geol. Surv. Can., Paper 78-1A, p.545-553.

_____, 1979, Personal communication : in Macqueen, R. W. and T. G. Powell, in press, Organic geochemistry of the Pine Point lead-zinc ore field and region, Northwest Territories, Canada : Econ. Geol.

_____, 1981, Notes to accompany maps and cross-sections, Middle Devonian barrier-complex of western Canada : Geol. Surv. Can., Open File : Report 761, 17 p.

Witherspoon, P. A., S. P. Neuman, M. L. Sorey, M. J. Lippman, 1975, Modeling geothermal systems : Univ. California, Lawrence Berkeley Laboratory, Report 3263, 68 p.

Wolery, T. J., 1978, Some chemical aspects of hydro-thermal processes at mid-oceanic ridges - a theoretical study. 1. Basalt-sea water reaction and chemical cycling between the oceanic crust and oceans. II. Calculations of chemical equilibrium between aqueous solutions and minerals : Ph.D. thesis, Northwestern University, Evanston, Illinois, 263 p.

_____, 1979a, Calculation of chemical equilibrium between aqueous solutions and minerals : The EQ3/EQ6 software package, UCRL-52658, Univ. California, Lawrence Livermore Laboratory, Livermore, Ca., 41 p.

_____, 1979b, Computer simulation of temperature-dependent equilibrium precipitation : Geothermal Resources Council, Trans., v.3, p.793-795.

_____, 1980, Chemical modeling of geologic disposal of nuclear waste : progress report and a perspective : UCRL-52748, Univ. of California, Lawrence Livermore Laboratory, Livermore, Ca., 66 p.

Wolery, T. J. and L. J. Walters, Jr., 1975, Calculation of equilibrium distributions of chemical species in aqueous solutions by means of monotone sequences : Math. Geology, v.7, p.99-115.

Wolf, K. H., (Ed.), 1976, Handbook of Strata-Bound and Stratiform Ore Deposits: (7 volumes), Elsevier, Amsterdam.

Woodside, W. and J. H. Messmer, 1961, Thermal conductivity of porous media, in (1) unconsolidated and (2) consolidated sands : Jour. Appl. Phys. v.32, p.1688-1699.

Yih, C., 1961, Flow of a non-homogeneous fluid in a porous medium : Jour. Fluid Mech., v.10, p.133-140.

Zienkiewicz, O. C., 1977, The Finite Element Method, 3rd ed. : McGraw-Hill, New York, 787 p.